energies

Special Issue Reprint

Modeling and Analysis of Power Systems

Edited by
Konrad Zajkowski

mdpi.com/journal/energies

MDPI

Modeling and Analysis of Power Systems

Modeling and Analysis of Power Systems

Guest Editor

Konrad Zajkowski

MDPI

Basel • Beijing • Wuhan • Barcelona • Belgrade • Novi Sad • Cluj • Manchester

Guest Editor
Konrad Zajkowski
Department of Energy
Koszalin University of Technology
Koszalin
Poland

Editorial Office
MDPI AG
Grosspeteranlage 5
4052 Basel, Switzerland

This is a reprint of the Special Issue, published open access by the journal *Energies* (ISSN 1996-1073), freely accessible at: https://www.mdpi.com/journal/energies/special_issues/S39D576G61.

For citation purposes, cite each article independently as indicated on the article page online and as indicated below:

Lastname, A.A.; Lastname, B.B. Article Title. *Journal Name* **Year**, *Volume Number*, Page Range.

ISBN 978-3-7258-8949-5 (Hbk)
ISBN 978-3-7258-8950-1 (PDF)
https://doi.org/10.3390/books978-3-7258-8950-1

Cover image courtesy of Konrad Zajkowski

Contents

About the Editor

Konrad Zajkowski

Konrad Zajkowski is an academic teacher, researcher and author of publications in electrical engineering and electric power engineering, affiliated with Koszalin University of Technology, Poland. He currently works at the Department of Energy, Faculty of Mechanical Engineering and Energy, where he is involved in teaching and research.

His research interests focus on the theory of power in electrical circuits, mathematical descriptions of phenomena in alternating-current circuits with nonsinusoidal waveforms, power compensation, switching overvoltages and their mitigation, transients in electrical circuits, the effects of nonlinearities on electrical parameters, and improving the efficiency of electric power transmission.

An important area of his research is the analysis of electrical circuits with nonsinusoidal voltage and current waveforms and power compensation. He employs, among other approaches, the theory of Current's Physical Components (CPC) and investigates power factor improvement in single-phase and three-phase systems, including systems with waveform distortion and load asymmetry. His scientific work also includes the modeling and analysis of electric power systems.

He is the author and co-author of numerous monographs, textbooks and teaching materials in electrical engineering. His academic output comprises more than one hundred scientific publications and several dozen conference papers, as well as monographs, textbooks and patents.

His current research focuses on power theory, analysis of circuits with nonsinusoidal waveforms, power compensation, and improving the efficiency of electric power systems. He combines scientific research with academic teaching, addressing both fundamental problems in circuit and power theory and practical issues related to electric power quality, power compensation and efficient electric power transmission.

energies

MDPI

Article

Transient Overvoltage Security Region and Overvoltage Comprehensive Suppression Method for the Entire Fault Process in Renewable Energy Collection System Under Asymmetric Fault

Biyang Wang [1], Jieyi Chen [2,*], Shirui Liu [2], Nan Xia [3] and Lei Luo [1]

[1] Electric Power Research Institute of State Grid Shaanxi Electric Power Co., Ltd., Xi'an 710048, China; wangbiyang1991@163.com (B.W.); loulei@sn.sgcc.com.cn (L.L.)
[2] School of Electrical and Electronic Engineering, North China Electric Power University, Beijing 102206, China; liusr0914@163.com
[3] State Grid Shaanxi Electric Power Research Institute, Xi'an 710100, China; pattyxianan@126.com
* Correspondence: 15630449959@163.com

Abstract

During the asymmetric short-circuit period and the fault recovery stage of the renewable energy collection system, the non-fault phase and the PCC point show transient overvoltage characteristics, respectively, which threaten the safe and stable operation of the system. Aiming at the transient overvoltage problem during the asymmetric fault of the renewable energy collection system, this paper first establishes the sequence component equivalent circuit of the renewable energy collection system, deduces the expression of non-fault phase overvoltage at the fault point considering asymmetric fault ride-through control of renewable energy, and reveals the influence of negative-sequence reactive current of renewable energy on non-fault phase overvoltage. Secondly, combined with the system equation and the constraints of overcurrent and overvoltage, the safety region of the renewable energy current reference value under asymmetric fault is established. On this basis, the transient overvoltage comprehensive suppression strategy based on the optimization of the current reference value during fault and the rapid identification of fault clearing time is proposed, which realizes the overvoltage suppression in the full process of asymmetric fault. Finally, the renewable energy collection system is built in the Matlab/Simulink R2023b simulation platform, and the correctness and effectiveness of the transient overvoltage analysis and suppression strategy proposed in this paper are verified.

Keywords: transient overvoltage; asymmetric short-circuit fault; new energy collection system; overvoltage suppression

1. Introduction

Low-voltage ride-through control is commonly adopted in renewable energy integration systems to support stable operation during faults. However, asymmetric short-circuit faults lead to transient overvoltage in the non-faulted phases, and after fault clearance, delayed control exit produces reactive power surplus, which further induces overvoltage at the grid connection point, easily causing generator disconnection and threatening system security and renewable energy absorption [1–3]. With large-scale renewable energy feeding into the main grid through high-voltage AC channels, and the collection areas lacking synchronous source support, transient overvoltage problems become increasingly prominent [4–6]. Therefore, analyzing the transient overvoltage mechanisms of renewable energy delivery systems under asymmetric faults and studying their suppression methods is an important basis for ensuring safe and stable system operation.

Existing studies on transient overvoltage in renewable energy transmission systems primarily focus on overvoltages occurring after the clearance of symmetric faults and during asymmetric faults. In symmetric fault scenarios, references [7–11] analyze the mechanisms of overvoltage caused by renewable energy after fault clearance, indicating that delayed withdrawal of low-voltage ride-through by renewable units results in reactive power surplus, which subsequently leads to overvoltage in the system. Reference [12] analyzes the mechanisms by which reactive power compensation devices produce a surplus of reactive power in the system. Reference [13] presents a method for calculating overvoltage caused by reactive power surplus under symmetric faults, while reference [14] proposes an evaluation approach for overvoltage in systems with multiple renewable energy plants. Regarding overvoltage mitigation under symmetric faults, reference [15] derives reasonable setpoints for renewable reactive current based on transient overvoltage expression following symmetric short-circuit clearance. Reference [16] introduces an adaptive reactive current compensation strategy, which adjusts generator current references based on measured system parameters to suppress overvoltage after symmetric fault clearance.

For asymmetric fault scenarios, existing studies primarily focus on analyzing and mitigating transient overvoltage during the fault. Reference [17] examines transient overvoltage issues under non-full-phase operation and indicates that the overvoltage magnitude is influenced by factors such as renewable power output and control strategies. Reference [18] proposes a method to calculate system overvoltage during asymmetric short circuits but does not detail how key factors affect the overvoltage characteristics. To address overvoltage suppression under unbalanced voltage sags, Reference [19] introduces a voltage support strategy at the point of common coupling (PCC) of renewable energy systems, which prevents the phase voltage magnitude at the grid connection point from exceeding defined limits during short-circuit faults. Reference [20] theoretically analyzed the dynamic processes of transient overvoltage at the rectifier station induced by commutation failures under different types of asymmetrical faults. Reference [21] proposed a transient overvoltage mitigation strategy based on reactive power support; however, its test cases are primarily limited to symmetrical fault scenarios, with little consideration given to asymmetrical ones. The above references focus only on suppressing overvoltage at renewable energy integration points during asymmetric short-circuit faults and do not consider the suppression of power-frequency overvoltage in non-faulted phases at the system fault location. In addition, current control strategies are designed only for overvoltage during the fault, with few addressing overvoltage after asymmetric fault clearance, making it difficult to achieve comprehensive overvoltage suppression throughout the entire asymmetric fault process.

This study addresses transient overvoltage in AC transmission systems delivering renewable energy under asymmetric short-circuit faults. It first quantitatively characterizes overvoltage in the unfaulted phases at the fault location and reveals the mechanism by which negative-sequence reactive current contributes to the overvoltage. Based on system constraints, a transient overvoltage safety region is then constructed. Building on this, a comprehensive mitigation method is proposed that suppresses transient overvoltage both during the fault and after fault clearance, utilizing the full-process voltage support capability of renewable energy. Finally, simulations validate the accuracy and effectiveness of the proposed approach.

https://doi.org/10.3390/en19163773

2. Analysis of Transient Overvoltage During Asymmetric Faults

2.1. AC Collection System for Renewable Energy

The AC transmission system of a direct-drive wind farm is illustrated in Figure 1. The wind farm connects to the 35 kV bus and is stepped up to 220 kV before delivery to the grid via AC transmission lines, with the fault located on the high-voltage AC line. The 0.69 kV/35 kV transformer employs a Dyn11 connection, while the 35 kV/220 kV transformer uses a YNd11 connection.

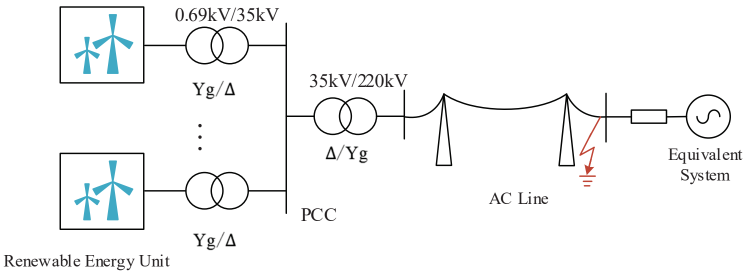

Figure 1. System structure diagram.

The grid-side converter of the direct-drive wind turbine adopts a control strategy based on a voltage-oriented dual current loop for positive and negative sequences. In this strategy, the positive- and negative-sequence electrical quantities are transformed into d-q coordinates of forward and reverse rotating reference frames, respectively, enabling decoupled control of the positive- and negative-sequence components. The converter is then controlled through the output of sinusoidal pulse width modulation (SPWM) signals. The control scheme is illustrated in Figure 2. The positive-sequence and negative-sequence voltage reference values provided by the current loop are

$$\begin{cases} v_{dref1} = k_{p1}\left(i_{dref1} - i_{d1}\right) + k_{i1}\int\left(i_{dref1} - i_{d1}\right)dt + \omega L_g i_{q1} + u_{d1} \\ v_{qref1} = k_{p1}\left(i_{qref1} - i_{q1}\right) + k_{i1}\int\left(i_{qref1} - i_{q1}\right)dt - \omega L_g i_{d1} + u_{q1} \\ v_{dref2} = k_{p2}\left(i_{dref2} - i_{d2}\right) + k_{i2}\int\left(i_{dref2} - i_{d2}\right)dt - \omega L_g i_{q2} + u_{d2} \\ v_{qref2} = k_{p2}\left(i_{qref2} - i_{q2}\right) + k_{i2}\int\left(i_{qref2} - i_{q2}\right)dt + \omega L_g i_{d2} + u_{q2} \end{cases} \tag{1}$$

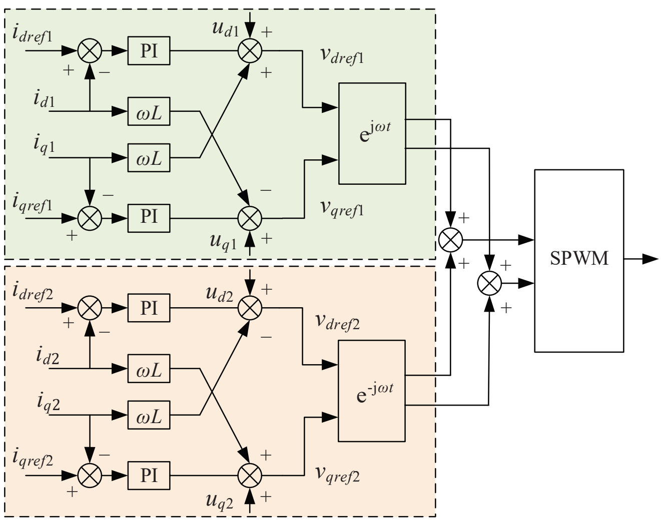

Figure 2. Positive- and negative-sequence dual current-loop control structure of the grid-side converter under asymmetric fault conditions.

In the equation, k_p and k_i represent PI control parameters, the subscripts 1 and 2 denote the positive-sequence and negative-sequence components, respectively, and the subscripts d and q denote the components of the electrical quantities on the *d-axis* and q-axis, respectively. L_g represents the AC-side inductance of the converter, u represents the voltage at the renewable energy grid connection point, and i represents the output current of the renewable energy source.

The control structure shown in Figure 2 is based on the positive- and negative-sequence dual current-loop control commonly used for grid-connected converters under unbalanced grid-voltage conditions [18]. The positive-sequence voltage and current components are transformed into the forward synchronous rotating reference frame, whereas the negative-sequence components are transformed into the reverse synchronous rotating reference frame. Therefore, the positive- and negative-sequence current components can be controlled separately.

In the positive-sequence current loop, i_{d1} and i_{q1} are regulated by PI controllers according to their reference values. With the adopted voltage-oriented control, i_{d1} mainly corresponds to the positive-sequence active current, while i_{q1} mainly corresponds to the positive-sequence reactive current. In the negative-sequence current loop, i_{d2} and i_{q2} are regulated in the reverse synchronous rotating reference frame.

It should be noted that the sign of the negative-sequence reactive current depends on the adopted current reference direction and reactive-power convention. To avoid ambiguity, in this paper, positive i_{q2} is defined as the negative-sequence capacitive reactive current output by the renewable energy converter, while negative i_{q2} corresponds to the absorption of negative-sequence inductive reactive current.

The ωL_g terms in Figure 2 are introduced as decoupling compensation terms for the converter-side inductor, and u_d, u_{q1}, u_{d2}, and u_{q2} are used as voltage feedforward terms. After PI regulation and decoupling compensation, the positive- and negative-sequence voltage references are transformed back to the stationary reference frame and synthesized as the modulation voltage reference. The SPWM module then generates the switching signals for the grid-side converter.

During normal operation, the wind turbine outputs the positive-sequence active current according to the active power command, while the positive-sequence reactive current and the negative-sequence current references are set to zero. When an asymmetric voltage sag is detected at the PCC, the converter switches to the asymmetric fault ride-through mode. In this paper, the asymmetric fault condition is identified when the positive-sequence voltage amplitude U_1 enters the low-voltage ride-through range and the negative-sequence voltage amplitude U_2 or the voltage unbalance factor U_2/U_1 exceeds a preset threshold. This condition corresponds to unbalanced short-circuit faults, such as two-phase-to-ground faults and phase-to-phase faults.

Under the asymmetric fault ride-through mode, the positive-sequence reactive current reference is generated according to the positive-sequence voltage deviation. It can be expressed as

$$i_{q1} = \begin{cases} 0, & U_1 \geq 0.9 \\ k_1(0.9 - U_1), & U_{\min} \leq U_1 < 0.9 \end{cases} \tag{2}$$

where U_1 is the positive-sequence voltage amplitude at the PCC and k_1 is the positive-sequence reactive current coefficient. The calculated current reference is further limited by the converter current capacity.

In this paper, the negative-sequence active current reference is set to zero, and positive i_{q2} is defined as the negative-sequence capacitive reactive current output by the renewable energy converter. This current is introduced to regulate the negative-sequence voltage component and suppress the overvoltage of the non-faulted phase during asymmetric

https://doi.org/10.3390/en19163773

faults. Therefore, i_{q2} is selected as the main optimization variable, and its feasible range is determined by the converter current limit, the PCC voltage limit, and the non-faulted phase voltage limit at the fault location.

During asymmetric faults, the short-circuit current provided by the renewable energy source is determined by its control strategy. Therefore, the renewable energy can be modeled as a current source, assuming that the actual output current equals its current reference. This study analyzes and calculates two types of asymmetric short-circuit faults: two-phase-to-ground faults and two-phase faults.

2.2. System Overvoltage Analysis During Two-Phase-to-Ground Fault

When a two-phase metal-to-ground fault occurs on an AC transmission line, the equivalent circuit for the system's sequence components can be established as shown in Figure 3, based on Figure 1, where the renewable energy source is modeled as a current source.

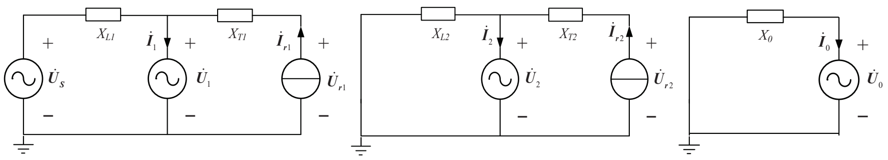

Figure 3. Each sequence circuit in the case of a two-phase grounding short circuit: (**a**) positive-sequence equivalent circuit; (**b**) negative-sequence equivalent circuit; (**c**) zero-sequence equivalent circuit.

In Figure 3, X_L is the sum of the line reactance on the grid side and the system equivalent reactance, whilst X_T is the sum of the line reactance on the renewable energy side and the transformer reactance. $\dot{\boldsymbol{U}}$ $\dot{I}$ are the phase vectors of the voltage and current to earth at the fault point. The subscripts 1, 2 and 0 represent positive-sequence, negative-sequence and zero-sequence quantities, respectively. The positive-sequence terminal voltage vector of the renewable energy source is $\dot{\boldsymbol{U}}_{r1} = U_{r1}\angle\delta_{u1}$, and the positive-sequence output current vector $\dot{I}r1$ is $I_{r1}\angle(\delta_{u1}-\Delta\delta_1)$. The expressions are

$$
\begin{array}{l}
I_{r1} = \sqrt{{I_{d1}}^2 + {I_{q1}}^2} \\
\Delta\delta_1 = \arctan\left(I_{q1}/I_{d1}\right)
\end{array}
\tag{3}
$$

where I_d and I_q are the active and reactive current components of the new energy source, respectively.

The phasor of the negative-sequence terminal voltage of the renewable energy source is $\dot{\boldsymbol{U}}_{r2} = U_{r2}\angle\delta_{u2}$; the phasor of the negative-sequence current of the renewable energy source $\dot{I}_{r2}$ is $I_{q2}\angle(\delta_{u2} + \Delta\delta_2)$, which has no active current component, and therefore $\Delta\delta_2 = 90^\circ$.

From Figure 3, the system circuit equations can be derived; for the purposes of analysis, line-to-ground capacitance and resistance are neglected. The forward voltage equation is

$$
\begin{cases}
\dot{\boldsymbol{U}}_{\boldsymbol{oc}1} = \dot{\boldsymbol{U}}_{\boldsymbol{S}} + jZ_{L1}\dot{\boldsymbol{I}}_{\boldsymbol{r}1} \\
Z_{eq1} = jZ_{L1} \\
\dot{\boldsymbol{U}}_1 = \dot{\boldsymbol{U}}_{\boldsymbol{oc}1} - \boldsymbol{Z}_{eq1}\dot{\boldsymbol{I}}_1 \\
\dot{\boldsymbol{U}}_{\boldsymbol{r}1} = \dot{\boldsymbol{U}}_1 + jZ_{T1}\dot{\boldsymbol{I}}_{\boldsymbol{r}1}
\end{cases}
\tag{4}
$$

https://doi.org/10.3390/en19163773

The negative-sequence voltage equation is

$$\begin{cases} \dot{\boldsymbol{U}}_{\boldsymbol{oc2}} = jZ_{L2}\dot{\boldsymbol{I}}_{\boldsymbol{r2}} \\ Z_{eq2} = jZ_{L2} \\ \dot{\boldsymbol{U}}_{\boldsymbol{2}} = \dot{\boldsymbol{U}}_{\boldsymbol{oc2}} - Z_{eq2}\dot{\boldsymbol{I}}_{\boldsymbol{2}} \\ \dot{\boldsymbol{U}}_{\boldsymbol{r2}} = \dot{\boldsymbol{U}}_{\boldsymbol{2}} + jZ_{T2}\dot{\boldsymbol{I}}_{\boldsymbol{r2}} \end{cases} \tag{5}$$

The zero-sequence voltage equation is

$$\begin{cases} \dot{\boldsymbol{U}}_{\boldsymbol{oc0}} = 0 \\ Z_{eq0} = jZ_0 \\ \dot{\boldsymbol{U}}_{\boldsymbol{0}} = -Z_{eq0}\dot{\boldsymbol{I}}_{\boldsymbol{0}} \end{cases} \tag{6}$$

The system boundary conditions in the event of a metal-to-ground fault on phases B and C are

$$\begin{cases} \dot{\boldsymbol{U}}_0 = \dot{\boldsymbol{U}}_1 = \dot{\boldsymbol{U}}_2 \\ \dot{\boldsymbol{I}}_0 + \dot{\boldsymbol{I}}_1 + \dot{\boldsymbol{I}}_2 = 0 \end{cases} \tag{7}$$

where $\dot{\boldsymbol{U}}_{oc}$ is the open-circuit voltage at the fault location, and Z_{eq} is the Davenport equivalent impedance at the fault location.

Substituting Equations (4)–(6) into Equation (7) yields the voltage phasor of the non-faulted phase A at the fault point as

$$\dot{\boldsymbol{U}}_{\boldsymbol{A}} = 3\dot{\boldsymbol{U}}_1 = 3\frac{Z_{eq2}Z_{eq0}\dot{\boldsymbol{U}}_{\boldsymbol{oc}1} + Z_{eq1}Z_{eq0}\dot{\boldsymbol{U}}_{\boldsymbol{oc}2}}{Z_{eq1}Z_{eq2} + Z_{eq1}Z_{eq0} + Z_{eq2}Z_{eq0}} \tag{8}$$

In this paper, $Z_{eq1} = Z_{eq2}$, so the voltage phasor of the non-faulty phase A at the fault point can be simplified to

$$\begin{cases} \dot{\boldsymbol{U}}_{\boldsymbol{A}} = \frac{3k}{1+2k}\left(\dot{\boldsymbol{U}}_{\boldsymbol{oc}1} + \dot{\boldsymbol{U}}_{\boldsymbol{oc}2}\right) \\ \dot{\boldsymbol{U}}_{\boldsymbol{oc}1} = \dot{\boldsymbol{U}}_{\boldsymbol{S}} + jX_{L1}\dot{\boldsymbol{I}}_{\boldsymbol{r}1} \\ \dot{\boldsymbol{U}}_{\boldsymbol{oc}2} = jZ_{L2}\dot{\boldsymbol{I}}_{\boldsymbol{r}2} \end{cases} \tag{9}$$

where $k = Z_{eq0}/Z_{eq1}$.

2.3. System Overvoltage Analysis for a Two-Phase Short Circuit

When a two-phase short-circuit fault occurs on the transmission line, the equivalent circuit diagram of the system is similar to that in Figure 3, but without the zero-sequence circuit. The positive-sequence and negative-sequence voltage equations of the system are identical to Equations (4) and (5). The boundary conditions for a short circuit between phases B and C are

$$\begin{cases} \dot{\boldsymbol{I}}_0 = 0 \\ \dot{\boldsymbol{U}}_1 = \dot{\boldsymbol{U}}_2 \\ \dot{\boldsymbol{I}}_1 + \dot{\boldsymbol{I}}_2 = 0 \end{cases} \tag{10}$$

It can be derived that the voltage of the non-faulty phase at the fault point is

$$\dot{\boldsymbol{U}}_{\boldsymbol{A}} = \dot{\boldsymbol{U}}_{\boldsymbol{oc}1} + \dot{\boldsymbol{U}}_{\boldsymbol{oc}2} \tag{11}$$

It can be observed that Equation (11) lacks the coefficient term $3k/(1 + 2k)$ compared to Equation (9). Therefore, when k is greater than 1, the magnitude of the transient overvoltage caused by a two-phase short circuit will be smaller than that caused by a two-phase-to-ground fault.

https://doi.org/10.3390/en19163773

For single-phase-to-ground faults, the method for calculating system transient overvoltage is similar to the approach described above. However, because the overvoltage is relatively low under single-phase-to-ground conditions, this study focuses on analyzing the system overvoltage under two-phase short-circuit faults.

2.4. Analysis of Factors Affecting Transient Overvoltage During Asymmetrical Faults

2.4.1. The Influence of Negative-Sequence Reactive Current During a Two-Phase Short Circuit

As can be seen from Equation (9), system overvoltages are primarily influenced by the positive-sequence and negative-sequence reactive currents from renewable energy sources. The following analysis examines two scenarios: when the wind turbine does not generate power, and when it generates positive-sequence active power.

First, we analyze the case where the renewable energy source outputs only positive-sequence reactive current and negative-sequence reactive current. From Equations (3) to (7), it can be deduced that $\dot{U}_{oc1}$ and $\dot{U}_{oc2}$ lie on the same line (i.e., these two phasors are in-phase or out-of-phase), and that $\dot{U}_{oc1}$ and $jx\dot{I}_{r1}$ are in-phase. When the renewable energy source outputs positive-sequence reactive current and outputs negative-sequence capacitive reactive current, the phasor relationships are shown in Figure 4. The phases of $\dot{U}_{oc1}$ and $\dot{U}_{oc2}$ are out of phase; therefore, when the negative-sequence reactive current absorbed by the renewable energy source is increased during a fault, the magnitude of $\dot{U}_{oc2}$ will increase accordingly, whilst the magnitude of $\dot{U}_{oc1} + \dot{U}_{oc2}$ will decrease. Consequently, as can be seen from Equation (9), the magnitude of the overvoltage on the non-faulted phase at the system fault point will decrease. Furthermore, when the positive-sequence reactive current output from the new energy source is increased, it follows from Equation (4) that $\left|\dot{U}_{oc1}\right|$ will increase, thereby exacerbating the overvoltage level in the non-faulty phase at the fault point.

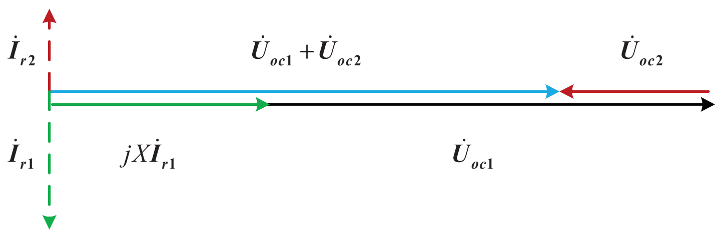

Figure 4. Electrical quantity phasor relationship diagram of two-phase grounding.

When the positive-sequence active current output by the renewable energy source is non-zero, Equations (4)–(7) yield that $\dot{U}_0$ is in phase with $\dot{U}_2$ but out of phase with $\dot{U}_1$. Furthermore, combining this with Equation (4) shows that $\dot{U}_{oc1}$ is in phase with $\dot{U}_1$. Combining this with the renewable energy control conditions yields that $jx\dot{I}_{r1}$ is in phase with $\dot{U}_1$. From the renewable energy control conditions and Equation (5), it follows that $\dot{U}_{oc2}$ is out of phase with $\dot{U}_{r2}$. From Equations (4) to (7), it follows that $\dot{U}_1$ and $\dot{U}_{r2}$ are out of phase, and from Equation (4), it is evident that $\dot{U}_{oc1}$ and $\dot{U}_1$ are in phase. It is easy to deduce that $\dot{U}_{oc1}$ and $\dot{U}_{oc2}$ are in phase, and it can also be shown that $\dot{U}_{oc1}$ and $\dot{U}_{oc2}$ are collinear. As shown in Figure 4, increasing the inductive negative-sequence reactive current absorbed by the renewable energy source can reduce the overvoltage of the non-faulted phase at the fault location. According to the adopted current reference direction, this absorption of inductive negative-sequence reactive current is equivalent to the injection of capacitive negative-sequence reactive current, which weakens the negative-sequence voltage component and mitigates the non-faulted phase overvoltage.

https://doi.org/10.3390/en19163773

The preceding analysis demonstrates that increasing the negative-sequence capacitive reactive current injected by the renewable energy source can increase the overvoltage of the unfaulted phase at the fault location.

2.4.2. The Effect of Negative-Sequence Reactive Current During a Two-Phase Short Circuit

As deduced from Equations (4), (5), and (10), the transient overvoltage of the unfaulted phase at the fault location during a phase-to-phase short circuit exhibits characteristics similar to those observed under a double-phase-to-ground fault. Specifically, increasing the negative-sequence capacitive reactive current injected by renewable energy systems mitigates the overvoltage in the unfaulted phase.

3. Safety Margin for New Energy Current Reference Values

3.1. Establishment of the Safety Margin for New Energy Current Reference Values

This paper analyzes the case of a two-phase earth fault occurring on an AC transmission line. Given the system parameters and *the reference values* for the forward active and reactive currents of the renewable energy source, i_{d1} and i_{q1}, Equations (4)–(7) can be coupled with the corresponding constraint equations. By solving this system of equations, *the corresponding* i_{q2} boundary values for different combinations of forward active and reactive currents from the renewable energy source can be determined. *The corresponding* i_{q2} boundary values can be obtained separately, and the boundary surface of the reverse-sequence reactive current from the renewable energy source can be constructed in a three-dimensional coordinate system with i_{d1} and i_{q1} as *the* x and *y axes and* i_{q2} as the z-axis. A boundary value surface for the negative-sequence reactive current of the renewable energy source can be constructed. In this paper, the constraint equations comprise three categories: 1. Phase current amplitude constraints for the renewable energy output. 2. Overvoltage amplitude constraints for the non-faulted phases at the fault point. 3. Phase voltage amplitude constraints at the renewable energy grid connection point.

Regarding the calculation of boundary values on i_{q2}, the primary consideration is the constraint on the phase current limit of the renewable energy source, for which the constraint equation is defined such that the phase current magnitudes of the three phases (A, B, C) of the renewable energy source are each equal to *the limit value* I_m:

$$\begin{cases} I_{rabc} = I_m = \sqrt{(I_{r1})^2 + (I_{r2})^2 + 2I_{r1}I_{r2}\cos(\varphi_i + \varphi)} \\ I_{r1} = \sqrt{(I_{d1})^2 + (I_{q1})^2} \\ I_{r2} = \sqrt{(I_{d2})^2 + (I_{q2})^2} \end{cases} \tag{12}$$

Here, I_{r1} and I_{r2} represent the positive-sequence and negative-sequence current amplitudes of the renewable energy source, respectively. φ_i denotes the difference between the initial phase angles of the positive-sequence and negative-sequence currents, where $\varphi = 0°/120°/-120°$.

Combining Equations (4)–(7) and (12) yields a boundary surface constrained by the phase current amplitude. The minimum surface is defined as the upper boundary of the parameter domain. When the negative-sequence reactive current reference remains below this boundary, the renewable energy unit avoids overcurrent conditions.

The voltage boundary constraints comprise two types: non-fault-phase voltage constraints and grid-connection-point voltage constraints. The first type of voltage boundary constraint is defined as follows: let the overvoltage of the non-fault phase at the fault point be equal to *the limit* U_{off}:

$$\left|\dot{U}_A\right| = 3\left|\dot{U}_1\right| = U_{off} \tag{13}$$

https://doi.org/10.3390/en19163773

Combining Equation (13) with Equations (4)–(7) yields the boundary surface for i_{q2} under the first voltage constraint. Monotonicity analysis demonstrates that selecting values above this boundary prevents the overvoltage of the unfaulted phase from exceeding the defined limits.

The second type of voltage boundary constraint is as follows: set the phase voltage magnitudes of *the three-phase voltage* U_{rabc} at the renewable energy grid connection point to equal *the limit* V_m, where the phase voltage magnitudes at the grid connection point are given by

$$\begin{pmatrix} \dot{U}_{ra} \\ \dot{U}_{rb} \\ \dot{U}_{rc} \end{pmatrix} = \begin{pmatrix} 1 & 1 & 1 \\ a^2 & a & 1 \\ a & a^2 & 1 \end{pmatrix} \begin{pmatrix} \dot{U}_{r1} \\ \dot{U}_{r2} \\ 0 \end{pmatrix} \quad (14)$$

Combining the constraint Equation (14) with Equations (4)–(7) yields the boundary surface for the negative-sequence reactive current, which is constrained by the phase voltage amplitude at the grid connection point of the renewable energy system.

The region enclosed by these boundary surfaces defines the safe operating area for the renewable energy current references. Selecting values within this area ensures that the renewable energy system avoids overcurrent conditions while maintaining both the voltage at the grid connection point and the unfaulted phase voltage at the fault location within their specified limits.

3.2. Case Study

This section takes as an example a BC-phase earth fault occurring near the system side on a 220 kV AC line. The 220 kV AC line is set to a length of 100 km, with line parameters as shown in Table 1. The system positive-sequence equivalent reactance is 0.25 p.u., the system negative-sequence equivalent reactance is 0.84 p.u., and the transformer leakage reactance is 0.05 p.u. I_m is set to 1.15 p.u., V_m to 1.1 p.u., and U_{off} to 1.2 p.u. During the fault, the forward active current of the renewable energy source is set to 0–0.25 p.u., and its forward reactive current to 0.3–0.65 p.u. Based on the safety-region calculation procedure described in Section 3.1, the feasible region of the negative-sequence capacitive reactive current reference of the renewable energy source is obtained, as shown in Figure 5.

Table 1. Unit length parameters of AC line.

	Reactance per Unit Length (p.u./km)
Line forward reactance	2.5×10^{-3}
Line zero-sequence reactance	7×10^{-3}

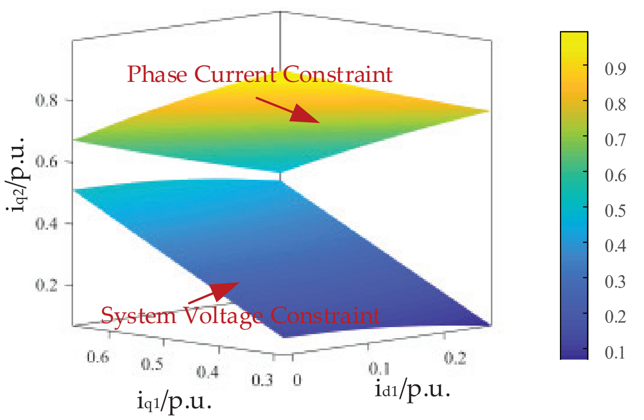

Figure 5. Renewable energy current reference value security region.

https://doi.org/10.3390/en19163773

Under the system parameters specified in this section, the phase voltage at the grid connection point remains within limits during a double-phase-to-ground fault, and therefore the corresponding surface is omitted from the figure. In Figure 5, the region enclosed by the upper surface derived from the renewable energy phase current constraint and the lower surface determined by the system overvoltage constraint defines the safe operating area for the current references. The voltage and current limits used for constructing the security region are selected according to relevant power-quality requirements, renewable energy ride-through requirements, and the converter current-limiting capability of the studied system. In this paper, V_m =1.1 p.u. is adopted as the upper limit of the phase voltage at the renewable energy grid connection point, and U_{off} = 1.2 p.u. is adopted as the transient overvoltage security boundary for the non-faulted phase at the fault location. The converter phase-current limit is set to I_m = 1.15 p.u. These limits are used to define the feasible current-reference region under asymmetric faults. Operating within this domain ensures that the converter output current, the PCC phase voltage, and the non-faulted phase voltage at the fault location remain within the predefined limits adopted in this study.

4. Comprehensive Method for Suppressing System Transient Overvoltages

To address the overvoltage characteristics associated with asymmetric faults, this paper proposes a coordinated suppression method that covers both the fault-on period and the post-clearance recovery period. During the asymmetric short-circuit period, the method aims to limit the overvoltage of the non-faulted phase at the fault location. After fault clearance, it suppresses the transient overvoltage at the renewable energy grid connection point caused by the delayed withdrawal of fault ride-through control and the resulting reactive current surplus. The proposed approach fully leverages the transient voltage control capabilities of renewable energy systems both during and after the fault to effectively suppress system overvoltage.

4.1. Method for Suppressing System Transient Voltage During Asymmetric Short Circuits

Based on the system topology shown in Figure 1, the relationship between the positive-sequence and negative-sequence voltage amplitudes at the PCC point and the system voltage is given by

$$\begin{aligned} V_1 &= \sqrt{(V_{g1})^2 - (\omega L I_{d1})^2} + \omega L I_{q1} \\ V_2 &= \sqrt{(V_{g2})^2 - (\omega L I_{d2})^2} - \omega L I_{q2} \end{aligned} \tag{15}$$

In the equation, V_1 and V_2 are the positive-sequence and negative-sequence voltage amplitudes at the PCC point, respectively; V_{g1} and V_{g2} are the positive-sequence and negative-sequence voltage amplitudes on the system side, respectively; and L is the equivalent line inductance. The relationship between *the* phase *voltage amplitude* V_{abc} at the PCC point and the positive-sequence and negative-sequence voltage amplitudes at the PCC point is given by

$$V_{abc} = \sqrt{(V_1)^2 + (V_2)^2 + 2V_1V_2\cos(\varphi_u + \varphi)} \tag{16}$$

where φ_u is the difference in initial phase angles between the positive-sequence and negative-sequence voltages at the PCC point. $\varphi = 0^\circ/120^\circ/-120^\circ$.

Taking into account that the renewable energy source terminal and the PCC point are connected via the Dy11 transformer, whose positive- and negative-sequence voltages are shifted by 30°, respectively, the expression for the phase voltage amplitude at the renewable energy source terminal can be derived as

$$V_{jabc} = \sqrt{(V_1)^2 + (V_2)^2 + 2V_1V_2\cos(\varphi_u + \varphi + 60^\circ)} \tag{17}$$

The expression for *the* three-phase *current amplitudes* I_{rabc} of the renewable energy output is

$$I_{rabc} = \sqrt{(I_{r1})^2 + (I_{r2})^2 + 2I_{r1}I_{r2}\cos(\varphi_i + \varphi)} \tag{18}$$

where I_{r1} and I_{r2} are the positive-sequence and negative-sequence current amplitudes of the renewable energy source, respectively. φ_i is the difference in initial phase angles between the positive-sequence and negative-sequence currents.

From Equations (14)–(17), it can be seen that by selecting appropriate current reference values, the objective of ensuring that phase voltages and phase currents do not exceed the limits can be achieved. V_{g1}, V_{g1}, φ_u, φ_i and other electrical quantities can be obtained through real-time system monitoring and extracted from the positive- and negative-sequence components. To ensure the safe grid connection of the renewable energy source during an asymmetric short circuit, the following constraints are set: (1) the phase voltage amplitudes at the PCC point and the generator terminal of the renewable energy source shall not exceed *the constraint value* V_m; and (2) the phase current amplitude of the renewable energy source output shall not exceed *the constraint value* I_m.

To limit the power-frequency overvoltage of the non-faulted phase at the fault location, the negative-sequence reactive current reference of the renewable energy source should be increased within the allowable current and voltage constraints. Therefore, the determination of the current reference is formulated as a constrained nonlinear optimization problem. Since the fmincon function in MATLAB R2023b solves minimization problems, the objective function is defined as $\min f(x) = -i_{q2}$, which is equivalent to maximizing the negative-sequence reactive current reference i_{q2}. The optimization is subject to the converter phase-current limit, the PCC phase voltage limit, and the non-faulted phase voltage limit at the fault location. In addition, the positive-sequence reactive current of the renewable energy source is calculated in accordance with national standards, and the expression is given by Equation (2), where k_1 is the positive-sequence reactive power ratio coefficient of the renewable energy source. The positive-sequence active current of the renewable energy source is set as a constant, and its negative-sequence active current is 0 p.u.

In summary, the calculation process for the renewable energy current reference values during an asymmetric short circuit is shown in Figure 6.

In principle, the renewable energy current reference calculated by the proposed method lies on the upper boundary of the safe operating area shown in Figure 5. Furthermore, the effectiveness of this strategy in mitigating the overvoltage of the unfaulted phase depends on additional factors, including the capacity of the renewable energy system and specific system parameters.

4.2. Comprehensive Suppression Method Accounting for Overvoltage Following Asymmetric Short-Circuit Clearance

Following the clearance of an asymmetric fault, the negative-sequence reactive current of renewable energy systems exhibits a withdrawal delay. Consequently, this current output not only fails to suppress the transient overvoltage but instead exacerbates the overvoltage level, as illustrated in Figure 7.

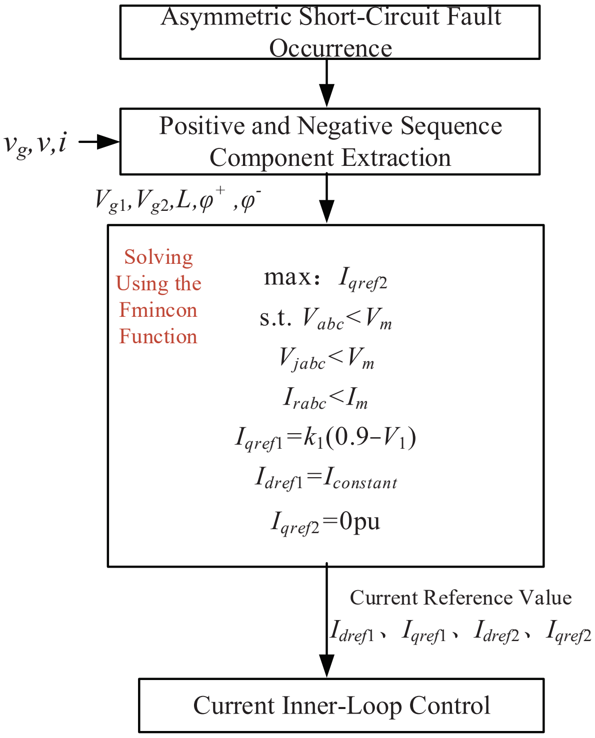

Figure 6. The current reference value calculation flow chart of renewable energy.

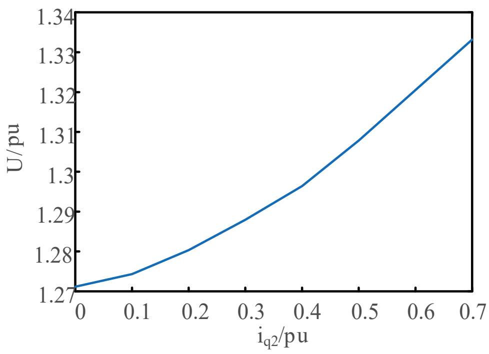

Figure 7. The influence of i_{q2} on transient overvoltage.

Given that the transient overvoltage following fault clearance primarily results from the delayed withdrawal of fault ride-through control in renewable energy systems, rapidly identifying the fault termination instant is essential for suppressing this overvoltage.

Consequently, this paper proposes a rapid fault clearance detection method based on the first derivative of the positive-sequence voltage amplitude at the point of common coupling. In the proposed fault-clearance detection method, the positive-sequence voltage amplitude at the PCC is first processed by a first-order low-pass filter to reduce the influence of measurement noise. The derivative of the filtered positive-sequence voltage amplitude is then calculated. When the derivative exceeds a predefined positive threshold, the fault is considered to be cleared, and the post-fault compensation control is activated.

During the LVRT exit-delay period after fault clearance, compensation terms are added to the positive- and negative-sequence reactive current references to offset the remaining reactive current commands generated by the LVRT controller. Specifically, once the fault-clearance condition is satisfied, the compensation mechanism is enabled and generates offset components that counteract the reactive current commands produced during the LVRT stage. As a result, the remaining positive- and negative-sequence reactive current

https://doi.org/10.3390/en19163773

commands are rapidly reduced to zero or near zero during the LVRT exit-delay period. When the LVRT controller is deactivated, the compensation mechanism is also disabled, and the additional control action is removed. Compared to traditional methods relying on voltage amplitude thresholds, this approach significantly reduces the detection delay and effectively suppresses the overvoltage.

Integrating the suppression methods presented in Section 4.1 with those detailed in this section yields a comprehensive mitigation strategy for system transient overvoltage, applicable both during asymmetric short-circuit faults and subsequent to fault clearance. Figure 8 illustrates the corresponding control block diagram.

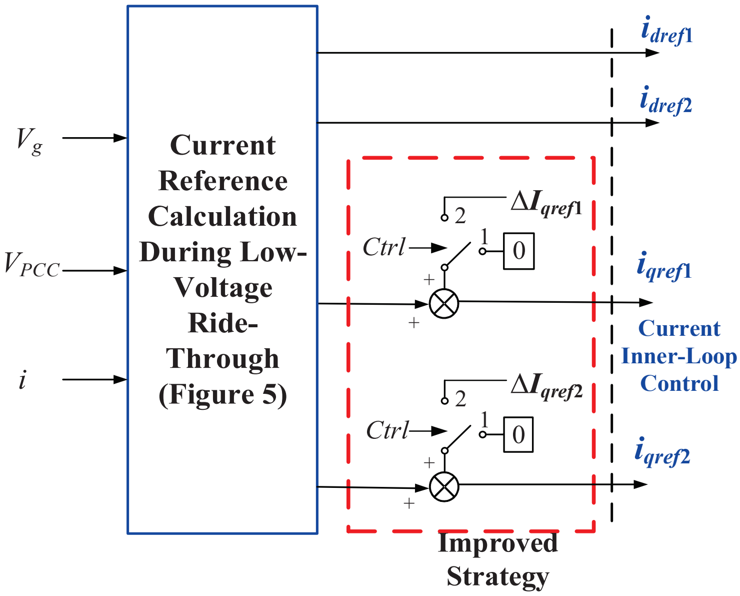

Figure 8. Transient overvoltage comprehensive suppression strategy diagram.

In Figure 8, the variable Ctrl serves as the enable signal for the control strategy proposed in this section. A value of 1 activates the strategy, whereas a value of 0 deactivates it. In this paper, the compensation component for the current reference is set to the negative value of the corresponding current reference.

5. Case Study Analysis

5.1. System Parameters and Simulation Scenarios

A system model, as shown in Figure 1, was constructed using MATLAB/Simulink: the wind turbine employs a voltage-source converter model, and during a fault, a positive- and negative-sequence dual current-loop control strategy based on grid voltage orientation is adopted. The wind turbine uses a multiplicative model, with a total capacity of 200 MVA. The 220 kV AC transmission line is set to a length of 100 km, with its parameters as shown in Table 1. An asymmetric fault occurs at the system end of the 220 kV AC transmission line at 0.4 s and is cleared at 0.8 s. All electrical quantities are expressed in normalized values, with reference values set at 200 MVA and 220 kV.

5.2. Effect of Negative-Sequence Reactive Current from Renewable Energy on System Overvoltage

During the fault, the positive-sequence active and reactive currents of the renewable energy source are 0.2 p.u. and 0.4 p.u., respectively, whilst the reference values for the negative-sequence reactive current are taken as 0 p.u., 0.1 p.u. and 0.3 p.u. The theoretical and simulated values of the non-fault phase voltage at the fault point during a BC phase-

https://doi.org/10.3390/en19163773

to-ground fault are shown in Table 2, and the waveforms of the non-fault phase voltage at the fault point under different short-circuit fault types are shown in Figure 9.

Table 2. Comparison of theoretical value and simulation value of non-fault phase voltage at fault point.

i_{q2}/p.u.	Theoretical Value/p.u.	Simulated Value/p.u.	Relative Error/%
0	1.265	1.281	1.26
0.1	1.234	1.249	1.22
0.3	1.172	1.184	1.02

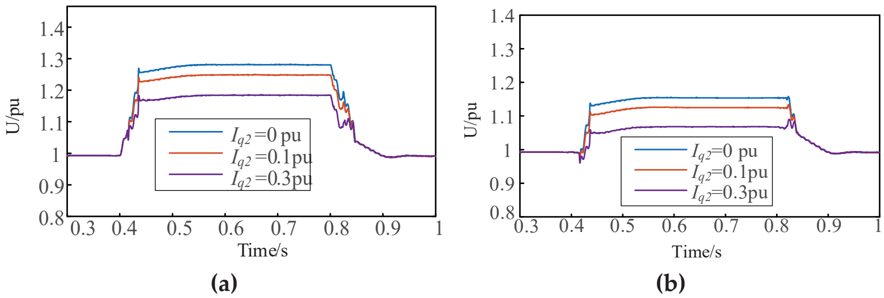

Figure 9. The influence of negative-sequence reactive current on transient overvoltage. (**a**) BC short-circuit to earth fault; (**b**) BC short-circuit fault.

Table 2 indicates that the theoretical and simulated values of the unfaulted phase voltage exhibit minimal deviation, demonstrating the high accuracy of the proposed mathematical model in calculating the system power frequency overvoltage during a fault. Furthermore, Figure 9 illustrates that an increase in the negative-sequence reactive current absorbed by renewable energy systems during the fault leads to a reduction in the unfaulted phase voltage. The results also confirm that the overvoltage condition induced by a double-phase-to-ground fault is more severe, which aligns with the preceding analytical findings.

5.3. Verification of System Overvoltage Suppression Methods During Asymmetric Faults

This section analyzes a scenario involving a BC-phase metallic earth fault occurring on an AC line close to the system side. The converter current limit I_m is set to 1.15 p.u.; the phase voltage limit V_m is set to 1.1 p.u. Two operating conditions are set out below to compare system overvoltages during the short-circuit event.

Condition 1: During the fault, the forward reactive power ratio coefficient k_1 of the renewable energy source is set to 1.2, the forward active current reference value is set to 0.2 p.u., and the reverse active current reference value of the renewable energy source is set to 0 p.u.

Condition 2: The positive-sequence current parameters remain the same as in Case 1, with the negative-sequence current reference fixed at 0.3 p.u.

Condition 3: The positive-sequence current parameters remain the same as in Case 1, while the negative-sequence current is adjusted to limit the PCC phase voltage according to the method described in [19].

Condition 4: The forward-sequence current parameters for the renewable energy source are the same as in Case 1, whilst the reference value for the reverse-sequence reactive current of the renewable energy source is derived using the method proposed in this paper.

https://doi.org/10.3390/en19163773

Figure 10 illustrates the voltage waveforms of the unfaulted phase at the fault location under the four operating conditions. The corresponding voltage and current waveforms for the second operating condition are presented in Figure 11.

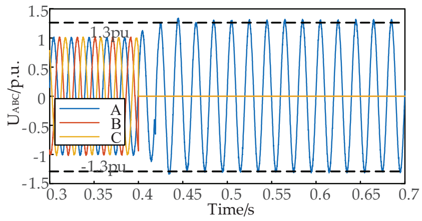

(**a**)

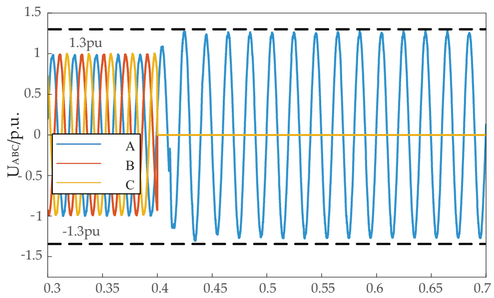

(**b**)

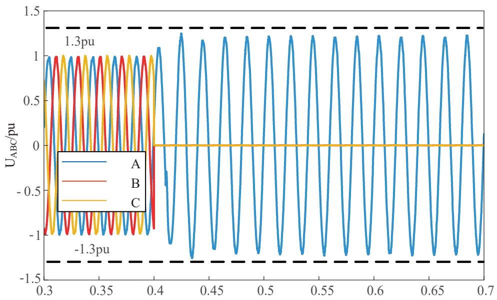

(**c**)

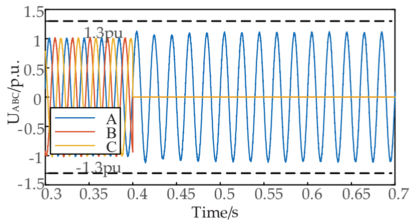

(**d**)

Figure 10. Three-phase voltage waveform of 220 kV fault point. (**a**) Operating Condition 1; (**b**) Operating Condition 2; (**c**) Operating Condition 3; (**d**) Operating Condition 4.

As shown in Figures 10 and 11, under Operating Condition 1, when the renewable energy source does not output negative-sequence current, the voltage of the non-faulted phase at the fault point exceeds 1.3 p.u.; under Operating Condition 4 following the application of the method described in this paper, the voltages at both the generator terminal and the grid connection point remain within limits, the output current does not exceed the limit value, and the overvoltage of the non-faulted phase is reduced to below 1.3 p.u.

We added simulations with 100 ms and 200 ms fault durations to verify the response capability of the proposed method under short-duration faults. The results demonstrate that the proposed fmincon-based current-reference calculation can still provide effective current references and suppress transient overvoltage under shorter fault durations. In

https://doi.org/10.3390/en19163773

addition, filtering of the measured input quantities has been added in the control process to reduce the influence of measurement delay, noise, and transient oscillations, thereby improving the practical robustness of the proposed control strategy.

This method fully utilizes the transient voltage control capability of renewable energy sources to effectively reduce power-frequency overvoltages during faults whilst ensuring safe grid connection.

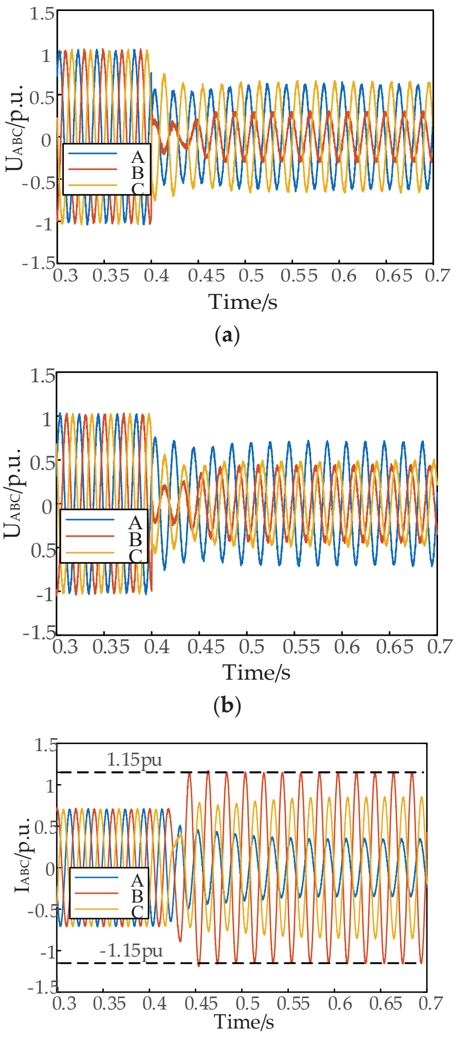

(**c**)

Figure 11. Control effect of Condition 4. (**a**) Three-phase voltage waveform at the PCC point; (**b**) three-phase voltage waveform at the renewable energy generator terminal; (**c**) three-phase current waveform of the renewable energy source.

5.4. Verification of Overvoltage Suppression Strategy Following Asymmetric Short-Circuit Clearance

In this paper, the control switching delay for renewable energy sources is set to 20 ms, the time constant of the inertial filter is set to 0.05 s, and the threshold for the first derivative of voltage is set to 0.3 p.u./s. During the ride-through of an asymmetric fault, the analysis of renewable energy sources follows the example of Scenario 4 in Section 5.2. After the fault is cleared, the following two scenarios are set up to compare the transient overvoltage conditions at the grid connection point of the renewable energy sources after the short circuit is cleared.

Condition 5: The additional control proposed in this paper is not activated after fault clearance.

Condition 6: The additional control proposed in this paper is activated after the fault is cleared.

A comparison of the control performance between Scenario 5 and Scenario 6 is shown in Figure 12.

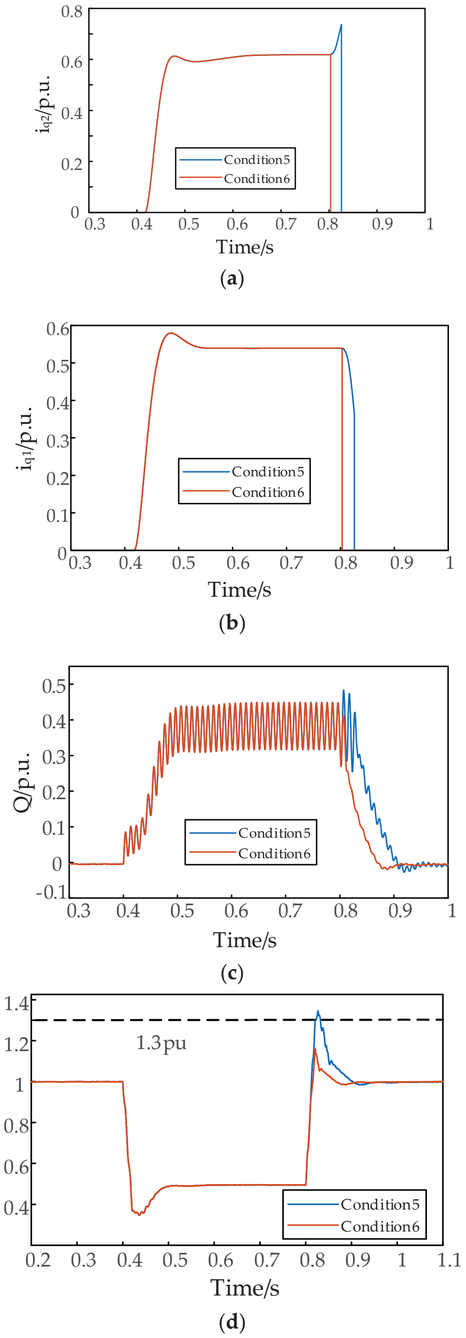

Figure 12. Comparison of control effect of Conditions 5 and 6. (**a**) Command value for negative-sequence reactive current of the renewable energy source; (**b**) command value for positive-sequence reactive current of the renewable energy source; (**c**) renewable energy reactive power output; (**d**) grid connection point voltage amplitude.

As shown in Figure 12, in Condition 4, following fault clearance, the retraction of both positive-sequence and negative-sequence reactive currents from the renewable energy source was relatively slow, resulting in a significant reactive power surplus. The transient overvoltage at the grid connection point exceeded 1.3 p.u., posing a risk of disconnection; under Operating Condition 6, following the application of the control method proposed

https://doi.org/10.3390/en19163773

in this paper, the reactive current began to recede at 0.803 s (approximately 20 ms earlier than in Operating Condition 3), and the overvoltage peak was reduced to 1.06 p.u., which is below 1.3 p.u., effectively suppressing the transient overvoltage.

In conclusion, the proposed strategy mitigates the overvoltage of the unfaulted phase during asymmetric short circuits and suppresses the overvoltage at the grid connection point following fault clearance, thereby ensuring the safe operation of the system.

6. Conclusions

This paper addresses the transient overvoltage issue in renewable energy AC transmission systems under asymmetric short circuits. It reveals the overvoltage mechanism of the unfaulted phase during the fault, establishes a safe operating area for the negative-sequence reactive current, and proposes a comprehensive transient overvoltage suppression method for the entire process that accounts for the conditions following fault clearance. The main conclusions are summarized as follows:

(1) During an asymmetric short-circuit fault, a power frequency overvoltage occurs on the unfaulted phase at the fault location. This overvoltage depends on the system parameters, alongside the positive-sequence and negative-sequence control parameters of the renewable energy system. Increasing the negative-sequence capacitive reactive current output by the renewable energy system reduces this power-frequency overvoltage during the fault.

(2) By integrating system voltage equations with overcurrent and voltage constraints, this paper establishes a safe operating area for transient overvoltage under asymmetric faults. Selecting values within this domain ensures that renewable energy systems avoid overcurrent conditions while maintaining both the voltage at the grid connection point and the unfaulted phase voltage at the fault location within their specified limits.

(3) This paper proposes a comprehensive transient overvoltage suppression method for the entire asymmetric fault process. By fully exploiting the voltage control capabilities of renewable energy systems under both steady-state and transient conditions, the proposed approach mitigates system transient overvoltage during asymmetric short circuits and subsequent to fault clearance. Simulation results demonstrate that the proposed strategy effectively suppresses overvoltage.

Author Contributions: Conceptualization, B.W., N.X. and L.L.; methodology, J.C.; software, S.L.; validation, B.W., N.X. and L.L.; formal analysis, B.W.; investigation, N.X.; resources, L.L.; data curation, B.W.; writing—original draft preparation, J.C.; writing—review and editing, S.L. and L.L.; visualization, B.W.; supervision, N.X.; project administration, L.L.; funding acquisition, B.W. All authors have read and agreed to the published version of the manuscript.

Funding: This research was funded by State Grid Corporation's Science and Technology Project Funding "Research and Application of Key Technologies and Control Systems for Enhancing the Transient Voltage Safety Level of New Energy Bases in the Near Area of Ultra-High Voltage Direct Current—Research on Transient Voltage Characteristics and Risk Assessment Methods", grant number 5226SX25000B.

Data Availability Statement: The original contributions presented in this study are included in the article.

Conflicts of Interest: Authors Biyang Wang and Lei Luo were employed by the company Electric Power Research Institute of State Grid Shaanxi Electric Power Co., Ltd., Xi'an, China; Author Nan Xia was employed by the company State Grid Shaanxi Electric Power Research Institute, Xi'an, China. The authors declare that this study received funding from State Grid Shaanxi Electric Power Company

https://doi.org/10.3390/en19163773

Science and Technology Projects. The funder was not involved in the study design, collection, analysis, interpretation of data, the writing of this article or the decision to submit it for publication.

References

1. Chen, G.; Li, M.; Xu, T.; Zhang, J.; Wang, C. Practice and challenge of renewable energy development based on interconnected power grids. *Power Syst. Technol.* **2017**, *41*, 3095–3103. [CrossRef]
2. Wang, X.; Liu, C.; Lin, W.; Xie, H. Influence of wind turbine fault ride-through characteristics on transient overvoltage of large-scale wind power DC transmission systems and parameter optimization. *Power Syst. Technol.* **2021**, *45*, 4612–4620. [CrossRef]
3. Jia, J.; Jin, Y.; Zhao, B.; Zhong, W.; Cheng, S.; Liu, T.; Xu, X.; Zheng, S. Influence and optimization of wind turbine low voltage ride-through control on system transient overvoltage. *Power Syst. Technol.* **2021**, *45*, 526–533. [CrossRef]
4. Luo, Y.; Yao, J.; Zhang, T.; Pei, J.; Zhang, F. Coordinated control strategy of sending-end system under monopole blocking scenario of large-scale wind power DC transmission system. *Trans. China Electrotech. Soc.* **2019**, *34*, 4108–4118. [CrossRef]
5. Xi, G.; Zhao, B.; Zheng, S.; Shen, L.; Jia, Q.; Yuan, C. Transmission capacity and enhancement measures of renewable energy base via UHV AC transmission system. *Electr. Power Constr.* **2022**, *43*, 131–138.
6. Yue, H.; Shao, G.; Xia, D.; Sun, M.; Liu, Y.; Wang, K. Reactive power control strategy of UHV DC weak sending-end system considering overvoltage suppression. *Autom. Electr. Power Syst.* **2020**, *44*, 172–179.
7. Fan, P.; Liu, F.; Wang, J.; Tang, L.; Dai, M. Review on transient overvoltage of large-scale renewable energy integration system. *Insul. Surge Arresters* **2023**, *6*, 94–102. [CrossRef]
8. Du, W.; Luo, Y.; Li, Y.; Wu, L.; Zhao, F.; Sun, D. Review of transient overvoltage caused by reactive power surplus in wind power integration system. *Proc. CSEE* **2022**, *42*, 3224–3239. [CrossRef]
9. Tu, J.; Zhang, J.; Liu, M.; Pan, Y.; Xi, G.; Yi, J. Mechanism analysis of large-disturbance transient overvoltage considering wind turbine dynamic characteristics. *Autom. Electr. Power Syst.* **2020**, *44*, 197–205.
10. Liu, H.; Wang, K. Influence of reactive current of new energy low voltage ride-through on transient voltage security constraints. *Electr. Power* **2022**, *55*, 152–158.
11. Zhao, H.; Yao, L.; Wang, W.; Zhang, W.; Chi, Y.; Li, Y. Analysis of high-voltage disconnection of large-scale wind power and coordinated preventive control strategy. *Autom. Electr. Power Syst.* **2015**, *39*, 43–48+65.
12. Lv, Q.; Xu, Z.; Li, H.; Xiao, J.; Wang, S. Influence of dynamic reactive power compensation on transient voltage of wind farm and control strategy. *Electr. Power Constr.* **2015**, *36*, 122–129.
13. Wang, T.; Pei, L.; Wang, J.; Wang, Z. Overvoltage suppression under commutation failure based on improved voltage-dependent current order limiter control strategy. *IEEE Trans. Ind. Appl.* **2022**, *58*, 4914–4922. [CrossRef]
14. Liu, X.; Shi, X.; Xin, H.; Zheng, D.; Gao, H.; Ni, Q. Fast overvoltage assessment method for multi-station renewable energy system during fault recovery period. *Autom. Electr. Power Syst.* **2023**, *47*, 168–175.
15. Xu, S.; Sun, H.; Wang, S.; Wang, J.; Bi, J. Overvoltage in high-proportion power electronic power systems (Part II): Mechanism of temporary power frequency overvoltage under AC symmetrical faults. *Proc. CSEE* **2024**, *44*, 1701–1712. [CrossRef]
16. Cao, B.; Zheng, Z.; Liu, H.; Xie, Q.; Jia, Z.; Wu, J. Overvoltage suppression strategy for direct-drive wind turbine after fault based on reactive current compensation. *Autom. Electr. Power Syst.* **2025**, *49*, 166–174.
17. Wu, L.; Wang, X.; Yang, Y.; Sun, Y.; Yu, S.; Sun, D. Power frequency overvoltage during open-phase operation after single transient fault clearing in renewable energy gathering system. *High Volt. Eng.* **2022**, *48*, 4362–4373.
18. Wang, S.; Chen, X.; Zheng, Z.; Li, J.; Zhang, Z.; Lin, R.; Wang, Y.; Lu, H. Electromagnetic transient study of asymmetric grounding and load shedding in offshore wind power transmission system with permanent magnet direct-drive wind turbines. *Proc. CSEE* **2024**, *44*, 827–838. [CrossRef]
19. Shabestary, M.M.; Mohamed, Y.A.-R.I. Asymmetrical Ride-Through and Grid Support in Converter-Interfaced DG Units Under Unbalanced Conditions. *IEEE Trans. Ind. Electron.* **2019**, *66*, 1130–1141. [CrossRef]
20. Han, Z.; Wang, T.; Wang, X.; Wang, Z.; Zhao, W. Analysis of transient overvoltage characteristics at the sending end during LCC-HVDC commutation failure induced by asymmetrical faults at the receiving end. *Power Syst. Technol.* **2025**, *49*, 1532–1540. [CrossRef]
21. Yang, H.; Liu, H.; Ding, Z.; Sun, Z.; Liu, C.; Cai, G.; Zhang, G. Two-stage optimal configuration of synchronous condensers in sending-end grid with high proportion of wind power considering short-circuit ratio enhancement and transient overvoltage suppression. *Power Syst. Technol.* **2024**, *48*, 540–552. [CrossRef]

https://doi.org/10.3390/en19163773

energies

Article

On the Use of Clarke Transformation for the Transient Analysis of Asymmetrical Faults in Three-Phase Power Systems

Diego Bellan

Department of Electronics, Information and Bioengineering, Politecnico di Milano, 20133 Milan, Italy; diego.bellan@polimi.it

Abstract

This work provides a theoretical/methodological contribution to the transient analysis of asymmetrical faults in three-phase systems. Transient analysis of three-phase systems is usually performed by resorting either to the instantaneous Symmetrical Component Transformation (SCT) or to numerical methods. In this paper, an analytical methodology based on the time-domain Clarke transformation is presented for the transient analysis of the most common asymmetrical faults. For each kind of asymmetrical fault, a specific circuit coupling between the Clarke $\alpha\beta0$ circuits is derived. Two main advantages are obtained over the SCT approach. First, the Clarke circuits involve real-valued voltages/currents, instead of complex variables as with the SCT. Second, the Clarke circuits $\alpha\beta0$ are not all coupled to each other. Therefore, the dynamic order of the Clarke equivalent circuits is lower than that of the SCT circuits. This property can be of interest in both the derivation of analytical and numerical solutions. A simple radial system is used to exemplify the proposed methodology.

Keywords: Clarke transformation; asymmetrical fault analysis; power quality; power system analysis; space vectors; time-domain analysis; transient analysis; voltage sags

1. Introduction

Transients are a common phenomenon in three-phase power systems. Indeed, transients can be due to external causes like lightning or internal intended/unintended causes like system operations and faults. Transient analysis is of paramount importance in modern power systems because, typically, they imply temporary overcurrents and overvoltages that could lead to malfunctioning and damage of system components [1].

As far as faults are concerned, extensive literature can be found about steady-state analytical calculation of voltage/current faults [2,3]. Such conventional approaches are mainly based on a proper adaptation of the well-known Symmetrical Component Transformation (SCT) operating on phasor variables.

On the contrary, when time-domain analysis (i.e., transient analysis) is required, the related literature appears fragmentary and less systematic, especially when asymmetrical faults are concerned. Actually, the inadequacy for transient analysis of the phasor SCT was soon recognized, and the time-domain Clarke transformation was recognized as more suited to transient analysis [4,5]. Papers [4,5], however, were not using the so-called power invariant form of the Clarke transformation, and therefore, a systematic and general derivation of equivalent circuits for asymmetrical faults was not provided.

Thus, asymmetrical faults were typically approached through numerical tools such as the well-known Electromagnetic Transient Program (EMTP) [6,7]. Other interesting methods have been introduced and studied in the past years, such as dynamic phasor modeling, able to provide accurate models of converter-dominated power systems, with remarkable computational speed gains [8,9].

As far as analytical approaches are concerned, providing deeper insight into transient phenomena, a further attempt to use the SCT for asymmetrical faults was introduced through the instantaneous SCT [10–12]. The main advantage of the instantaneous SCT is the use of the same interconnections of sequence circuits as for asymmetrical faults in the sinusoidal steady state. An important drawback, however, is the introduction of complex time-domain voltages and currents in the resulting dynamic circuits.

In the past few years, the Clarke transformation was rediscovered as a powerful tool well-suited for manipulating time-domain variables. The first systematic application of the Clarke transformation for transient analysis of asymmetrical faults was proposed in [13], where it was also made clear that the Clarke equivalent circuits can also be useful for numerical analysis. Advantages of the Clarke transformation over the instantaneous SCT were confirmed in [14], where a simplified equivalent circuit was obtained for the single-phase fault.

This paper is based on the systematic use of the Clarke transformation for the transient analytical solution of asymmetrical faults, i.e., single-phase and double-phase grounded/ungrounded faults. For each kind of asymmetrical fault, a proper circuit coupling between Clarke α, β, and zero circuits is derived, allowing the exact analytical transient solution of the resulting dynamic circuit. Moreover, it is shown that the Clarke equivalent circuits have lower dynamic order with respect to the corresponding instantaneous SCT equivalent circuits. This point leads to simpler analytical solutions and provides deeper insight into the transient phenomena.

Clarke transformation is also the basis for the definition of voltage/current space vectors [15–18]. A voltage/current space vector is a complex-valued time function where the real and imaginary parts are given by the α and β components of a Clarke-transformed voltage/current, respectively. In the ideal unfaulted case, the trajectory of the voltage space vector on the complex plane is circular. On the contrary, in the case of an asymmetrical fault, the trajectory of the voltage space vector on the complex plane is elliptical, where the inclination angle of the ellipse allows the classification of the kind of fault [19–30]. Figure 1 shows the classification angles for single-phase (S) and double-phase (D) faults [30]. Notice that in [30], only the special case of a steady-state single-phase fault was considered. In this paper, however, the transient solution through the Clarke transformation is proposed, and a more general fault condition is considered, including asymmetrical double-phase faults. Thus, the results derived in the paper also allow straightforward detection, classification, and characterization of a specific kind of fault. Moreover, the impact of circuit parameters on the effectiveness of fault characterization can be readily determined.

The general methodology introduced in this paper can be outlined as follows. The main assumption is the three-phase symmetry of the system, apart from the fault section where fault constraints are typically asymmetrical. The symmetric part of the three-phase system is processed according to the Clarke transformation. Thus, three circuits, named α, β, and zero, with transformed topology and variables can be defined. The asymmetrical part, i.e., the fault section, is characterized by specific constraints on the phase variables, depending on the kind of fault (i.e., single/double-phase, grounded/ungrounded). The constraints on the phase variables, once Clarke transformed, become constraints on the α, β, and 0 variables at the fault location. Through specific mathematical derivations, it is shown that such constraints can be represented as proper circuit elements (mainly ideal transformers) coupling the α, β, and 0 circuits. Thanks to such simple equivalent circuits, the three-phase transient can be easily solved in the time domain for each specific kind of

https://doi.org/10.3390/en19112580

fault. It is worth highlighting that such an approach is not approximate, but it provides a rigorous and exact analytical solution, equivalent to the instantaneous SCT solution. Numerical simulations of transients in a three-phase radial system validate the correctness of the proposed analytical approach.

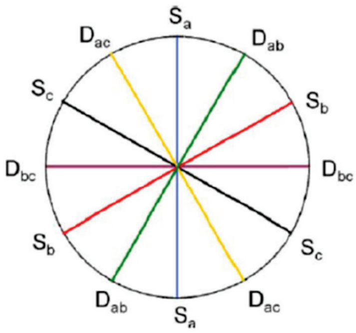

Figure 1. The voltage space vector shows an elliptical behavior on the complex plane, where the inclination angle of the ellipse depends on the kind of fault. Single-phase faults ($S_{a,b,c}$) correspond to 0°, 60°, and 120°. Double-phase faults ($D_{ab,bc,ac}$) correspond to 30°, 90°, and 50° [30].

The paper is organized as follows. In Section 2, the instantaneous SCT is discussed. In Section 3, the Clarke transformation and some topological aspects are reported. In Section 4, the analytical derivations for the single-phase fault, the double-phase grounded/ungrounded faults, and the introduction of the related equivalent circuits are presented in detail. In Section 5, a comparison between the instantaneous SCT and Clarke equivalent circuits for transient analysis is presented. Numerical validation of the derived analytical results and equivalent circuits is reported in Section 6 for a three-phase radial system. Finally, conclusions are presented in Section 7.

2. Conventional Transient Analysis Through Instantaneous SCT

Transient analysis of three-phase systems was introduced in [10] with specific reference to rotating electric machines. The methodology, however, can be readily extended to general power systems as shown in [11]. The basic underlying idea consists of extending the conventional SCT, originally introduced in the phasor domain, to time-domain variables. Therefore, by considering a column vector of time-domain phase voltages $\boldsymbol{v}_{abc} = \begin{bmatrix} v_a & v_b & v_c \end{bmatrix}^T$, the instantaneous SCT (ISCT) is defined as:

$$\boldsymbol{v}_{pn0} = \begin{bmatrix} \overline{v}_p \\ \overline{v}_n \\ v_0 \end{bmatrix} = \boldsymbol{S}\boldsymbol{v}_{abc} = \frac{\mathbf{1}}{\sqrt{\mathbf{3}}} \begin{bmatrix} 1 & a & a^2 \\ 0 & a^2 & a \\ 1 & 1 & 1 \end{bmatrix} \begin{bmatrix} v_a \\ v_b \\ v_c \end{bmatrix} \tag{1}$$

where $\boldsymbol{S}$ is the SCT matrix in the power invariant form such that $\boldsymbol{S}^{-1} = \boldsymbol{S}^{*T}$, $a = e^{j\frac{2\pi}{3}}$, $\overline{v}_p$ and $\overline{v}_n$ are complex-valued voltages such that $\overline{v}_n = \overline{v}_p^*$, whereas v_0 is a real-valued voltage. Of course, the same transformation given in (1) holds for phase currents.

Notice that since the ISCT (1) is based on the same transformation matrix $\boldsymbol{S}$ as the conventional SCT, asymmetrical-fault transient analysis leads to the same equivalent circuits commonly used for the steady-state analysis of asymmetrical faults. This point will be detailed in Section 5 where the ISCT approach will be compared with the Clarke components approach proposed in this paper.

https://doi.org/10.3390/en19112580

3. Clarke Transformation and Three-Phase Circuit Analysis

Let us consider a column vector of time-domain phase voltages $\boldsymbol{v}_{abc}$. The Clarke transformation of $\boldsymbol{v}_{abc}$ is defined as [4–6]:

$$\boldsymbol{v}_{\alpha\beta 0} = \begin{bmatrix} v_\alpha \\ v_\beta \\ v_0 \end{bmatrix} = \boldsymbol{T}\boldsymbol{v}_{abc} = \sqrt{\frac{2}{3}} \begin{bmatrix} 1 & -\frac{1}{2} & -\frac{1}{2} \\ 0 & \frac{\sqrt{3}}{2} & -\frac{\sqrt{3}}{2} \\ \frac{1}{\sqrt{2}} & \frac{1}{\sqrt{2}} & \frac{1}{\sqrt{2}} \end{bmatrix} \begin{bmatrix} v_a \\ v_b \\ v_c \end{bmatrix} \tag{2}$$

where the transformation matrix $\boldsymbol{T}$ is defined in the power invariant form, from the *abc* domain to the transformed $\alpha\beta 0$ domain. This property is of paramount importance in order to define consistent equivalent circuits in the Clarke domain.

The main feature of the Clarke transformation is the diagonalization of balanced three-phase component matrices. As a remarkable example, for a symmetrical mutual inductor in the time domain, we obtain [30]:

$$\begin{aligned} \begin{bmatrix} v_\alpha \\ v_\beta \\ v_0 \end{bmatrix} &= \boldsymbol{T} \begin{bmatrix} L_{ph} & L_m & L_m \\ L_m & L_{ph} & L_m \\ L_m & L_m & L_{ph} \end{bmatrix} \boldsymbol{T}^{-1} \tfrac{d}{dt} \begin{bmatrix} i_\alpha \\ i_\beta \\ i_0 \end{bmatrix} = \\ &= \begin{bmatrix} L_{ph} - L_m & 0 & 0 \\ 0 & L_{ph} - L_m & 0 \\ 0 & 0 & L_{ph} + 2L_m \end{bmatrix} \tfrac{d}{dt} \begin{bmatrix} i_\alpha \\ i_\beta \\ i_0 \end{bmatrix} = \\ &= \begin{bmatrix} L_\alpha & 0 & 0 \\ 0 & L_\beta & 0 \\ 0 & 0 & L_0 \end{bmatrix} \tfrac{d}{dt} \begin{bmatrix} i_\alpha \\ i_\beta \\ i_0 \end{bmatrix} \end{aligned} \tag{3}$$

Thus, three uncoupled equations were obtained in (3). Moreover, by considering that $L_\alpha = L_\beta$, the first two equations can be combined in one complex equation as:

$$\overline{v} = v_\alpha + jv_\beta = L\frac{d}{dt}\left(i_\alpha + ji_\beta\right) = L\frac{d}{dt}\overline{i} \tag{4}$$

where the voltage/current space vectors $\overline{v}$ and $\overline{i}$ have been introduced.

In case of a three-phase sinusoidal voltage source with phase voltages $\boldsymbol{e} = \begin{bmatrix} e_a & e_b & e_c \end{bmatrix}^T$, by using the Clarke transformation, we obtain the following space vector:

$$\overline{e} = e_\alpha + je_\beta = E_p e^{j\omega t} + E_n^* e^{-j\omega t} \tag{5}$$

where E_p and E_n are the positive/negative sequence components provided by the phasor SCT [29,30]:

$$\boldsymbol{E}_S = \begin{bmatrix} E_p \\ E_n \\ E_0 \end{bmatrix} = \boldsymbol{S}\boldsymbol{E} = \frac{1}{\sqrt{3}} \begin{bmatrix} 1 & a & a^2 \\ 1 & a^2 & a \\ 1 & 1 & 1 \end{bmatrix} \begin{bmatrix} E_a \\ E_b \\ E_c \end{bmatrix} \tag{6}$$

Under sinusoidal steady state, the trajectory of the space vector $\overline{e}$ is elliptical, and the semi-major axis r_M, the semi-minor axis r_m, and inclination angle φ, are given by [29,30]:

$$r_M = \left|E_p\right| + \left|E_n^*\right|, \qquad r_m = \left|\left|E_p\right| - \left|E_n^*\right|\right| \tag{7}$$

$$\varphi = \frac{1}{2}\left[arg\left(E_p\right) + arg\left(E_n^*\right)\right] \tag{8}$$

Clarke equivalent circuits in the $\alpha\beta 0$ variables can be obtained by transforming three-phase components as in (2) and by transforming three-phase symmetrical connections. The most common three-phase connections are the star connections, where the star center can

https://doi.org/10.3390/en19112580

be either non-accessible or accessible to connect the three-phase system to single-phase networks [30].

3.1. Star Connection with Non-Accessible Center

Figure 2 shows a star connection with a non-accessible star center. By assuming a reference terminal G valid for the whole three-phase system, the star connection can be considered a three-port network characterized by the following independent relationships:

$$v_a = v_b, \qquad v_b = v_c, \qquad i_a + i_b + i_c = 0 \tag{9}$$

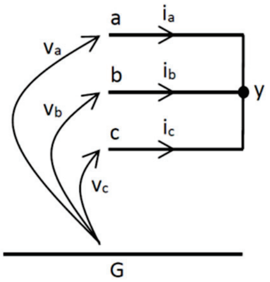

Figure 2. A star connection with a non-accessible center [30].

By using (9) in the Clarke transformation (2), we obtain:

$$v_\alpha = v_\beta = 0 \tag{10}$$

$$i_0 = 0 \tag{11}$$

i.e., the star connection with a non-accessible center is equivalent to a short circuit in the $\alpha\beta$ domains and an open circuit in the 0 domain.

3.2. Star Connection with Accessible Center

Figure 3 shows a star connection with an accessible star center. The star center is normally used to connect the three-phase system to a single-phase circuit. This connection can be treated as a four-port network whose independent relationships are given by:

$$v_a = v_y, \quad v_b = v_y, \quad v_c = v_y, \quad i_a + i_b + i_c = i_y \tag{12}$$

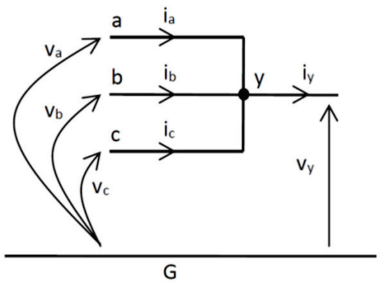

Figure 3. A star connection with an accessible center [30].

By using (12) in the Clarke transformation (2), we obtain that this kind of connection is a short circuit in the $\alpha\beta$ domains, whereas in the 0 domain:

$$v_0 = \sqrt{3} v_y \tag{13}$$

$$i_0 = \frac{1}{\sqrt{3}} i_y \tag{14}$$

https://doi.org/10.3390/en19112580

i.e., the interconnection between the 0 (three-phase) domain and the single-phase domain can be represented as an ideal transformer with a turn ratio $\sqrt{3}$ (see Figure 4). The well-known properties of ideal transformers can be readily used to analyze circuits in the 0 domain and the interconnections with single-phase circuits.

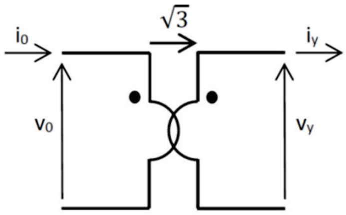

Figure 4. A zero-component equivalent circuit of a star connection with an accessible center [30].

4. Clarke Transient Analysis of Asymmetrical Faults

In this section, the time-domain analysis of asymmetrical faults based on the Clarke transformation recalled in Section 3 will be developed. In particular, the following faults will be considered: (a) single-phase faults, (b) double-phase grounded faults, (c) double-phase ungrounded faults.

Figure 5 shows the effect of Clarke transformation on the circuit variables. In the *abc* domain, phase voltages and currents belonging to the symmetrical part of the three-phase circuit are coupled, whereas the asymmetrical fault can usually be represented as uncoupled phase constraints. On the contrary, after Clarke transformation, the $\alpha\beta0$ variables in the symmetrical portion of the three-phase circuit are uncoupled, whereas the asymmetrical fault constraints result in coupled $\alpha\beta0$ variables. Thus, the $\alpha\beta0$ circuits result in coupled circuits at the fault location only. The effect of the Clarke transformation is, therefore, to move the circuit coupling from the whole three-phase system (i.e., the left side in Figure 5) to the asymmetrical fault only (i.e., the right side in Figure 5).

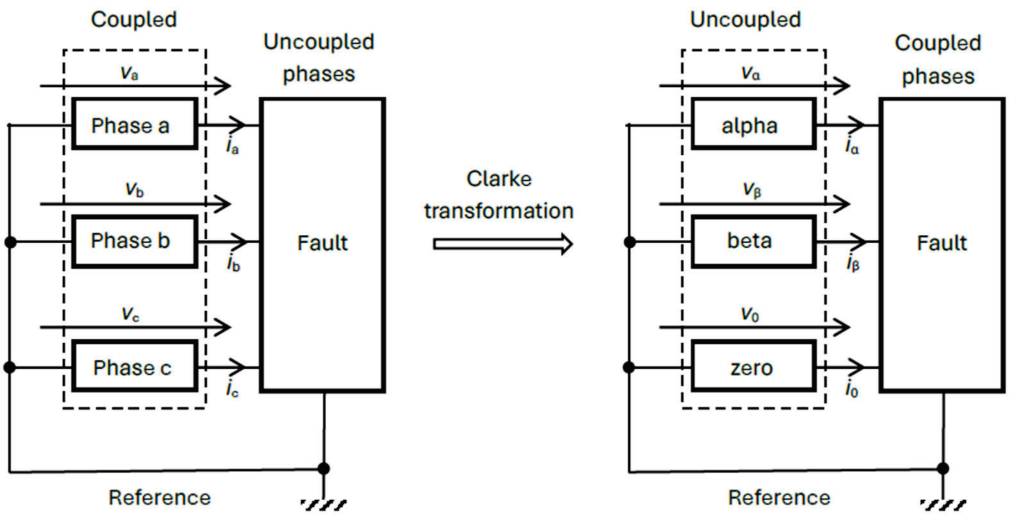

Figure 5. Clarke-transformed variables at an asymmetrical fault location.

4.1. Single-Phase Faults

A single-phase fault can be represented as in Figure 6, where only the switch corresponding to the faulted phase is closed. For the sake of simplicity, we assume a resistive fault R_f; however, a generic *RLC* fault could be considered in the proposed time-domain analysis.

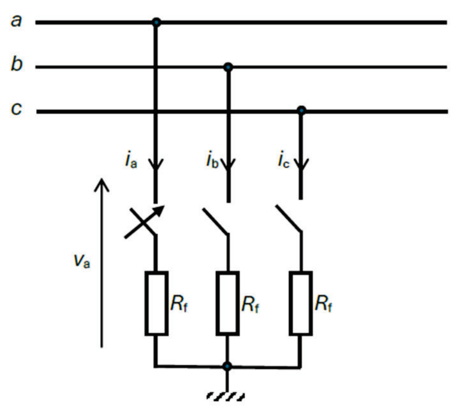

Figure 6. A single-phase fault implemented as the closure of one switch only. Fault of phase a is obtained by closing switch a.

By assuming that the faulted phase is phase a, the corresponding fault constraints on the phase variables are given by:

$$v_a = R_f i_a,\ i_b = i_c = 0 \tag{15}$$

By using (15) in the Clarke transformation defined in (2), we can readily obtain the αβ0 voltages and currents:

$$\boldsymbol{v}_{\alpha\beta 0} = \begin{bmatrix} v_\alpha \\ v_\beta \\ v_0 \end{bmatrix} = \sqrt{\frac{2}{3}} \begin{bmatrix} 1 & -\frac{1}{2} & -\frac{1}{2} \\ 0 & \frac{\sqrt{3}}{2} & -\frac{\sqrt{3}}{2} \\ \frac{1}{\sqrt{2}} & \frac{1}{\sqrt{2}} & \frac{1}{\sqrt{2}} \end{bmatrix} \begin{bmatrix} R_f i_a \\ v_b \\ v_c \end{bmatrix} = \sqrt{\frac{2}{3}} \begin{bmatrix} R_f i_a - \frac{v_b + v_c}{2} \\ \sqrt{3}\frac{v_b - v_c}{2} \\ \frac{R_f i_a + v_b + v_c}{\sqrt{2}} \end{bmatrix} \tag{16}$$

$$\boldsymbol{i}_{\alpha\beta 0} = \begin{bmatrix} i_\alpha \\ i_\beta \\ i_0 \end{bmatrix} = \sqrt{\frac{2}{3}} \begin{bmatrix} 1 & -\frac{1}{2} & -\frac{1}{2} \\ 0 & \frac{\sqrt{3}}{2} & -\frac{\sqrt{3}}{2} \\ \frac{1}{\sqrt{2}} & \frac{1}{\sqrt{2}} & \frac{1}{\sqrt{2}} \end{bmatrix} \begin{bmatrix} i_a \\ 0 \\ 0 \end{bmatrix} = \sqrt{\frac{2}{3}} \begin{bmatrix} i_a \\ 0 \\ \frac{1}{\sqrt{2}} i_a \end{bmatrix} \tag{17}$$

From (17), we observe that $i_\beta = 0$, i.e., β is an open circuit. Moreover:

$$i_0 = \frac{1}{\sqrt{2}} i_\alpha \tag{18}$$

By taking into account (17) in (16), for the α and 0 circuits, we obtain:

$$v_\alpha = R_f i_\alpha - \frac{v_b + v_c}{\sqrt{6}} \tag{19}$$

$$v_0 = R_f i_0 + \frac{v_b + v_c}{\sqrt{3}} \tag{20}$$

Thus, from (18)–(20) we can readily obtain the circuit representation of coupling between α and 0 circuits through an ideal transformer with a turn ratio $n = -1/\sqrt{2}$ as in Figure 7, where the open β circuit is also represented.

Notice that, according to the space vector definition (4), the β component of the voltage is not affected by the fault, whereas the transient of the α component is affected by the coupling with the 0 circuit. As far as the current space vector is considered, we can observe that its β component is zero. Thus, the current transient is fully described by the α component of the current space vector, affected by the coupling with the 0 circuit.

https://doi.org/10.3390/en19112580

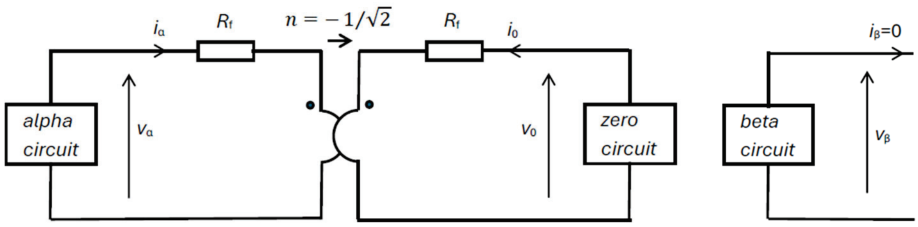

Figure 7. Clarke circuit representation of a single-phase fault.

Finally, once the $\alpha\beta0$ circuits in Figure 7 are solved, the phase *abc* variables at the fault location can be recovered through the inverse Clarke transformation. As far as the voltages are concerned, we obtain:

$$v_{abc} = \begin{bmatrix} v_a \\ v_b \\ v_c \end{bmatrix} = \sqrt{\frac{2}{3}} \begin{bmatrix} 1 & 0 & \frac{1}{\sqrt{2}} \\ -\frac{1}{2} & \frac{\sqrt{3}}{2} & \frac{1}{\sqrt{2}} \\ -\frac{1}{2} & -\frac{\sqrt{3}}{2} & \frac{1}{\sqrt{2}} \end{bmatrix} \begin{bmatrix} v_\alpha \\ v_\beta \\ v_0 \end{bmatrix} = \sqrt{\frac{2}{3}} \begin{bmatrix} \mathrm{Re}\{\overline{v}\} + \frac{1}{\sqrt{2}} v_0 \\ \mathrm{Re}\{a^2\overline{v}\} + \frac{1}{\sqrt{2}} v_0 \\ \mathrm{Re}\{a\overline{v}\} + \frac{1}{\sqrt{2}} v_0 \end{bmatrix} \tag{21}$$

where $\overline{v}$ is the space vector defined in (4), and $\mathrm{Re}\{\cdot\}$ takes the real part.

As far as the *abc* currents are considered, in this case, only i_a is different from zero. From (17), we readily obtain:

$$i_a = \sqrt{\frac{3}{2}} i_\alpha = \sqrt{3} i_0 \tag{22}$$

4.2. Double-Phase Grounded Faults

Double-phase grounded faults involve two phases and the ground. In the general case, a double-phase fault can be represented as in Figure 8, where only two switches are closed. By closing the switches *b* and *c*, the corresponding constraints on the phase variables are given by:

$$i_a = 0,\ v_b = R_{f1} i_b + R_{f2}(i_b + i_c),\ v_c = R_{f1} i_c + R_{f2}(i_b + i_c) \tag{23}$$

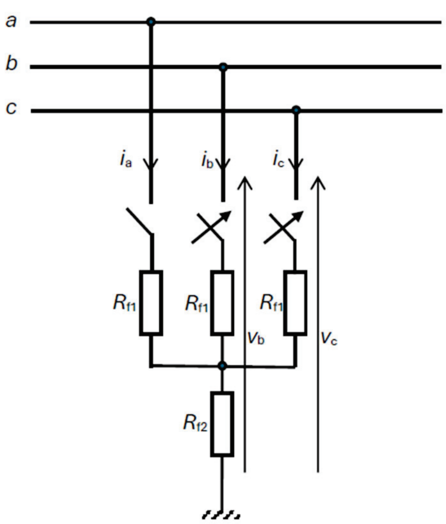

Figure 8. Circuit representation of double-phase grounded faults. By closing only the switches *b* and *c*, the corresponding two phases are involved in the fault.

By using (23) in the Clarke transformation defined in (2), we can readily obtain the $\alpha\beta0$ voltages and currents:

$$
\boldsymbol{v}_{\alpha\beta0} = \begin{bmatrix} v_\alpha \\ v_\beta \\ v_0 \end{bmatrix} = \sqrt{\tfrac{2}{3}} \begin{bmatrix} 1 & -\frac{1}{2} & -\frac{1}{2} \\ 0 & \frac{\sqrt{3}}{2} & -\frac{\sqrt{3}}{2} \\ \frac{1}{\sqrt{2}} & \frac{1}{\sqrt{2}} & \frac{1}{\sqrt{2}} \end{bmatrix} \begin{bmatrix} v_a \\ R_{f1} i_b + R_{f2}(i_b + i_c) \\ R_{f1} i_c + R_{f2}(i_b + i_c) \end{bmatrix} = = \sqrt{\tfrac{2}{3}} \begin{bmatrix} v_a - \frac{1}{2}\left(R_{f1} + 2R_{f2}\right)(i_b + i_c) \\ \frac{\sqrt{3}}{2} R_{f1}(i_b - i_c) \\ \frac{1}{\sqrt{2}}\left[v_a + \left(R_{f1} + 2R_{f2}\right)(i_b + i_c)\right] \end{bmatrix} \tag{24}
$$

$$
\boldsymbol{i}_{\alpha\beta0} = \begin{bmatrix} i_\alpha \\ i_\beta \\ i_0 \end{bmatrix} = \sqrt{\frac{2}{3}} \begin{bmatrix} 1 & -\frac{1}{2} & -\frac{1}{2} \\ 0 & \frac{\sqrt{3}}{2} & -\frac{\sqrt{3}}{2} \\ \frac{1}{\sqrt{2}} & \frac{1}{\sqrt{2}} & \frac{1}{\sqrt{2}} \end{bmatrix} \begin{bmatrix} 0 \\ i_b \\ i_c \end{bmatrix} = \sqrt{\frac{2}{3}} \begin{bmatrix} -\frac{1}{2}(i_b + i_c) \\ \frac{\sqrt{3}}{2}(i_b - i_c) \\ \frac{1}{\sqrt{2}}(i_b + i_c) \end{bmatrix} \tag{25}
$$

From (24) and (25), using simple algebra, we obtain:

$$
i_0 = -\sqrt{2} i_\alpha \tag{26}
$$

and

$$
v_\alpha = \sqrt{\frac{2}{3}} v_a + \left(R_{f1} + 2R_{f2}\right) i_\alpha \tag{27}
$$

$$
v_\beta = R_{f1} i_\beta \tag{28}
$$

$$
v_0 = \frac{1}{\sqrt{3}} v_a + \left(R_{f1} + 2R_{f2}\right) i_0 \tag{29}
$$

Therefore, the α and 0 circuits can be represented as coupled circuits through an ideal transformer with a turn ratio $n = \sqrt{2}$, whereas the β circuit is uncoupled and loaded with the fault resistor R_{f1} (see Figure 9).

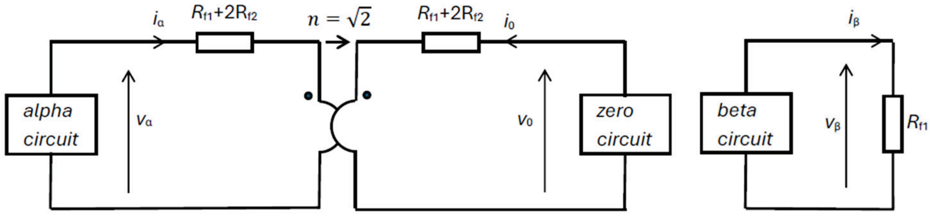

Figure 9. Equivalent circuits in the Clarke domain for the double-phase grounded fault.

Notice that in this case, the transient involves all three components αβ0. Moreover, fault grounding results in circuit coupling between α and 0 circuits.

4.3. Double-Phase Ungrounded Faults

In the special case of an ungrounded double-phase fault, the fault resistor R_{f2} in Figure 8 is replaced by an open circuit (see Figure 10).

By taking into account the current constraint $i_a = i_y = 0$, we can write:

$$
i_c = -i_b \tag{30}
$$

Thus, the phase voltages in this case are given by:

$$
\begin{aligned} v_a &= v_{ay} + v_y \\ v_b &= v_{by} + v_y = R_f i_b + v_y \\ v_c &= v_{cy} + v_y = -R_f i_b + v_y \end{aligned} \tag{31}
$$

By using (30) and (31) in the Clarke transformation defined in (1), we can readily obtain the αβ0 voltages and currents:

$$\boldsymbol{v}_{\alpha\beta 0} = \begin{bmatrix} v_\alpha \\ v_\beta \\ v_0 \end{bmatrix} = \sqrt{\frac{2}{3}} \begin{bmatrix} 1 & -\frac{1}{2} & -\frac{1}{2} \\ 0 & \frac{\sqrt{3}}{2} & -\frac{\sqrt{3}}{2} \\ \frac{1}{\sqrt{2}} & \frac{1}{\sqrt{2}} & \frac{1}{\sqrt{2}} \end{bmatrix} \begin{bmatrix} v_{ay} + v_y \\ R_f i_b + v_y \\ -R_f i_b + v_y \end{bmatrix} = \sqrt{\frac{2}{3}} \begin{bmatrix} v_{ay} \\ \sqrt{3} R_f i_b \\ \frac{1}{\sqrt{2}} (v_{ay} + 3 v_y) \end{bmatrix} \tag{32}$$

$$\boldsymbol{i}_{\alpha\beta 0} = \begin{bmatrix} i_\alpha \\ i_\beta \\ i_0 \end{bmatrix} = \sqrt{\frac{2}{3}} \begin{bmatrix} 1 & -\frac{1}{2} & -\frac{1}{2} \\ 0 & \frac{\sqrt{3}}{2} & -\frac{\sqrt{3}}{2} \\ \frac{1}{\sqrt{2}} & \frac{1}{\sqrt{2}} & \frac{1}{\sqrt{2}} \end{bmatrix} \begin{bmatrix} 0 \\ i_b \\ -i_b \end{bmatrix} = \sqrt{\frac{2}{3}} \begin{bmatrix} 0 \\ \sqrt{3} i_b \\ 0 \end{bmatrix} \tag{33}$$

Notice that v_α and v_β are not dependent on v_y. Moreover, since $i_\alpha = i_0 = 0$, the α and 0 circuits are open circuits, whereas the β circuit is closed on the fault resistor R_f, such that (see Figure 11):

$$v_\beta = R_f i_\beta \tag{34}$$

as in the grounded fault case (28). Thus, in the ungrounded double-phase fault, the transient involves only the β circuit. This is the opposite behavior of the single-phase fault described in Section 4.1. The α and 0 circuits remain in the steady-state open-circuit condition; therefore, they can be readily solved as transient-free circuits.

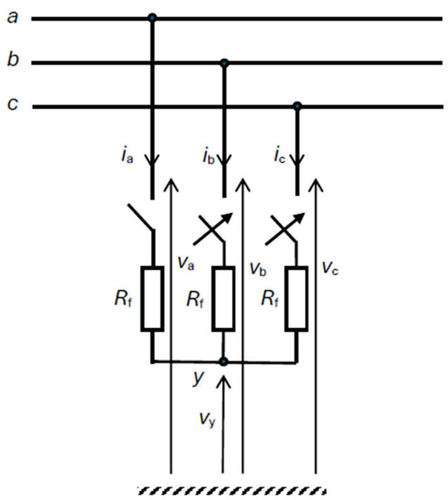

Figure 10. Circuit representation of double-phase ungrounded faults. By closing only the switches *b* and *c*, the corresponding two phases are involved in the fault.

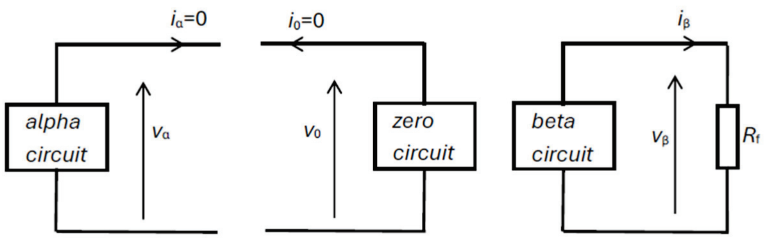

Figure 11. Equivalent circuits in the Clarke domain for the double-phase ungrounded fault.

Once i_β is calculated by solving the transient β circuit, i_b can be recovered from (33) as $i_b = i_\beta / \sqrt{2}$. Moreover, the phase voltages can be recovered from the inverse Clarke transformation (21).

https://doi.org/10.3390/en19112580

5. Comparison Between Clarke and ISCT Transient Analysis

Transient analyses by adopting Clarke and ISCT approaches will be compared using the three-phase system depicted in Figure 12. It will be shown that since the Clarke approach provides equivalent circuits where the α, β, and 0 components are not all coupled, the dynamic order of each equivalent circuit is lower than the equivalent circuit corresponding to the ISCT approach. Equivalent circuits with reduced dynamic order require simpler calculations in both numerical and analytical/hand approaches.

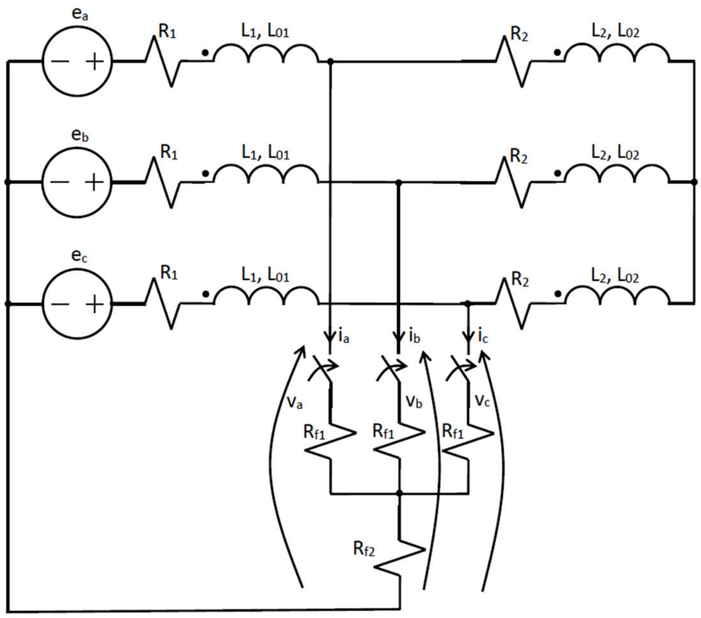

Figure 12. A three-phase system used to compare the Clarke and the ISCT approaches.

As far as the single-phase fault is concerned, i.e., only switch *a* in Figure 12 is operated, the ISCT provides the equivalent circuit in Figure 13 where $R_f = R_{f1} + R_{f2}$, and the three sequence circuits are connected in series. Notice that the circuit in Figure 13 is a third-order dynamic circuit. In fact, despite the number of inductors being five, the number of independent inductors is three.

In Figure 14, the Clarke equivalent circuits corresponding to Figure 7 are shown. It is apparent that the β circuit is independent of the α and 0 circuits. Actually, the α-0 circuit is a second-order dynamic circuit, whereas the β circuit is a first-order circuit, such that the whole dynamic order remains equal to three. Moreover, notice that the β circuit has no transients; thus, it requires the steady-state solution only. Therefore, by adopting the Clarke approach, a second-order dynamic circuit must be solved instead of a third-order circuit as in the ISCT approach.

As far as the double-phase grounded fault is concerned, the ISCT approach provides the equivalent circuit represented in Figure 15, where the three sequence circuits are connected in parallel. The effective dynamic order of the circuit, i.e., the number of independent inductors, is four. Figure 16 shows the equivalent circuits provided by the Clarke approach corresponding to Figure 9. Notice that in this case, the β circuit is independent of the α-0 circuit. Moreover, both the Clarke circuits are second-order dynamic circuits. Thus, the whole dynamic order remains equal to four, but the two independent circuits provided by the Clarke approach require simpler calculations because each of them is a second-order circuit whose solution can be readily obtained by hand calculations.

https://doi.org/10.3390/en19112580

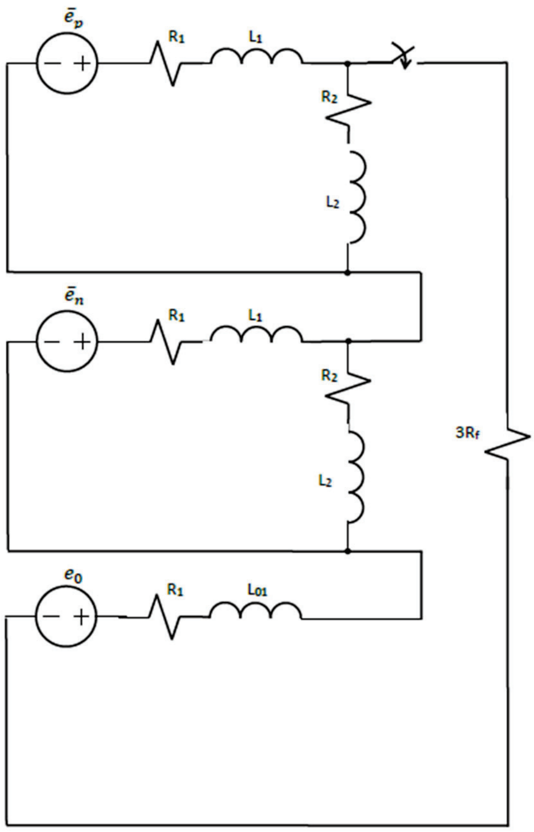

Figure 13. ISCT equivalent circuit for a single-phase fault.

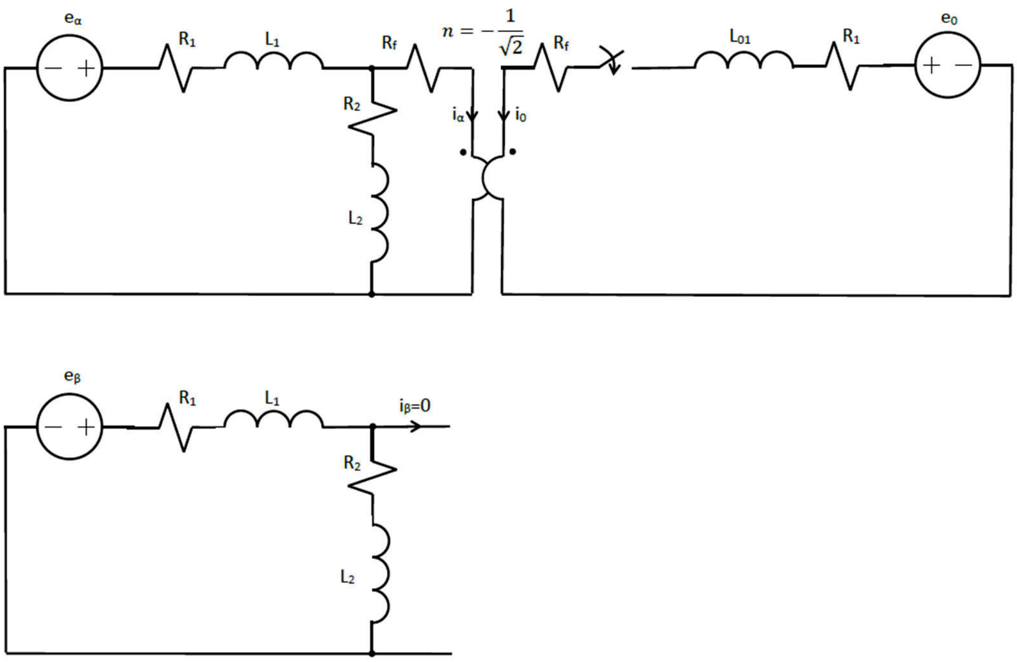

Figure 14. Clarke equivalent circuits for a single-phase fault.

As far as the double-phase ungrounded fault is concerned, the ISCT provides the equivalent circuit represented in Figure 17. Notice that it can be derived from Figure 15 by letting $R_{f2} \to \infty$. The circuit in Figure 17 is a third-order dynamic circuit. Figure 18 shows the equivalent circuits obtained from the Clarke approach, corresponding to Figure 11. The three Clarke circuits are independent. Moreover, the α circuit is in steady state, whereas

https://doi.org/10.3390/en19112580

the 0 circuit is an open circuit. The transient is represented only by the β circuit, which is a second-order dynamic circuit.

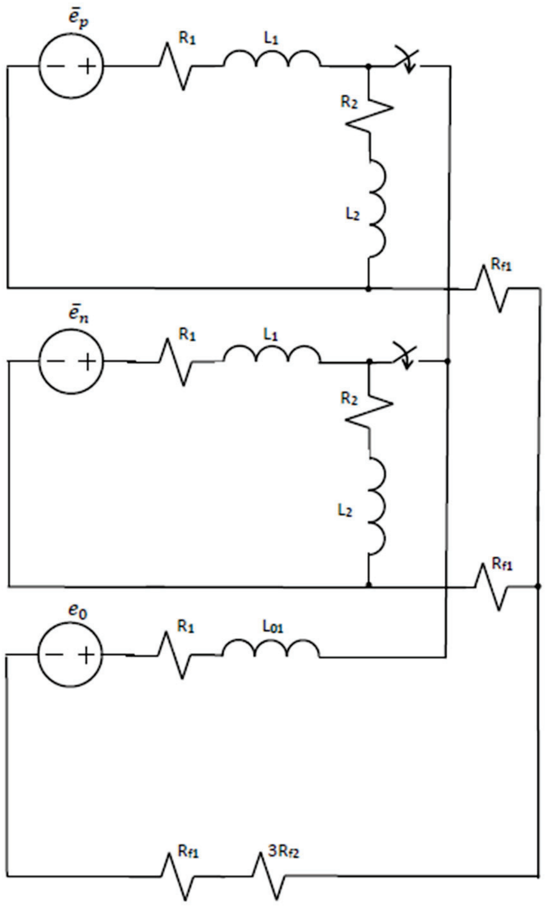

Figure 15. ISCT equivalent circuit for a double-phase grounded fault.

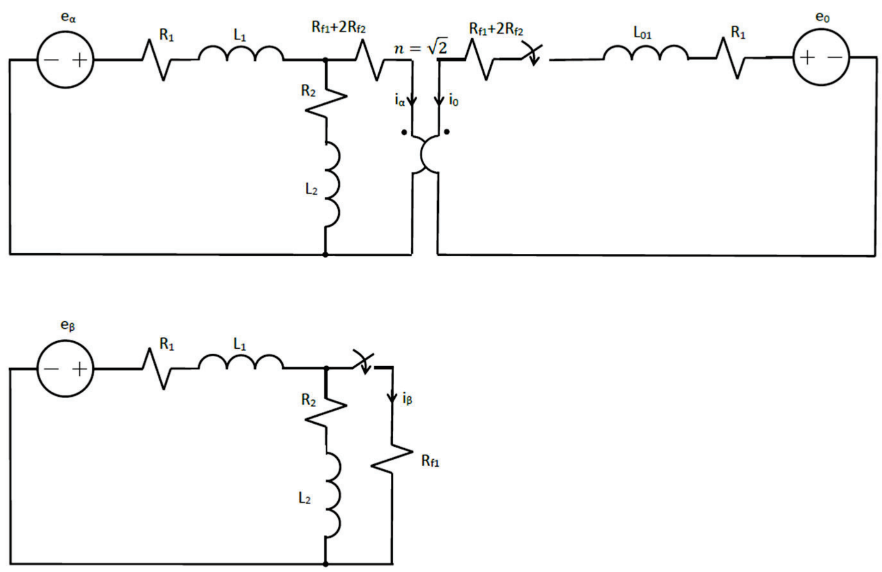

Figure 16. Clarke equivalent circuits for a double-phase grounded fault.

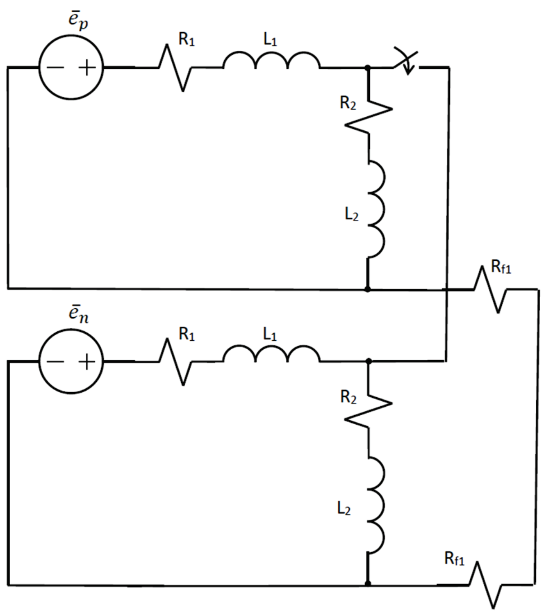

Figure 17. ISCT equivalent circuit for a double-phase ungrounded fault.

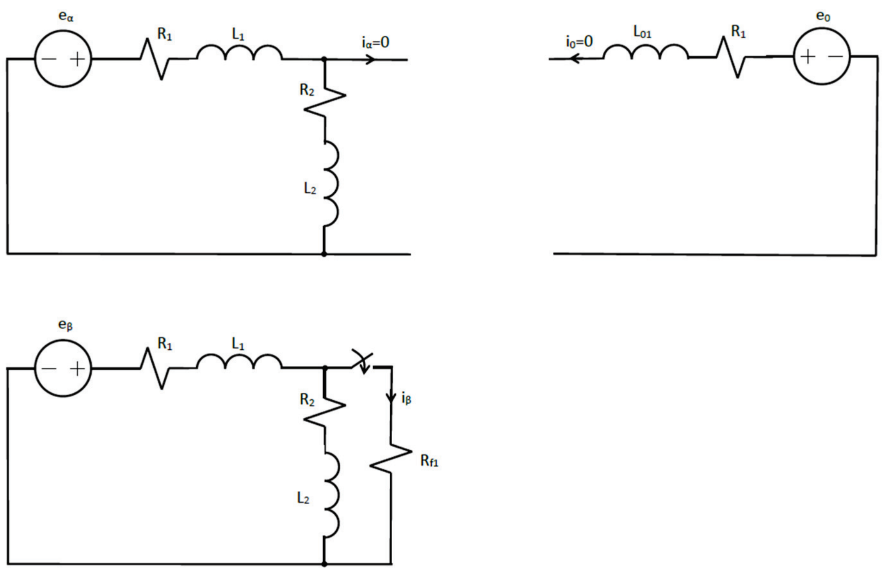

Figure 18. Clarke equivalent circuits for a double-phase ungrounded fault.

6. Numerical Validation

The analytical results derived in Section 4 were validated through numerical simulation in Matlab/Simscape R2025b of the simple radial system depicted in Figure 19.

The equivalent balanced generator is characterized by a 60 Hz phase voltage equal to $1/\sqrt{2}$ kV, positive/negative reactance $X_g = 0.5\ \Omega$ and resistance $R_g = 0.1\ \Omega$, zero sequence reactance $X_{0g} = 0.25\ \Omega$, and grounding reactance $X_{gr} = 0.2\ \Omega$ (see Table 1). The transformer, with a unity turn ratio, has a series positive/negative reactance $X_T = 0.1\ \Omega$ and zero sequence reactance $X_{T0} = 0.05\ \Omega$. The line is modeled with positive/negative sequence reactance $X_{line} = 0.3\ \Omega/\text{km}$ and resistance $R_{line} = 0.1\ \Omega/\text{km}$, and zero sequence reactance $X_{0line} = 0.9\ \Omega/\text{km}$. The fault is located at a distance d from bus 1.

The three fault cases analyzed in Section 4 were implemented by assuming fault locations d and fault resistance R_f as parameters. For each case, the transient currents at the fault location and the locus of the voltage space vector at bus 1 were evaluated and plotted. Analytical and numerical results have always overlapped; therefore, in the following figures, no distinction has been made between analytical and numerical curves. Moreover, load effects were also negligible. Actually, in the existing literature, fault conditions are studied by neglecting the load [11,14,22].

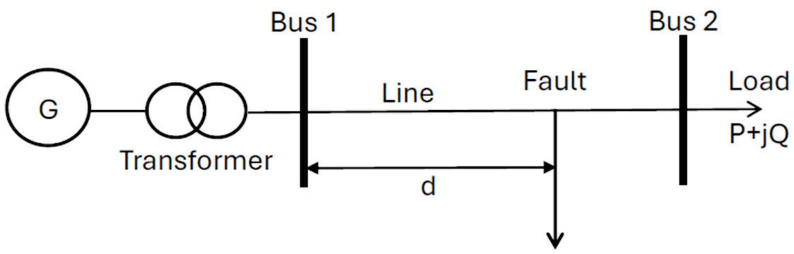

Figure 19. The radial system used to validate the analytical results. The fault location is at a distance d from bus 1.

Table 1. Data of the components in the radial system depicted in Figure 14.

Components	Connection	Parameters
Generator	Grounded Y	Pos./neg. : $R = 0.1\ \Omega,\ X = 0.4\ \Omega$ Zero : $X_0 = 0.2\ \Omega$, Ground : $X_{gr} = 0.2\ \Omega$
Transformer	Grounded Y-Y, 1/1 kV	Pos./neg. : $X = 0.1\ \Omega$ Zero : $X_0 = 0.05\ \Omega$
Line		Pos./neg. : $R = 0.1\ \Omega/\text{km},\ X = 0.3\ \Omega/\text{km}$ Zero : $X_0 = 0.9\ \Omega/\text{km}$
Load		$S = 10$ MVA, pf $= 0.9$

6.1. Single-Phase Faults

Single-phase faults, described in Section 4.1, have been implemented in Matlab/Simscape in order to validate the analytical results. In particular, the current i_α and the corresponding fault current i_a were evaluated at a fault location $d = 10$ km for two different values of fault resistance, i.e., $R_f = 0$ and $R_f = 1\ \Omega$ (see Figure 20). Clearly, a lower value of R_f results in a larger excursion of the fault current and a larger time constant. This behavior is more evident in Figure 21, where the fault location is $d = 1$ km. Indeed, in this case, the line parameters have a lower impact, and therefore, the fault current has a larger excursion in the case of a fault with zero resistance.

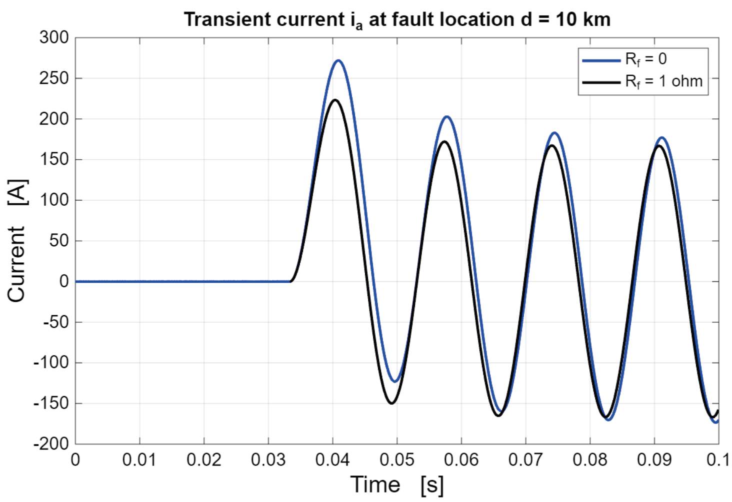

Figure 20. Transient behavior of the phase current i_a for a single-phase fault after two cycles at 60 Hz. The location of the fault is $d = 10$ km from bus 1, and two different values for the fault resistance are considered.

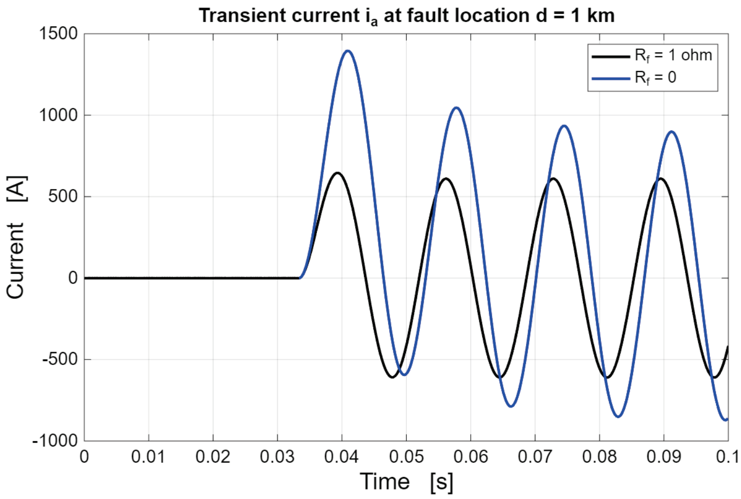

Figure 21. Transient behavior of the phase current i_a for a single-phase fault after two cycles at 60 Hz. The location of the fault is $d = 1$ km from bus 1, and two different values for the fault resistance are considered.

Figure 22 shows the behavior of the transient fault current i_a for different values of the generator ground reactance X_{gr}. Clearly, as expected, by increasing the ground reactance, the fault current decreases.

Figure 23 shows the phase voltages v_{abc} at a fault location $d = 10$ km for fault resistance $R_f = 0$. Overvoltage of unfaulted phases b and c is evident.

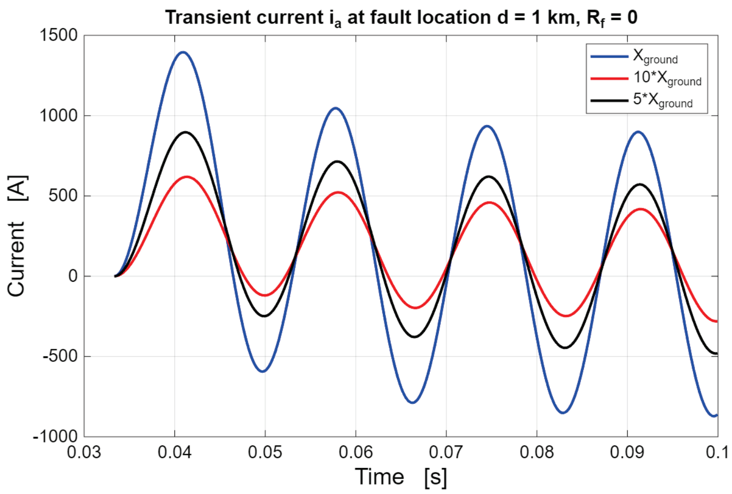

Figure 22. Transient behavior of the phase current i_a for a single-phase fault after two cycles at 60 Hz. The location of the fault is $d = 1$ km from bus 1, and three different values for the generator ground reactance are considered.

Figure 24 shows the behavior of the voltage space vector at bus 1 in the case of a fault with $R_f = 0$. The black curve shows the circular ideal trajectory in the case of no fault. The blue curve shows the trajectory in the case of a fault location $d = 10$ km, whereas the red curve shows the trajectory in the case of a fault location $d = 1$ km. Clearly, at a smaller distance, the detection of the single-phase fault becomes more evident, since the elliptical trajectory with inclination angle 90° can be readily detected. Figure 25 shows the voltage space vector in the case of a fault with $R_f = 1\ \Omega$. Notice that the fault resistance results in a slight deviation of the ellipse inclination and a smaller difference between $d = 1$ km and $d = 10$ km. Thus, as was expected, faults with larger resistance result in lower detection capability of the space vector trajectory. The apparent double red curve is due to the transient behavior.

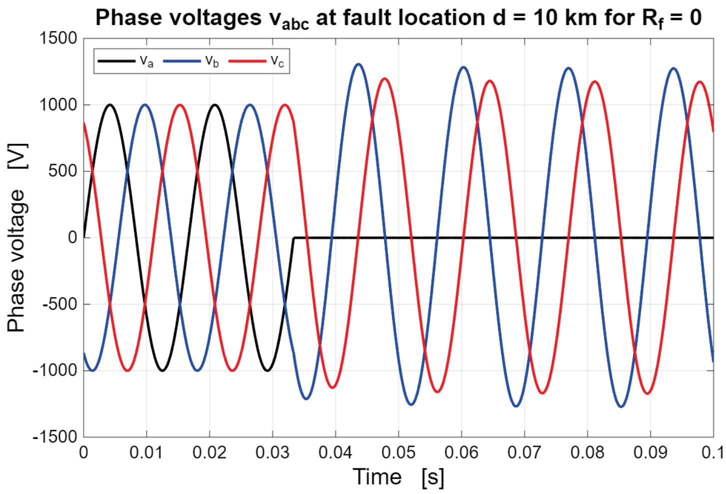

Figure 23. Transient behavior of the phase voltages v_{abc} for a single-phase fault with $R_f = 0$ after two cycles at 60 Hz. The location of the fault is $d = 10$ km from bus 1.

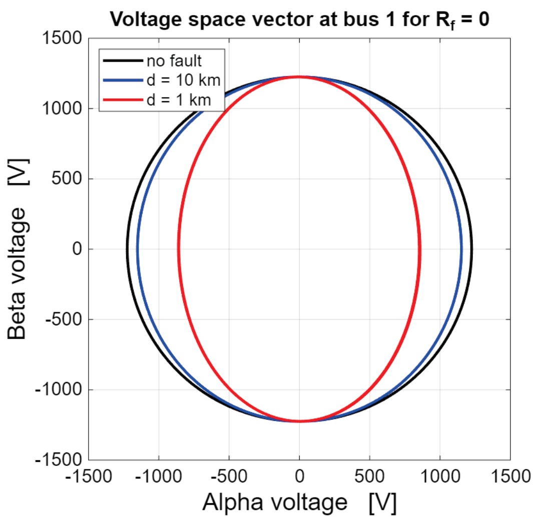

Figure 24. Trajectory of the voltage space vector at bus 1 in the case of fault resistance $R_f = 0$. The black curve corresponds to the ideal circular trajectory in the case of no fault. The blue trajectory was obtained for a fault location $d = 10$ km, whereas the red trajectory corresponds to a fault location $d = 1$ km.

6.2. Double-Phase Grounded Faults

Double-phase grounded faults, described in Section 4.2, have been implemented in Matlab/Simscape in order to validate the analytical results. In particular, the currents i_α and i_β and the corresponding fault current $(i_b + i_c)$ were evaluated at a fault location $d = 10$ km for two different values of fault resistance, i.e., $R_{f2} = 0$ and $R_{f2} = 1\ \Omega$, with $R_{f1} = 0$ (see Figure 26). A lower value of R_{f2} results in a larger excursion of the fault current and a larger time constant. This behavior is more evident in Figure 27 where the fault location is $d = 1$ km. Indeed, in this case, the line parameters have a lower impact, and therefore, the fault current has a larger excursion in the case of a fault with zero resistance.

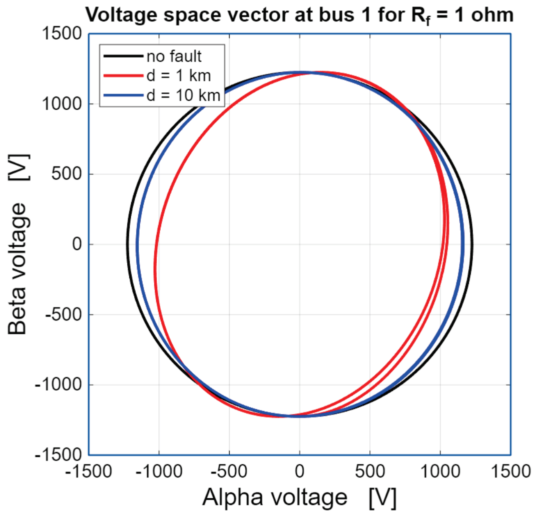

Figure 25. Trajectory of the voltage space vector at bus 1 in the case of fault resistance $R_f = 1\ \Omega$. The black curve corresponds to the ideal circular trajectory in the case of no fault. The blue trajectory was obtained for a fault location $d = 10$ km, whereas the red trajectory corresponds to a fault location $d = 1$ km.

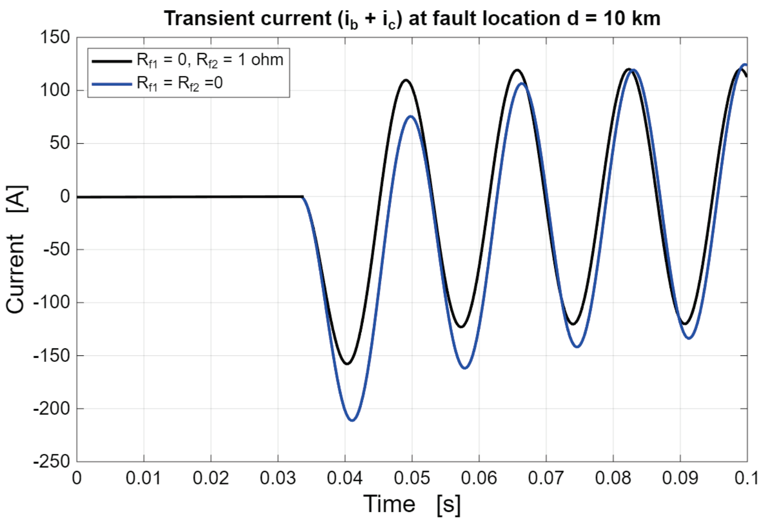

Figure 26. Transient behavior of the fault current $(i_b + i_c)$ for a grounded double-phase fault after two cycles at 60 Hz. The location of the fault is $d = 10$ km from bus 1, and two different values for the fault resistance R_{f2} are considered.

Figure 28 shows the behavior of the transient fault current $(i_b + i_c)$ for different values of the generator ground reactance X_{gr}. Clearly, as expected, by increasing the ground reactance, the fault current decreases.

Figure 29 shows the behavior of the voltage space vector at bus 1 in the case of a fault with $R_{f2} = 0$. The black curve shows the circular ideal trajectory in the case of no fault. The blue curve shows the trajectory in the case of a fault location $d = 10$ km, whereas the red curve shows the trajectory in the case of a fault location $d = 1$ km. Clearly, at a smaller distance, the detection of the double-phase fault becomes more evident since the elliptical trajectory with inclination angle 0° can be readily detected. Figure 30 shows the voltage space vector in the case of a fault with $R_{f2} = 1\ \Omega$. Notice that, according to the analytical results, the fault resistance R_{f2} affects only the α component, not the β component. In fact, the red curves in Figures 29 and 30 have a different horizontal excursion, but they keep the same vertical excursion. The detection capability of the space vector trajectory remains effective since the phase-to-phase fault resistance R_{f1} is kept to zero.

https://doi.org/10.3390/en19112580

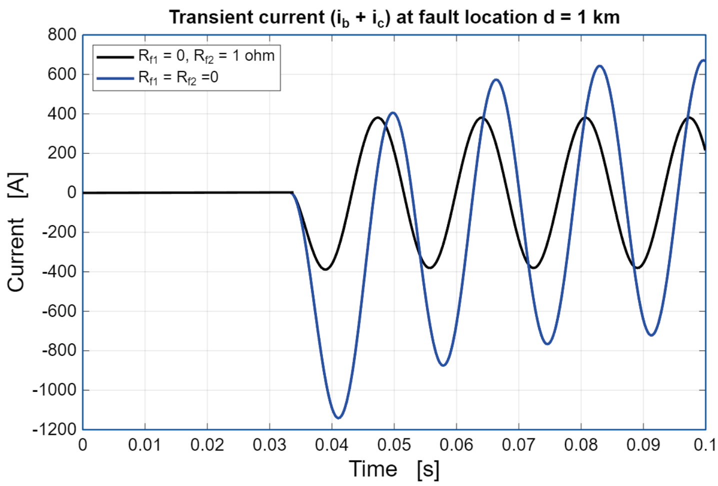

Figure 27. Transient behavior of the fault current $(i_b + i_c)$ for a grounded double-phase fault after two cycles at 60 Hz. The location of the fault is $d = 1$ km from bus 1, and two different values for the fault resistance R_{f2} are considered.

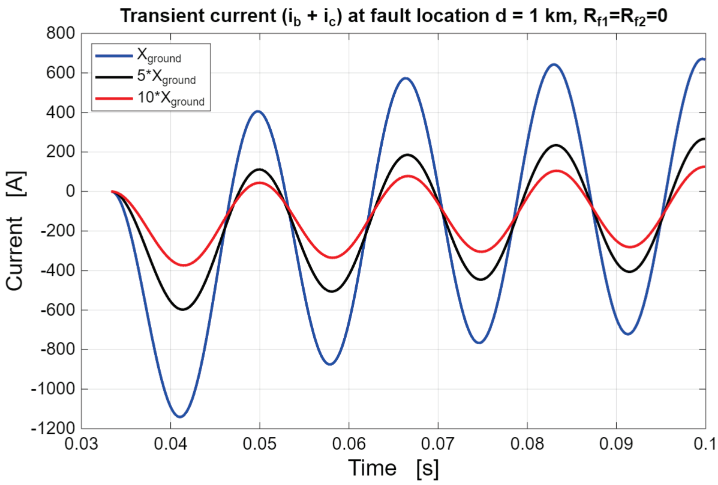

Figure 28. Transient behavior of the fault current $(i_b + i_c)$ for a double-phase fault after two cycles at 60 Hz. The location of the fault is $d = 1$ km from bus 1, and three different values for the generator ground reactance are considered.

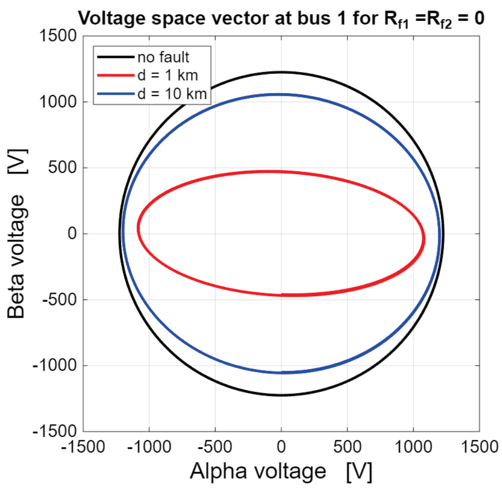

Figure 29. Trajectory of the voltage space vector at bus 1 in the case of fault resistances $R_{f1} = R_{f2} = 0$. The black curve corresponds to the ideal circular trajectory in the case of no fault. The blue trajectory was obtained for a fault location $d = 10$ km, whereas the red trajectory corresponds to a fault location $d = 1$ km.

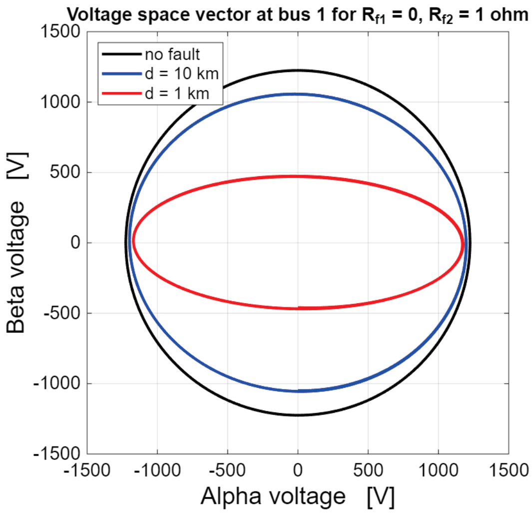

Figure 30. Trajectory of the voltage space vector at bus 1 in the case of fault resistances $R_{f1} = 0$, $R_{f2} = 1\ \Omega$. The black curve corresponds to the ideal circular trajectory in the case of no fault. The blue trajectory was obtained for a fault location $d = 10$ km, whereas the red trajectory corresponds to a fault location $d = 1$ km.

6.3. Double-Phase Ungrounded Faults

Double-phase ungrounded faults, described in Section 4.3, have been implemented in Matlab/Simscape in order to validate the analytical results. In particular, the currents i_β and the corresponding fault current $i_b = i_\beta/\sqrt{2}$ were evaluated at a fault location $d = 10$ km for two different values of fault resistance, i.e., $R_f = 0$ and $R_f = 1\ \Omega$ (see Figure 31). A lower value of R_f results in a larger excursion of the fault current and a larger time constant. This behavior is more evident in Figure 32, where the fault location is $d = 1$ km. Indeed, in this case, the line parameters have a lower impact, and therefore, the fault current has a larger excursion in the case of a fault with zero resistance.

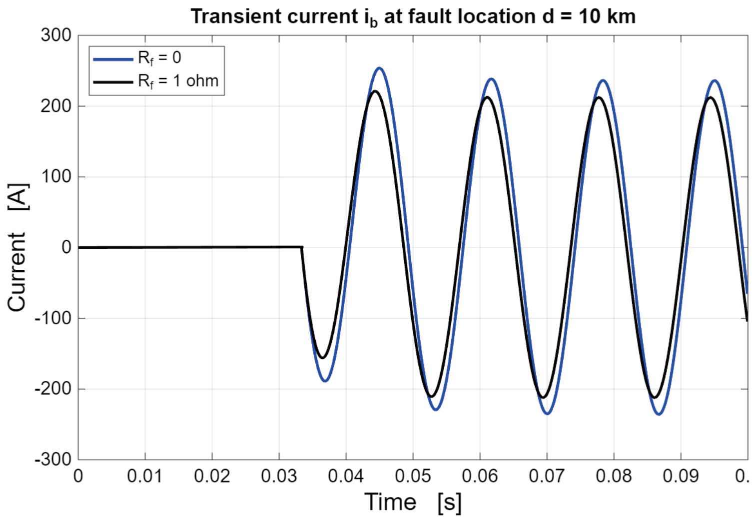

Figure 31. Transient behavior of the phase current i_b for a double-phase ungrounded fault after two cycles at 60 Hz. The location of the fault is $d = 10$ km from bus 1, and two different values for the fault resistance are considered.

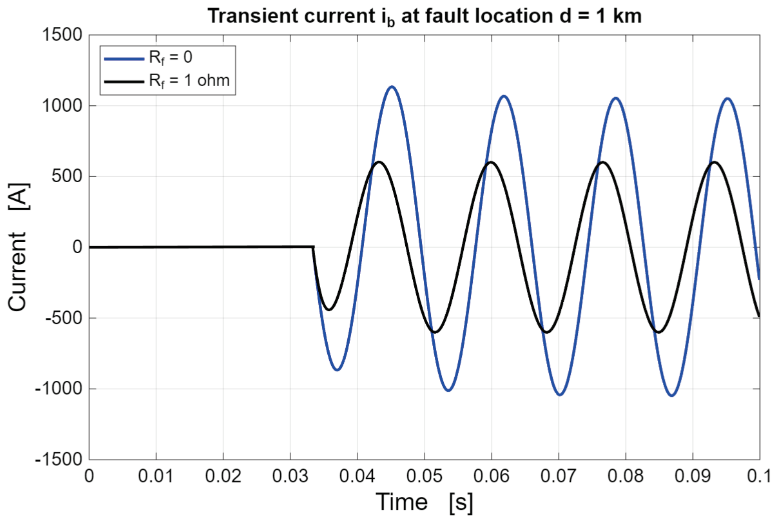

Figure 32. Transient behavior of the phase current i_b for a double-phase ungrounded fault after two cycles at 60 Hz. The location of the fault is $d = 1$ km from bus 1, and two different values for the fault resistance are considered.

Figure 33 shows the effect of voltage unbalance on the transient fault current i_b. The blue curve corresponds to the balanced case, already represented in Figure 32, where the generator voltages E_b and E_c have phase displacement $\pm 120°$ with respect to E_a. The black curve corresponds to the unbalanced case, where E_b and E_c have phase displacement $\pm 135°$ with respect to E_a. The red curve corresponds to the unbalanced case where E_b and E_c have phase displacement $\pm 150°$ with respect to E_a. Notice that by increasing the phase displacement with respect to E_a, the voltage source e_β in Figure 18 decreases its magnitude. Thus, a corresponding decrease in the transient fault current in Figure 33 can be observed.

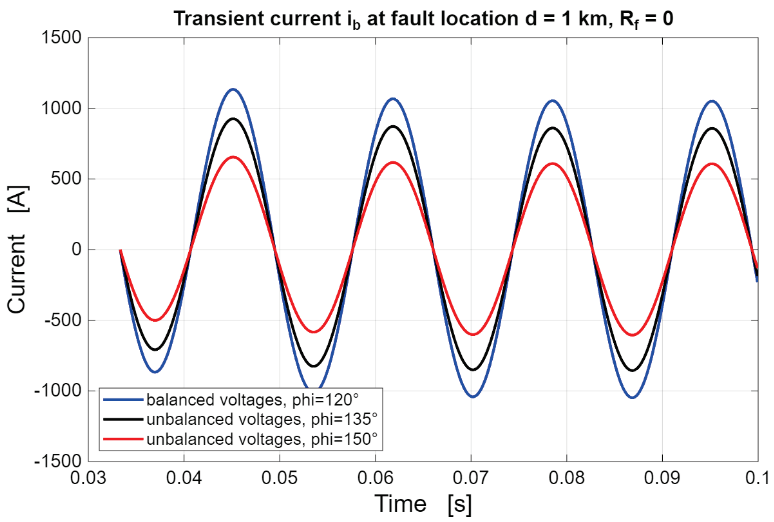

Figure 33. Transient behavior of the phase current i_b for a double-phase fault after two cycles at 60 Hz. The location of the fault is $d = 1$ km from bus 1, and three different values for the generator voltage unbalance are considered.

Figure 34 shows the behavior of the voltage space vector at bus 1 in the case of a fault with $R_f = 0$. The black curve shows the circular ideal trajectory in the case of no fault. The blue curve shows the trajectory in the case of a fault location $d = 10$ km, whereas the red curve shows the trajectory in the case of a fault location $d = 1$ km. Clearly, at a smaller distance, the detection of the double-phase fault becomes more evident, since the elliptical trajectory with inclination angle 0° can be readily detected. Figure 35 shows the voltage space vector in the case of a fault with $R_f = 1\ \Omega$. Notice that, according to the analytical results, the fault resistance R_f affects only the β component, not the α component. In fact, the red curves in Figures 34 and 35 have a different vertical excursion, but they keep the same horizontal excursion. Notice that the fault resistance results in a slight deviation of the ellipse inclination and a smaller difference between $d = 1$ km and $d = 10$ km. Thus, as was expected, faults with a larger resistance result in lower detection capability of the space vector trajectory. The transient behavior is also evident in the blue and red curves.

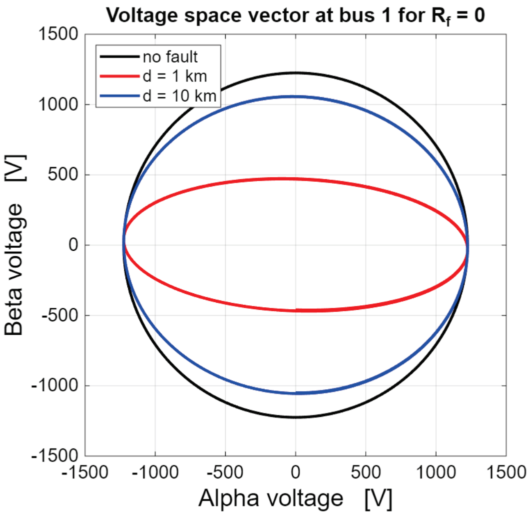

Figure 34. Trajectory of the voltage space vector at bus 1 in the case of fault resistance $R_f = 0$. The black curve corresponds to the ideal circular trajectory in the case of no fault. The blue trajectory was obtained for a fault location $d = 10$ km, whereas the red trajectory corresponds to a fault location $d = 1$ km.

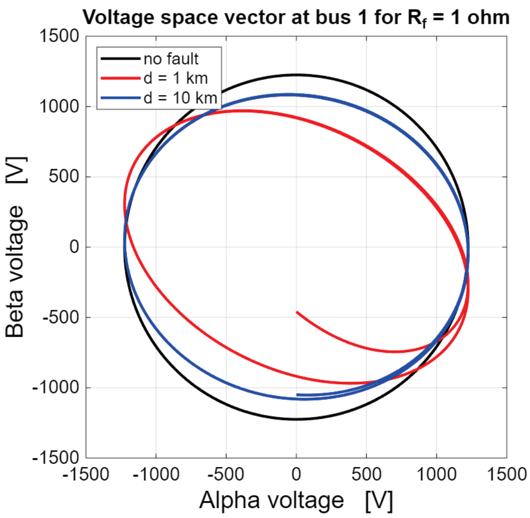

Figure 35. Trajectory of the voltage space vector at bus 1 in the case of fault resistance $R_f = 1\ \Omega$. The black curve corresponds to the ideal circular trajectory in the case of no fault. The blue trajectory was obtained for a fault location $d = 10$ km, whereas the red trajectory corresponds to a fault location $d = 1$ km.

7. Conclusions

The systematic analytical investigation of the Clarke transient analysis of asymmetrical faults in three-phase systems was presented and compared with the ISCT approach. The

https://doi.org/10.3390/en19112580

proposed Clarke approach proved to be advantageous for two main reasons. First, the derived equivalent circuits are defined in terms of real-valued voltages and currents. Second, the dynamic order of the Clarke equivalent circuits is lower than the corresponding ISCT circuits because the $\alpha\beta0$ circuits are not all coupled. Thus, the main results of the paper have a theoretical value when compared with the ISCT, whereas the application domain is the same as that of the ISCT.

Future work will be devoted to extending the proposed methodology to simultaneous faults and phase interruptions.

Funding: This research received no external funding.

Data Availability Statement: The original contributions presented in this study are included in the article. Further inquiries can be directed to the corresponding author(s).

Conflicts of Interest: The author declares no conflicts of interest.

References

1. Bollen, N.; Styvaktakis, E.; Yu-Hua Gu, I. Categorization and analysis of power system transients. *IEEE Trans. Power Deliv.* **2005**, *20*, 2298–2306. [CrossRef]
2. Tleis, N. *Power Systems Modeling and Fault Analysis*, 2nd ed.; Academic Press: Cambridge, MA, USA, 2019.
3. Chicco, G.; Mazza, A. 100 years of symmetrical components. *Energies* **2019**, *12*, 450. [CrossRef]
4. Duesterhoeft, W.C.; Schulz, M.W.; Clarke, E. Determination of instantaneous currents and voltages by means of alpha, beta, and zero components. *AIEE Trans.* **1951**, *70*, 1248–1255. [CrossRef]
5. Hsiao, T. Fault analysis by modified alpha, beta, and zero components—Parts I–II. *AIEE Trans. Part III* **1962**, *81*, 136–146. [CrossRef]
6. Martinez-Velasco, J.A. *Transient Analysis of Power Systems*; John Wiley & Sons: Hoboken, NJ, USA, 2015.
7. Zanetta, L.C., Jr. *Understanding Electromagnetic Transients in Power Systems*; IEEE Press: Piscataway, NJ, USA, 2025.
8. Stankovic, A.M.; Aydin, T. Analysis of asymmetrical faults in power systems using dynamic phasors. *IEEE Trans. Power Syst.* **2000**, *15*, 1062–1068. [CrossRef]
9. Ghimire, P.; Poudel, S.; Shirazi, M.; Hummels, D.M.; Tonkoski, R. Application of phasor modeling in power systems: A review. *IEEE Access* **2026**, *14*, 28573–28594. [CrossRef]
10. Lyon, W. *Transient Analysis of Alternating-Current Machinery*; John Wiley & Sons: New York, NY, USA, 1954.
11. Paap, G.C. Symmetrical components in the time domain and their application to power network calculations. *IEEE Trans. Power Syst.* **2000**, *15*, 522–528. [CrossRef]
12. Miao, Z.; Fan, L. A Laplace-domain circuit model for fault and stability analysis considering unbalanced topology. *IEEE Trans. Power Syst.* **2023**, *38*, 1787–1790. [CrossRef]
13. Owen, M. Transient analysis using component transforms. In Proceedings of the PEAM 2011: IEEE Power Engineering and Automation Conference, Wuhan, China, 8–9 September 2011.
14. Dell'Olmo, J.; Gatta, F.M.; Geri, A.; Graziani, M.; Lauria, S.; Maccioni, M. Clarke transform based fast assessment of switching overvoltages in an MV distribution network. *Electr. Power Syst. Res.* **2022**, *212*, 108255. [CrossRef]
15. Aller, J.M.; Bueno, A.; Paga, T. Power system analysis using space-vector transformation. *IEEE Trans. Power Syst.* **2002**, *17*, 957–965. [CrossRef]
16. Bellan, D.; Superti-Furga, G. Space-vector state-equation analysis of three-phase transients. *J. Electr. Syst.* **2018**, *14*, 188–198.
17. Bellan, D. Clarke transformation solution of asymmetrical transients in three-phase circuits. *Energies* **2020**, *13*, 5231. [CrossRef]
18. Bellan, D. Analytical investigation of the properties of transients in unbalanced three-phase four-wire networks. *Energies* **2022**, *15*, 9122. [CrossRef]
19. Ignatova, V.; Granjon, P.; Bacha, S. Space vector method for voltage dips and swells analysis. *IEEE Trans. Power Deliv.* **2009**, *24*, 2054–2061. [CrossRef]
20. Alam, M.R.; Muttaqi, K.M.; Bouzerdoum, A. Characterizing voltage sags and swells using three-phase voltage ellipse parameters. *IEEE Trans. Ind. Appl.* **2015**, *51*, 2780–2790. [CrossRef]
21. Camarillo-Peñaranda, J.R.; Ramos, G. Fault classification and voltage sag parameter computation using voltage ellipses. *IEEE Trans. Ind. Appl.* **2019**, *55*, 92–97. [CrossRef]
22. Camarillo-Peñaranda, J.R.; Ramos, G. Characterization of voltage sags due to faults in radial systems using three-phase voltage ellipse parameters. *IEEE Trans. Ind. Appl.* **2018**, *54*, 2032–2040. [CrossRef]

https://doi.org/10.3390/en19112580

23. García-Sánchez, T.; Gómez-Lázaro, E.; Muljadi, E.; Kessler, M.; Molina-García, A. Approach to fitting parameters and clustering for characterizing measured voltage dips based on two-dimensional polarisation ellipses. *Renew. Power Gener. IET* **2017**, *11*, 1335–1343. [CrossRef]
24. Bagheri, A.; Bollen, M.H.J. Space phasor model-based monitoring of voltages in three-phase systems. In Proceedings of the 18th International Conference on Harmonics and Quality of Power (ICHQP), Ljubljana, Slovenia, 13–16 May 2018.
25. Li, S.; Xie, L.; Liu, Y. Fast Identification Method for Voltage Sag Type and Characteristic. In Proceedings of the IECON 2019—45th Annual Conference of the IEEE Industrial Electronics Society, Lisbon, Portugal, 14–17 October 2019.
26. Bagheri, A.; Bollen, M.H.J.; Gu, I.Y.H. Improved characterization of multi-stage voltage dips based on the space phasor model. *Electr. Power Syst. Res.* **2018**, *154*, 319. [CrossRef]
27. Alam, M.R.; Muttaqi, K.M.; Bouzerdoum, A. A new approach for classification and characterization of voltage dips and swells using 3-D polarization ellipse parameters. *IEEE Trans. Power Del.* **2015**, *30*, 1344–1353. [CrossRef]
28. Alam, M.R.; Muttaqi, K.M.; Saha, T.K. Classification and Localization of Fault-Initiated Voltage Sags Using 3-D Polarization Ellipse Parameters. *IEEE Trans. Power Deliv.* **2020**, *35*, 1812–1822. [CrossRef]
29. Bellan, D. Probability Density Function of Three-Phase Ellipse Parameters for the Characterization of Noisy Voltage Sags. *IEEE Access* **2020**, *8*, 185503–185513. [CrossRef]
30. Bellan, D. Clarke Circuit Analysis for Space-Vector Ellipse Characterization of Phase-to-Ground Faults in Three-Phase Radial Systems. *WSEAS Trans. Circuits Syst.* **2023**, *22*, 243–250. [CrossRef]

energies

Article

Life-Cycle Analysis and Decision Model for Utilization of Distribution Transformers

Velichko Tsvetanov Atanasov [1,*], Dimo Georgiev Stoilov [2], Nikolina Stefanova Petkova [3] and Nikola Nedelchev Nikolov [2]

1 Technical College of Sofia, Technical University of Sofia, 1000 Sofia, Bulgaria
2 Faculty of Electrical Engineering, Technical University of Sofia, 1000 Sofia, Bulgaria; dstoilov@tu-sofia.bg (D.G.S.); n_nikolov@tu-sofia.bg (N.N.N.)
3 Faculty of Automatics, Technical University of Sofia, 1000 Sofia, Bulgaria; npetkova@tu-sofia.bg
* Correspondence: vtcatanasov@tu-sofia.bg; Tel.: +359-889-231-201

Abstract

This paper presents a comprehensive life-cycle analysis of distribution transformers, based on realized measurements of the increased power losses as a result of their long-term service under real-world conditions. The study is based on aggregated measured data from extensive fleets of oil-immersed distribution transformers characterized by diverse designs, manufacturing vintages, and service lives. The evolution of no-load losses and short-circuit losses is analyzed as a function of operational duration, structural characteristics, and the specific technologies employed for windings and magnetic core construction. Statistical models describing the variation in these losses are presented, highlighting the limitations of the static assumptions commonly utilized in power distribution network planning. On this basis, an approximation of the time evolution of the transformer's total power and energy losses is proposed as appropriate for implementation in a life-cycle analysis model. Furthermore, the impacts of thermal loading and abnormal operating conditions—such as unbalanced loads, frequent short circuits, and repeated overheating of the transformer oil—are analyzed as drivers of accelerated transformer aging. These effects are integrated into a unified life-cycle framework, enabling the quantitative assessment of loss variations and their associated operational expenditures (OPEX). A numerical example is provided to evaluate the cost-effectiveness of "repair vs. replacement" scenarios, utilizing a discounted cash flow analysis that incorporates a carbon component. The findings establish a methodological foundation for a broader assessment of technical condition and energy performance, identifying the optimal intervention point for repair or replacement to support decision-making for Distribution System Operators (DSOs) amidst increasing requirements for efficiency and decarbonization.

Keywords: distribution transformers; life-cycle cost (LCC); loss increase during service time; no load losses; short circuit losses; asset management; repair versus replacement; carbon emissions; operational mode severity

1. Introduction

Distribution transformers are key equipment in power distribution networks, and their long-term operational reliability and energy efficiency directly affect power supply reliability and operating costs. The optimal operational life of distribution transformers, according to [1], is usually assumed to be between 30 and 40 years, depending on design features, cooling conditions and operating mode. However, a significant part of the transformer fleet in power distribution networks continues to be operated significantly beyond the specified optimal operational life. In a number of power distribution systems, published studies show that approximately 55% of installed distribution transformers exceed this age limit [2,3]. In addition, published models for estimating the expected service life, based on real operating modes and insulation aging, show that under favorable conditions and limited thermal stress, individual transformers can reach a service life significantly longer, in some cases up to the order of 70–80 years [4]. In the passport documentation of distribution transformers, manufacturers provide the main electrical and energy parameters. In this study, the term "passport data" is used to denote the technical parameters specified by the manufacturer, including nameplate data and factory test results obtained under standardized test conditions at the time of production and commissioning. Accordingly, "passport losses" refer to the manufacturer-declared loss values reported in the documentation.

The regulatory documents and technical standards regulating the testing and passport data of transformers do not contain a quantitative description of the change in these parameters during long-term operation, nor are dependencies given that take into account the aging of active materials and the influence of real operating modes [5]. In real-world conditions, decisions to manage aging transformers are most often made when a fault, insulation deterioration, increased losses, or mechanical defects occur. In such situations, the operator is faced with a strategic choice: repair and continued operation or replacement with a new transformer. This choice is often based primarily on the initial capital costs, without a systematic quantitative assessment of the long-term consequences of parameter degradation, loss changes, and environmental impact.

Although the Life-Cycle Cost (LCC) methodology is widely used in the power industry, most published studies consider losses as static quantities [6–8]. In the existing literature, several main approaches to transformer life-cycle assessment have been identified and discussed here. Some studies apply classical LCC models based on the summation of investment costs and the evaluation of losses using constant parameters [9]. Other approaches use annualized cost methods based on the Capital Recovery Factor (CRF), which convert the initial investment into equivalent annual costs [10]. In addition, methods based on discounted cash flow (DCF) are applied, where all costs are expressed in present value terms over a defined analysis period [11]. While CRF-based approaches express costs as equivalent annual values, the DCF method used in this study evaluates costs in present value terms, allowing a more accurate representation of time-dependent loss evolution and ageing effects. This makes the DCF approach particularly suitable for modelling long-term degradation processes in distribution transformers. However, in most of these approaches, transformer losses are treated as constant values derived from passport data, without considering their time-dependent evolution under real operating conditions.

Additionally, the influence of specific network operating modes and the carbon footprint of operating losses are usually not integrated into a single quantitative model. As a result of long-term thermal loading, insulation aging, mechanical impacts and other real operating conditions, a gradual increase in power and, respectively, energy losses, as well as changes in the thermal and electrical characteristics of transformers, is observed [12]. In the context of energy transition and decarbonization, the need for a more precise assessment of the long-term effects of repair–replacement solutions is becoming increasingly significant. This requires the development of an integrated framework that links parameter degradation (increase in losses over time), real operating modes, economic evaluation and environmental aspects into a single analytical model [13]. The aim of this work is to develop a life-cycle cost model and to demonstrate its application to decision-making

https://doi.org/10.3390/en19081858

regarding the repair or replacement of distribution transformers. The proposed approach accounts for the evolution of losses over time, real loading conditions, and the associated economic and environmental effects. The main research question addressed in this study is whether the integration of time-dependent loss evolution and environmental cost components significantly influences the economic decision between repair and replacement of distribution transformers.

2. Research Gap and Scientific Contribution

The analysis of the available literature and engineering practice reveals three main shortcomings:

- Lack of a quantitative relationship between operating mode and change in parameters.

Changes in parameters are usually associated with age, but indicators are rarely introduced that quantitatively reflect the influence of specific network conditions (length of low voltage (LV) lines, load, climate conditions, type of conductor).

- Assumption of constant losses.

In most LCC models, the nominal no-load and short-circuit losses are used as constant parameters, without taking into account their increase over time in real operation.

- Fragmented economic and environmental assessment

Economic analysis and carbon assessment are often considered separately, without integration into a common discounted criterion for strategy selection. These limitations can lead to suboptimal solutions, especially for transformers in the late stage of their life cycle, when the accelerated growth of losses has a significant impact on the overall costs.

Scientific Contribution of the Study

The main contributions of this study can be formulated as follows:

- An analysis and model for the time-dependent variation of no-load losses and short circuit losses is presented, based on measured data after long-term operation, and a distinction is realized between different production periods and design solutions.
- Analytic functional dependences for the estimation of the time changes of no-load and short-circuit losses are proposed, and on this basis, an approach for estimation of the evolution of annual energy losses is presented and implemented.
- A structured life-cycle model is formulated to compare "repair" and "replacement" scenarios, based on a discounted cash flow analysis over a given evaluation horizon.
- A carbon component related to operating losses is integrated, which allows for the evaluation of asset management strategies in the context of decarbonization.
- A transparent and applicable methodological framework is proposed, suitable for use by electricity distribution network operators when making decisions about aging transformers.

In this way, the study builds on classical static LCC approaches and offers an integrated analytical framework linking parameter degradation, operating modes, economic efficiency and environmental aspects into a single life cycle estimation model.

3. Methodological Framework

This subsection offers a clear methodological "bridge" between the traditional static LCC approach (where no load losses and short circuit losses are assumed to be constant and equal to passport values) and a dynamic model of losses, dependent both on the age **t** and on the operation mode severity to the network. The review of the world literature on the considered problem shows that widely used formulas capitalize passport no load and

https://doi.org/10.3390/en19081858

short circuit losses, which can systematically underestimate future energy loss costs for old assets. However, operational measurements and analyses document that idle losses can increase significantly compared to passport losses (e.g., on average +23% at an average age of 31.6 years; in some samples, the average excess is >50%), and there is also data for an increase in losses by 5.65–6.25% after 18 years of operation [14]. Along with age, operation mode factors such as harmonics, asymmetry, thermal cycling, and short circuits increase losses. It has been experimentally shown, for example, that voltage harmonics can increase iron losses by about 20.8% at nominal voltage, as well as increase the operating temperature and accelerate aging [15]. On this basis, several alternative functional forms (linear, exponential, piecewise linear/piecewise exponential, and stochastic) for the variation of the no-load losses $\boldsymbol{\Delta P_0(t)}$ and short circuit losses $\boldsymbol{\Delta P_{SC}(t)}$ are formalized (here $\boldsymbol{\Delta P_0(t)}$ denotes the no-load losses as a function of operating time, and $\boldsymbol{\Delta P_{SC}(t)}$ represents the short circuit losses in rated operation as a function of operating time), the input data and methods for parameter estimation are described, and a short numerical example is provided. All variables and symbols used in the following analysis are explicitly defined at their first occurrence in the text. In particular, clear notation is introduced to distinguish between manufacturer-declared (passport) values and measured values obtained after prolonged operation.

In this study, a clear distinction is made between core losses and no-load losses, as well as between copper losses and load losses. Core losses refer specifically to losses in the magnetic core, while no-load losses represent the losses measured under open-circuit conditions and reported in manufacturer documentation. The present work is focused on life-cycle assessment and decision-making. Therefore, to use clear, simple figures, our analysis is based on no-load and short-circuit losses, which are quantities available in technical specifications and can also be measured in operational practice. In our descriptions, a constant (not depending on the load, mainly determined by the core/iron losses) power loss component is regarded, and it is approximated with no load losses. Also, a variable (dependent on the load level, mainly determined by the copper losses) power loss component is regarded, and it is approximated on the basis of the short circuit loss. Therefore, in our approach, the change in no-load losses, mainly due to changes in the condition of the magnetic core, and the change in the short circuit loss, mainly due to changes in the condition of the transformer's windings, provide key information in the assessment of the life cycle of distribution transformers.

3.1. Evolution of No-Load Losses in Long-Term Operation

During operation, the magnetic core is subjected to cyclic thermal loads, vibrations caused by magnetostrictive phenomena, and mechanical impacts during switching the transformer on and off. These factors can lead to partial displacement and loosening of the laminations, disruption of magnetic contact between them, and a local increase in air gaps in the magnetic circuit [16]. As a result, the effective magnetic reluctance increases, leading to local changes in magnetic induction and an increase in hysteresis and eddy current losses [17]. Therefore, the analysis of the change in no-load losses, as an operational indicator of the condition of the magnetic core, is a key element in the assessment of the life cycle of distribution transformers. A number of published studies [18,19] show that the magnetic system of transformers undergoes changes during prolonged operation as a result of thermal aging and mechanical impacts, which result in a change in these losses. In distribution transformers manufactured before the year 2000, for a significant part of the cases, magnetic cores with conventional end-to-end or early overlapping constructions were used, which leads to a less favorable magnetic flux distribution in the lamination connection zones. As a result, the no-load losses specified in the manufacturer's documentation for these transformers are higher compared to modern designs, which use step-lap or multi-step-lap magnetic cores. It has been shown in the literature that step-lap connections can lead to a reduction in core losses between 2–4.4%, and multi-step-lap designs have been introduced with the aim of significantly reducing no-load losses. This section presents an analysis of changes in no-load losses during the long-term operation of distribution transformers, based on operational measurements and statistical data processing. The presented analysis builds on the authors' previous measurement campaign reported in [20], which included 200 oil-immersed 20/0.4 kV distribution transformers operated in indoor transformer substations and supplying mainly household and small industrial consumers. The sample comprised 100 transformers with conventional "front splice" magnetic cores and 100 transformers with "multi-step lap" cores, covering rated powers from 50 kVA to 630 kVA and a wide range of commissioning years and service durations.

For the statistical analysis, the transformers were grouped by manufacturing period and by five-year service intervals, which allowed comparison between the no-load losses specified in the manufacturer's documentation and the measured values after prolonged operation. The loss-growth parameter was estimated from the measured dataset using a least-squares fitting procedure. In our previous study, the exponential approximation showed acceptable accuracy, with a root mean square error of about 5.9% for an additional validation group of 10 transformers. For this reason, the exponential form is adopted here as a basis for long-term life-cycle modelling. Table 1 summarizes the manufacturer-specified and experimentally measured averaged no-load losses for distribution transformers with different rated powers S_r, grouped by main production periods. The specified values are derived from published regulatory requirements and survey studies that reflect typical design solutions and magnetic materials used during the respective production periods [21–23]. The measured values reflect the actual state of no-load losses after long-term operation.

Table 1. Evolution of no-load losses of distribution transformers with different rated power S_r over various manufacturing periods, including both manufacturer-declared (passport) values and averaged measured values after prolonged operation.

Sr (kVA)	ΔP_0 (1970–1990)		ΔP_0 (1990–2002)		ΔP_0 (2002–2025)	
	$\Delta P_{0,pasp}$ (W)	$\Delta P_{0,real}$ (W)	$\Delta P_{0,pasp}$ (W)	$\Delta P_{0,real}$ (W)	$\Delta P_{0,pasp}$ (W)	$\Delta P_{0,real}$ (W)
50	300–230	470	230–190	342	125–81	260
100	450–400	668	400–320	548	210–130	420
160	500–460	850	460–400	690	300–189	530
250	780–650	1140	650–600	800	310–270	600
400	1100–930	1640	930–900	1600	430–397	1220
630	1580–1400	2430	1400–1300	2320	860–540	1745

The values show a clear trend of decreasing the nominal no-load losses over time, which can be explained by the transition from conventional end-jointed magnetic cores to step-lap designs, as well as by the improved quality of electrical steel. At the same time, the averaged measured values indicate that, with continued operation, the no-load losses increase significantly from their initial nominal values. This deviation can be due to both long-term mechanical and structural changes in the magnetic system and the differences between the factory test conditions and the real operating modes; it cannot be unambiguously interpreted as an increase in losses. Proving a real increase in no-load losses requires a comparison of measurements made under identical conditions at different times during the operating period, which data are rarely available in practice. It should be noted that the passport values for no-load losses presented in Table 1 are valid mainly for the initial period of operation and reflect the condition of the transformers during the first few years after commissioning. Presenting passport values as a range reflects the diversity of manufacturers, standards and technological levels during the considered periods, while the measured values characterize the actual change in losses over prolonged operation. Due to the lack of systematic measurements on the same equipment at different times of their operational life, these data do not allow unambiguous proof of a temporal increase in losses, but rather reflect the difference between the passport and operational conditions. The obtained results support the hypothesis that during prolonged operation, changes in no-load losses may occur due to mechanical and structural changes in the magnetic system. The analysis of the averaged experimentally measured values shows that in transformers with an operating life of more than approximately 20 years, an accelerated increase in no-load losses is observed. For the considered groups, the average annual increase rate reaches about 2.6% per year, which is significantly higher than during the initial period of operation. This annualized value is consistent with the five-year loss increment identified in the authors' earlier statistical study [24]. It is therefore used here as a representative parameter for transformers with service lives exceeding approximately 20 years, primarily in the pre-2000 design groups. This increase can be approximated by an exponential function that describes the relationship between the real losses and the operating life and allows a quantitative reflection of the accelerated aging character in the later stages of the transformer life cycle:

$$\boldsymbol{\Delta P_{0,real}(t) = \Delta P_{0,pasp} \cdot \left(1 + \frac{r}{100}\right)^{t}} \quad (1)$$

where $\mathbf{\Delta P_{0,real}}$—real no-load losses after t years of operation, kW;

$\mathbf{\Delta P_{0,pasp}}$—rated losses at idle (no load) run, kW;

$\boldsymbol{r}$—average annual growth rate of no-load losses, %;

$\boldsymbol{t}$—duration of operation, years.

It should be emphasized that the analyses and experimental results presented so far relate primarily to distribution transformers manufactured before 2000. In modern distribution transformers equipped with step-lap magnetic circuits, the analysis of the measured data presented in Table 1 shows that in these transformers, the average annual increase in no-load losses is of the order of 1.5–2%, which confirms the positive effect of the improved design solutions.

3.2. Model for Estimating the Change in Short Circuit Losses

The losses in the windings of transformers are determined by the active resistance of the windings and the current flowing through them. Unlike the losses in the magnetic system, which are weakly dependent on the load, the losses in the windings are highly sensitive to the temperature mode, the load mode and the duration of operation [25]. During long-term operation, the active resistance of the windings can change as a result of a number of factors, including thermal aging of the insulation, relaxation of mechanical stresses in the conductors, local deformations due to electrodynamic forces, as well as oxidation processes and changes in the contact connections [26]. These processes lead to a gradual increase in the active losses and to a deviation of the actual short-circuit losses from the passport values. During long-term operation, increased loading, temperature fields and the prolonged action of mechanical and electrodynamic forces can lead to changes in the mechanical properties of the windings, affecting their mechanical stability and material parameters, including resistance. This has been confirmed in analyses published in [27,28], where it is shown that temperature and loading conditions affect the mechanical stability of the windings, which is directly related to changes in the parameters of the active materials and losses during long-term operation. In distribution transformers, the design of the windings has also evolved over time. While older designs often use multi-layer rectangular or round windings, together with thicker conductors for the LV windings, in more modern

https://doi.org/10.3390/en19081858

transformers, especially low voltage, the windings are often realized as flat wide strips (foil windings), which provide more uniform current distribution, better cooling and higher mechanical strength at high currents [29]. The values of the passport short-circuit losses, grouped by transformer nominal power and production period, are presented in Table 2. The data illustrate the technological evolution of distribution transformers during the decades under consideration.

Table 2. Manufacturer-declared (passport) short-circuit losses (ΔPsc) for distribution transformers with different rated powers Sr and production periods.

Rated Power Sr (kVA)	ΔPsc (W) 1970–1990	ΔPsc (W) 1990–2000	ΔPsc (W) 2000–2010	ΔPsc (W) 2010–2022
50	1100	1090	875	750
100	2200	1800	1475	1250
160	3100	2350	1850	1750
250	3500	3250	2400	2350
400	5000	4600	3350	3250
630	7200	5400	4650	4600

In previous studies by the authors [29], based on operational measurements of distribution transformers, it was shown that with an operation duration of more than approximately 20 years, the losses in the windings increase steadily. There, distribution transformers with secondary windings of two construction types were analyzed. For transformers with foil windings, the analysis covers the first four five-year periods from the beginning of operation, while for transformers with rectangular conductor cross-section, later operational periods were considered. Such stratification allows for a comparative analysis at different operation durations. The obtained results show that for transformers with foil windings, the level of copper losses in individual five-year intervals remains in a relatively narrow range. Therefore, the time dependence of losses is considered in five-year intervals, rather than in individual calendar years, which provides a more stable statistical assessment and reduces the influence of random operational deviations. The analysis of the averaged measured values shows that the equivalent average five-year rate of increase is of the order of 1–2%, which is lower than the observed rate of increase in no-load losses, but has a significant impact on the total operating losses under load. Based on the averaged experimental data, a simplified exponential model is proposed to describe the change in short circuit losses during long-term operation-

$$\Delta P_{\mathbf{SC,real}}(t) = \Delta P_{SC,\mathbf{pasp}} \cdot \left(\mathbf{1} + \frac{r_{\mathrm{SC}}}{\mathbf{100}}\right)^{t/5} \quad (2)$$

where: $\Delta P_{\mathbf{SC,real}}$—the real losses in the windings under rated loading after t years of operation, kW;

$\Delta P_{\mathbf{SC,pasp}}$—rated losses in the windings declared by the transformer producer, kW;

r_{SC}—equivalent average annual growth rate of short circuit losses, %;

t—duration of operation, years.

Unlike no-load losses, which are largely independent of loading conditions, load losses depend directly on the actual current and operating temperature. Therefore, when estimating the life cycle costs of transformers, these losses are characterized by high variability between individual facilities, which necessitates the use of average values, load profiles and statistical approaches, as adopted in the established methodologies for LCC analysis. As emphasized by Zhan et al. (2024) [30,31], the life-cycle analysis of transformers includes not only aggregate costs, but also an assessment of influencing factors such as voltage level and winding method, which have a significant effect on the structure and variability of

https://doi.org/10.3390/en19081858

LCC values. They used the TOPSIS methodology to weight the factors influencing the life cycle costs of transformers and identify the most significant influencing parameters through statistical approaches. Including the change in load losses in the life-cycle oriented assessment allows for a more realistic modeling of energy losses and operating costs of distribution transformers in the long term [32]. This is of particular importance in the management of an aging transformer fleet, where decisions for replacement, modernization or extension of the service life should be based not only on passport data, but also on the actual change in parameters during operation.

3.3. Operating Modes of Distribution Transformers and Their Impact on Losses and Life Cycle

Unlike the nominal conditions under which the passport characteristics are determined, in practice, transformers often operate under complex and variable operation modes, including asymmetric loading, cyclic overloads, powering long low-voltage power lines and frequent transients [33]. The real operation modes of distribution transformers have a significant impact on the thermal loading, aging processes and long-term changes in the main parameters determining energy losses during the service life [34]. In a number of distribution networks, especially in sparsely populated areas, mountainous and resort areas, transformers supply long low-voltage power lines with uneven distribution of loads between phases, as well as consumers with diverse daily, weekly and seasonal load schedules. These conditions lead to significant fluctuations in the currents in the windings and, as a consequence, in the temperature of the windings and the oil, which forms recurring thermal cycles throughout the day, week and year and throughout the entire operational period [35]. The design features of distribution transformers also have a significant impact on the way in which the actual operating modes affect their thermal and mechanical status. Older transformers, manufactured before the beginning of the year 2000, in the majority of cases are equipped with an expansion vessel (conservator), which allows free compensation of the volumetric changes of the transformer oil during temperature fluctuations. In this type of construction, mechanical stresses caused by the thermal expansion of the oil are avoided, thereby limiting the loading of the main tank [36]. In modern distribution transformers, hermetically sealed structures are widely used, in which there is no separate expansion vessel, and the compensation for volumetric changes in the oil is achieved through elastic deformation of the tank and cooling fins. Under normal operating conditions, this approach has a number of advantages, including limiting moisture absorption and a more stable quality of the insulation system. However, under adverse operating conditions, such as frequent overloads, asymmetric loading and repeated short circuits in long low-voltage power lines, intense and repeated thermal cycles are formed, which lead to cyclic changes in the pressure in the tank [37]. This creates prerequisites for the accumulation of fatigue in the material of the cooling fins and the tank and for the deterioration of cooling conditions during long-term operation. This aspect is recognized in industry guidelines for transformer equipment maintenance and evaluation, which support the monitoring of mechanical condition and reliability of tank components throughout the transformer life cycle [38].

In the manufacturers' technical documentation, the life of distribution transformers is usually defined by the design service life, rather than by the maximum number of thermal expansion cycles of the tank and cooling fins. Hermetically sealed transformers are designed to allow for repeated thermal cycles resulting from daily and seasonal variations in load and ambient temperature. In typical operation, this corresponds to the order of one to two complete thermal cycles per day, which, over a design service life of 30–40 years, results in tens of thousands of expansion and contraction cycles. When operating under adverse conditions, characterized by frequent overloads and repeated short circuits, the amplitude and frequency of thermal cycles increase, leading to accelerated fatigue of the tank material and the cooling fins and shortening the effective life of the transformer [39]. In this context, the differences in the design performance between transformers with an expansion tank and hermetically sealed transformers should be taken into account when analyzing the operating conditions, losses and life cycle, especially when operating in networks with increased accident rates and unfavorable load profiles. In a previous study by the authors, published in [40], an analysis of the thermal and structural behavior of hermetically sealed distribution transformers under adverse operating conditions was performed. It has been established that the temperature changes of the transformer oil cause cyclic expansion and contraction of the tank walls and cooling fins due to the volumetric changes of the oil and the corresponding variations of the internal pressure. With a typical daily load profile, these processes can be interpreted as one or more complete thermal cycles per day, which, over a design service life of the order of 35 years, leads to an accumulation of more than 25,000 expansion and contraction cycles. These results are used as a reference basis for assessing the cumulative effect of thermal cycles on the structural stability and change of the parameters determining the effective life cycle of hermetically sealed distribution transformers.

3.4. Life Cycle Carbon Assessment of Distribution Transformers

Decisions regarding the management of the life cycle of distribution transformers (extension of operation, repair, modernization or replacement) have not only technical and economic consequences, but also significant environmental consequences. From the perspective of carbon footprint, emissions can be considered in three main groups:

- emissions associated with the production, transport and logistics of a new transformer or with the performance of repair activities;

The distribution of CO_2 emissions between the main material components of a typical oil-filled distribution transformer is presented in Figure 1. The analysis refers to a representative transformer with a power of 400 kVA. It is based on the results of a previous study by the authors, in which calculations of the quantities of materials used and the corresponding emission factors for the main structural elements of the transformer were performed. As can be seen from the figure, the magnetic core (electrical steel) has the largest contribution to the total carbon footprint and forms approximately 35% of the total emissions. This is mainly due to the significant mass of the electrical steel used and the relatively high carbon intensity of its production. The transformer windings, usually made of copper or aluminum, represent the second largest source of emissions with approximately 24% of the total. The remaining components have a smaller but significant contribution. Transformer oil accounts for about 12% of emissions, while the tank and structural elements of the enclosure contribute approximately 10%. Additional structural and insulating elements, summarized as other parts and accessories, account for about 11% of emissions. The energy required for the manufacture and assembly of the transformer accounts for approximately 8% of the total carbon footprint.

The resulting distribution shows that the majority of embodied emissions are related to the production of the main metallic materials used in the construction of the transformer [40].

- emissions caused by technical (mainly electric energy) losses during operation (operational emissions);
- emissions related to decommissioning, recycling, and recovery of material resources.

In distribution transformers, the operational component usually dominates over the long term, as energy losses in the magnetic system and windings accumulate continuously and are translated into indirect CO_2 emissions, depending on the carbon intensity of the electricity production mix. In a previous study by the authors, an approach was proposed to assess and compare carbon emissions for two alternatives—repair of a damaged transformer and replacement with a new one, taking into account both the carbon footprint of the materials used and the repair activities, and the emissions caused by energy losses during the remaining period of operation. In the present context, this approach allows linking the results for the long-term change in losses with a quantitative assessment of the environmental impact of different asset management strategies. Table 3 presents the manufacturer-declared no-load (ΔP_0) and short-circuit losses (ΔP_{SC}) for distribution transformers manufactured in the period 1970–1990, as well as for modern transformers (2010–2022). Based on the total energy losses, the equivalent annual CO_2 emissions associated with the operational mode have been estimated.

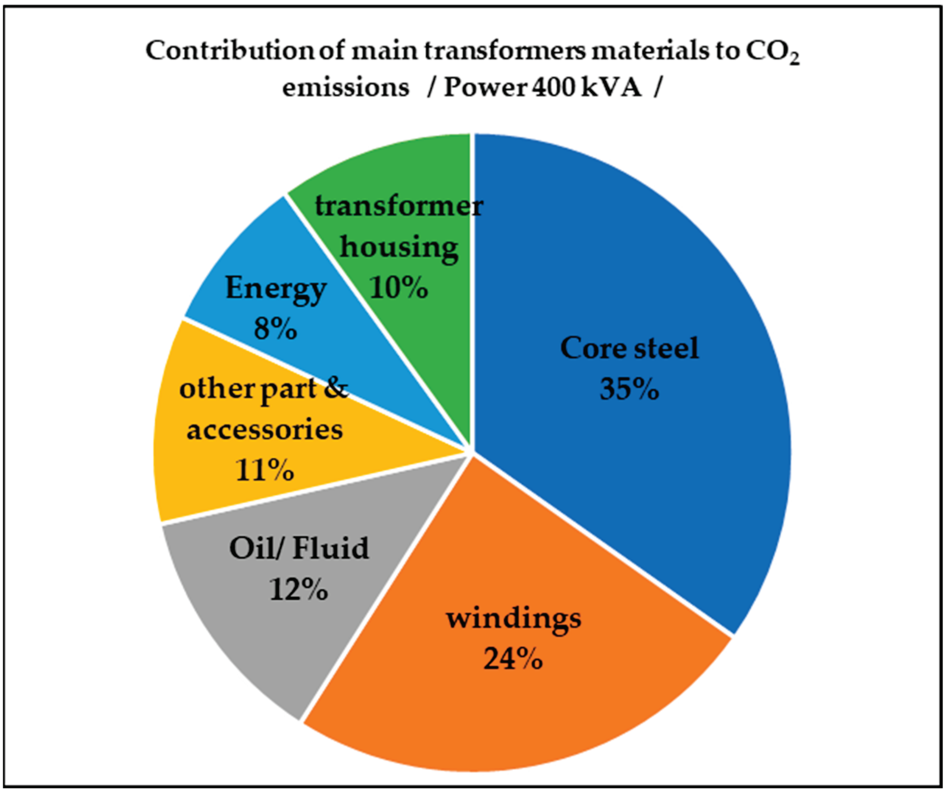

Figure 1. Contribution of the main transformer material groups to embodied CO_2 emissions for a 400 kVA oil-immersed distribution transformer.

Table 3. Power losses and corresponding annual CO_2 emissions of distribution transformers, calculated based on total annual energy losses under representative operating conditions.

Sr kVA	ΔP_0 (W) 1970–1990	ΔPsc (W) 1970–1990	CO_2 t/year	ΔP_0 (W) 2010–2022	ΔPsc (W) 2010–2022	CO_2 t/year
50	230	1100	2.4	81	750	0.6
100	400	2200	3.8	130	1250	0.9
160	500	3100	4.8	189	1750	1.4
250	780	3500	6.4	220	2350	1.9
400	1100	5000	9	340	3250	2.7
630	1580	7200	12	450	4600	3.8

The presented data show a significant reduction in losses for modern transformers. Depending on the rated power, the no-load ΔP_0 and short circuit losses ΔP_{sc} are reduced respectively approximately 3.5 and 1.5 times compared to transformers manufactured

https://doi.org/10.3390/en19081858

before 2000. This leads to a proportional reduction in annual CO_2 emissions associated with the operational phase. The effect is particularly pronounced for transformers with higher rated power, where the absolute difference in annual emissions reaches several tons of CO_2 per unit of equipment. Accumulated over time, this effect can have a significant impact on the carbon balance of the electricity distribution company. The results obtained have direct relevance for life cycle analysis and for the evaluation of transformer fleet management strategies. For transformers that have exceeded the recommended operational life ($\geq$40 years), there is a need to compare the two effects. When the analysis is limited to financial costs alone, the comparison is traditionally made using the Total Annual Cost (TAnC) method. Including carbon emissions as an additional criterion extends the assessment to the environmental life cycle and allows for more comprehensive and sustainable decision-making. On the other hand, for relatively new transformers with low losses and a significant residual resource, repair and extension of operation can lead to a lower overall carbon footprint, as the emissions associated with the production and logistics of new equipment are avoided. In this way, integrating the carbon component into the life-cycle analysis, based on the evolution of losses and reflecting operating modes, allows for the formulation of "repair–replacement" solutions in a broader context of sustainable asset management. In this context, the cost of CO_2 emissions is not attributed directly to transformers, but is incorporated through electricity generation costs in regions with carbon pricing mechanisms, such as the EU with its Emissions Trading System.

4. Life-Cycle Decision Model for Repair or Replacement of Distribution Transformers

Distribution transformers are long-term assets, for which decisions to repair or replace should be based not only on the initial capital costs, but also on the change in energy losses, operating modes and residual operating life. In the practice of electricity distribution companies, such decisions are most often imposed as a result of an accident or a serious deterioration in the technical condition of the transformer. In these cases, operators are faced with a choice of whether to repair and continue the operation of the existing facility or replace it with a new one. At present, there is no unified methodology or regulatory standard that would support this decision through a quantitative assessment that takes into account the long-term consequences of both approaches. In most cases, the choice is based on empirical considerations, short-term economic factors or available budget constraints.

The algorithm presented in Figure 2 describes the structure of the proposed model for making a decision on the repair or replacement of a distribution transformer. The model uses three main groups of input parameters—technical, economic and operational. On this basis, a model for assessing the costs during the life cycle (Life-Cycle Cost—LCC) is built, which also includes models reflecting the increased losses in the magnetic core and windings over time. By calculating the energy losses and the corresponding CO_2 emissions, a complex assessment of the economic and environmental effects is performed, which allows for a choice between two possible scenarios—repair of the existing transformer or its replacement with a new one. The model compares two possible scenarios: the first one is carrying out repairs and continuing operation, the second one is replacement with a new transformer and its operation for the same period. The main selection criterion is minimizing the present value of the residual life cycle costs, defined for our purposes as the sum of the capital costs and the discounted costs of energy losses over the time period for which the operator plans to operate the asset and is willing to assume the relevant technical and economic risk.

https://doi.org/10.3390/en19081858

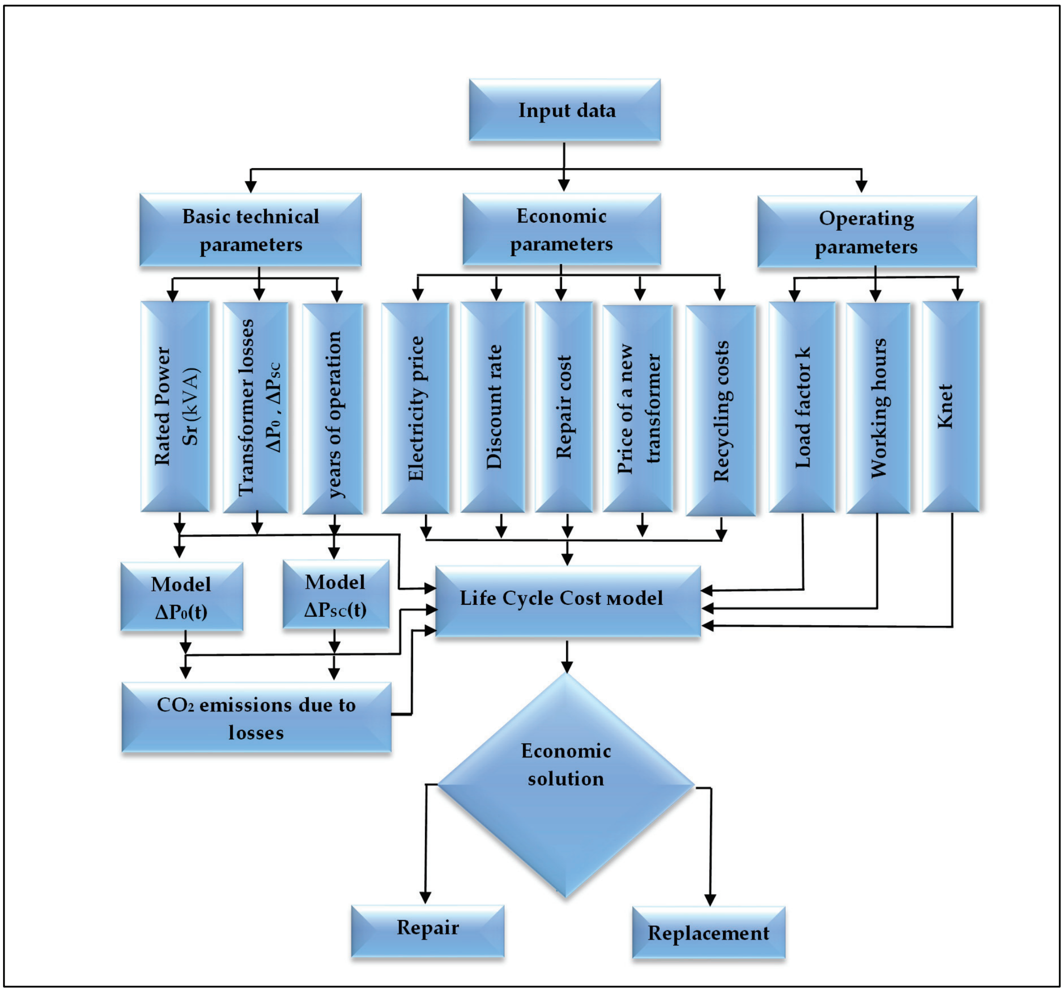

Figure 2. Flowchart of the proposed decision-making model for utilization (repair or replacement) of a distribution transformer, illustrating the sequence of calculations, including loss evaluation, economic assessment, and the integration of environmental (CO_2) costs.

4.1. Total Costs Under the Repair Scenario

The present value of the total costs in the "repair" scenario is defined as:

$$TC_R = C_R + \sum_{t=1}^{T_R} \frac{C_{loss,R}(t)}{(1+i)^t} \tag{3}$$

C_R—capital cost of repair [€]. This value is the price from the quote received from a licensed repair company for the repair plus transportation costs.

T_R—The estimated period of operation after repair [years]. The estimated period is defined as the remaining operational resource up to 35 years of design life. For transformers older than 20 years, a fixed horizon of 15 years is assumed in order to ensure a comparable analysis in the late stage of the life cycle.

i—discount rate. The value of 6% corresponds to a typical regulatory or capital rate of return in the energy sector.

$C_{loss,R}(t)$—the financial value of the operating losses in year t. To take into account that the economic burden of losses for the operator may differ from the final market price c_e of electricity, a coefficient α_{loss} is introduced, which determines the effective price of energy to cover the energy losses: $c_{eff}(t) = \alpha_{loss} \cdot c_e(t)$

$$C_{loss,R}(t) = E_{loss,R}(t) \cdot c_{eff}(t) \tag{4}$$

https://doi.org/10.3390/en19081858

Annual energy losses

The annual energy losses in MWh for the "repair" scenario are calculated as:

$$E_{loss,R}(t) = \frac{t_{ann}\ \Delta P_{0,R}(t) + 8760\ k_{eq}^2\ \Delta P_{SC,R}(t)}{1000} \tag{5}$$

$\Delta P_{0,R}(t)$—no-load losses in year t of the assessment period after the repair [kW];

$\Delta P_{SC,R}(t)$—maximum load losses in year t of the assessment period after repair [kW];

t_{ann}—effective annual working time [h/year];

k_{eq}—is the equivalent load factor, which determines the real load losses. The parameter reflects the long-term load profile and has a significant impact on life cycle costs. It is determined according to the RMS approach:

$$k_{eq} = \sqrt{\frac{1}{T}\int_0^T k^2(\tau)\ d\tau} \tag{6}$$

$$k(\tau) = \frac{S(\tau)}{S_r},$$

where $S(\tau)$ is the instantaneous load of the transformer for time moment τ.

To account for their growth over time, no-load losses ΔP_0 are considered as a function of the year of the assessment period.

Respectively, no-load losses for the repairment scenario are estimated with:

$$\Delta P_{0,R}(t) = \Delta P_{0,R}(0) \cdot \left(1 + \alpha_0\right)^{t-1} \tag{7}$$

where α_0 is the annual rate of increase in no load losses. t = 1 corresponds to the first year after the repair.

Short-circuit losses (5-year rate applied)

In the model, the short circuit losses are described by a 5-year rate of change:

$$\Delta P_{SC,R}(t) = \Delta P_{SC,R}(0) \cdot \left(1 + \alpha_{SC,5y}\right)^{\frac{t}{5}} \tag{8}$$

$\alpha_{SC,5y}$—short circuit loss growth rate for a 5-year period;

t—year of the assessment period after the repair; $t = 1$ corresponds to the first year after the repair was carried out.

This approach reflects the fact that the degradation of the wiring system and contact resistances is statistically more pronounced over longer intervals, which is why the increase is modeled on a 5-year basis.

4.2. Total Costs Under the Replacement Scenario

In the "replacement" scenario, the total costs are determined analogously:

$$TC_N = C_N + \sum_{t=1}^{T_R} \frac{C_{loss,N}(t)}{(1+i)^t} \tag{9}$$

where: C_N is the capital cost of a new transformer, including delivery and installation.

The financial value of the operating losses in year t in the case of replacement with a new transformer.

$C_{loss,N}(t)$—are determined using an approach similar to that of the scenario (repair one) already considered. For new transformers, the loss increases during the years of operation are negligible, i.e., we assume $\alpha_0 = 0$, $\alpha_{SC,5y} = 0$ unless a specific long-term degradation scenario is considered.

https://doi.org/10.3390/en19081858

Integrated criterion with carbon component.

Annual CO_2 emissions are defined as:

$$\boldsymbol{CO_{2,R}(t) = E_{loss,R}(t) \cdot \gamma_{CO_2}(t) \qquad CO_{2,N}(t) = E_{loss,N}(t) \cdot \gamma_{CO_2}(t)} \tag{10}$$

where $\gamma_{CO_2}(t)$ is a coefficient for carbon dioxide emissions when producing an unit of electricity.

The annual costs associated with overcoming the damages caused by carbon dioxide are, respectively:

$$\begin{aligned} \boldsymbol{C_{CO_2,R}(t)} &= \boldsymbol{CO_{2,R}(t) \cdot c_{CO_2}(t)} \\ \boldsymbol{C_{CO_2,N}(t)} &= \boldsymbol{CO_{2,N}(t) \cdot c_{CO_2}(t)} \end{aligned} \tag{11}$$

where $\boldsymbol{c_{CO2}(t)}$ is the price of the emissions during the year t. The present value (discounted value) of the carbon component for both options:

$$\boldsymbol{PV_{CO_2,R} = \sum_{t=1}^{T_R} \frac{C_{CO_2,R}(t)}{(1+i)^t} \quad ; PV_{CO_2,N} = \sum_{t=1}^{T_R} \frac{C_{CO_2,N}(t)}{(1+i)^t}} \tag{12}$$

The integrated criterion values become:

$$\boldsymbol{TC_R^* = TC_R + PV_{CO_2,R}} \tag{13}$$

$$\boldsymbol{TC_N^* = TC_N + PV_{CO_2,N} - Scrap,}$$

where ***Scrap*** is the income as result of the sale of the replaced transformer for recycling.

The selection criterion is:

$$\boldsymbol{TC_R^* < TC_N^* \Rightarrow repair \qquad TC_R^* \geq TC_N^* \Rightarrow replacement} \tag{14}$$

The presented model provides a quantitative and transparent framework for making a decision between repair and replacement of distribution transformers under comparable operating conditions. By integrating economic and environmental factors, it allows for an informed choice based on minimizing life-cycle costs and assessing long-term technical risk.

5. Case Study

In order to demonstrate the applicability of the proposed life-cycle model, a realistic numerical example of a distribution transformer with a rated power of 400 kVA, operated for 40 years, which failed as a result of a fault, is considered. After a technical inspection, it was found that the transformer is subject to restoration. A licensed repair company provides a quote for a capital repair at a cost of C_R = € 3000 (including transport). Alternatively, the operator can scrap the damaged transformer (sell it for recycling), obtaining $Scrap = 600$ € and replacing it with a new one with the same rated power, the market price of which (including delivery and installation) amounts to C_N = € 15,000. The decision is analyzed for an assessment period T_R = 15 years (according to the accepted rule for transformers older than 30 years). The goal is to determine which scenario minimizes the present value of the total life-cycle costs, including capital costs, operating losses and carbon component. The selected example reflects typical practical conditions in distribution networks and allows for a clear illustration of the proposed methodology. It also enables a comparative evaluation of the sensitivity of the results to key technical and economic parameters.

Input data

Rated power: $\boldsymbol{S_r}$ = 400 kVA, Age: 40 years, Evaluation period: $\boldsymbol{T_R}$ = 15 years, Discount rate: $\boldsymbol{i}$ = 6%, Equivalent load factor: $\boldsymbol{k_{eq}}$ = 0.60 => $\boldsymbol{k_{eq}^2}$ = 0.36, Effective annual operating hours: $\boldsymbol{t_{ann}}$ = 8600 h/year, Electricity price: $\boldsymbol{c_e}$ = € 0.15/kWh, Loss value coefficient: $\alpha_{loss} = 0.40$, Effective price: c_{eff} = € 0.06/kWh, Post-repair base losses (t = 1): $\Delta P_{(0,R)}$ **(0)** = 1640 W, $\Delta P_{(SC,R)}$ **(0)** = 4500 W, Aging parameters: α_0 = 2.6% (annual) $\alpha_{(SC,5y)}$ = 1% (for 5 years), New transformer: $\Delta P_{(0,N)}$ = 189 W, $\Delta P_{(SC,N)}$ = 3250 W α_0 = 0, $\alpha_{(SC,5y)}$ = 0, Carbon intensity: $\gamma(CO_2)$ = 0.00025 "tCO_2/kWh. These parameters are representative, i.e., they reflect typical operating and economic conditions for distribution networks in Bulgaria and provide a realistic basis for the comparative life-cycle assessment.

1. Scenario "Repair"

1.1 Annual losses for the year t

$$E_{loss,R}(t) = \frac{t_{ann}\Delta P_{0,R}(t) + 8760 * k_{eq}^2 \Delta P_{SC,R}(t)}{1000}$$

$$E_{loss,R}(1) = 28295 \text{ kWh/year}$$

1.2 Financial value of lost energy:

$$C_{loss,R}(1) = E_{loss,R}(1) \cdot c_{eff}(1) = 28295 \cdot 0.06 = € \ 1697.71/\text{year}$$

1.3 Increases of power losses

- No load losses $\Delta P_{0,R}(t) = 1640(1.026)^{t-1}$
- Short circuit losses (1% every 5 years): $\Delta P_{SC,R}(t) = 4500(1.01)^{(t-1)/5}$.

1.4 Present value of energy losses

for $i = 6\%$ we get approximately $PV_{loss,R} \approx € \ 17995$

Therefore $TC_R = C_R + PV_{loss,R}$, $TC_R = 3000 + 17995$

$$TC_R \approx € \ 20995$$

This result represents the total discounted cost of the repair scenario over the considered evaluation period. The evolutions of losses and respective discounted costs are presented in Table 4.

Table 4. Annual power losses, total energy losses, costs of the energy losses, and present values of these costs, corresponding to the "repair" scenario for the considered distribution transformer over the evaluation period.

Year	$\Delta P_{0,R}$, W	$\Delta Psc_{,R}$, W	$E_{loss,R}$, kWh	$C_{loss,R}$, €	Discounted Values of $C_{loss,R}$, €
1	1640	4500.00	28,295.2	1697.71	1601.62
2	1683	4508.96	28,690.17	1721.41	1532.05
3	1726	4517.95	29,094.74	1745.68	1465.71
4	1771	4526.95	29,509.14	1770.55	1402.44
5	1817	4535.96	29,933.64	1796.02	1342.09
6	1865	4545.00	30,368.49	1822.11	1284.52
7	1913	4554.05	30,813.96	1848.84	1229.58
8	1963	4563.13	31,270.33	1876.22	1177.16
9	2014	4572.22	31,737.87	1904.27	1127.14
10	2066	4581.32	32,216.89	1933.01	1079.38
11	2120	4590.45	32,707.67	1962.46	1033.80
12	2175	4599.59	33,210.52	1992.63	990.28
13	2232	4608.76	33,725.75	2023.55	948.72
14	2290	4617.94	34,253.69	2055.22	909.03
15	2349	4627.14	34,794.65	2087.68	871.12

https://doi.org/10.3390/en19081858

2. "Replacement" scenario

For a modern 400 kVA transformer (period 2002–2025), the model uses the average passport no-load losses $\boldsymbol{\Delta P_{0,N}} = \mathbf{413.5}$ W, and short-circuit losses $\boldsymbol{\Delta P_{SC,N}} = \mathbf{3250}$ W.

In this case, the loss increases are negligible, i.e., we admit $\boldsymbol{\alpha_0}$= 0, $\boldsymbol{\alpha_{(SC,5y)}}$ = 0.

2.1 The annual energy losses are estimated according to the expression:

$$\boldsymbol{E_{loss,N}(t) = \frac{t_{ann}\Delta P_{0,N}(t) + 8760 * k_{eq}^2 \Delta P_{SC,N}(t)}{1000}}$$

The result is: $\boldsymbol{E_{loss,N} = 13805.3}$, $\mathbf{kWh/year}$

2.2 Financial value

$$\boldsymbol{C_{loss,N} = 13805.3 \cdot 0.06}$$

$$\boldsymbol{C_{loss,N} = \text{€}\ 828.32/\mathrm{year}}$$

2.3 Present value

$$\boldsymbol{PV_{loss,N} \approx \text{€}\ 8045}$$

$$\boldsymbol{TC_N = 15000 + 8045 - 600}$$

$$\boldsymbol{TC_N \approx \text{€}\ 22445}$$

3. Comparison

Since $\boldsymbol{TC_R < TC_N}$ the repair scenario is economically preferable for the analyzed conditions. The numerical example shows that for a 400 kVA transformer with 40 years of operation, the relatively low repair cost and moderate load level lead to lower life-cycle costs for the repair scenario over the 15-year horizon. However, under higher load levels, higher electricity prices, or stronger carbon pricing policies, replacement may become the preferred strategy.

6. Results

Based on the approach illustrated with the presented numerical example, an economic comparison was carried out between two alternative asset management strategies: capital repair of groups of existing transformers and replacement with new ones of the same rated power. The analysis considers both the initial capital costs and the discounted value of the operating losses over the selected evaluation period. In the "repair" scenario, the total life-cycle costs include the cost of the repair and the present value of the operating losses after the repair is completed. In the "replacement" scenario, the total costs consist of the investment required for the purchase and installation of a new transformer and the discounted value of its operating losses during the same assessment horizon. The results obtained for the presented example show that under the considered operating conditions, the "repair" scenario leads to lower total life-cycle costs. The calculated present value of the total costs in this case is approximately € 20,995, while in the case of replacement with a new transformer, the total costs reach around € 22.45. Therefore, for the given operating parameters, load conditions and economic assumptions, repair appears to be the economically preferable option for the considered 15-year evaluation period. The obtained result illustrates that when the repair cost is relatively low, and the transformer operates under moderate loading conditions, the economic advantage of replacement may not compensate for the higher initial investment in a new transformer. The presented example concerns a commonly used transformer rating (400 kVA). The proposed methodology is applicable to other ratings (e.g., 50–800 kVA), with results depending on the relative contributions of constant (approximated in our model using no-load) and variable (approximated in

https://doi.org/10.3390/en19081858

our model using short circuit) losses, as well as the specific operating modes expressed with k_{eq}.

7. Discussion

The results obtained show that the economic feasibility of repairing or replacing distribution transformers depends on the combination of technical and economic factors, among which the load magnitude, the age of the transformer, the assessment period and the price of electricity are of particular importance. At moderate values of the load factor, load losses represent a relatively limited share of the total operating losses. In this case, the difference between the losses of the repaired and the new transformer remains relatively small, which means that the lower initial investment in the repair compensates for the higher operating losses of the old facility. Therefore, under such conditions, repair often turns out to be an economically justified strategy, especially when the cost of the repair is significantly lower than the cost of a new transformer. However, with higher loads, the role of load losses increases significantly. Since older transformers are usually characterized by higher losses at higher load levels, the operating costs of the repaired transformer increase significantly. In these conditions, replacing with a new transformer becomes strategically more advantageous, as its lower losses lead to a reduction in long- term energy loss costs.

7.1. Influence of Load Factor

The load factor has a significant impact on the economic comparison between the two scenarios, as it determines the relative share of load losses in the total loss balance of the transformer. At lower values of the load factor, the contribution of load losses to the total operating losses is smaller. Under such conditions, the difference between the losses of the repaired transformer and those of a new transformer remains relatively limited. Consequently, the lower capital cost of the repair may offset the higher operational losses of the older unit, making repair the economically justified option. As the load factor increases, the share of load losses in the total losses becomes more significant. Since older transformers generally exhibit higher short-circuit losses, an increase in the load factor leads to higher operational costs in the repair scenario. As a result, the economic advantage gradually shifts towards the replacement scenario. The analysis indicates that there exists a threshold value of the load factor at which the preferred decision changes and the replacement of the transformer becomes the more economically advantageous strategy.

7.2. Impact of the Carbon Price

In addition to the purely economic costs, the analysis also considers the environmental impact associated with the carbon emissions resulting from the electricity required to cover transformer losses. Higher operating losses in older transformers lead to increased indirect carbon emissions. When a carbon price is introduced, these emissions represent an additional cost component in the life-cycle assessment. The results indicate that an increase in the carbon price improves the economic competitiveness of new transformers, as they are characterized by significantly lower operating losses and consequently lower associated emissions. Under such conditions, the replacement option may become preferable even when the repair cost is relatively low. This demonstrates that policies aimed at internalizing the cost of carbon emissions can significantly influence asset management decisions regarding the repair or replacement of distribution transformers. Overall, the results confirm that the proposed life-cycle analysis model enables a systematic and transparent comparison between repair and replacement strategies while simultaneously accounting for economic factors, operational losses, and environmental impacts. The assessment period used in the life cycle analysis also has a significant impact on the choice

https://doi.org/10.3390/en19081858

between the two scenarios. With a shorter assessment horizon, the impact of the initial capital costs is more pronounced, which usually favors repair. Conversely, with a longer analysis period, the accumulation of operational losses becomes more important, which increases the economic attractiveness of more efficient new transformers. Additionally, the inclusion of carbon emissions in the analysis extends the traditional economic assessment by taking into account the environmental effects of operational losses. When introducing a price for carbon emissions, the difference between older and newer transformers increases, as the lower losses of new facilities lead to lower indirect emissions. This means that at higher carbon prices, transformer replacement can become more economically competitive, even when the initial investment is higher. From a distribution network management perspective, these results show that decisions to repair or replace cannot be based solely on the age of the transformer or the cost of the repair. Instead, the complex influence of operating modes, long-term energy losses, and the regulatory framework related to energy efficiency and decarbonization needs to be taken into account. It should be noted that this study focuses on traditional power frequency transformers, which represent the bulk of the existing transformer fleet in distribution networks. Although new technological concepts such as Solid-State Transformers (SST) [41] are considered a promising direction for the future development of power systems, their design, operational characteristics and economic parameters differ significantly from those of classical transformers and are therefore not included within the framework of the presented considerations. The proposed model however, also allows for their not very complicated inclusion in such an integrated assessment, and can be further developed as a tool to support broader asset management decisions in power distribution companies.

8. Limitations

The proposed methodological framework is based on deterministic loss coefficients derived from available field data and assumes representative operating conditions over the considered assessment horizon. The trajectories of electricity prices, the choice of discount rate and emission factors are considered through scenario input parameters, rather than through full probabilistic uncertainty modeling. Furthermore, the approach does not explicitly model stochastic transformer failures and the associated outage costs. These factors may have an impact on real economic outcomes and represent a potential direction for future model development. Despite these limitations, the proposed approach allows for a systematic assessment of the economic and environmental aspects of the decisions for utilization of distribution transformers.

9. Conclusions

In this study, a structured life cycle analysis model is developed, and its application to support decisions about further utilization (repair or replacement) of aging distribution transformers is illustrated. The proposed methodological framework integrates capital costs, time-dependent operational losses, realistic load modes, and discounted cash flow analysis into a single analytical structure. By introducing dynamic dependencies for the changes in no-load and short circuit losses on which base the time evolution of total power and energy losses in the transformer is estimated, and with the possibility of including a carbon component, the model provides a consistent and transparent basis for comparing alternative asset management strategies within a given time horizon. The presented numerical example shows that the economically optimal solution is highly sensitive to key parameters such as the equivalent load factor, the rate of change in losses, and the discount rate used. In the case of a 40-year-old transformer with a rated capacity of 400 kVA, evaluated for a period of 15 years, the "repair" scenario turns out to be economically preferable

https://doi.org/10.3390/en19081858

under moderate load conditions and limited losses. However, when a carbon price is included, the "replacement" scenario gradually becomes more competitive due to lower operational losses and, consequently, lower associated emissions. The developed model represents a practical tool for a systematic and data-based assessment of transformers at the end of their life cycle and can support electricity distribution network operators in making decisions in the face of changing market and regulatory requirements. The proposed methodology can be extended by including stochastic load dynamics, variable electricity prices, probabilistic failure analysis, and asset portfolio optimization. In summary, the proposed approach contributes to more transparent, cost-effective, and environmentally sound asset management solutions in modern electricity distribution networks operating in the context of energy transition and increasing decarbonization requirements.

Author Contributions: Conceptualization, V.T.A.; methodology, V.T.A. and D.G.S.; validation, V.T.A. and D.G.S.; formal analysis, V.T.A.; investigation, V.T.A., D.G.S., N.S.P. and N.N.N.; data curation, V.T.A. and D.G.S.; writing—original draft preparation, V.T.A.; writing—review and editing, V.T.A., D.G.S., N.S.P. and N.N.N.; visualization, V.T.A.; supervision, V.T.A. All authors have read and agreed to the published version of the manuscript.

Funding: This research received no external funding.

Data Availability Statement: The original contributions presented in the study are included in the article; further inquiries can be directed to the corresponding author.

Acknowledgments: The publishing of this work has been accomplished with financial support by the European Regional Development Fund within the Operational Programme "Bulgarian national recovery and resilience plan", procedure for direct provision of grants "Establishing of a network of research higher education institutions in Bulgaria", and under Project BG-RRP-2.004-0005.

Conflicts of Interest: The authors declare no conflicts of interest.

References

1. Liang, Z.; Fang, Y.; Cheng, H.; Sun, Y.; Li, B.; Li, K.; Zhao, W.; Sun, Z.; Zhang, Y. Innovative Transformer Life Assessment Considering Moisture and Oil Circulation. *Energies* **2024**, *17*, 429. [CrossRef]
2. Kunicki, M.; Borucki, S.; Cichoń, A.; Frymus, J. Modeling of the Winding Hot-Spot Temperature in Power Transformers: Case Study of the Low-Loaded Fleet. *Energies* **2019**, *12*, 3561. [CrossRef]
3. Lundgaard, L.E.; Hansen, W.; Linhjell, D.; Painter, T.J. Aging of oil-impregnated paper in power transformers. *IEEE Trans. Power Deliv.* **2004**, *19*, 230–239. [CrossRef]
4. Feng, D.Y.; Wang, Z.D.; Jarman, P. Modeling thermal life expectancy of the UK transmission power transformers. In Proceedings of the 2012 International Conference on High Voltage Engineering and Application, Shanghai, China, 17–20 September 2012; pp. 540–543. [CrossRef]
5. Olivares-Galván, J.C.; Georgilakis, P.S.; Ocon-Valdez, R. A review of transformer losses. *Electr. Power Compon. Syst.* **2009**, *37*, 1046–1062. [CrossRef]
6. Georgilakis, P.S. Environmental cost of distribution transformer losses. *Appl. Energy* **2011**, *88*, 3146–3155. [CrossRef]
7. Amoiralis, E.I.; Tsili, M.A.; Kladas, A.G. Economic evaluation of transformer selection in electrical power systems. In *The XIX International Conference on Electrical Machines-ICEM 2010*; IEEE: New York, NY, USA, 2010.
8. Wijayapala, W.D.A.S.; Gamage, S.R.K.; Bandara, H.M.S.L.G. Determination of capitalization values for no load loss and load loss in distribution transformers. *Eng. J. Inst. Eng. Sri Lanka* **2016**, *49*, 11–20. [CrossRef]
9. Amoiralis, E.I.; Tsili, M.A.; Kladas, A.G. Transformer Design and Optimization: A Literature Survey. *IEEE Trans. Power Deliv.* **2009**, *24*, 1999–2024. [CrossRef]
10. Wang, S.; Luo, F.; Fo, J.; Lv, Y.; Wang, C. Two-stage spatiotemporal decoupling configuration of SOP and multi-level electric-hydrogen hybrid energy storage based on feature extraction for distribution networks with ultra-high DG penetration. *Appl. Energy* **2025**, *398*, 126438. [CrossRef]
11. Shrieves, R.E.; Wachowicz, J.M., Jr. Free cash flow (FCF), economic value added (EVA™), and net present value (NPV): A reconciliation of variations of discounted-cash-flow (DCF) valuation. *Eng. Econ.* **2001**, *46*, 33–52. [CrossRef]
12. Godina, R.; Rodrigues, E.M.G.; Matias, J.C.O.; Catalão, J.P.S. Effect of loads and other key factors on oil-transformer ageing: Sustainability benefits and challenges. *Energies* **2015**, *8*, 12147–12186. [CrossRef]

13. Vinogradov, A.V.; Bolshev, V.E.; Ward, M.O.; Makhiyanova, N.V.; Dolomaniuk, L.V. Justification for creating a mobile complex to assess electric energy loss in power transformers during the operation process. *E3S Web Conf.* **2019**, *124*, 02009. [CrossRef]
14. Dao, T.; Phung, B.T. Effects of voltage harmonic on losses and temperature rise in distribution transformers. *IET Gener. Transm. Distrib.* **2018**, *12*, 347–354. [CrossRef]
15. Chen, J.; Duan, N.; Zhou, X.; Wang, Z. Diagnostic Model for Transformer Core Loosening Faults Based on the Gram Angle Field and Multi-Head Attention Mechanism. *Appl. Sci.* **2024**, *14*, 10906. [CrossRef]
16. Tada, H.; Fujimura, H.; Yashiki, H. Influence of magnetostriction on hysteresis loss of electrical steel sheet. *J. Magn. Magn. Mater.* **2013**, *326*, 217–219. [CrossRef]
17. Kumar, G.K.; Vynatheya, S.; Kumar, A. Condition assessment of transformer core CRGO steels due to thermal ageing and their evaluation. In *Proceedings of the 2017 3rd International Conference on Condition Assessment Techniques in Electrical Systems (CATCON), Rupnagar, India, 16–18 November 2017*; IEEE: New York, NY, USA, 2017.
18. Altayef, E.; Anayi, F.; Packianather, M.S.; Kherif, O. On the effects of lamination artificial faults in a 15 kVA three-phase transformer core. *IEEE Access* **2022**, *10*, 19348–19355. [CrossRef]
19. *IEC 60076-7:2018*; Power Transformers—Loading Guide. International Electrotechnical Commission: Geneva, Switzerland, 2018.
20. Atanasov, V.; Stoilov, D.; Mechkov, E. Changes of iron losses during the service of distribution transformers. In *Proceedings of the 2022 14th Electrical Engineering Faculty Conference (BulEF), Varna, Bulgaria, 14–17 September 2022*; IEEE: New York, NY, USA, 2022.
21. Olivares, J.C.; Kulkarni, S.V.; Cañedo, J.; Escarela-Perez, R.; Driesen, J.; Moreno, P. Impact of the Core Joint Design Parameters on Transformer Losses. *Int. J. Power Energy Syst.* **2003**, *23*, 151–157.
22. *IEC 60076-1:2011*; Power Transformers—Part 1: General. International Electrotechnical Commission: Geneva, Switzerland, 2011.
23. European Commission. *Commission Regulation (EU) No 548/2014 Implementing Directive 2009/125/EC with Regard to Small, Medium and Large Power Transformers*; European Commission: Brussels, Belgium, 2014.
24. León-Martínez, V.; Peñalvo-López, E.; Andrada-Monrós, C.; Sáiz-Jiménez, J.Á. Load Losses and Short-Circuit Resistances of Distribution Transformers According to IEEE Standard C57.110. *Inventions* **2023**, *8*, 154. [CrossRef]
25. Mavrikakis, N.; Siderakis, K. Effects of Aging on Condition of In-Service Transformer Oil: The Study Case of 150 kV/20 kV Substations in Crete. *Energies* **2025**, *18*, 4900. [CrossRef]
26. Chen, J.; Zhang, Z.; Gao, Z.; Wu, J. Analysis of the Mechanical Stability of Power Transformer Windings Considering the Influence of Temperature Field. *Energies* **2025**, *18*, 1374. [CrossRef]
27. Jia, X.; Lin, M.; Su, S.; Wang, Q.; Yang, J. Numerical study on temperature rise and mechanical properties of winding in oil-immersed transformer. *Energy* **2022**, *239*, 121788. [CrossRef]
28. *IEEE Std C57.12.00*; 2015 Standard for General Requirements for Liquid-Immersed Distribution, Power, and Regulating Transformers. IEEE: New York, NY, USA, 2015.
29. Atanasov, V.; Stoilov, D.; Nikolov, N. Changes of copper losses during the service of distribution transformers. In *Proceedings of the 2022 V International Conference on High Technology for Sustainable Development (HiTech), Sofia, Bulgaria, 6–7 October 2022*; IEEE: New York, NY, USA, 2022.
30. Seddik, M.S.; Shazly, J.; Eteiba, M.B. Thermal Analysis of Power Transformer Using 2D and 3D Finite Element Method. *Energies* **2024**, *17*, 3203. [CrossRef]
31. Zhan, L.; Chang, H.; Zhu, X.; Zhao, X.; Wei, G.; Cai, Z.; Xie, H.; Zhao, X.; Chen, H. Analysis of Factors Influencing Life-Cycle Costs of Transformers Based on TOPSIS Method. *Energies* **2024**, *17*, 5912. [CrossRef]
32. IEEE. IEEE Guide for Determination of Maximum Winding Temperature Rise in Liquid-Immersed Transformers. In *IEEE Std C57.169-2023 (Revision of IEEE Std 1538-2000)*; IEEE: New York, NY, USA, 2023; pp. 1–53. [CrossRef]
33. Janic, Z.; Gavrilov, N.; Roketinec, I. Influence of cooling management to transformer efficiency and ageing. *Energies* **2023**, *16*, 4626. [CrossRef]
34. Kersting, W.H. Distribution system modeling and analysis. In *Electric Power Generation, Transmission, and Distribution*; CRC Press: Boca Raton, FL, USA, 2018; Volume 26.
35. Harker, K. *Power System Commissioning and Maintenance Practice*; No. 24; IET: London, UK, 1998.
36. Lee, S.; Lee, J.Y.; Yun, J.C.; Park, J.Y.; Woo, J.H. Development of thermal and structural design technology for a hermetically sealed oil transformer. *Struct. Under Shock. Impact XII* **2013**, *126*, 179–190.
37. Yun, J.C.; Lee, S.W.; Park, J.Y.; Lee, J.Y. Structural Integrity Evaluation of a Corrugated Type Radiator for a Hermetically Sealed Oil Transformer. In *Proceedings of the ASME 2011 Pressure Vessels and Piping Conference, Baltimore, MD, USA, 17–21 July 2011*; Volume 3: Design and Analysis; ASME: New York, NY, USA, 2011; pp. 877–887. [CrossRef]
38. Kamvar, B.A.; Herfati, D.; Tavakkol, A.; Milani, K.R. Calculation of Mechanical Stresses in Hermetically Sealed Transformers. 2007. Available online: https://www.semanticscholar.org/paper/CALCULATION-OF-MECHANICAL-STRESSES-IN-HERMETICALLY-Kamvar-Tavakkol/8b9b86705fba5b2cc112225d3f4fb5aca7cd3b13 (accessed on 10 February 2026).
39. Atanasov, V. Effects of Contingency Overheating of Hermitized Distribution Transformers. In *Proceedings of the 2023 15th Electrical Engineering Faculty Conference (BulEF), Varna, Bulgaria, 16–19 September 2023*; IEEE: New York, NY, USA, 2023.

https://doi.org/10.3390/en19081858

40. Atanasov, V.; Stoilov, D. Study on Carbon Emissions Born During the Life Cycle of Distribution Transformers. In Proceedings of the 2023 15th Electrical Engineering Faculty Conference (BulEF), Varna, Bulgaria, 16–19 September 2023; pp. 1–4. [CrossRef]
41. Hinov, N. Solid-State Transformers in the Global Clean Energy Transition: Decarbonization Impact and Lifecycle Performance. *Energies* **2026**, *19*, 558. [CrossRef]

energies

Article

Modeling and Calibration Using Micro-Phasor Measurement Unit Data for Yeonggwang Substation

Peng Li [1,2], Chung-Gang Kim [3], Sung-Hyun Choi [1], Kyung-Min Lee [1] and Yong-Sung Choi [1,*]

1 Department of Electrical Engineering, Dongshin University, Naju 58245, Republic of Korea; lipeng@dsu.ac.kr (P.L.); a01077386349@gmail.com (S.-H.C.); kmlee@dsu.ac.kr (K.-M.L.)
2 College of Electronic Engineering, Changchun College of Electronic Technology, Lan Jia Campus, Changchun 130114, China
3 Kalon E&M Co., Ltd., Naju 58326, Republic of Korea; hakjae52@naver.com
* Correspondence: yschoi67@dsu.ac.kr

Abstract

Against the backdrop of high-proportion renewable energy grid integration, modeling accuracy for substations incorporating wind and solar power is critical. Traditional modeling methods rely on theoretical parameters and lack sufficient accuracy. This study uses the 154 kV/23 kV Yeonggwang Substation in Jeollanam-do, South Korea (connected to three wind farms and three solar power plants, with 35 Micro-Phasor Measurement Unit (μPMU) measurement points deployed) as a case study. It investigates three-phase detailed modeling using Power System Computer Aided Design (PSCAD) and μPMU data-driven calibration. Based on substation topology and equipment parameters, a simulation model encompassing main transformers, transmission lines, renewable energy units, and loads was established. A hierarchical calibration system of "data preprocessing—parameter identification—iterative correction" was constructed, employing an iterative optimization strategy of "main grid layer—renewable energy layer—load layer." A multi-objective optimization function centered on voltage, current, and power was developed. Verification results show that after calibration, the mean relative error rates (MRE) for voltage, current, active power and reactive power are 2.46%, 2.57%, 2.52% and 3.96% respectively, with mean error reduction rates (MERRs) of 80%, 82.75%, 81.33%, and 74.94% compared to pre-calibration values. The uniqueness of the calibration method proposed in this study lies in its use of actual μPMU measurement data to drive PSCAD model parameter calibration, achieving precise matching with the actual characteristics of the substation. This provides a reference method for modeling and digital twin construction of similar substations, demonstrating significant engineering application value.

Keywords: steady-state simulation; micro-phasor measurement unit data; substation modeling; data-driven calibration

1. Introduction

Recent efforts in the power industry have increasingly focused on developing next-generation intelligent transmission grid platforms that leverage advanced sensing, communication, and control technologies to enable more reliable, efficient, and flexible system operation, particularly in the context of high renewable energy integration and real-time wide-area monitoring [1,2]. As the core hub for power conversion and dispatch, the accuracy of substation simulation models directly determines the reliability of grid operation analysis, fault simulation, and dispatch optimization. PSCAD/EMTDC, as the core tool for power system electromagnetic transient simulation, has been widely applied in substation modeling. However, existing practices still face numerous challenges, struggling to meet the demands of complex power grids. Traditional PSCAD modeling heavily relies on design manual parameters and theoretical calculations, exhibiting issues such as strong parameter dependency, pronounced subjectivity, and excessive simplification of topologies. Furthermore, existing research predominantly focuses on theoretical parameter setting or limited measurement validation, with few explorations into full-station calibration under high penetration levels based on multi-point μPMU data. Particularly for special voltage levels like 154 kV/23 kV, customized solutions are lacking for main transformer equivalent modeling and line impedance calculation, leading to significant deviations between models and actual operating conditions [3–5]. Concurrently, the high penetration of renewable energy sources (wind and solar) has introduced strong fluctuations and bidirectional power flow characteristics into substation operations. Existing modeling approaches inadequately characterize the coupled behavior of multiple renewable energy sources, further exacerbating model accuracy deficiencies. To enhance the accuracy of new energy-related models, existing research predominantly adopts hybrid technical approaches as follows: optimizing wind speed prediction accuracy through hybrid machine learning models provides precision support for modeling the fluctuating characteristics of wind power fed into substations [6]. The proposed hybrid optimization algorithm offers an algorithmic reference for optimizing model parameters in multi-energy coordinated dispatch at substations [7]. Focusing on improving photovoltaic system modeling accuracy, the approach combining topology simplification with intelligent algorithms offers valuable insights for precise modeling of the photovoltaic input side at substations [8].

Micro-Phasor Measurement Unit (μPMU) Compared to traditional Supervisory Control and Data Acquisition (SCADA) systems with 4 s data acquisition cycles and lower synchronization accuracy, the μPMU offers microsecond-level time synchronization capability. It enables real-time capture of critical electrical signals such as voltage magnitude, phase angle, and frequency, with a maximum data sampling rate of 256 times per power frequency cycle. This allows for precise detection of dynamic operational details within substations [9,10]. Therefore, μPMU-based calibration is crucial in this study. Conducting model calibration using actual μPMU measurement data to establish a closed-loop research system of "modeling-measurement-calibration" has become an important method for enhancing the accuracy of substation simulation models [11].

Current research on power system monitoring and microgrid modeling has established a solid foundation. μPMU can address the limitations of SCADA systems, such as low accuracy and sampling rates, thereby enhancing the precision of state estimation [12]. Additionally, they can assist in transmission line loss monitoring and corona loss calculation [13]. Ensuring the performance of μPMU in field applications is a critical issue. Related research has proposed a field testing and calibration framework incorporating calibrators and analysis centers, and has improved accuracy through methods such as signal denoising [14]. In the microgrid domain, PSCAD has been applied to model microgrids with multiple distributed resources. Related studies have explored grid-connected and islanded operation modeling, energy storage control, and other issues [15], laying the groundwork for research integrating PSCAD modeling with μPMU data calibration.

The data-driven calibration method proposed in this study is tailored to the practical modeling needs of substations. By leveraging actual PMU measurement data to construct calibration logic, it accurately captures the dynamic characteristics of core parameters such as voltage and phase angle without requiring complex parameter iterations. This approach effectively mitigates the interference of complex substation operating environments on calibration results, providing reliable support for subsequent simulation model optimization

https://doi.org/10.3390/en19030834

and fault analysis. Compared to existing PSCAD-PMU calibration research, this approach replaces traditional synchronous parameter estimation with hierarchical calibration. By decoupling core and secondary parameters, it resolves multi-parameter coupling interference, enhancing calibration specificity and computational efficiency [16]. It achieves deep alignment between PMU high-frequency, high-precision data and PSCAD modeling while balancing calibration accuracy and engineering practicality. This method can be implemented using existing substation data and adapts to real-world operational requirements.

The Yeonggwang Substation in South Jeolla Province, South Korea, serves as a critical node for regional voltage transformation, handling the conversion from 154 kV to 23 kV. This substation exemplifies South Korea's typical medium-voltage conversion standards and features a high penetration rate of renewable energy. Three wind farms and three photovoltaic power stations are connected to its transmission lines. Accurate modeling of this substation is crucial for ensuring the safe and stable operation of the regional power grid [17,18]. Therefore, we selected the Yeonggwang Substation as our research subject to conduct PSCAD modeling and μPMU data calibration studies. First, we constructed a PSCAD model covering the entire line, including the main grid, new energy units, and transmission lines. Subsequently, based on data from 35 deployed μPMU measurement points, we designed a hierarchical iterative calibration strategy to achieve precise optimization of model parameters. Finally, we quantitatively verified the calibration effectiveness by comparing metrics such as voltage, power, and relative error. The proposed "PSCAD modeling + multi-point μPMU calibration" technical solution effectively addresses the limitations of traditional modeling accuracy. It provides a technical reference for precise modeling of substations at special voltage levels while offering a reliable simulation tool for operational optimization, fault prediction, and analysis/evaluation at the Yeonggwang Substation. This approach holds significant theoretical and practical engineering value [19,20].

The subsequent sections of this paper are organized as follows: Section 2 outlines the rationale for substation modeling and the fundamental parameters of μPMU data. Section 3 details the implementation process of the full-line PSCAD modeling for Yeonggwang Substation. Section 4 proposes a hierarchical iterative calibration method based on 35 μPMU data points, presenting and analyzing the modeling and calibration results. Finally, Section 5 summarizes the research conclusions and future directions.

2. Fundamentals of PSCAD Modeling for Yeonggwang Substation

PSCAD modeling theory forms the foundation for substation simulation modeling. Based on electromagnetic transient simulation mechanisms, it achieves precise replication of power system dynamic processes through core logic such as the node voltage method. Its applicability spans multiple power engineering domains, including transmission and transformation system component modeling and renewable energy integration simulation. This study clarifies the simulation principles and applicable boundaries of the software, with a focus on elucidating the core logic of power system component modeling. It provides a solid theoretical foundation for subsequent detailed modeling of key components and renewable energy units at the Yeonggwang Substation.

2.1. Topological Structure Analysis of Yeonggwang Substation

The Yeonggwang substation in South Jeolla Province, South Korea, has installed a 35-μPMU(the device is a μPMU manufactured by Korea's Green Information System Co., Ltd., Gwangju, Republic of Korea) [21,22], Figure 1 shows the single-line diagram of the Yeonggwang substation. As shown in Figure 1, the high-voltage side of the substation is 154 kV, and the low-voltage side is 23 kV. Additionally, the installation locations of the

https://doi.org/10.3390/en19030834

35 μPMUs are marked in Figure 1 (#1–#35). The 154 kV area was connected to Baeksu WP, Jaewon PV, and Hamgumi PV. The 22.9 kV area was connected to Honam WP, DSE (PV), and Jeonnam TP (WP).

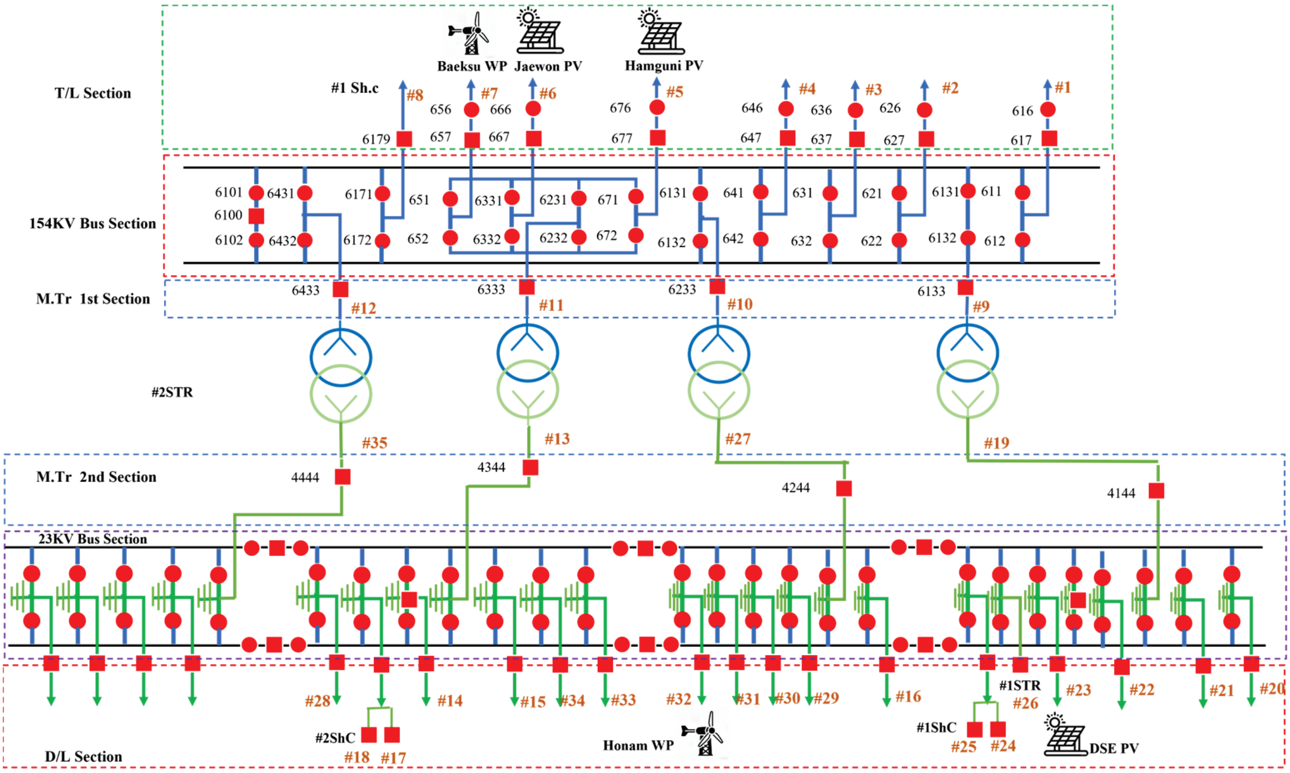

Figure 1. A single-line diagram of the Yeonggwang substation.

2.2. *Analysis of Main Transformer Structure and Parameters*

The four transformers at Yeonggwang Substation each have a rated capacity of 45 MW. These three-phase winding transformers are connected in a Y/Y/Delta configuration. Their high-voltage windings are connected in parallel to the 154 kV busbar, their medium-voltage windings are connected in parallel to the 23 kV busbar, and their low-voltage windings are connected in parallel to the 6.6 kV busbar. Specific parameters are shown in Table 1.

Table 1. Main transformer parameters of Yeonggwang Substation.

	#1 Transformer	#2 Transformer	#3 Transformer	#4 Transformer
Rated capacity	45 MW	45 MW	45 MW	45 MW
frequency	60 Hz	60 Hz	60 Hz	60 Hz
High Voltage	154 kV	154 kV	154 kV	154 kV
Medium Voltage	23 kV	23 kV	23 kV	23 kV
Low Voltage	6.6 kV	6.6 kV	6.6 kV	6.6 kV
Forward-Sequence Leakage Inductance (1–2)	10.2% AT 15 MW	14.6% AT45 MW	14.24% AT5 WM	15.2% AT45 MW
Forward-Sequence Leakage Inductance (1–3)	8.15% AT 5 MW	7.93% AT15 MW	7.44% AT5 MW	8.25% AT15 MW
Forward-Sequence Leakage Inductance (2–3)	2.75% AT 5 MW	2.10% AT15 WM	2.07% AT5 MW	2.18% AT15 MW

https://doi.org/10.3390/en19030834

3. Detailed PSCAD Modeling Process for Yeonggwang Substation

3.1. Building PSCAD Models

3.1.1. A 154 kV Incoming Line and Busbar Modeling

Due to the lack of detailed resistance and reactance parameters for the incoming line, the unit length resistance and reactance values were estimated by referencing the general parameter ranges for 154 kV overhead lines in the "Electrical Design Manual for Power Engineering" and considering the line design length. This enabled the configuration of the line model parameters. The busbar employs the "Busbar" ideal busbar module, neglecting its inherent resistive and capacitive losses. The connection relationship between the 154 kV incoming busbar and the high-voltage side of the main transformer is explicitly defined.

3.1.2. Main Transformer Modeling

The "3 Winding Transformer" standard module in PSCAD was selected, with core parameters designed based on the specific transformer specifications in Table 1, including rated capacity, rated voltage ratio, and positive-sequence leakage reactance.

3.1.3. A 23 kV Feeder and Load Modeling

The outgoing lines also employ distributed parameter line modules, with resistance and reactance values estimated based on the 23 kV line design length and standard unit parameters. The load utilizes the "fixed_Load" composite load model, calculating actual active power P and reactive power Q from voltage, current, and phase angle data in the μPMU. However, due to the unknown load power type, constant power (P), constant impedance (Z), and constant current (I) loads at 60%, 30%, and 10% respectively (matching typical distribution network load proportions at this voltage level). After initial calibration, precise adjustments are made using μPMU data.

3.1.4. Detailed Construction of Wind Power and Photovoltaic Models

Due to confidentiality restrictions in practical power systems, detailed manufacturer-specific parameters of wind turbines and photovoltaic units—such as blade pitch control coefficients, rotor diameter, or PV module open-circuit and short-circuit characteristics—were not available. Only the rated power and rated voltage levels of each renewable unit were obtained.

Under this constraint, the renewable generation units were modeled as grid-side equivalent power-controlled units, rather than detailed device-level physical models. The objective of the modeling was to accurately represent the power injection behavior at the point of interconnection, which is consistent with the spatial and temporal resolution of μPMU measurements.

For wind power units, the DFIG Wind Turbine module from the PSCAD standard library was employed. To ensure reproducibility, the modeling procedure is summarized as follows:

- Rated capacity configuration: The rated active power of the DFIG model was set according to the known rated capacity of the wind power unit, ensuring that the steady-state active power output matches the actual operating level.
- Grid connection and voltage level: The wind turbine model was connected to the 154 kV substation bus through a step-up transformer. The modeling focus was placed on the electrical quantities at the grid connection point, including active power, reactive power, and voltage magnitude.
- Control mode selection: The wind power unit was operated in a constant active power control mode, while the reactive power (or voltage) control followed the default configuration of the PSCAD standard model to match the observed μPMU measurements.

https://doi.org/10.3390/en19030834

- Default internal parameters: Parameters related to aerodynamic characteristics, mechanical dynamics, and internal control loops were retained at their PSCAD default values, due to the absence of verifiable field data. This avoids introducing unsubstantiated assumptions and ensures that the model can be reproduced directly using the standard library.
- For multiple wind power units, identical electrical and control parameters were used, with individual units distinguished only by their identifiers. This modeling strategy ensures consistency across units and facilitates replication. The wind power module is illustrated in Figure 2.

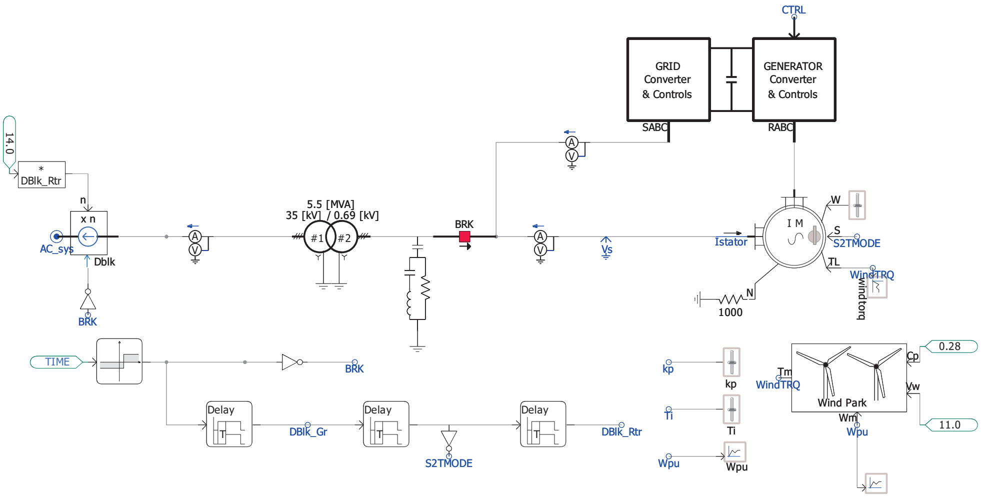

Figure 2. Wind power generation model.

The photovoltaic model is constructed using the "Simple Solar Farm" base module in PSCAD, which integrates core submodules including the PV array, inverter, and MPPT controller. Key modifications during modeling are as follows: ① calculate the number of series and parallel modules based on known PV rated power and rated voltage: assuming a single PV module has a rated power of 100 kW and rated voltage of 154 V, the number of series and parallel modules is estimated using the relationships: "Total rated power = Single module power × Number of parallel modules" and "Array rated voltage = Single module voltage × Number of series modules". "Array rated voltage = single-module voltage × number of series connections." (Due to the lack of detailed module parameters, this estimation is solely for matching rated power and voltage and does not involve modifying internal module characteristics); ② adjust the inverter's rated output power and voltage to match the PV array's rated parameters, ensuring the inverter can stably convert the array's generated electricity into 154 kV AC for grid integration; ③ retain the standard model's irradiance and temperature input defaults: standard irradiance 1000 W/m^2, standard temperature 25 °C. These parameters can be adjusted later to simulate PV output variations under different irradiance and temperature conditions. The key electrical waveforms at the PV array model's common connection point (POC) are shown in Figure 3.

3.2. Initial Model Construction and Validation

After completing the implementation of all components and control modules, an initial model verification was conducted to ensure topological integrity and numerical correctness of the PSCAD model. This step focused on verifying the connectivity logic and parameter consistency of key components, particularly the rated power and voltage levels of the main transformer and renewable generation units. The overall model topology exported from PSCAD is shown in Figure 4.

https://doi.org/10.3390/en19030834

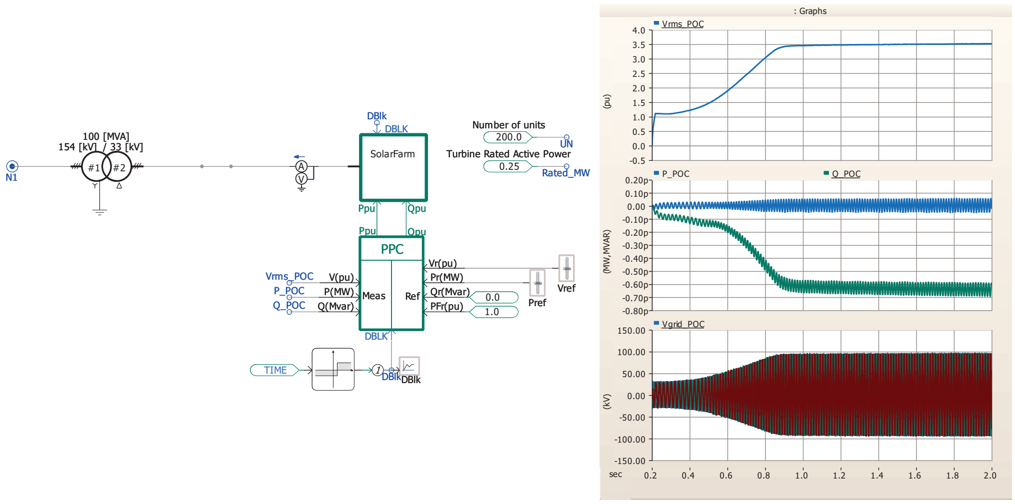

(**a**) (**b**)

Figure 3. Photovoltaic module: (**a**) photovoltaic model circuit; (**b**) electrical waveform at the public connection point (POC) of a photovoltaic array.

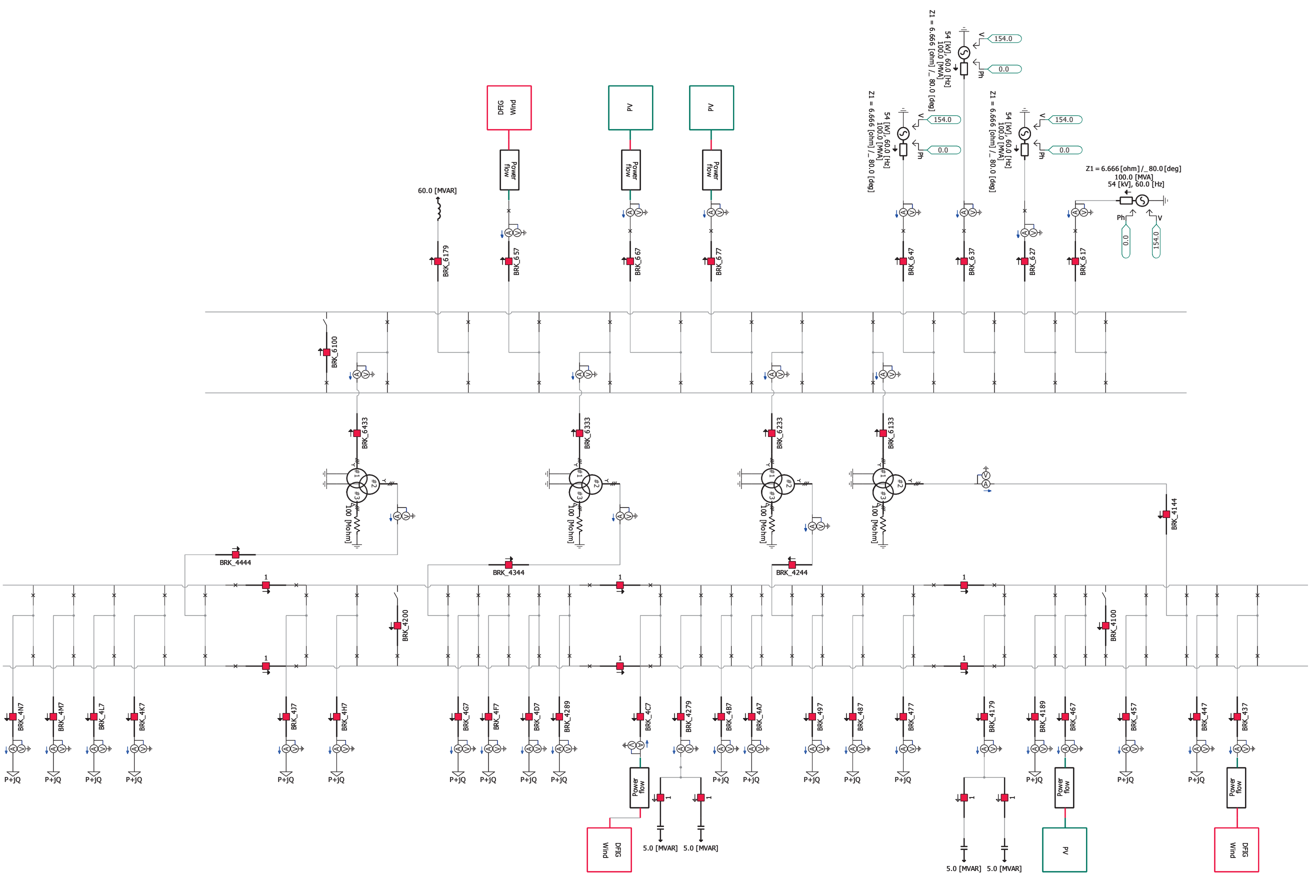

Figure 4. Yeonggwang Substation PSCAD model diagram.

Since the renewable generation units were developed based on modified PSCAD standard models and detailed manufacturer parameters were unavailable, the initial verification was limited to steady-state operating conditions, and complex dynamic performance tests were not conducted at this stage. The purpose of this initial verification was not to evaluate calibration accuracy, but to confirm that the model provides a physically reasonable baseline for subsequent μPMU-based calibration.

https://doi.org/10.3390/en19030834

Accordingly, no-load and rated-load tests were performed as sanity checks. The verification criteria included waveform quality, RMS magnitude consistency, and system frequency stability. Specifically, steady-state waveforms were required to exhibit no obvious numerical oscillations or abnormal harmonic distortion; RMS values were checked to ensure consistency in order of magnitude, with deviations within ±15% used solely as an indicator to identify gross modeling or configuration errors; and system frequency was required to remain stable within 60 Hz ± 0.5 Hz.

4. μPMU Data-Driven PSCAD Model Calibration Method

4.1. Hierarchical Iterative Least-Squares Calibration for PSCAD Model with μPMU Data

The core objective of model calibration is to refine PSCAD model parameters using μPMU measurement data, ensuring simulation outputs closely match the actual operational characteristics of substations. This study employs a hierarchical iterative least-squares optimization method for calibration. Its core principle involves constructing a multi-objective optimization function using key electrical quantities—such as voltage, current, and power—synchronously measured by μPMU as reference values. Through iterative adjustment of model parameters, the method minimizes the error between simulated and measured values while constraining parameter adjustments within the boundaries of equipment physical characteristics. Compared to traditional parameter-based calibration methods, this approach leverages synchronized multi-point measurement data from distributed μPMU to achieve station-wide calibration without blind spots.

4.2. μPMU Data Acquisition and Preprocessing

4.2.1. Data Collection Specifications

1. Time synchronization is achieved through GPS-based time stamping with microsecond-level accuracy, consistent with the IEEE C37.118 standard [23] for μPMU measurements. The sampling rate is set to 60 Hz, which is sufficient to accurately capture steady-state operating characteristics, while also reflecting dynamic variations caused by renewable generation fluctuations and load changes.
2. Acquisition Parameters: A total of 35 μPMU measurement data points encompass phase voltage, current, and phase angle for 154 kV/23 kV busbars and critical equipment. Active power P and reactive power Q are calculated. The μPMU data used for calibration verification consists of one full month (1 July 2023–31 July 2023) of actual measurement data under all operating conditions. Tables 2 and 3 display raw data patterns from four μPMUs at a specific moment, timestamped 10 July 2023, 12:00.

Table 2. Raw data for μPMU frequencies, voltages, and voltage phasors #1–#4.

ID	f (Hz)	V_A (V)	δ_A (°)	V_B (V)	δ_B (°)	V_C (V)	δ_C (°)
#1	60.042	91,960.59	−47.23	92,150.64	−167.519	91,727.66	72.546
#2	60.041	91,849.45	−53.238	92,138.69	−173.521	91,651.93	66.496
#3	60.041	91,863.62	−53.341	92,068.79	−173.602	91,665.11	66.434
#4	60.042	91,878.20	−53.963	92,148.16	−174.268	91,657.13	65.748

Table 3. Raw data for μPMU current and current phase angle #1–#4.

ID	I_A (A)	δ_A (°)	I_B (A)	δ_B (°)	I_C (A)	δ_C (°)
#1	294.879	−39.86	309.017	−161.479	298.132	75.486
#2	300.945	−44.901	312.034	−168.901	295.406	70.442
#3	50.46	152.319	49.817	19.767	31.087	−145.561
#4	104.022	123.802	128.044	−8.223	115.045	−125.41

https://doi.org/10.3390/en19030834

3. Acquisition Duration: Continuous collection of one month's full operational condition data, encompassing scenarios such as rated load operation, renewable energy output fluctuations (morning/evening peaks), load variations, and faults. This ensures μPMU data comprehensively cover all operational states.

4.2.2. Data Preprocessing Workflow

Raw μPMU data may contain noise, outliers, and missing values that affect calibration accuracy. A standardized preprocessing workflow with clear and actionable steps is designed as follows:

1. Outlier identification: Considering the strong coupling characteristics of multiple indicators (e.g., voltage, current, phase angle, and power) in μPMU data, the Mahalanobis distance method is adopted for multivariate outlier detection. Specifically, the Mahalanobis distance between each sample point and the center of the multivariate normal distribution constructed by voltage, current, phase angle, and power is calculated. Subsequently, the chi-square test is employed to determine the outlier threshold, so as to identify and eliminate abnormal data points caused by equipment faults, communication interference, and other factors (such as voltage sudden changes and current zero-crossing interruptions).
2. Missing value imputation: Use linear interpolation to fill sparse missing data, ensuring time series continuity.
3. Data synchronization alignment: Use the GPS timestamp in μPMU data as the reference to adjust the time step and start time in PSCAD simulations, achieving one-to-one correspondence between simulated and measured data.

4.3. Calibration Metrics and Objective Functions

4.3.1. Core Calibration Metrics

To comprehensively evaluate model accuracy, key metrics were selected covering amplitude, power, and phase characteristics. All metrics employ relative deviation to eliminate the impact of different units of measurement:

1. Three-phase average voltage relative deviation:

$$\Delta U = \frac{|U_s - U_m|}{U_m} \tag{1}$$

2. Three-phase average current relative deviation:

$$\Delta I = \frac{|I_s - I_m|}{I_m} \tag{2}$$

3. Active Power Relative Deviation:

$$\Delta P = \frac{|P_s - P_m|}{P_m} \tag{3}$$

4. Relative Deviation of Reactive Power:

$$\Delta Q = \frac{|Q_s - Q_m|}{Q_m} \tag{4}$$

5. Relative deviation of phase angle:

$$\Delta \theta = \frac{|\theta_s - \theta_m|}{\theta_m} \tag{5}$$

https://doi.org/10.3390/en19030834

where U_S, I_s, P_s, Q_s and θ_s represent the PSCAD model simulation values, while U_m, I_m, P_m, θ_m, and Q_m represent the μPMU measured values.

To quantify the improvement in accuracy before and after model calibration, the mean error reduction rate (MERR) is defined, calculated as follows:

$$MERR = \left(\frac{MRE_{before} - MRE_{after}}{MRE_{before}} \right) \tag{6}$$

where MRE_{before}, MRE_{after} represent the average relative error of each indicator before and after calibration.

4.3.2. Multi-Objective Optimization Objective Function

Construct a comprehensive deviation objective function, incorporating weighting coefficients to reflect the engineering priority levels of different indicators.

$$J = \omega_P \cdot \Delta P + \omega_Q \cdot \Delta Q + \omega_U \cdot \Delta U + \omega_I \cdot \Delta I + \omega_\theta \cdot \Delta\theta \tag{7}$$

where ΔP, ΔQ, ΔU, ΔI and $\Delta\theta$ represent the average relative deviations of the 35 measurement point indicators, respectively. Weighting coefficients: ω_P = 0.25, ω_Q = 0.1, ω_U = 0.25, ω_I = 0.15, ω_θ = 0.3. The weighting coefficients are selected based on the physical sensitivity of each quantity to network parameters. Higher weight is assigned to the positive-sequence voltage angle due to its strong dependence on network topology and reactance, while lower weight is assigned to reactive power considering its sensitivity to local control and measurement uncertainty.

4.3.3. Constraints

1. Parameter adjustment range constraints: The adjustment range for all model parameters (including line impedance, transformer leakage reactance, and rated power of new energy units) must not deviate excessively from actual physical parameters to prevent parameters from diverging from the actual operating characteristics of equipment.
2. Maximum deviation for core indicators ΔP, ΔU, $\Delta I \leq 3\%$; maximum deviation for non-core indicator $\Delta Q \leq 5\%$ (meeting engineering simulation accuracy requirements).

Objective function convergence threshold: the difference between the objective functions of two consecutive iterations satisfies $|J_{K+1} - J_K| \leq 10^{-3}$, where k denotes the current iteration number.

4.3.4. Identifiability Analysis

To verify the unique identifiability of the selected calibrated parameters, an analysis is conducted based on the existing configuration of 35 μPMU measurement points and the calibration scheme: the 35 measurement points are evenly distributed across 154 kV/23 kV buses, the primary and secondary sides of main transformers, new energy grid-connected points, and load outgoing lines. Each point synchronously collects three-phase voltage, current, phase angle, active power, and reactive power, forming more than 350 independent measurement dimensions. In contrast, the number of parameters to be calibrated (including line impedance, transformer leakage reactance, new energy unit output parameters, and load proportion coefficients, etc.) is only about 40, providing significant data redundancy that lays the foundation for the unique identification of parameters. Meanwhile, the hierarchical calibration strategy of “main grid layer → new energy layer → load layer” effectively decouples the parameter coupling between different components. Each parameter group is supported by dedicated measurement point data, avoiding ambiguity in identification caused by mutual interference among multiple parameters. Verified via

https://doi.org/10.3390/en19030834

numerical simulation, the Jacobian matrix of the objective function with respect to the calibrated parameters is non-singular, satisfying the mathematical condition for unique identifiability and ensuring that the selected parameters can be uniquely determined using the existing μPMU measured data.

4.4. Layered Iterative Calibration Process

Given the criticality of substation equipment and the interdependence of its parameters, a three-tier iterative calibration process has been designed: "Main Grid Layer → Renewable Energy Layer → Load Layer." This approach mitigates interference from multi-parameter coupling, enhancing calibration efficiency and precision. The specific steps are as follows:

4.4.1. Calibration Tier Classification and Adjustment Strategy

The calibration hierarchy, adjustment targets, core parameters, adjustment logic, and constraint conditions are clearly defined as shown in Table 4. The adjustment logic is designed based on the physical relationship between parameters and electrical quantities, ensuring each adjustment is targeted.

Table 4. Error-feedback-based hierarchical iterative parameter update rule.

Calibration Level	Adjustment Target	Core Adjustment Parameter	Adjustment Method
Main Grid	154 kV T/L	Resistance per unit length R, reactance X	Data-measured > Data-simulated Increase R/X (by 1% each time), or decrease it accordingly.
	Main Transformer	Positive-sequence leakage reactance (Phase 1–/ Phase 1–3/Phase 2–3)	U-simulated < U-measured, Decrease leakage reactance (by 0.5% each time); conversely, increase it.
New Energy Sources	WP	Rated power of rotor	P-simulated < P-measured Increase (by 1% each time), or decrease
	PV	Inverter output voltage threshold, rated power	Fine-tune the voltage threshold in 0.5 kV increments; adjust the rated power in 1% increments.
Load	23 kV Load	Constant power P/Constant impedance Z/Constant current I ratio	P-simulated < P-measured, Increase the proportion of P by 5% and decrease the proportion of Z by 5%.

For three-winding transformer calibration, select leakage reactance parameters from the high-to-medium and high-to-low windings. These parameters directly influence power transmission and voltage distribution between the main grid and distribution network sides and can be precisely identified using power and voltage data from the main transformer's high- and low-voltage side μPMU measurement points. The leakage reactance between the medium- and low-voltage windings has a relatively minor impact on system steady-state characteristics. It is fixed using the manufacturer's nameplate rated value, with the resulting error meeting engineering application requirements.

https://doi.org/10.3390/en19030834

4.4.2. Iterative Calibration Steps

1. Initial Deviation Assessment: Run the initial PSCAD model to calculate the relative deviation of four metrics across 35 measurement points. Sort by descending deviation and identify critical measurement points with deviations exceeding 10%.
2. Main Grid Layer Calibration: Prioritize adjusting parameters of 154 kV lines and main transformers. After each parameter adjustment, run steady-state simulations to verify deviation changes at corresponding measurement points until core indicator deviations $\leq$3% for all main grid layer measurement points.
3. Renewable Energy Layer Calibration: Based on the calibrated main grid layer model, adjust wind and solar unit parameters. Focus on matching renewable energy output fluctuation characteristics to ensure grid connection point power and voltage deviations meet standards.
4. Load Layer Calibration: Finally, adjust parameters of the 23 kV composite load model to adapt to the impact of load changes on busbar voltage.
5. Global Verification and Iteration: After completing one round of layered calibration, calculate the deviation of all measurement points. If any measurement point fails to meet standards, return to the corresponding layer for repeated adjustments.

4.4.3. Iteration Termination Criteria

Iteration terminates when any of the following conditions is met, ensuring balance between optimization accuracy and efficiency:

1. Error Convergence Criteria: The average relative deviation for core indicators across 35 monitoring points was $\leq$3%, while the average relative deviation for non-core indicators was $\leq$5%.
2. Convergence criterion for the objective function: The difference between the objective functions of two consecutive iterations satisfies $|J_{K+1} - J_K| \leq 10^{-3}$.
3. Maximum Iteration Threshold: When the iteration count within a single layer reaches the preset upper limit of 80 iterations (numerical experiments indicate that under typical operating conditions, the objective function typically converges within 50–70 iterations).

4.5. Test Results and Analysis

Based on the following configuration, Intel Core i7-13700K 2.4GHz + 32GB DDR5 RAM, the total computation time for a single full calibration cycle is approximately 2 h and 40 min.

Based on data from 35 μPMU measurement points, statistical validation of key indicators for the calibrated model was conducted. All parameters demonstrated significant error reduction post-calibration, as shown in Figure 5, average voltage error decreased from 12.3% to 2.46%, average current error dropped from 14.9% to 2.57%, the average active power error decreased from 13.5% to 2.52%, and the average reactive power error decreased from 15.8% to 3.96%, significantly improving the model's accuracy.

After calibration, the average relative voltage error remained below 3%, as shown in Figure 6. The relative errors at each measurement point clustered within the range of 1.65% to 2.95%, exhibiting uniform distribution with no significantly outlying high-error points. The maximum error was 2.95%, the minimum was 1.65%, and the average was only 2.57%. This result demonstrates that the model achieves stable voltage calibration accuracy across all 35 measurement points at the substation, with all points meeting standards. It enables "precision matching without blind spots" for substation voltage parameters, fully validating the model's comprehensive coverage and reliable accuracy.

https://doi.org/10.3390/en19030834

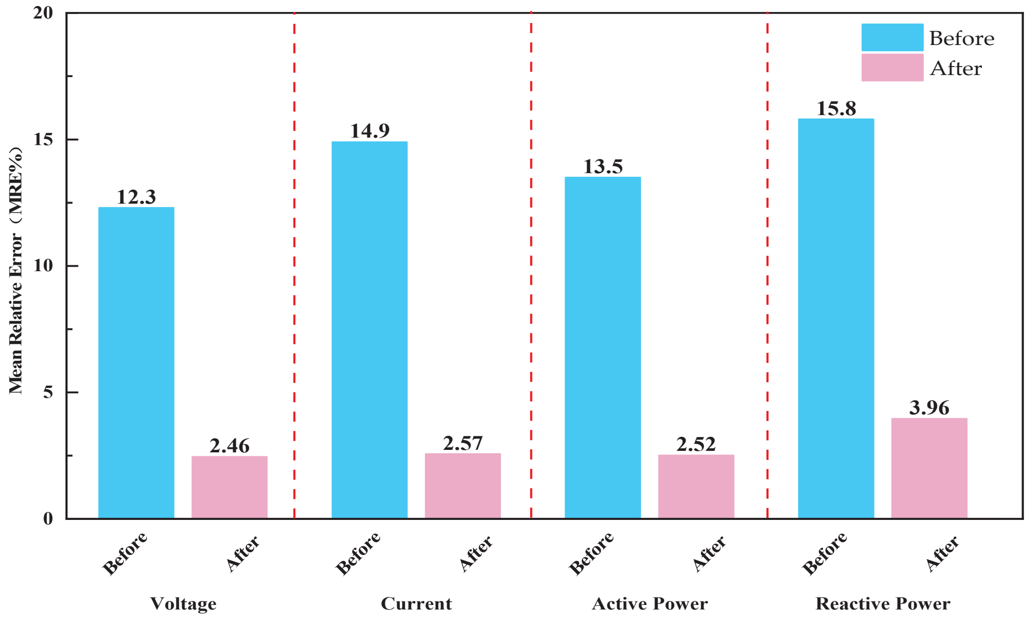

Figure 5. Comparison of average error for each parameter before and after calibration.

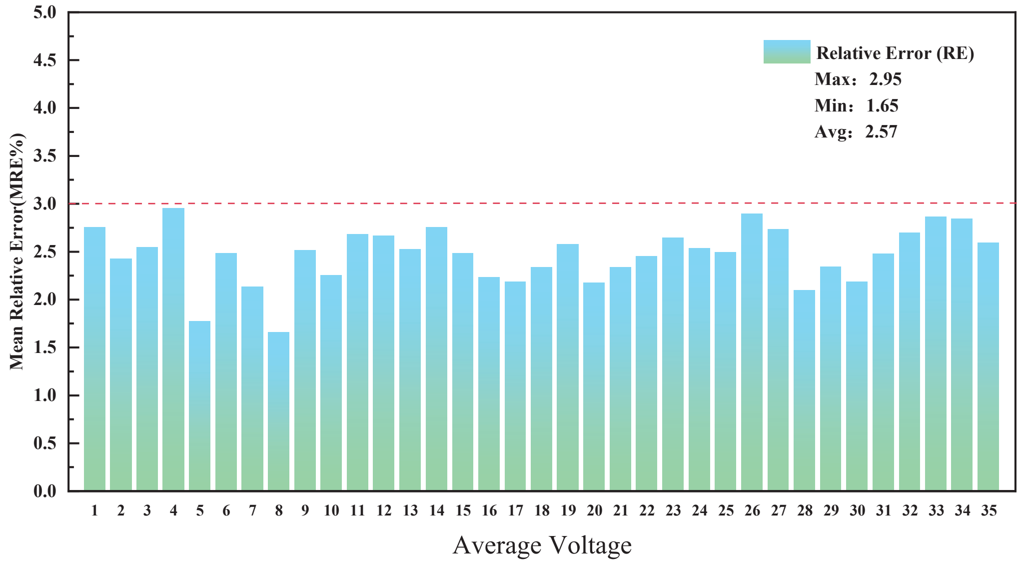

Figure 6. Average voltage error chart.

To verify the stability of the model voltage, one measurement point was selected for each of the busbar, transformer side, and load side. After 60 s of steady-state operation, the voltage output remained stable within the error range, as shown in Figure 7. The voltage fluctuation trends of the three measurement points were highly consistent, exhibiting the characteristic of periodic minor fluctuations; the deviation between the simulated values and measured values remained consistently within a narrow range, with only slight numerical differences observed. This result confirms that the established PSCAD simulation model can accurately reproduce the quasi-static fluctuation characteristics of three-phase voltages in actual substations, demonstrating a high degree of dynamic consistency between the model outputs and field measurement data.

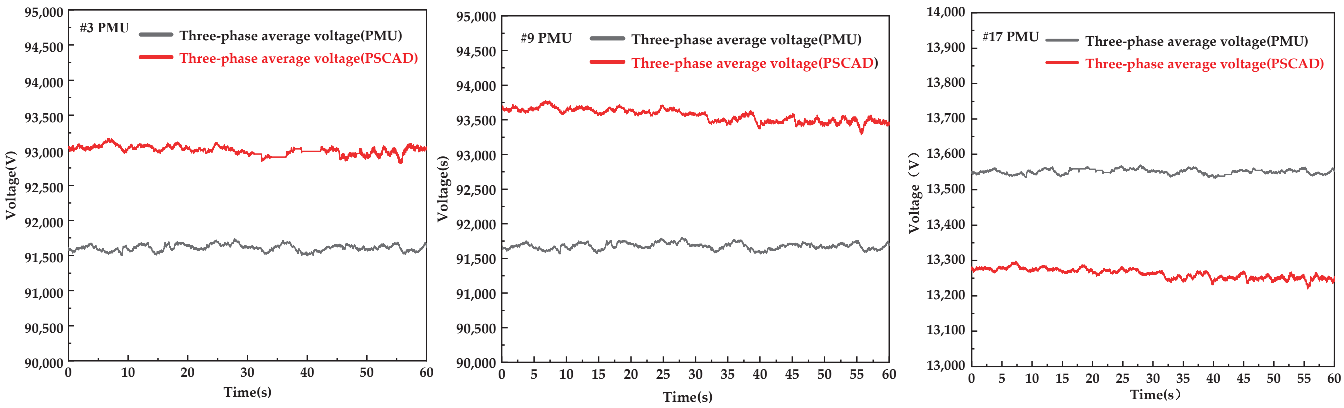

Figure 7. Comparison of µPMU and simulated voltage under steady-state conditions.

Figure 8 illustrates the dynamic changes in phase angle errors between measured data and PSCAD simulation results for three Micro-Phasor Measurement Units (µPMUs), namely #3, #9, and #17, over a 0–60 s time window. The blue curves represent real-time fluctuations in phase angle error, while the red horizontal lines indicate the average error values for the corresponding periods. Overall, the phase angle errors of the three µPMUs exhibit good consistency, with the phase angle error being less than 3° for the vast majority of the time and maintaining a low average error level: the error fluctuation of #3 µPMU is the smallest, with an average error of only 0.70°; the average error of #9 µPMU is 0.986°; although the error fluctuation of #17 µPMU is relatively significant, it remains within 3° for most periods, with an average error of 1.975°. This overall indicates that the established PSCAD simulation model has a high phase angle matching degree with the measured data, and the overall error level is controllable.

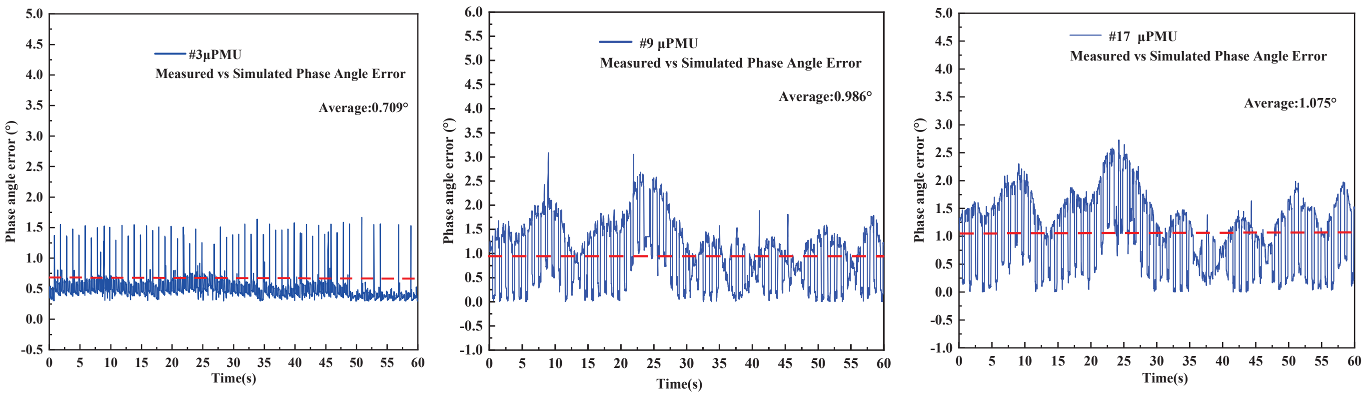

Figure 8. Phase angle error plot: measured vs. simulated data.

To verify that the average power error complies with calibration standards, it is characterized via Figure 9. Power errors are primarily concentrated within the 2.3–2.9% range, with the 2.4–2.5% interval exhibiting the highest relative frequency approaching 30%, while frequencies in marginal intervals are lower. Simultaneously, the red Gaussian fitting curve closely aligns with the histogram distribution trend, indicating that the power error distribution approximates a normal distribution. The results reveal a concentrated and stable distribution pattern for power errors, with no extreme outliers. This confirms the model's consistency and stability in power parameter calibration accuracy.

https://doi.org/10.3390/en19030834

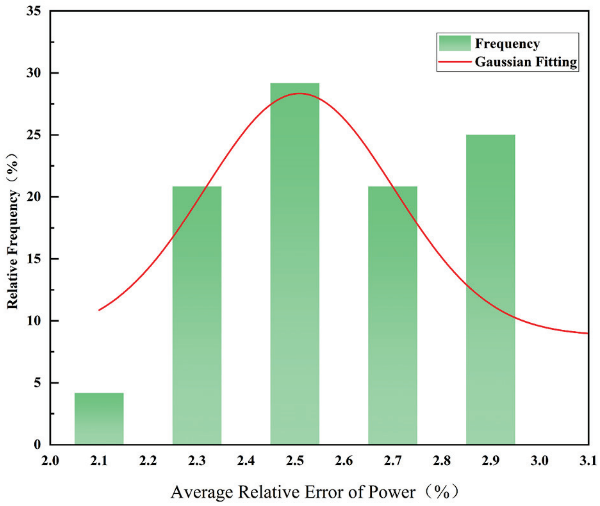

Figure 9. Voltage mean relative error distribution.

Finally, to visually represent the average relative errors of key parameters after model calibration, Figure 10 presents a box plot. As shown, the error ranges for ΔU, ΔI, and ΔP are all concentrated within the 1.5–2.5 interval. The narrow box and low data dispersion indicate that the error distributions for these three parameters are more compact, demonstrating superior precision stability. In contrast, the error range for ΔQ is significantly broader, concentrated between 3.0 and 4.5, with relatively higher data dispersion. Overall, the errors in voltage, current, and active power exhibit stronger concentration and stability. Only the error dispersion for reactive power is slightly higher. This reflects that after model calibration, the error states of most core electrical parameters are controllable, and their accuracy performance is consistent.

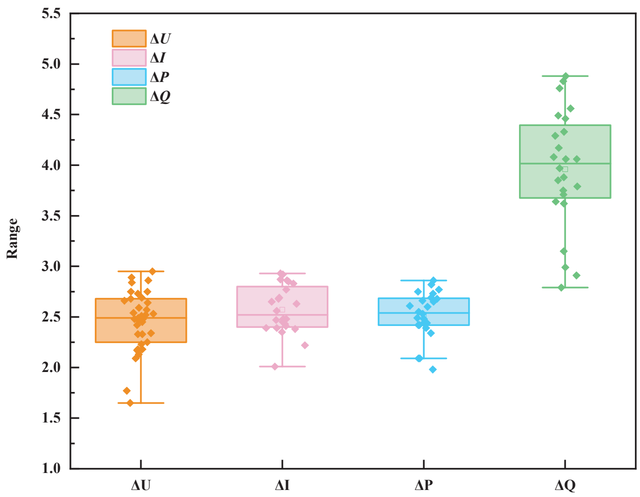

Figure 10. Mean relative error of each key parameter.

5. Conclusions

This study focused on the Yeonggwang Substation, completing PSCAD modeling and μPMU data-driven calibration research. Based on μPMU measurement point data, a hierarchical calibration system was established, controlling deviations in core parameters such as voltage, current, and power within 3% of actual measurements. This model provides a reliable tool for substation operation optimization and fault analysis, while the proposed calibration method offers a generalizable reference for modeling similar substations.

https://doi.org/10.3390/en19030834

Although this study established a data-driven hierarchical calibration method for substation PSCAD models using μPMU data and validated its effectiveness, several limitations remain. The method was only validated at the Yeonggwang Substation, which possesses comprehensive measurement equipment, and is not applicable to sites with sparse measurement points. The capability to simulate harmonics and sub-synchronous oscillations was neither discussed nor validated, limiting its support for complex dynamic scenarios. Furthermore, the offline calibrated simulation model does not equate to a digital twin, as the latter requires real-time interconnection and predictive capabilities that remain unachieved. The measurement uncertainty inherent to μPMUs themselves was also not thoroughly investigated. Future work will explore transient and fault scenarios while addressing these shortcomings to enhance the method's applicability and engineering utility.

Author Contributions: Methodology, P.L.; writing—original draft preparation, P.L.; research conceptualization and design, C.-G.K.; data acquisition and analysis, S.-H.C.; formal analysis, K.-M.L.; writing—review and editing, Y.-S.C. All authors have read and agreed to the published version of the manuscript.

Funding: This research was supported by the Regional Innovation System and Education (RISE) program through the Jeollanamdo RISE center, funded by the Ministry of Education (MOE) and the Jeollanamdo, Republic of Korea (2025-RISE-14-004).

Data Availability Statement: The original contributions presented in this study are included in the article. Further inquiries can be directed to the corresponding author.

Acknowledgments: The authors would like to thank all those who provided valuable comments and suggestions to improve the quality of this study.

Conflicts of Interest: Author Chung-Gang Kim was employed by the company Kalon E&M Co., Ltd. The remaining authors declare that the research was conducted in the absence of any commercial or financial relationships that could be construed as a potential conflict of interest.

Abbreviations

μPMU	Micro-Phasor Measurement Unit
PV	Photovoltaic
MRE	Mean Relative Error
MERR	Mean Error Reduction Rates
PMU	Phasor measurement units
SCADA	Supervisory Control and Data Acquisition
T/L	Transmission Line
D/L	Distribution Line
M.Tr	Main Transformer
WP	Wind Power
RESs	Renewable Energy Sources
URTDSMS	Unified Real Time Dynamic State Measurement System

References

1. Park, J.; Yun, S.-J. Social determinants of residential electricity consumption in Korea: Findings from a spatial panel model. *Energy* **2022**, *239*, 122272. [CrossRef]
2. Chu, K.H.; Lim, J.; Mang, J.S.; Hwang, M.-H. Evaluation of strategic directions for supply and demand of green hydrogen in South Korea. *Int. J. Hydrogen Energy* **2022**, *47*, 1409–1424. [CrossRef]
3. Yue, C.; Wang, D.; Qi, Q. Simulation Analysis of Wind Turbine Grid Operation Based on PSCAD. *IOP Conf. Ser. Mater. Sci. Eng.* **2019**, *631*, 042027. [CrossRef]
4. Wu, H.; Wang, L.; Xing, H.; Liu, Z.; Zhang, A. Modeling and simulation of extra high voltage magnetically controlled shunt reactor based on PSCAD. *J. Phys. Conf. Ser.* **2023**, *2584*, 012077. [CrossRef]

https://doi.org/10.3390/en19030834

5. Rusina, A.G.; Serohvostov, D.A.; Kolesnikov, D.I.; Arestova, A. PSCAD as a Tool for Development of a Simulation Model for a Power System with Renewable Energy Sources. In Proceedings of the 2020 Ural Smart Energy Conference (USEC), Yekaterinburg, Russia, 13–15 November 2020; pp. 39–42. [CrossRef]
6. Hou, Z.; Liu, J.; Shao, Z.; Ma, Q.; Liu, W. Machine Learning Innovations in Renewable Energy Systems with Integrated NRBO-TXAD for Enhanced Wind Speed Forecasting Accuracy. *Electronics* **2025**, *14*, 2329. [CrossRef]
7. Liu, J.; Hou, Z.; Wang, B.; Yin, T. Optimizing Microgrid Energy Management via DE-HHO Hybrid Metaheuristics. *Comput. Mater. Contin.* **2025**, *84*, 4729–4754. [CrossRef]
8. Adar, M.; Babay, M.-A.; Boussif, M.; Khaouch, Z.; Abbassi, Z.; Najih, Y.; Mabrouki, M. Optimization of Photovoltaic System Modelling: A Comparative Study and Experimental Validation Using Bond Graph Methodology and a Genetic Algorithm. In *Applied Mathematics, Modeling and Computer Simulation*; IOS press: Amsterdam, The Netherlands, 2024. [CrossRef]
9. Zhu, J.; Gao, W.; Li, Y.; Guo, X.; Zhang, G.; Sun, W. Power System State Estimation Based on Fusion of PMU and SCADA Data. *Energies* **2024**, *17*, 2609. [CrossRef]
10. Rehman, H.U.; Ritschel, U. DC-Link Voltage Control and Power Management of BESS Integrated Wind Power System Using PSCAD. In Proceedings of the 2024 IEEE 4th International Conference on Power, Electronics and Computer Applications (ICPECA), Shenyang, China, 26–28 January 2024; pp. 776–781. [CrossRef]
11. Gupta, P.; Gajbhiye, R.; Gajjar, G.; Navalkar, P.; Soman, S. Towards a Three Phase Local Substation IT Calibrator using PMU Data. In Proceedings of the 2022 22nd National Power Systems Conference (NPSC), New Delhi, India, 17–19 December 2022; pp. 1–6. [CrossRef]
12. Wakti, M.H.; Putranto, L.M.; Hadi, S.P.; Yasirroni, M.; Marsiano, A.F.D. PMU Location Determination in a Hybrid PMU-SCADA System. In Proceedings of the 2020 12th International Conference on Information Technology and Electrical Engineering (ICITEE), Yogyakarta, Indonesia, 6–8 October 2020; pp. 245–250. [CrossRef]
13. Pavičić, I.; Holjevac, N.; Ivanković, I.; Brnobić, D. Model for 400 kV Transmission Line Power Loss Assessment Using the PMU Measurements. *Energies* **2021**, *14*, 5562. [CrossRef]
14. Xu, S.; Liu, H.; Bi, T. Field PMU Test and Calibration Method—Part I: General Framework and Algorithms for PMU Calibrator. *J. Mod. Power Syst. Clean Energy* **2022**, *10*, 1507–1518. [CrossRef]
15. Blackwelder, A.; Niraula, P.; Brescia, J.; Kelk, L.; Ramabhotla, S. Modeling and Simulation of a Microgrid Using PSCAD. In Proceedings of the 2025 57th North American Power Symposium (NAPS), Knoxville, TN, USA, 26–28 October 2025; pp. 1–6. [CrossRef]
16. Lin, L.; Wu, W.; Shangguan, Z.; Wshah, S.; Elmoudi, R.; Xu, B. HPT-RL: Calibrating Power System Models based on Hierarchical Parameter Tuning and Reinforcement Learning. In Proceedings of the 2020 19th IEEE International Conference on Machine Learning and Applications (ICMLA), Miami, FL, USA, 14–17 December 2020; pp. 1231–1237. [CrossRef]
17. Masmali, M.; Elimy, M.I.; Fterich, M.; Touti, E.; Abbas, G. Comparative Studies on Load Frequency Control with Different Governors connected to Mini Hydro Power Plant via PSCAD Software. *Eng. Technol. Appl. Sci. Res.* **2024**, *14*, 12975–12983. [CrossRef]
18. Li, A.; Liu, C.; Su, C.; Wang, Y.; Xu, Y.; Kong, L. Study on the Topological Transformation of Electromagnetic Transient Models in PSCAD and ADPSS. In Proceedings of the 2024 IEEE 8th Conference on Energy Internet and Energy System Integration (EI2), Tianjin, China, 29 November–2 December 2024; pp. 931–935. [CrossRef]
19. Sandhya, K.; Chatterjee, K. Study the impact of renewable and non-renewable energy sources on micro-grid using time series data based information transfer. *Energy Rep.* **2024**, *11*, 4957–4966. [CrossRef]
20. Lee, J.S.; Kang, S.H. A study on a current transformer modelling method considering core magnetic saturation characteristics for PSCAD/EMTDC. In Proceedings of the 18th International Conference on Developments in Power System Protection (DPSP APAC 2025), Melbourne, Australia, 8–11 January 2025; pp. 495–500. [CrossRef]
21. Lee, K.-M.; Park, C.-W. High-Precision Analysis Using μPMU Data for Smart Substations. *Energies* **2024**, *17*, 4907. [CrossRef]
22. An, J.; Jung, D.; Jeong, K.; Ji, C.; Hong, T.; Lee, J.; Kapp, S.; Choi, J. Energy-environmental-economic assessment of green retrofit policy to achieve 2050 carbon-neutrality in South Korea: Focused on residential buildings. *Energy Build.* **2023**, *289*, 113059. [CrossRef]
23. Martin, K.E.; Benmouyal, G.; Adamiak, M.G.; Begovic, M.; Burnett, R.O.; Carr, K.R. IEEE Standard for Synchrophasors for Power Systems. *IEEE Trans. Power Deliv.* **1998**, *13*, 73–77. [CrossRef]

https://doi.org/10.3390/en19030834

energies

MDPI

Article

Technical and Economic Comparative Analysis of Nuclear Power Plants: AP1000 and SMR

Natalia Kasińska, Agata Mielcarek, Jakub Sierchuła, Radosław Szczerbowski and Bartosz Ceran *

Institute of Electric Power Engineering, Poznan University of Technology, Piotrowo 3A, 60-965 Poznan, Poland; natalia.kasinska@put.poznan.pl (N.K.); agata.mielcarek@put.poznan.pl (A.M.); jakub.sierchula@put.poznan.pl (J.S.); radoslaw.szczerbowski@put.poznan.pl (R.S.)
* Correspondence: bartosz.ceran@put.poznan.pl

Abstract: Due to the necessity of decarbonising and transforming the Polish energy mix, topic of using nuclear power plants as one of the key low-carbon generation sources is returning to the public debate. This paper compares a large, system-wide AP1000 nuclear power plant with a new concept based on small modular reactors (SMRs), specifically NuScale 60 MW_e. Computer models of secondary loops of the generating units were used for the analysis, and basic operating parameters were determined. A consistent modelling approach was used to evaluate technical, thermodynamic, and economic indicators. As a result, a relationship between total capital expenditures and unit electricity generation cost was developed. For example, if the investment outlays, taking into account the freeze, for a large-scale nuclear power plant are USD 8 billion, then the investment outlays for an SMR power plant should be below USD 0.4 billion in order to ultimately ensure a lower or equal unit discounted cost of electric energy generation. Assuming stable power demand, the AP1000 reactor power plant remains the most cost-effective technology, offering favourable economies of scale. However, modular units are characterised by shorter lead times and greater flexibility of application in different areas of the energy industry. Therefore, in the decarbonisation process, it is essential to develop both analysed technologies in parallel.

Keywords: energy transformation; nuclear power; comparative analysis; energy analysis; economic analysis; AP1000; SMR

1. Introduction

The increasing energy demand, which is correlated with a growing population and rapid industrialisation, indicates that the challenges of transforming the energy sector focus on efficiency, reliability, sustainability, and environmental protection. In this context, nuclear power plants (NPPs) present an effective solution for combating global warming as they offer a cleaner alternative for the generation of electric energy. These low-carbon generation sources are characterised by relatively low fuel consumption. Furthermore, nuclear power has a negligible impact on the environment regarding greenhouse gas emissions. In contrast, power plants that utilise lignite or hard coal frequently face discussions surrounding the transfer of harmful pollutants into the atmosphere. For instance, one of Poland's largest generating units, the Bełchatów Power Plant, emits approximately 30 million tonnes of carbon dioxide (CO_2) annually [1]. Moreover, according to the Polish transmission system operator (*Polskie Sieci Elektroenergetyczne S.A.*, Warsaw, Poland), as of the end of 2024, coal-fired power plants accounted for about 63% of national electric energy production [2].

In contrast to Poland, where coal-fired power plants are the dominant energy source, France's energy sector is mainly shaped by nuclear power plants. Based on [3], it can be observed that their share in total electric energy production in 2024 is almost 68%. According to information provided by the International Atomic Energy Agency, France currently operates 57 nuclear reactors [4].

The different structures of the above-mentioned energy mixes affect not only energy security but also greenhouse gas emissions. When comparing these two countries in terms of daily CO_2 emissions, clear differences can be seen. Using the example of one selected day (8 May 2024), the data presented in [5] are as follows—for Poland, generation of electric energy was charged with transferring 754 gCO_2/kWh to the atmosphere, while for France it was 18 gCO_2/kWh. Thus, the daily emission factor for the Polish power industry was almost 42 times higher than for the French power industry. In the light of global efforts to achieve climate neutrality, such a significant difference puts Poland in a particularly difficult situation.

Climate protection is a major civilizational undertaking. For this reason, it cannot be carried out within the borders of a single country. Moreover, actions related to energy transition should also focus on raising awareness among the general public. Education in the field of nuclear energy and the development of appropriate human resources are important needs that will influence further technological progress in the nuclear sector. Cizeli et al. [6] highlight the importance of a European education strategy as a kind of foundation for the future of nuclear technologies, including modern small modular reactors (SMRs) solutions. Nuclear power has been a major part of the energy mix of many countries for decades, providing electric energy in a stable, low-carbon and resilient way. The lack of appropriately qualified people may be a barrier to the further development of this sector.

For many years, technological advances in nuclear power have mainly focused on large power units, with installed capacity often exceeding 1000 MW_e. However, recently, with changing social, economic and environmental circumstances, there has been increasing interest in SMRs, which are designed to reduce capital costs through series production. The study [7] provides a comprehensive overview of the state of SMR technology worldwide, identifying both the opportunities and barriers that need to be overcome for this innovative technology to fully establish itself on the market. SMRs are seen as a potential catalyst for the expansion of nuclear power in developing countries and regions with underdeveloped transmission infrastructure. It is also important to identify the factors determining the success of SMR technology implementation. The paper [8] analysed the characteristics and potential advantages of modular solutions compared to large-scale nuclear reactors. The author described issues related to economics, safety and public acceptance. In addition, the author emphasised that technical and legal challenges (appropriate regulations or obtaining licences) may hinder the widespread implementation of SMRs. In turn, publication [9] drew attention to the need for innovative solutions in the field of operation and maintenance of modular power plants. The article describes an analysis of cost reduction strategies through the introduction of modern operational solutions, automation and design simplification. It is pointed out that such an approach can significantly increase the competitiveness of SMRs on the market. Due to the specific nature of SMRs and high safety requirements, accurate and rapid fault diagnosis is of great importance. In article [10], researchers focused on developing an intelligent method for diagnosing faults in SMRs. The authors proposed a hybrid approach combining artificial intelligence algorithms and machine learning methods. The research demonstrated high accuracy in fault classification and the effectiveness of the algorithm in conditions of measurement disturbances and uncertainty. The developed method allows for the rapid detection of any irregularities and their classification without the need for human intervention. Other factors analysed in [11] in terms of the operational capacity of a single power plant operator were the size of the facility and the simplicity and compactness of SMR solutions. The authors found that it is possible to safely supervise 3 to 5 reactors during normal operation, but only up to 2 during start-up/shutdown or refuelling operations.

SMR solutions respond to the challenges of building and operating large nuclear power plant units, which are characterised by high generating capacity, making them attractive sources of electric energy in the context of covering base load in the power system. However, their implementation is associated with high investment costs, long construction times, and complex licensing procedures. In the literature and engineering practice, the implementation of SMRs on the market is often described using the categories FOAK (first-of-a-kind) and NOAK (nth-of-a-kind) [12–14]. The FOAK model refers to the first unit implemented in a given technological configuration, which involves overcoming a number of regulatory, organisational and design barriers. For this reason, FOAK projects are usually characterised by higher investment costs, longer implementation times and greater technological and financial risk. In contrast, the NOAK category refers to subsequent reactors built on the basis of a proven design, which allows for the use of learning effects and standardisation. In practice, this means a reduction in capital and operating costs, a shorter implementation schedule and greater predictability of the investment process. From the point of view of the development of innovative SMR technologies, the transition from the FOAK to NOAK phase will be a necessary condition for achieving their market competitiveness and widespread implementation in national energy mixes around the world. According to data available in the literature [15,16], it can be seen that nuclear power plants can have a unit capital expenditure ratio of $2100 to $6900/kW. The lower values ($2100–3000/kW) are observed in countries with well-established nuclear programs and lower costs (e.g., China, South Korea), while the higher values ($6000–7000+/kW) are typical for first-of-a-kind units built in new markets (e.g., the USA, Europe) or in cases where significant project difficulties are encountered. In the context of SMR technology profitability analyses, the authors of publication [17] pointed to the relationship between construction costs, energy efficiency and market conditions. The conclusions presented in the paper show that SMRs can be competitive under the right investment and legal conditions. These analyses are complemented by research [18], which describes long-term forecasts and scenarios that will enable the United States to achieve climate neutrality by 2050. The paper emphasises the need for long-term investment, regulatory changes and political support to achieve these goals.

There is also a study about the increasing risk of exceeding budgets and schedules for the construction of nuclear power plants, examples of which include delays in projects such as Olkiluoto 3 (Finland)—10 years, or Vogtle units 3 and 4 (USA)—4 years [19]. Furthermore, a study by Stewart and Shirvan [20] assessed the impact of various factors that increase the risk of delays in work schedules for four types of generation III+ water reactors. It was noted that design changes and consequent performance declines were a factor causing significant delays. Another issue related to the supply chain was a small part that adversely affected the commissioning date.

In a review of the available literature, it is noticeable that there is a lack of comprehensive comparative studies that directly contrast large nuclear units with modular reactors in terms of energy analysis. Many studies devoted to technical, economic or environmental analyses of each of these solutions have already been published. Thus, there is a clear research gap that could be important for future energy strategies and investment decisions related to the ongoing energy transition.

2. Problem Description, Novelty and Original Contribution

A fundamental transformation of the Polish energy sector requires a well-considered diversification of generation sources and investment in solutions that ensure energy independence, a stable electric energy supply and low emissions. Reforming the domestic energy sector in a manner consistent with the European Union's climate policy involves a thorough examination of alternative electric energy generation technologies. Because of the above, and the numerous discussions on the role of nuclear power in the power system, and, in particular, the newly designed modular solutions—SMRs, the selection of appropriate nuclear technologies to meet the objectives of Poland's Energy Policy until 2040 is a significant step towards a fair transition.

There is no doubt that replacing coal power with nuclear power is the best way to reduce the CO_2 emission factor. In the national arena, a debate has appeared as to whether it is better to build a system power plant or to rely on the development of distributed energy through the use of modular solutions. This topic raises a number of questions and concerns among the public.

The research problem of this paper focuses on the development of a model to compare the two types of nuclear power plants (large-scale and modular). This will provide a more comprehensive picture of the advantages and disadvantages of the two technologies when assessing (energy or economic), which of these solutions can better meet the needs of the national power system. The results of the analyses can then serve as a tool to support decision-making in the field related to the development of the generation sector. Furthermore, the work makes an original and useful contribution through:

- The development of secondary loop models that enable the mapping of the operating parameters of various generating units, both large-scale and modular. The simulated technological systems also include a comprehensive comparative analysis from an energy perspective;
- Application of the models in the context of the transformation of the Polish energy sector—thanks to this, potential development paths for nuclear technologies can be identified, which increases the practical value of the research and its strategic importance;
- Comparison of large-scale reactors with modern, modular units, which is a valuable addition to the research conducted so far, which very often focuses only on one type of technology;
- An economic analysis examining the impact of technical and economic parameters on the relationship between the unit discounted cost of generating electric energy in a large-scale nuclear power plant and a small-scale modular power plant.

3. Model and Method Description

The research methodology was based on a comparison of two modern nuclear reactor concepts: the large unit, the AP1000, and the small modular NuScale reactor, with a unit capacity of 60 MW_e. NuScale was selected as a reference SMR due to its advanced licensing status—it is the first SMR to receive U.S. NRC design approval—as well as the availability of detailed technical data. Its integral PWR design with passive safety systems and natural circulation makes it a representative example of the current generation of light-water SMRs. While other SMRs are under development, such as the BWRX-300 (a 300 MW_e boiling water reactor) or the Rolls-Royce SMR (~470 MW_e beyond IAEA SMR definition), they differ significantly in size, cycle type or system layout. Choosing a single, well documented design allowed for a consistent comparison of economic and operational indicators.

As a first step, technical and operational data for both technologies were collected and compared. On this basis, the secondary loop of the AP1000 unit was modelled, and the technological layout of the secondary loop of a nuclear power plant with a modular reactor was designed. The results obtained were used to evaluate parameters such as gross electrical power, cooling water flow, gross power plant efficiency and nuclear fuel (heat) utilisation rate.

As part of the economic comparative analysis, a general correlation was derived for the difference between the unit discounted generation costs of a large-scale nuclear power plant and a modular power plant. The derivation of the correlation made it possible to define the parameters determining the advantage of economic reasonableness of the compared technologies to each other.

The results of the analysis provide a basis for determining the efficiency (cost-effectiveness) of the implementation of each technology, depending on local demand.

3.1. Energy Analysis

Computer models of nuclear power units with PWR-type reactors of 60 and 1100 MW electrical output were used for the comparative analysis. Based on the data contained in [21,22] and using the EBSILON®*Professional* 16.0 programme, schematics of the thermal systems of the mentioned generating units were developed. The models are presented in Figures 1 and 2.

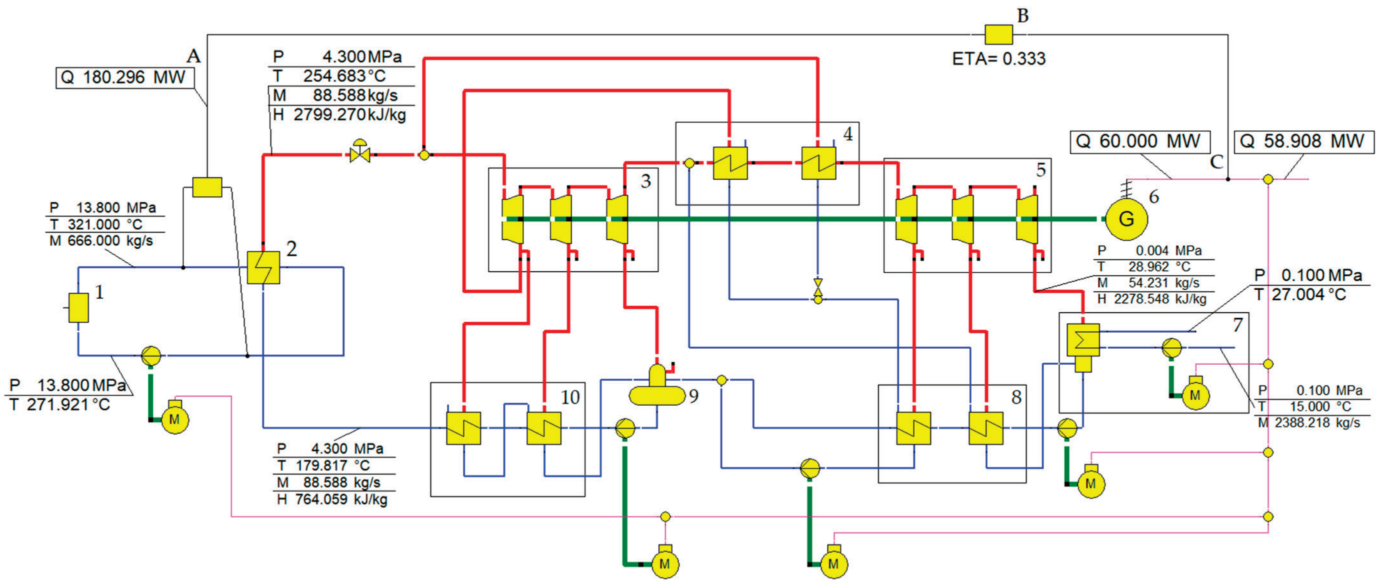

Figure 1. Diagram of the modelled secondary cycle of a nuclear power plant (SMR) with key parameters; H—enthalpy [kJ/kg]; M—mass flow [kg/s]; P—pressure [MPa]; Q—energy flow [MW]; T—temperature [°C]; ETA—efficiency [-]; factor designation: red line—steam; blue line—water; green line—shaft power; pink line—electric energy; 1—reactor; 2—steam generator; 3—high-pressure part of the steam turbine; 4—drain and interstage steam superheater; 5—low-pressure part of the steam turbine; 6—generator; 7—cooling water system; 8—low-pressure regenerative feedwater heaters; 9—deaerator; 10—high-pressure regenerative feedwater heaters; A—thermal power of the reactor; B—efficiency of the power plant; C—generated electrical power (gross and net); own elaboration based on [21].

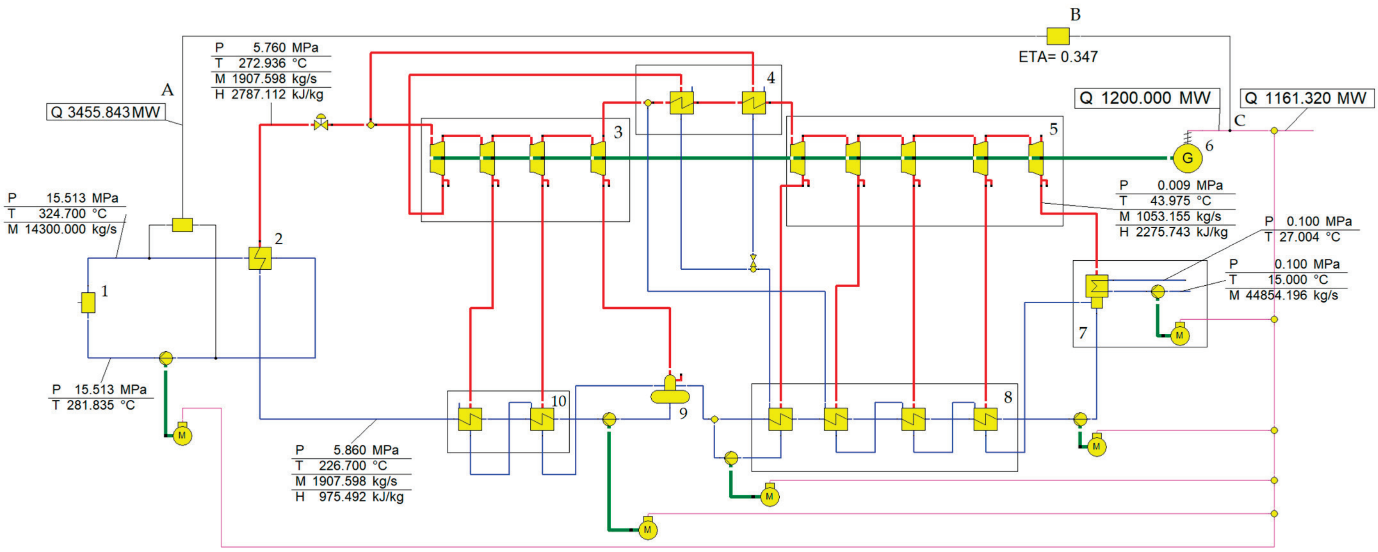

Figure 2. Diagram of the modelled secondary cycle of a nuclear power plant (AP1000) with key parameters; H—enthalpy [kJ/kg]; M—mass flow [kg/s]; P—pressure [MPa]; Q—energy flow [MW]; T—temperature [°C]; ETA—efficiency [-]; factor designation: red line—steam; blue line—water; green line—shaft power; pink line—electric energy 1—reactor; 2—steam generator; 3—high-pressure part of the steam turbine; 4—drain and interstage steam superheater; 5—low-pressure part of the steam turbine; 6—generator; 7—cooling water system; 8—low-pressure regenerative feedwater heaters; 9—deaerator; 10—high-pressure regenerative feedwater heaters; A—thermal power of the reactor; B—efficiency of the power plant; C—generated electrical power (gross and net); own elaboration based on [21,22].

Despite differences in reactor design, most modern nuclear power plants use the Rankine cycle—this is a proven thermodynamic cycle in which heat from nuclear fission is converted into mechanical energy and then into electricity. In NPP systems where a saturated steam thermal cycle is used, the expansion of the working fluid in the high-pressure part of the turbine leads to its partial condensation (it changes to a wet steam state). The unwanted phenomenon can be seen from the course of the parameter changes shown in the temperature-entropy diagrams (Figure 3). Therefore, one method of improving the efficiency of the saturated steam cycle was applied to the process systems studied. Steam driers (moisture separation) were modelled along with interstage superheating. In addition, it can be seen from the T-s diagrams that the steam expansion on the last turbine stage is characterised by a moisture content that does not exceed the allowed 13%. It should also be added that the cycle begins in the condenser, where the working fluid is in a wet vapour state, as it has expanded at the individual stages of the steam turbine (thermodynamic transformation 1–2). Waste heat is removed from the system by cooling water flowing through pipes inside the condenser. The process of condensing the working fluid is visible on the T-s diagrams as an isobaric and isothermal transformation (2–3). The use of low- and high-pressure regenerative heaters improves the efficiency of the Rankine cycle and increases the temperature of the feed water. The working fluid is then compressed by a pump to the pressure prevailing in the steam generator so that it can be heated in the next step (isobaric transformation 3–4) by absorbing heat from the fission reaction of atomic nuclei and evaporating to a saturated vapour state (isothermal and isobaric transformation 4–5). The steam is directed to the high-pressure part of the turbine, where it partially expands (transformation 5–6), performing work. As mentioned above, the parameters of the working fluid decrease, so in order to prevent further deterioration, a dryer (isothermal transition 6–7) and an interstage superheater (isobaric transition 7–1) are brought into the system. After increasing the parameters of the working medium, it is directed to the low-pressure part of the turbine, thus closing the thermodynamic cycle.

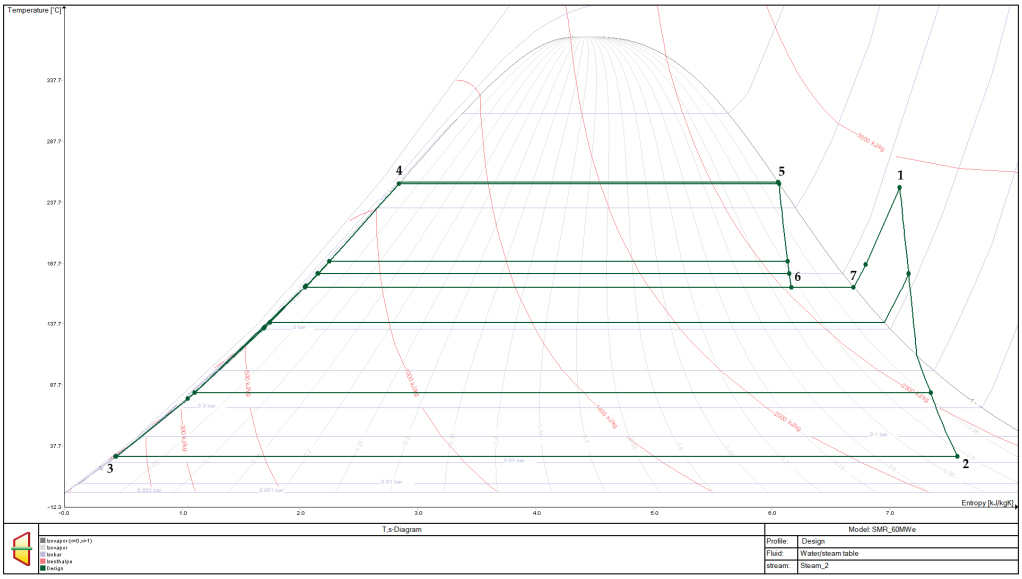

(**a**)

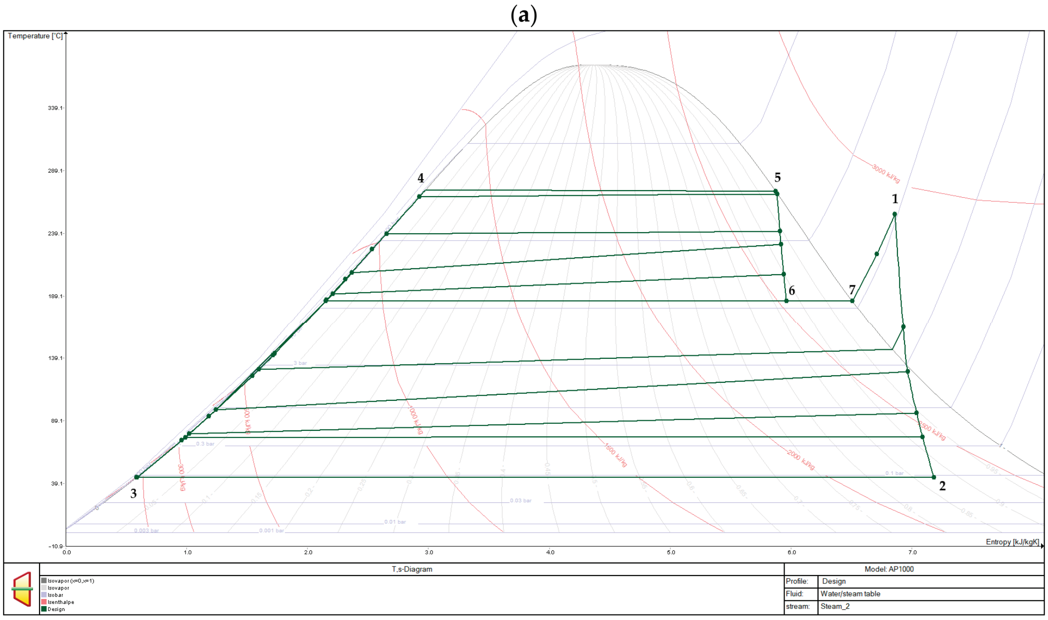

(**b**)

Figure 3. Rankine thermal cycle for saturated steam—temperature-entropy diagram—(**a**) modular nuclear power plant (SMR); (**b**) AP1000 nuclear power plant.

To ensure a consistent comparison between the large-scale AP1000 unit and the selected SMR design, the thermal cycle of the small modular reactor was modelled with steam reheat, analogous to the AP1000 configuration. Although the reference SMR design (NuScale, 60 MW_e) is an integral pressurised water reactor with a simplified, once through steam generator and no provision for steam reheat, this modelling assumption was made intentionally. The goal was to maximise the thermal efficiency of the SMR cycle for the purpose of comparison under equivalent boundary conditions. While integral SMRs do not include reheat within the reactor pressure vessel, certain multi-module plant configurations could potentially include a reheat system in the shared secondary loop, improving the overall efficiency. Without reheat, the thermal efficiency of such an SMR unit would be expected to drop to approximately 30%, due to lower steam parameters and simplified turbine design. Nevertheless, this assumption does not affect the general conclusions of the study, as the economic trends and relative performance between the two technologies remain the same or very similar.

In the case of feedwater preheating systems, four preheaters—two low-pressure and two high-pressure—as well as a deaerator, are designed in the SMR solution. Feedwater reheating in the higher power unit is carried out using two heat exchangers on the high-pressure side and four low-pressure heaters. Important parameters taken from data sheets for the modelled nuclear technologies are summarised in Table 1.

Table 1. Selected technological parameters of the analysed nuclear power plants own elaboration based on [21].

Parameter		Unit	AP1000	SMR [1]
thermal power of the reactor		MW_t	3400	200
gross (and net) electrical power		MW_e	1200 (1100)	60 (57)
reactor coolant	mass flow	t/h	51,480	2397.6
	pressure	MPa	15.513	13.8
	temperature (inlet)	°C	279.4	265
	temperature (outlet)	°C	324.7	321
fresh steam	pressure	MPa	5.76	4.3
	temperature	°C	272.8	-
condenser pressure		kPa	9.1	-
feedwater temperature		°C	226.7	-
calculated efficiency of the power plant		%	34.7	33.3

[1] parameters for one module.

Performing further energy analysis of the secondary loops of the modelled units focused on simulating different loads on the nuclear reactor side. Thus, it was possible to examine the changes in individual parameters in the simulated systems. In addition, the usage of the simulation results obtained, as well as Equation (1), allowed the determination of operating characteristics for the subsequent comparison of large-scale technology with modular technology.

The following equation was used to determine the nuclear fuel utilisation rate:

$$q = \frac{3.6}{\eta_{el}}\left[\frac{\text{GJ}}{\text{MWh}}\right] \tag{1}$$

where

η_{el}—gross power plant efficiency.

In addition, the indicators that were determined in EBSILON®*Professional* are:

- Fresh steam flow—D;
- Cooling water flow in the condenser—D_{cw};
- Gross electrical power—P_{el_gross};
- Gross power plant efficiency—η_{el}.

3.2. Economic Analysis

To make economic comparisons of different types of power plants, the calculated costs of electricity generation should be used, as they include all cost elements. Calculated costs of generating electricity are the own costs increased by the costs of servicing investment outlays used to build the power plant (capital servicing costs), including interest on the loan taken out for construction. It is permissible to include interest on capital (accumulation) and depreciation in a total rate, dependent on the interest rate on capital and the depreciation period of the power plant, expressed by the discount rate.

Investment outlays, operational costs and production effects should be reduced to comparable values using discounting. A commonly used methodology is that developed in the late 1970s by UNIPEDE and then adopted by the European Union and other countries, according to which the unit discounted cost of generation is determined as the ratio of the total discounted costs of building and operating a power plant during its "life", including investment outlays, maintenance and repair costs and fuel costs, to the discounted amount of electric energy produced during that period:

$$k^j = \frac{I_{[0]} + \sum_{t=1}^{N} \frac{KU_t + A_t \cdot k_{pt}}{(1+p)^t}}{\sum_{t=1}^{N} \frac{P_t \cdot T_t}{(1+p)^t}} \tag{2}$$

where

$I_{[0]}$—capital expenditure taking into account the freeze during the construction of the power plant;

N—lifespan of a power plant;

KU_t—maintenance and repair costs per year t;

A_t—amount of electricity produced in a year t ($A_t = P_t \cdot T_t$);

k_{pt}—cost of fuel used to produce a unit of energy;

p—discount rate;

P_t—installed capacity of power plants in the year t;

T_t—time of use of installed capacity t [23].

The amount of electric energy produced is taken into account in calculations as net energy introduced into the power system. This means the electric energy generation after taking into account the consumption for the power plant's own needs, which translates into the value of the time of use of the installed capacity [23].

Investment outlays taking into account the freeze during the power plant construction period $I_{[0]}$ are calculated from the correlation:

$$I_{[0]} = \sum_{t=0}^{t=-(B-1)} I_t \cdot (1+p)^{-t} \tag{3}$$

where

B—construction period [years];

I_t—capital expenditure in the year t (nominal) [23].

A general quantitative comparison of electric energy generation costs in large-scale nuclear power plants with those in small-scale modular power plants is a difficult task due to large discrepancies in published, estimated, and forecasted economic data for various types of nuclear projects. As the literature review has shown, the incurred or forecasted capital expenditures and, consequently, the unit discounted cost of electric energy generation may take on extremely different values [24–26].

In order to analyse the factors influencing the relationship between the costs of electric energy generation in a large-scale nuclear power plant and a small-scale modular nuclear power plant, a relationship for their difference was defined:

$$\Delta k^j = k^j_{LSNPP} - k^j_{SMR} \tag{4}$$

If $k^j_{LSNPP} > k^j_{SMR}$, then $\Delta k^j > 0$. This means that the unit discounted cost of electricity generation in a large-scale nuclear power plant is higher, thus electricity production is more profitable in the case of SMR technology.

If $k^j_{LSNPP} < k^j_{SMR}$, then $\Delta k^j < 0$. This means that the unit discounted cost of electricity generation in a small-scale modular nuclear power plant is higher, and therefore electricity production is more profitable in the case of a large-scale nuclear power plant.

Equation (4), describing Δk^j, is expanded below in order to determine the relation of electric energy generation costs in the compared technological variants taking into account the main techno-economic factors:

$$\Delta k^j = k^j_{LSNPP} - k^j_{SMR} = \\ = \frac{I_{[0],LSNPP} + \sum_{t=1}^{N} \frac{KU_{t,LSNPP} + A_{t,LSNPP} \cdot k_{pt,LSNPP}}{(1+p)^t}}{\sum_{t=1}^{N} \frac{P_{t,LSNPP} \cdot T_{t,LSNPP}}{(1+p)^t}} - \frac{I_{[0],SMR} + \sum_{t=1}^{N} \frac{KU_{t,SMR} + A_{t,SMR} \cdot k_{pt,SMR}}{(1+p)^t}}{\sum_{t=1}^{N} \frac{P_{t,SMR} \cdot T_{t,SMR}}{(1+p)^t}} \quad (5)$$

where

$LSNPP$—large-scale nuclear power plant;

SMR—small modular reactor.

It was assumed that:

- Maintenance and repair costs (fixed costs) are proportional to the installed capacity of the nuclear power plant (single-core system), i.e.,:

$$KU_{t,LSNPP} = k^j_{UT} \cdot P_{t,LSNPP} \quad (6)$$

$$KU_{t,SMR} = k^j_{UT} \cdot P_{t,SMR} \quad (7)$$

  where

  k^j_{UT}—unit cost of maintenance and repairs (fixed) [USD/kW].

- The installed capacity of the power plant is constant throughout the entire life of the facility, i.e.,:

$$P_{t,LSNPP} = const = P_{LSNPP} \quad (8)$$

$$P_{t,SMR} = const = P_{SMR} \quad (9)$$

- The time of use of the installed power is constant throughout the entire life of the facility and the same for both investments under consideration, i.e.,:

$$T_{t,LSNPP} = T_{t,SMR} = const = T \quad (10)$$

- The cost of fuel used to produce a unit of electricity expressed in [USD/MWh] can be expressed as the product of the cost of fuel (primary energy) expressed in USD/GJ and the unit consumption of nuclear energy by individual power plants, expressed in GJ/MWh, constant throughout the entire life of the facility, i.e.,:

$$k_{pt,LSNPP}\left[\frac{\text{USD}}{\text{MWh}}\right] = k_{pt,LSNPP}\left[\frac{\text{USD}}{\text{GJ}}\right] \cdot q_{pt,LSNPP}\left[\frac{\text{GJ}}{\text{MWh}}\right] = const = k_{p,LSNPP} \cdot q_{LSNPP} \quad (11)$$

$$k_{pt,SMR}\left[\frac{\text{USD}}{\text{MWh}}\right] = k_{pt,SMR}\left[\frac{\text{USD}}{\text{GJ}}\right] \cdot q_{pt,SMR}\left[\frac{\text{GJ}}{\text{MWh}}\right] = const = k_{p,SMR} \cdot q_{SMR} \quad (12)$$

  where

  q—unit consumption of nuclear fuel energy [GJ/MWh].

- Fuel cost [USD/GJ] is independent of technology:

$$k_{p,LSNPP} = k_{p,SMR} = k_p \quad (13)$$

- The operating period N is the same for both power plants considered.

Taking into account the above assumptions, Formula (5) can be written in the form:

$$
\begin{aligned}
&\Delta k^j = \\
&= \frac{I_{[0],LSNPP} + \sum_{t=1}^{N} \dfrac{k_{UT}^j \cdot P_{LSNPP} + P_{LSNPP} \cdot T \cdot k_p \cdot q_{LSNPP}}{(1+p)^t}}{\sum_{t=1}^{N} \dfrac{P_{LSNPP} \cdot T}{(1+p)^t}} - \frac{I_{[0],SMR} + \sum_{t=1}^{N} \dfrac{k_{UT}^j \cdot P_{t,SMR} + P_{SMR} \cdot T \cdot k_p \cdot q_{SMR}}{(1+p)^t}}{\sum_{t=1}^{N} \dfrac{P_{SMR} \cdot T}{(1+p)^t}} = \\
&= \frac{I_{[0],LSNPP}}{\sum_{t=1}^{N} \dfrac{P_{LSNPP} \cdot T}{(1+p)^t}} + \frac{\sum_{t=1}^{N} \dfrac{k_{UT}^j \cdot P_{LSNPP}}{(1+p)^t}}{\sum_{t=1}^{N} \dfrac{P_{LSNPP} \cdot T}{(1+p)^t}} + \frac{\sum_{t=1}^{N} \dfrac{P_{LSNPP} \cdot T \cdot k_p \cdot q_{LSNPP}}{(1+p)^t}}{\sum_{t=1}^{N} \dfrac{P_{LSNPP} \cdot T}{(1+p)^t}} \\
&\quad - \frac{I_{[0],SMR}}{\sum_{t=1}^{N} \dfrac{P_{SMR} \cdot T}{(1+p)^t}} - \frac{\sum_{t=1}^{N} \dfrac{k_{UT}^j \cdot P_{t,SMR}}{(1+p)^t}}{\sum_{t=1}^{N} \dfrac{P_{SMR} \cdot T}{(1+p)^t}} - \frac{\sum_{t=1}^{N} \dfrac{P_{SMR} \cdot T \cdot k_p \cdot q_{SMR}}{(1+p)^t}}{\sum_{t=1}^{N} \dfrac{P_{SMR} \cdot T}{(1+p)^t}} = \\
&= \frac{1}{T \cdot \sum_{t=1}^{N} (1+p)^{-t}} \\
&\quad \cdot \left[\frac{I_{[0],LSNPP}}{P_{LSNPP}} + k_{UT}^j \cdot \sum_{t=1}^{N} (1+p)^{-t} + T \cdot k_p \cdot q_{LSNPP} \cdot \sum_{t=1}^{N} (1+p)^{-t} - \frac{I_{[0],SMR}}{P_{SMR}} - k_{UT}^j \right. \\
&\quad \left. \cdot \sum_{t=1}^{N} (1+p)^{-t} - T \cdot k_p \cdot q_{SMR} \cdot \sum_{t=1}^{N} (1+p)^{-t} \right] = \\
&= \frac{1}{T \cdot \sum_{t=1}^{N} (1+p)^{-t}} \cdot \left[\frac{I_{[0],LSNPP}}{P_{LSNPP}} - \frac{I_{[0],SMR}}{P_{SMR}} + T \cdot k_p \cdot \sum_{t=1}^{N} (1+p)^{-t} \cdot (q_{LSNPP} - q_{SMR}) \right]
\end{aligned}
\tag{14}
$$

The analysis aims to compare unit costs of electricity generation for nuclear power plants on a diametrically different scale. It is worth mentioning that the initial capital cost for 1 core only can be distributed over multiple cores. Such an approach lowers the value of unit capital costs. However, this economic indicator was not considered. Instead of it, the economic analysis assesses the range of total capital expenditures for a single investment, taking into account the freeze.

The presented economic analysis assumes that SMR cost estimates were taken as projected future costs after some learning (approaching NOAK costs), rather than one-off prototype costs (FOAK). Additionally, the considered capital expenditures refer to a power plant with a single core and the necessary facility. For this reason, the value of repair and maintenance costs was assumed at a stable and proportional level without scaling for multiple cores.

Both large-scale reactor (AP1000) and the selected small modular reactor (SMR) are light-water reactors operating with standard low-enriched uranium (LEU) fuel. Consequently, both units are assumed to rely on the same conventional fuel supply chains, with no significant differences in uranium procurement, enrichment, or fabrication technologies.

Therefore, the assumption that the unit fuel cost per unit of thermal energy is the same for both technologies, which is justified for the purposes of this comparison. This simplification ensures consistency in the economic model and allows a clearer focus on the influence of other plant-scale parameters, such as thermal efficiency and capital intensity.

Based on the above equation, the following conclusions can be drawn:

- The relationship between the unit discounted costs of electric energy generation for a large-scale nuclear power plant and a small-scale modular nuclear power plant depends primarily on the capital expenditures and the cost of the fuel used to produce a unit of electricity, or more precisely, at the same fuel purchase price, on the fuel primary energy used per unit of electricity produced.

- Due to the so-called "scale effect", the unit consumption of nuclear energy fuel in a large-scale nuclear power plant translates into reduced operating costs compared to a small-scale modular power plant.
- It is predicted that the relative (per unit of installed capacity) investment outlays of modular power plants will be reduced in relation to large-scale power plants. This is supported by the expected dissemination of technology, serial production, shorter implementation time, etc.
- The relation between the unit electricity generation costs of the variants under consideration will be determined by the strength of the above effects. In other words, will the difference in costs be influenced to a greater extent by the "scale effect" and the reduction in fuel costs in a large-scale power plant, or will the effect of serial production and the reduction in relative investment outlays prove to be more significant?
- Since both factors: investment outlays and unit consumption of nuclear fuel energy, strongly depend on the technology used and the specificity of the project, in order to obtain a clear answer in the decision-making process, each case should be considered individually.

4. Results and Discussion

The results obtained from simulation studies carried out on models implemented in the EBSILON®*Proffesional* environment provided valuable information from both technical and energy and economic aspects. These results provide a basis for understanding the differences between the nuclear technologies studied and their potential applications in the context of the transformation of the Polish energy sector.

4.1. Energy Analysis

Large-scale power plants are characterised by lower specific fuel consumption, which makes them extremely advantageous for large national investments. In addition, the slightly higher fresh steam parameters achieved in a nuclear power plant equipped with an AP1000 reactor result in higher fuel energy efficiency when operating at near-rated unit power (90–100)%P_{el}. The efficiency of the large-scale power plant analysed reaches about 34.7%, compared to about 33.3% for the modular solution.

Another important aspect is the possibility of integration into the National Power System (NPS). The AP1000 technology is better suited to the needs of replacing large centralised generating units (currently operating coal-fired power plants). On the other hand, the SMR solution, thanks to its modularity, offers greater flexibility both in terms of installed capacity and the possibility of locating it close to final consumers or industrial plants (adaptation to the needs of distributed generation).

The analysis of the obtained characteristics allows the assessment of the correlations between the different operating parameters of nuclear generating units. The adopted power variation range of (25–100)% of rated power is consistent with the physical design constraints of nuclear reactors. It not only minimises the risk of fuel damage, but also allows electricity production to be adapted to the fluctuating demand in the power system (load following operation). Thus, a spike or drop in load will not lead to the activation of the steam discharge system or the need to shut down the reactor.

Moreover, the very wide range from 25% to 100% of nominal power for both type of reactors was adopted for the purposes of sensitivity analysis, representing a theoretical scenario such as load following operation or emergency power reduction. AP1000 is technically capable of load-following operation by reducing power output to approximately 20–30% of nominal capacity if required. However, in practice, such low-load operation is not optimal and very rare in large power systems. The 25% power level should not be seen as a typical operating point for AP1000, but rather as a boundary case for modeling purposes. In a PWR, reducing power to such level can be achieved by adjusting control rods position or increasing boron concentration in water.

Figure 4 shows the dependence of reactor thermal power as a function of gross electrical power generated for the two technologies compared.

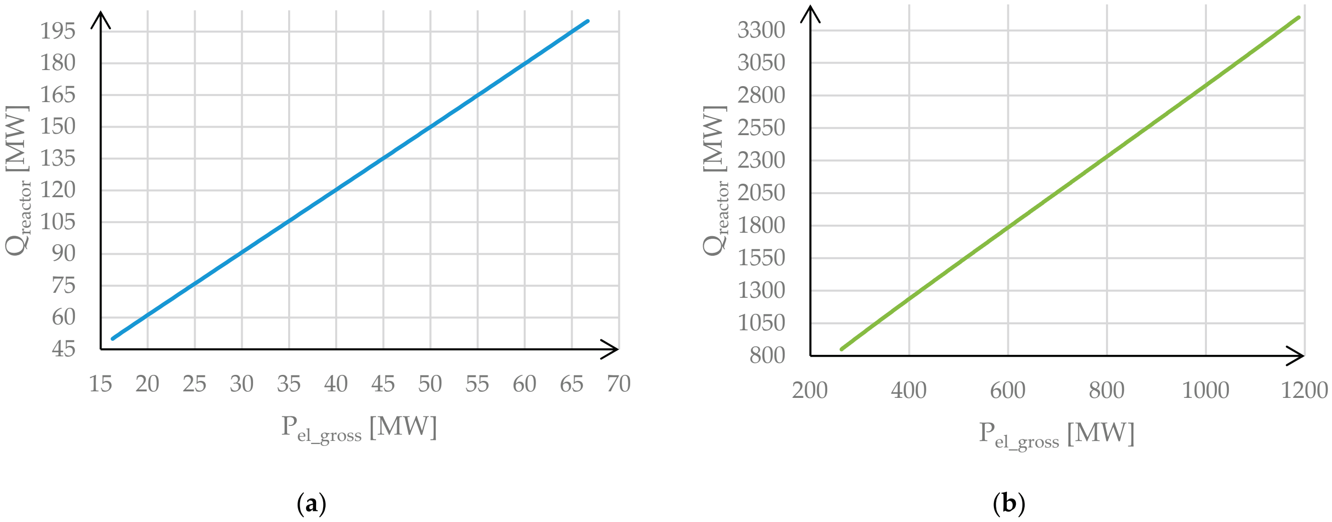

Figure 4. Graphs of reactor thermal output as a function of gross electric energy generated—(**a**) SMR nuclear power plant (1 module, 60 MW_e); (**b**) AP1000 nuclear power plant.

From the study, it can be seen that, in both the high-powered unit and the modular unit (SMR), increasing the thermal output of the reactor results in a linear increase in the generated electrical output. Maintaining the stability of power processes in a power plant involves a number of factors, including proportional changes on the electricity generation side or the fresh steam flow rate. If more heat is supplied to the steam generator, it will be possible to increase the output energy of the plant (production of the working medium). This will then translate into an increasing load on the steam turbine—increased electricity generation and the need to remove a significant amount of waste heat from the system (an increase in the demand for D_{cw} cooling water (Figure 5) necessary for condensation of the steam in the condenser). This relationship follows directly from the energy balance (conservation of energy principle).

When selecting a location for an NPP, it is important to bear in mind the need for cooling water to receive waste heat from the steam-water cycle. It becomes important to select a suitable site, which should be close to large reservoirs of water (river, lake, sea or ocean), with modular SMR technology offering greater location options due to the much lower cooling water requirements of the thermal cycle. A cooling water flow of approximately 150,000 t/h must be assumed for operation of the AP1000 at rated output for Δt_{cw} = 12 °C. For SMR operation at rated output, the cooling water flow is 8500 t/h.

Figure 6 shows the relationship between the nuclear-to-electricity conversion efficiency as a function of the unit load.

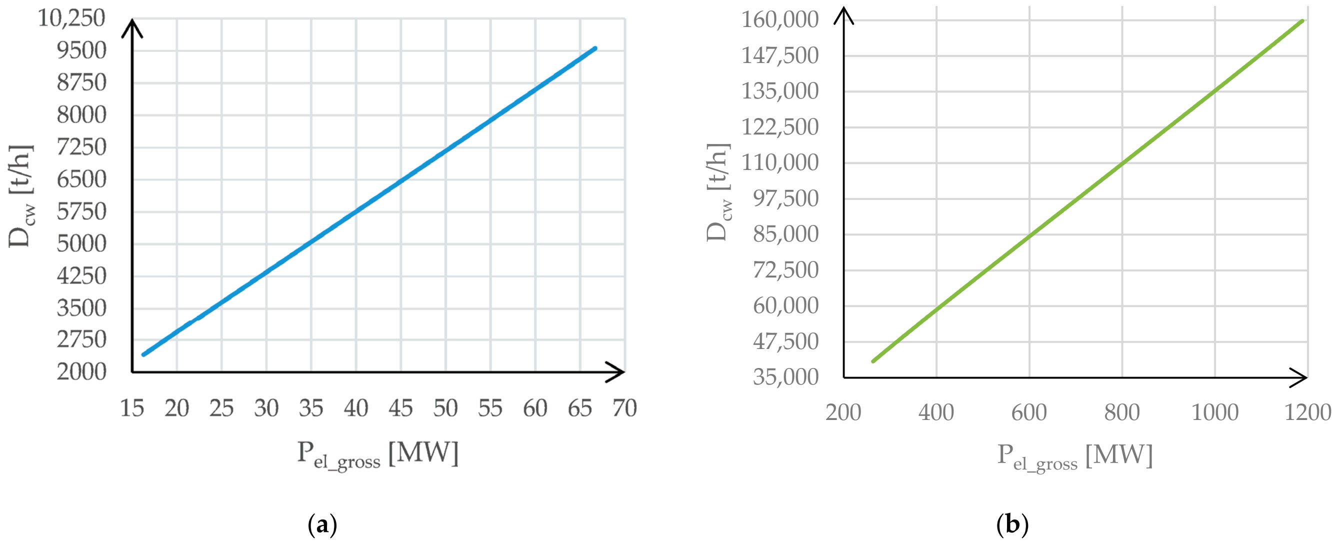

Figure 5. Graphs of cooling water flow as a function of gross electric energy generated—(**a**) SMR nuclear power plant (1 module, 60 MW_e); (**b**) AP1000 nuclear power plant.

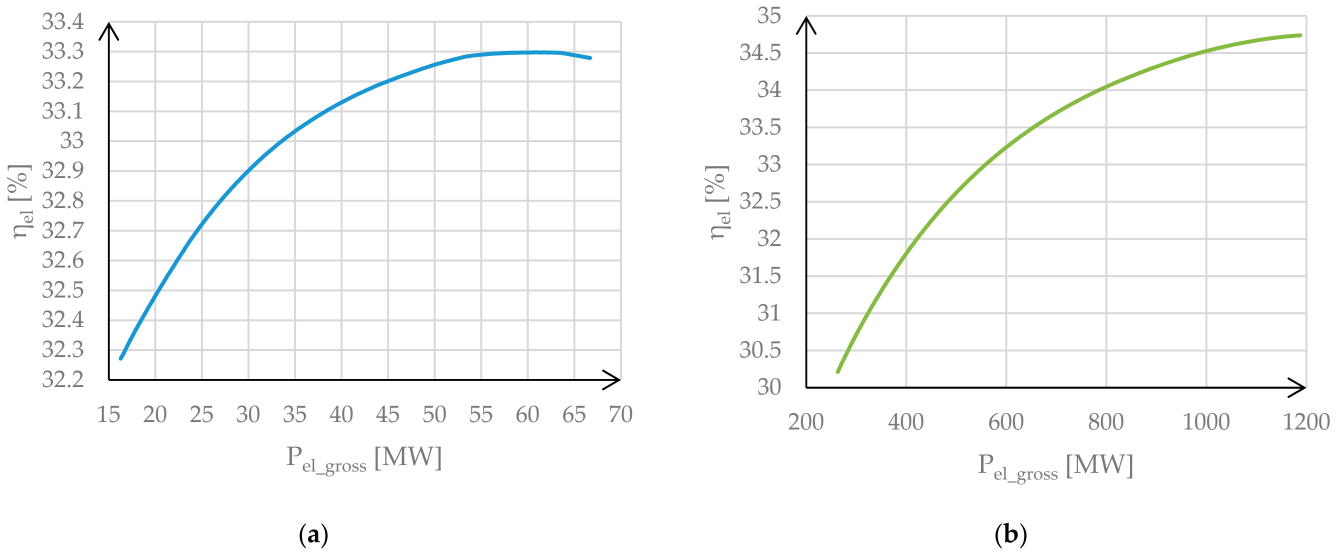

Figure 6. Graphs of gross power plant efficiency as a function of gross electric energy generated—(**a**) SMR nuclear power plant (1 module, 60 MW_e); (**b**) AP1000 nuclear power plant.

From Figure 6, it can be seen that as the amount of heat generated in the reactor increases, the gains in primary energy efficiency decrease. In the considered load range of the AP1000 nuclear power plant generator, the efficiency decreases from the nominal value of 34.5% by about 4 p.p., while in the case of the SMR, the efficiency relative to the nominal load decreases by about 1 p.p. This is due to the modularity of the solution and the much smaller range of variation in steam parameters as a function of load. From the point of view of power plant operation, aiming to operate in the highest efficiency range will minimise costs and energy losses.

Figure 7 shows the relationship between the nuclear fuel utilisation factor and the gross electrical power generated.

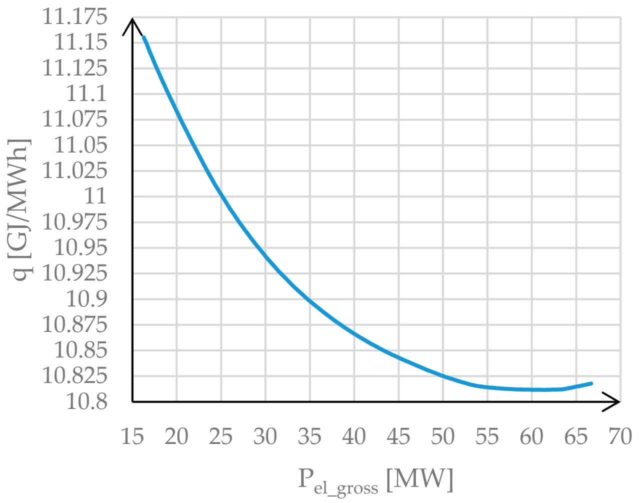

(**a**)

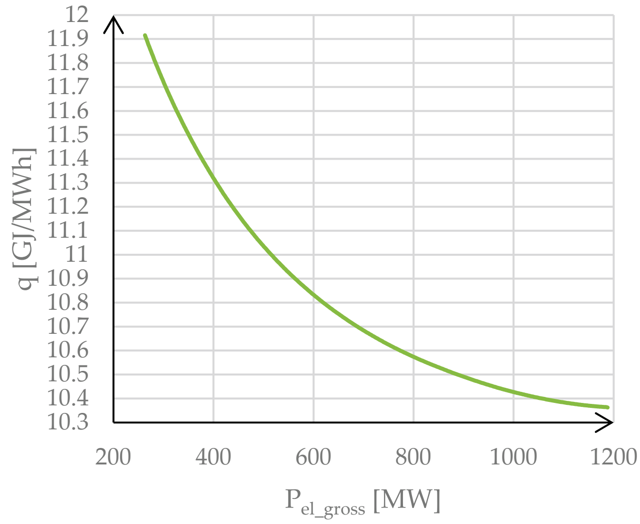

(**b**)

Figure 7. Graphs of nuclear fuel utilisation rate as a function of gross electric energy generated—(**a**) SMR nuclear power plant (1 module, 60 MW_e); (**b**) AP1000 nuclear power plant.

As the load increases, the value of the ratio of the use of nuclear energy of the fuel for the production of electric power decreases, while for the AP1000 technology in the considered range of power changes of 200–1200 MW, the q ratio changes its value in the range of 11.9–10.36 GJ/MWh, while for SMR the value of the q ratio changes in the load range by a small value of 0.32 GJ/MWh. The small change in the value of the q index is due to the modular design of the solution and the selection of parameters, already at the design stage, so that the operation of the SMR units in the partial load ranges is characterised by the highest possible efficiency. Thus, the examined parameter indicates that the power plant gains clearly in energy efficiency only at higher reactor thermal power values (increased electricity generation). The values of q were taken into account in the economic analysis.

4.2. Economic Analysis

For example, the derived relationship (Formula (14)) was used to compare a large-scale nuclear power plant with an AP1000 reactor and a NuScale 60 MW SMR. Considering that the ratio of installed powers of the compared power plants is 20 $\left(\frac{P_{LSNPP}}{P_{SMR}} = \frac{1200\ \text{MW}}{60\ \text{MW}}\right)$, the equation for the difference in the unit cost of electricity generation can be written as:

$$\begin{aligned}\Delta k^j &= \frac{1}{T \cdot \sum_{t=1}^{N} (1+p)^{-t}} \cdot \left[\frac{I_{[0],LSNPP}}{20 \cdot P_{SMR}} - \frac{I_{[0],SMR}}{P_{SMR}} + T \cdot k_p \cdot \sum_{t=1}^{N} (1+p)^{-t} \cdot (q_{SMR} - q_{p,SMR}) \right] = \\ &= \frac{0.05 \cdot I_{[0],LSNPP} - I_{[0],SMR}}{T \cdot \sum_{t=1}^{N} (1+p)^{-t} \cdot P_{SMR}} + (q_{LSNPP} - q_{SMR}) \cdot k_p\end{aligned} \quad (15)$$

In order to answer the question under what techno-economic conditions the generation of electricity in SMRs will be more economically viable than in a large-scale nuclear power plant, the following condition should be defined:

$$\Delta k^j > 0 \quad (16)$$

Using Equation (15), the above condition becomes:

$$\frac{0.05 \cdot I_{[0],LSNPP} - I_{[0],SMR}}{T \cdot \sum_{t=1}^{N} (1+p)^{-t} \cdot P_{SMR}} + (q_{LSNPP} - q_{SMR}) \cdot k_p > 0 \quad (17)$$

After mathematical transformations:

$$I_{[0],LSNPP} > 20 \cdot I_{[0],SMR} - 20 \cdot (q_{LSNPP} - q_{SMR}) \cdot k_p \cdot T \cdot \sum_{t=1}^{N} (1+p)^{-t} \cdot P_{SMR} \tag{18}$$

The following data were adopted for further analysis:

- Fuel cost (primary energy)—k_p = 1.4 [USD/GJ];
- Unit consumption of nuclear energy fuel for AP1000 when working at rated power—$q_{LSNPP} = 10.36 \left[\frac{\text{GJ}}{\text{MWh}}\right]$;
- Unit consumption of nuclear energy fuel for SMR when working at rated power—$q_{SMR} = 10.81 \left[\frac{\text{GJ}}{\text{MWh}}\right]$;
- Period of operation of the power plant—N = 60 years;
- Annual time of use of installed power, with availability of 90%—T = 7884 h;
- Discount rate—p = 0.07.

After taking into account the above values of selected quantities in the condition regarding the difference in unit discounted costs of electricity generation, the relationship between investment outlays for the compared technologies is obtained:

$$I_{[0],LSNPP} > 20 \cdot I_{[0],SMR} - 20 \cdot (q_{LSNPP} - q_{SMR}) \cdot k_p \cdot T \cdot \sum_{t=1}^{N} (1+p)^{-t} \cdot P_{SMR} \tag{19}$$

$$I_{[0],LSNPP} > 20 \cdot I_{[0],SMR} - 20 \cdot (10.36 - 10.81) \cdot 5 \cdot 7884 \cdot \sum_{t=1}^{60} (1+0.07)^{-t} \cdot 60 \tag{20}$$

$$I_{[0],LSNPP} > 20 \cdot I_{[0],SMR} + 83.7 \cdot 10^6 \tag{21}$$

Expressing the relationship in billions of USD:

$$I_{[0],LSNPP} > 20 \cdot I_{[0],SMR} + 83.7 \tag{22}$$

The above condition defines the relationship between capital expenditures taking into account the freeze for the compared power plants. If the condition is met, the unit discounted cost of generating electricity in a small-scale NuScale 60 MW modular nuclear power plant is lower than the cost for a large-scale nuclear power plant with an AP1000 reactor.

Figure 8 shows the relationship between the capital expenditures taking into account the freeze for a large-scale nuclear power plant with an AP1000 reactor and the expenditures for a small-scale NuScale 60 MW modular nuclear power plant, ensuring that the unit discounted generation costs in these plants are equal: $k^j_{LSNPP} = k^j_{SMR}$.

Figure 8 addresses the large variability of possible estimates in terms of costs connected to nuclear power plants. Instead of estimating and indicating single specific values of capital expenditures for comparing investments, the ranges of these quantities and their influence on relation between unit electricity generation costs were considered. Figure 8 shows the line defining capital expenditures configurations for which unit electricity generation costs are equal in both compared investments. Additionally, there are defined the spaces over and under this line, which consists of configurations resulting in an opposing relationship between unit electricity generation costs—respectively: $k^j_{SMR} < k^j_{LSNPP}$ and $k^j_{SMR} > k^j_{LSNPP}$.

According to the relationship presented in Figure 8, if, for example, the investment outlays, taking into account the freeze, for a large-scale nuclear power plant are USD 8 billion, then the investment outlays for an SMR power plant should be below USD

0.4 billion in order to ultimately ensure a lower or equal unit discounted cost of electric energy generation.

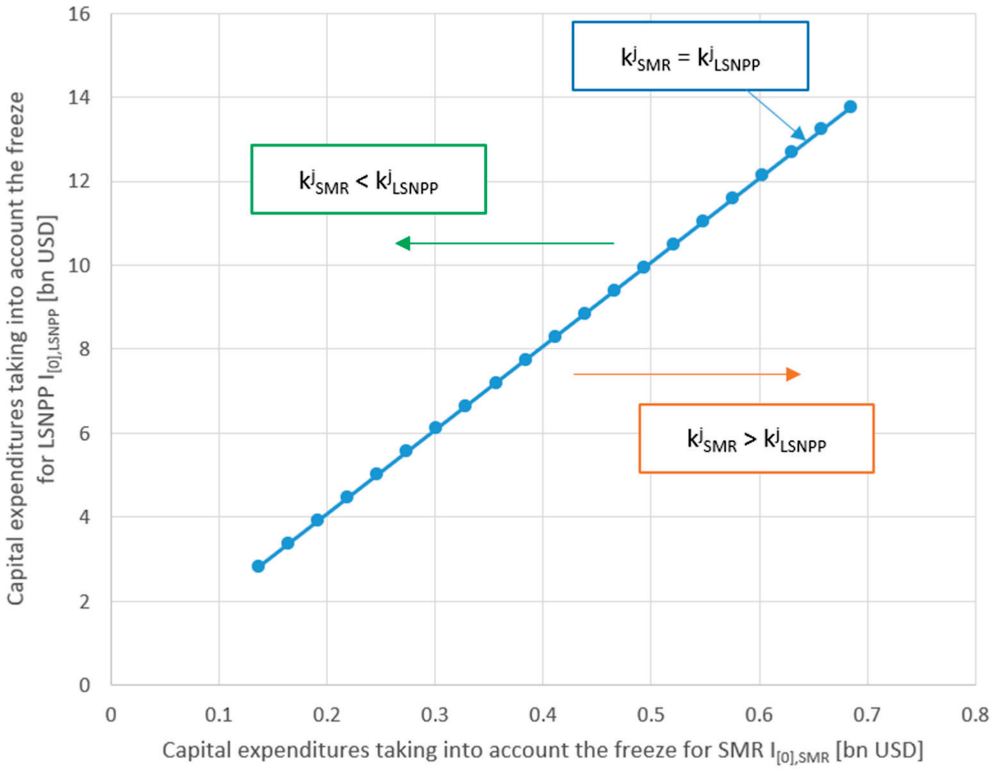

Figure 8. The relationship $I_{[0],LSNPP} = f\left(I_{[0],SMR}\right)$ with $k^j_{SMR} = k^j_{LSNPP}$ on the example of a power plant with AP1000 and NuScale 60 MW reactor.

The presented method of relative economic evaluation of two compared nuclear technologies allows for determining the impact of technical and economic parameters on the mutual relationship between the discounted unit costs of generating electricity without the need to determine their exact value. Determining the value of the discounted unit cost of generating electricity for nuclear technologies is challenging due to the difficulties in estimating the level of costs incurred for construction and operation. The presented method of economic analysis is therefore universal and generalised. The main determinants, which have by far the greatest impact on the unit cost of generating electric energy in nuclear technologies and on the obtained results, are the investment outlays. Their values can significantly differ and be shaped depending on the degree of complexity and organisational constraints of large-scale projects, or the development and popularisation of SMR technology.

5. Conclusions

Both compared investments—AP1000 nuclear power plant and the 60 MW_e SMR power plant—can have a crucial role to play in the transformation of the Polish power generation sector, with the AP1000 as the foundation for large-scale zero-carbon electric energy generation (system base operation), and the SMR as a distributed and flexible solution to support the decarbonisation of industry. The implementation of nuclear technologies could significantly reduce CO_2 emissions, improve energy security, as well as ensure a stable electric energy supply in conditions of constantly increasing shares of renewable energy sources in Poland's energy mix.

As the reference SMR in this analysis, the NuScale 60 MW_e was chosen, primarily because it is a pressurised water reactor, the same type as the AP1000. This ensures that the comparison between the two technologies is made on the basis of comparable thermodynamic and safety principles, even though they differ significantly in scale. Furthermore, NuScale was seriously considered for deployment in Poland, similarly to AP1000, which reinforces its relevance in our context. It also has the most advanced licensing status.

Comparing the two technologies, it can be seen that the AP1000 reactor has a higher electric energy generation efficiency when operating at rated power (approximately 34.7% compared to 33.3% for the SMR system). This translates into a lower nuclear fuel utilisation rate of between 10.36 and 11.88 GJ/MWh for the AP1000, compared to 10.81–11.15 GJ/MWh for the SMR unit. This dependence translates into a difference in operating costs related to the purchase of nuclear fuel.

Despite the lower efficiency, modular solutions can offer a number of advantages, such as shorter investment lead times, the possibility of series production and greater location flexibility. Investments can be made close to end-users or in areas with underdeveloped transmission infrastructure. In terms of cooling water requirements, this is one factor that is important in the choice of location, making SMRs more suitable for regions far from large water reservoirs or with limited water resources. However, in unit terms, the difference is insignificant.

Since facilities of completely different scales were compared, the unit discounted cost of electricity generation was used as the evaluation parameter. The economic analysis shows that the cost-effectiveness of both solutions is strongly dependent and the most sensitive on capital expenditures. As the main variable, the investment outlays taking into account the freeze during the power plant construction period $I_{[0]}$ was used. Moreover, the sensitivity of the results on these quantities for both investments was examined. It is worth mentioning that the impact of changes in discount rate was examined indirectly, because, it affects the value of the investment outlays taking into account the freeze during the power plant construction period: $I_{[0]} = \sum_{t=0}^{t=-(B-1)} I_t \cdot (1+p)^{-t}$. The advantage of the method is the lack of necessity to specify the value of unit investment outlays, which characterises significant variability.

The presented methodology of economic analysis is adequate for single-module power plants. It is particularly significant in the case of SMR units, because initial costs for 1 core only can be distributed over multiple added cores. Such an approach lowers the value of unit capital cost or unit maintenance and repair costs. In order to take into account the effect of modularity on economic efficiency, a relationship should be developed that scales unit costs with the number of cores in the reactor building. However, the closer the number of modules used in an SMR brings its rated power to that of the AP1000, the less justified their use as a replacement for a large-scale power plant seems. Therefore, the analysis focuses on comparing a large-scale power plant with a small-capacity unit, whose roles in the system may be complementary.

As the two technologies can complement each other, a hybrid deployment strategy should be considered. High-capacity reactors should be built in regions with adequate grid infrastructure and access to water, while SMRs can act as distributed sources to replace decommissioned coal-fired units or serve as process heat sources for industry.

The developed model, with its potential for further expansion, is a valuable tool to support the much-needed decision-making associated with the implementation of nuclear power in the country. In future research work, it is worth extending the analysis to include external factors such as regulatory risk, energy market development scenarios and the potential for integration of nuclear technology in hybrid energy systems (e.g., cogeneration, district heating, hydrogen production).

It may be particularly important to deepen research into the application of small modular reactors (SMRs) in the district heating sector, which in Poland faces challenges related to the need to reduce greenhouse gas emissions and decarbonise the heating infrastructure.

Extending the current model to include variants for the use of SMRs for district heating production would allow the development of scenarios for their implementation in district heating systems. However, a comprehensive legal framework, institutional support and outreach activities aimed at increasing public acceptance of nuclear power in heating applications will be required for the successful implementation of this technology.

Author Contributions: Conceptualization, B.C. and A.M.; methodology, N.K. and A.M.; software, N.K.; validation, B.C., J.S. and R.S.; formal analysis, B.C., J.S. and R.S.; investigation, N.K.; resources, N.K. and R.S.; data curation, N.K.; writing—original draft preparation, N.K. and A.M.; writing—review and editing, B.C. and A.M.; visualization, N.K.; supervision, B.C. and J.S.; project administration, B.C.; funding acquisition, B.C. All authors have read and agreed to the published version of the manuscript.

Funding: This research was funded by the Ministry of Education and Science, grant number 0711/SBAD/4662.

Data Availability Statement: The original contributions presented in this study are included in the article. Further inquiries can be directed to the corresponding author(s).

Conflicts of Interest: The authors declare no conflicts of interest.

Abbreviations and Symbols

The following abbreviations and symbols are used in this manuscript:

BWR	boiling water reactor
FOAK	first-of-a-kind
IAEA	International Atomic Energy Agency
LEU	low-enriched uranium
LSNPP	large-scale nuclear power plant
LUEC	levelized unit electricity cost
NOAK	nth-of-a-kind
NPP	nuclear power plant
NPS	National Power System
PWR	pressurised water reactor
SMR	small modular reactor
UNIPEDE	International Union Producers Distributors of Electrical Energy
A_t	amount of electricity produced in a year t
B	construction period [years]
D	fresh steam mass flow [t/h]
D_{cw}	cooling water mass flow in the condenser [t/h]
$I_{[0]}$	capital expenditure taking into account the freeze during the construction of the power plant
I_t	capital expenditure in the year t (nominal)
k_{pt}	cost of fuel used to produce a unit of energy
k_{UT}^{j}	unit cost of maintenance and repairs (fixed) [PLN/kW]
KU_t	maintenance and repair costs per year t
N	lifespan of a power plant
η_{el}	gross power plant efficiency [%]
p	discount rate
P_{el_gross}	gross electrical power [MW]
P_t	installed capacity of power plants in the year t

q	nuclear fuel utilisation rate [GJ/MWh]
$Q_{reactor}$	thermal power of the reactor [MW]
T_t	time of use of installed capacity t
Δt_{cw}	cooling water temperature difference [°C]

References

1. PGE Górnictwo i Energetyka—CO2 Emission—Bełchatów Power Plant. Available online: https://elbelchatow.pgegiek.pl/Ochrona-srodowiska/Ograniczenie-emisji-dwutlenku-wegla (accessed on 25 May 2024).
2. PSESA—Quantitative Data on the Operation of the NPS in 2024. Available online: https://www.pse.pl/dane-systemowe/funkcjonowanie-kse/raporty-roczne-z-funkcjonowania-kse-za-rok/raporty-za-rok-2024 (accessed on 15 May 2025).
3. Our World in Data—Electricity Production by Source in France. Available online: https://ourworldindata.org/grapher/electricity-prod-source-stacked?country=~FRA (accessed on 15 May 2025).
4. IAEA—Power Reactor Information System—France. Available online: https://pris.iaea.org/PRIS/CountryStatistics/CountryDetails.aspx?current=FR (accessed on 15 May 2025).
5. Electricity Maps. Available online: https://app.electricitymaps.com/map?lang=pl (accessed on 15 May 2025).
6. Cizelj, L.; Pesznyak, C.; Starflinger, J.; Lazaro Pavel, G.; Wastin, F.; Michailidou, E. Towards strategic agenda for European nuclear education, training, and knowledge management. *Nucl. Eng. Des.* **2024**, *420*, 113001. [CrossRef]
7. Hussein, E.M.A. Emerging small modular nuclear power reactors: A critical review. *Phys. Open* **2020**, *5*, 100038. [CrossRef]
8. Lee, J.I. Review of Small Modular Reactors: Challenges in Safety and Economy to Success. *Korean J. Chem. Eng.* **2024**, *41*, 2761–2780. [CrossRef]
9. Jin, I.J.; Bang, I.C. The time for revolutionizing small modular reactors: Cost reduction strategies from innovations in operation and maintenance. *Prog. Nucl. Energy* **2024**, *174*, 105288. [CrossRef]
10. Ren, C.; Lei, J.; Liu, J.; Hong, J.; Hu, H.; Fang, X.; Yi, C.; Peng, Z.; Yang, X.; Yu, T. Research on an Intelligent Fault Diagnosis Method for Small Modular Reactors. *Energies* **2024**, *17*, 4049. [CrossRef]
11. Hartmann, J.; Hyvärinen, J.; Rintala, V. The operator and the seven small modular reactors—An estimate of the number of reactors that a single reactor operator can safely operate. *Nucl. Eng. Des.* **2024**, *418*, 112929. [CrossRef]
12. Mignacca, B.; Locatelli, G. Economics and finance of Small Modular Reactors: A systematic review. *Renew. Sustain. Energy Rev.* **2020**, *118*, 109939. [CrossRef]
13. Nuclear Energy Agency, Organisation For Economic Co-Operation and Development. In *Unlocking Reductions in the Construction Costs of Nuclear: A Practical Guide for Stakeholders*; OECD: Paris, France, 2020. Available online: https://www.oecd-nea.org/upload/docs/application/pdf/2020-07/7530-reducing-cost-nuclear-construction.pdf (accessed on 13 August 2025).
14. IAEA Nuclear Energy Series No. NR-T-1.18. In *Technology Roadmap for Small Modular Reactor Deployment*; International Atomic Energy Agency: Vienna, Austria, 2021. Available online: https://www-pub.iaea.org/MTCD/Publications/PDF/PUB1944_web.pdf (accessed on 13 August 2025).
15. Vegel, B.; Quinn, J.C. Economic evaluation of small modular nuclear reactors and the complications of regulatory fee structures. *Energy Policy* **2017**, *104*, 395–403. [CrossRef]
16. Shirvan, K.; Harwick, J.C. *Overnight Capital Cost of the Next AP1000*; Final Report; MIT-ANP-TR-193; Massachusetts Institute of Technology: Cambridge, MA, USA, 2022.
17. Asuega, A.; Limb, B.J.; Quinn, J.C. Techno-economic analysis of advanced small modular nuclear reactors. *Appl. Energy* **2023**, *334*, 120669. [CrossRef]
18. Fam, A.; Fam, S. Review of the US 2050 long term strategy to reach net zero carbon emissions. *Energy Rep.* **2024**, *12*, 845–860. [CrossRef]
19. Skuza, M.; The Renaissance of Nuclear Energy. Global Technological Competition and Development Prospects of the Nuclear Sector in the Context of Geopolitical Changes and Climate Crisis. *Sprawy Międzynarodowe* **2024**, *77*.
20. Robb Stewart, W.; Shirvan, K. Construction schedule and cost risk for large and small light water reactors. *Nucl. Eng. Des.* **2023**, *407*, 112305. [CrossRef]
21. Status Report—NuScale SMR (NuScale Power, LLC). Available online: https://share.google/Lz63H4ymj8ZMz49yh (accessed on 10 April 2025).
22. Vogtle Electric Generating Plant, Units 3 and 4, Updated Final Safety Analysis Report, Revision 12 (AP1000). Available online: https://www.nrc.gov/docs/ML1224/ML12249A432.pdf (accessed on 10 April 2025).
23. Kamrat, W. (Ed.) *Energy Management Under Market Conditions*; Modelling-Economics-Management (In Polish: Gospodarka Energetyczna w Warunkach Rynkowych. Modelowanie-Ekonomika-Zarządzanie); Wydawnictwo Naukowe PWN: Warszawa, Czech Republic, 2023.

24. Westinghouse Electric Announces New Small Modular Reactor Borrowing from Its AP1000 Nuclear Technology. Available online: https://www.utilitydive.com/news/westinghouse-smr-small-modular-reactor-nuclear-technology-ap1000-ap300/649418/ (accessed on 13 August 2025).
25. Westinghouse AP300/US Company Unveils 'Game-Changing' Mid-Sized Nuclear Reactor. Available online: https://www.nucnet.org/news/us-company-unveils-game-changing-mid-sized-nuclear-reactor-5-4-2023 (accessed on 13 August 2025).
26. Stewart, W.R.; Shirvan, K. Capital cost estimation for advanced nuclear power plants. *Renew. Sustain. Energy Rev.* **2022**, *155*, 111880. [CrossRef]

energies

MDPI

Article

Leveraging Dynamic Pricing and Real-Time Grid Analysis: A Danish Perspective on Flexible Industry Optimization

Sreelatha Aihloor Subramanyam, Sina Ghaemi, Hessam Golmohamadi, Amjad Anvari-Moghaddam and Birgitte Bak-Jensen *

Department of Energy, Aalborg University, 9220 Aalborg, Denmark; sasu@energy.aau.dk (S.A.S.); sigh@energy.aau.dk (S.G.); hessamgolmoh@energy.aau.dk (H.G.)
* Correspondence: bbj@energy.aau.dk

Abstract: Flexibility is advocated as an effective solution to address the growing need to alleviate grid congestion, necessitating efficient energy management strategies for industrial operations. This paper presents a mixed-integer linear programming (MILP)-based optimization framework for a flexible asset in an industrial setting, aiming to minimize operational costs and enhance energy efficiency. The method integrates dynamic pricing and real-time grid analysis, alongside a state estimation model using Extended Kalman Filtering (EKF) that improves the accuracy of system state predictions. Model Predictive Control (MPC) is employed for real-time adjustments. A real-world case studies from aquaculture industries and industrial power grids in Denmark demonstrates the approach. By leveraging dynamic pricing and grid signals, the system enables adaptive pump scheduling, achieving a 27% reduction in energy costs while maintaining voltage stability within 0.95–1.05 p.u. and ensuring operational safety. These results confirm the effectiveness of grid-aware, flexible control in reducing costs and enhancing stability, supporting the transition toward smarter, sustainable industrial energy systems.

Keywords: dynamic pricing; MILP; real-time grid analysis; Kalman filter; industrial energy optimization; flexible assets; aquaculture case study; Model Predictive Control

1. Introduction

The increasing integration of renewable energy sources and price-responsive consumers driven by the goal of achieving a carbon-free society by 2050 [1] has led to greater uncertainty and variability in power systems, thereby intensifying the need for sufficient flexibility. Flexibility provision approaches can generally be categorized into three main parts: demand-side, generation-side, and storage-based solutions [2]. However, emerging technologies that create links between the power sector and other domains such as water pumps underscore the growing importance of sector coupling as a source of flexibility. In this context, the optimal operation of water pumping systems in industrial clusters near water from the sea not only provides valuable flexibility to the power system but also presents an opportunity for profit maximization. Therefore, it is crucial to explore how the optimal energy management of such systems can be implemented, taking into account the technical constraints of the power grid and the accurate state estimation of water levels.

In recent years, several studies have investigated the optimal energy management of the water–energy nexus. The authors of [3] developed a mixed-integer nonlinear programming model for the day-ahead scheduling of integrated water and power systems, incorporating flexible components such as variable-speed pumps. Their results demonstrated a 4.6% reduction in operational costs compared to the case where the two systems are optimized independently. The authors of [4,5] analyzed the optimal energy mix for water-pumping systems, comparing renewable and non-renewable sources alongside demand-response flexibility. According to the results, a hybrid setup of biomass-based distributed generation, photovoltaics, and time-of-use demand response minimizes cost; applying the Generalized Reduced Gradient nonlinear optimization yields energy costs of 0.018 USD/kWh (with carbon tax) and 0.016 USD/kWh (without).

The impact of a water distribution network comprising multiple pumps and tanks on the optimal day-ahead scheduling of the power system was analyzed in [6] using a mixed-integer linear programming approach. A flexible power-water flow model was introduced in [7] to optimize the scheduling of energy-intensive assets in water systems, such as water treatment and desalination plants, as well as variable-speed pumps and tanks, thereby highlighting their contribution to power system flexibility. Due to the strong interdependence between water distribution grids and power systems, largely stemming from the prevalence of variable-speed pumps, a nonlinear conjunctive optimization model was developed in [8], which achieved a 10% reduction in total system costs. In the context of smart energy communities, ref. [9] introduced a water–energy nexus model aimed at minimizing the community's operating costs. The model used integer variables to capture the on/off status of pumps, and the results confirmed its superior cost efficiency compared to separately optimizing each sector. In [10], a hardware-in-the-loop testbed for a water distribution system was employed to validate a real-time economic dispatch model for integrated energy and water systems. The study also utilized machine learning techniques to solve the optimization problem efficiently.

Researchers have proposed strategies to optimize integrated water–electricity systems. A three-step approach improved computational efficiency, cutting curtailment and operational costs by over 50% [11]. Optimal tank design and joint energy–water storage enhanced flexibility and water quality [12,13], while a robust data-driven model improved peak load handling and uncertainty management [14]. Transfer delay modeling using electrical–water analogies also supported wind integration [15]. Solar-powered pumping with battery storage improved control performance [16], and standalone PV systems enabled crisis-resilient water supply [17]. Smart meters and 5G supported real-time pump energy reduction and water quality assurance [18]. An integrated nexus model showed the role of water storage in energy planning [19]. Metaheuristic optimization minimized pump energy use while maintaining water standards [20]. IoT-enabled smart tanks enhanced monitoring, leakage detection, and control [21]. Based on a Neuro fuzzy logic algorithm, optimal energy management of the system of batteries and wind turbines for supplying water pumping has been suggested in [22]. Additionally, in [23], the authors proposed a Takagi–Sugeno fuzzy model for the optimal energy management of a hybrid system that consists of a photovoltaic system, a wind turbine, and a battery for supplying water to a rural region without access to the main grid. A mixed integer nonlinear programming approach was proposed in [24] for optimizing the management of water and energy integration as a virtual power plant model for an irrigation system. A machine-learning-based optimal pump operation scheduling model was proposed in [25], taking into account dynamic load fluctuations, electricity prices, and the technical constraints of the system. An economic model predictive model was proposed in [26] for estimating the optimal scheduling for seawater pumping systems, utilizing demand-side management, batteries, and solar energy for load shifting as well as peak shaving. For convenience, Table 1 is presented below to compare our proposed work with state-of-the-art studies.

Table 1. Comparison of state-of-the-art studies with this work.

Paper (Ref.)	Optimisation/Control Method	Closed-Loop	Grid-Voltage	Price/DR	Storage Modelled	Experimental/ Validation
[3]	MINLP, day-ahead co-optimization	—	—	✓	Water tanks	—
[4]	Hybrid PV/wind sizing	—	—	✓	Battery	—
[5]	Conceptual flexibility model	—	—	✓	Water tanks	—
[6]	MILP, day-ahead scheduling	—	—	✓	Water tanks	—
[7]	MILP, day-ahead scheduling	—	—	✓	Water tanks	—
[8]	Nonlinear conjunctive optimization	—	—	✓	Water tanks	—
[9]	MILP, micro WEN	—	—	✓	Battery + tanks	—
[10]	Data-driven economic dispatch	∼	—	✓	Tanks	HIL bench
[11]	Three-step cost minimization	—	—	✓	Tanks	—
[12]	Tank-size optimization	—	—	—	Water tanks	—
[13]	Joint electricity–water storage sizing	—	—	—	Battery + tanks	—
[14]	Two-stage robust optimization	—	—	✓	Battery + tanks	—
[15]	Delay-aware scheduling	—	—	✓	Tanks	—
[16]	MPC for PV-pump	∼	—	—	Battery	Lab
[17]	Stand-alone PV sizing	—	—	—	Battery	Field (crisis)
[18]	MILP with water-quality limits	—	—	✓	Tanks	—
[19]	Integrated E-W-F resource planning	—	—	—	Water storage	—
[20]	Meta-heuristic pump scheduling	—	—	✓	—	—
[21]	IoT monitoring/control	—	—	—	—	Prototype
[22]	Neuro-fuzzy EMS	∼	—	—	Battery	—
[23]	Takagi–Sugeno EMS	∼	—	—	Battery	—
[24]	MINLP virtual power plant	—	—	✓	Battery	—
[25]	ML pump scheduling	—	—	✓	—	—
[26]	Economic MPC, seawater pumps	∼	—	✓	Battery	Simulation
This Paper	**MILP + EKF + MPC**	✓	✓	✓	Water Tank	Industrial field data

✓ Feature is included in the study. ∼ Partially addressed or limited support.

While prior demand-response research within the water–energy nexus has predominantly focused on either economic scheduling or advanced control and monitoring, few studies have addressed a fully integrated, real-time, closed-loop architecture that combines both aspects. This paper proposes and validates a closed-loop, grid-aware energy management scheme for an industrial saltwater pumping facility in Denmark. The proposed method consists of three key steps: First, an EKF reconstructs tank levels, flow rates, and busbar voltage from noisy or incomplete SCADA data. Then, in the second step, a mixed-integer linear programming (MILP) model is developed to co-optimize pump on/off schedules based on 24 h electricity price forecasts, incorporating both hydraulic and voltage-band constraints. Finally, in the third step, a hourly receding-horizon MPC layer continuously updates and resolves the MILP using the latest state estimates. The main contributions of this study are as follows:

1. The objective function incorporates quadratic penalties on deviations from real-time EKF state estimates, ensuring that the economic optimizer does not propose hydraulically or electrically infeasible actions even in the presence of sensor drift or failure.
2. Voltage-band constraints are co-optimized alongside pump operations, transforming the water process from a passive price-taker into an active asset within the distribution grid.
3. A unified linearized model simultaneously represents tank mass balances and nodal voltage behavior, enabling integration of hourlyl optimization with second-level dynamic simulation.

The remainder of the paper is structured as follows: Section 2 describes the methodological framework and the Danish industrial saltwater pumping case study, including the integration of dynamic electricity pricing and real-time grid analysis. Section 3 elaborates the mathematical formulation, highlighting how the MILP model and EKF are employed to enable real-time state estimation and grid-aware scheduling. Section 4 presents simulation results, highlighting cost savings, voltage stability, and system flexibility, and illustrates the model's potential for active industrial participation in smart grid operations. Section 5 concludes with key findings.

2. Materials and Methods

The primary objective of this study is to optimize the operational strategy of a saltwater distribution system located in Denmark, in order to minimize both energy consumption and operational costs while simultaneously ensuring system flexibility and grid stability. This Danish case study exemplifies the nation's progressive approach toward sustainable and smart industrial energy use. The optimization strategy is achieved through the integration of advanced state estimation techniques—specifically the EKF—to accurately estimate real-time water flow rates and tank levels. Furthermore, the optimization framework incorporates real-time electricity pricing signals, enabling the system to dynamically adjust pump operations in response to grid demands, thus supporting Denmark's broader goals for intelligent demand-side management.

2.1. Description of Saltwater Distribution System

The saltwater distribution network comprises four interconnected tanks designed to supply water from the sea to an industrial aquaculture facility. The saltwater distribution network used in this study is shown in Figure 1. The system's flexibility and control responsiveness are evaluated based on this configuration, which serves as a representative example of Denmark's potential for integrated water–energy optimization in coastal industries.

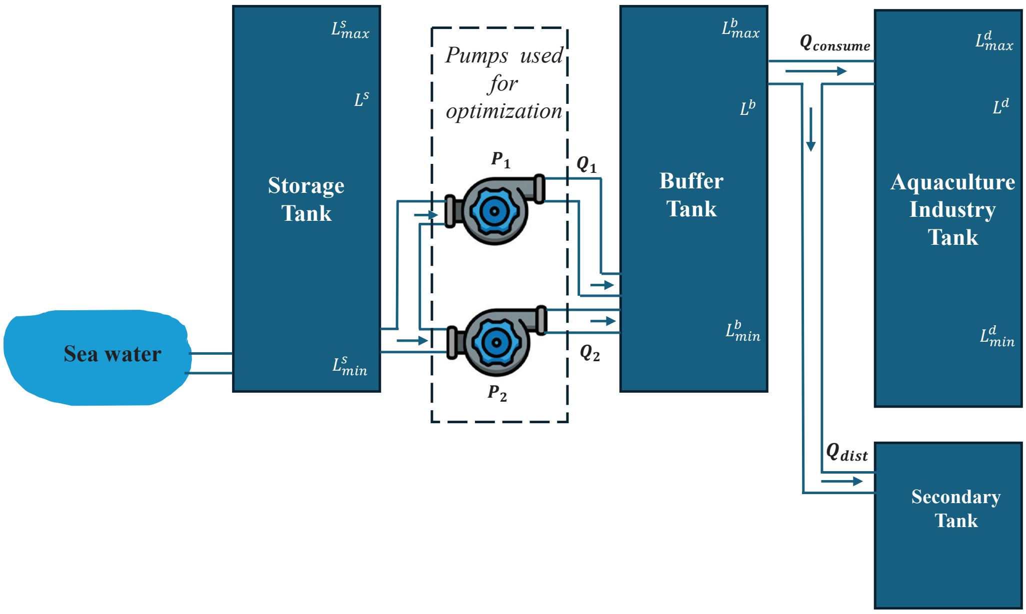

Figure 1. Schematic representation of the saltwater distribution network comprising four interconnected tanks: storage, buffer, aquaculture industry, and secondary tank. The diagram highlights the pump layout and flow directions used in the MILP-based optimization. This setup is used to evaluate system flexibility, energy efficiency, and control responsiveness in a real industrial context.

Tank 1, designated as the storage tank, serves as the primary reservoir, collecting water directly from the sea. The water level in this tank varies according to gravitational inflows influenced by tidal conditions.

Tank 2, referred to as the buffer tank, is supplied with saltwater from the storage tank via two electrically driven centrifugal pumps. Each pump has a rated capacity of 250 m^3/h and consumes 22.5 kWh under full operational load. The buffer tank serves as an intermediary node, regulating water flow to downstream units while mitigating flow variability.

Tank 3, identified as the aquaculture industry tank, receives water exclusively from the buffer tank. This tank supplies the aquaculture process directly, thus maintaining a continuous and stable inflow that is essential to prevent operational disturbances in the industrial system.

In parallel, a secondary tank is also connected to the buffer tank. This unit has a relatively constant water demand, maintained within the range of 15 to 20 m^3/h throughout the operational period. Furthermore, the aquaculture industry tank and secondary tanks are modeled as fixed-load units with time-dependent water consumption profiles. Their demand is treated as an external input, rather than an optimization variable.

2.2. Optimization Framework of Saltwater Distribution System

To minimize energy costs while ensuring safe and reliable operation, we propose an optimization framework that jointly optimizes pump scheduling and water flow dynamics in a saltwater distribution system. The framework integrates MILP for pump scheduling (see Equation (1)), EKF for real-time state estimation of critical variables such as tank water levels ($\hat{L}_b(t), \hat{L}_s(t), \hat{L}_d(t)$), flow rates ($\hat{Q}_1(t), \hat{Q}_2(t)$), and voltage magnitude ($\hat{V}(t)$) (Equations (17)–(20)), and MPC for closed-loop control that adapts to disturbances and future system behavior using the estimated states and optimized trajectories (Equation (16)).

The optimization process is constrained by a set of operational and physical limitations to ensure safe and efficient system performance. These include the enforcement of minimum and maximum allowable water levels for each tank (buffer: $L_b(t)$, storage: $L_s(t)$, aquaculture: $L_d(t)$) to prevent overflow or dry-out conditions (Equations (5)–(7)), as well as adherence to pump capacity limits and ramping constraints ($Q_1(t)$, $Q_2(t)$, $P_i(t)$) (Equations (8), (9), (12) and (13)).

Additionally, the framework incorporates real-time electricity pricing signals $\lambda(t)$ that vary dynamically over the optimization horizon, allowing for cost-effective scheduling. Mass balance equations are also applied to govern the inflow and outflow dynamics at each tank node, ensuring hydraulic consistency across the distribution network (Equations (2)–(4)).

For each time step, the EKF first estimates the current system states. These estimates are then passed to the MILP module, which computes the optimal pumping schedule. Finally, the MPC utilizes the MILP-generated trajectories and EKF outputs to determine and issue control actions ($P_1(t), P_2(t)$) for the next time interval, ensuring closed-loop implementation and adherence to system constraints (Equation (16)).

To assess the effectiveness of the proposed optimization and control architecture, two simulation scenarios are considered. In the first, a baseline case is implemented, representing business-as-usual operation with static pump schedules and no real-time optimization. In contrast, the optimized scenario incorporates the full integration of MILP-based scheduling, EKF-based state estimation, and MPC for dynamic real-time control. The MILP problem is formulated and implemented using the Pyomo optimization framework and solved using the open-source CBC (Coin-or branch-and-cut) solver, enabling a practical evaluation of the model's performance in achieving cost efficiency, voltage stability, and operational flexibility under real-world conditions. The Algorithm 1 and the mathematical equations used in the algorithm are given below.

Algorithm 1 MPC Optimization Framework with EKF and MILP

1: **Input:** Time-series SCADA data: $P_{1\_meas}(t)$, $P_{2\_meas}(t)$, tank inflows/outflows, $Q_{consume}(t)$, Q_{dist}, voltage readings, electricity prices
2: **Output:** Optimized control actions: $P_1(t)$, $P_2(t)$, $Q_1(t)$, $Q_2(t)$, $L_b(t)$, $L_s(t)$, $L_d(t)$, $V(t)$, $E(t)$, $C(t)$

State Estimation via EKF

3: Initialize EKF state vector:

$$X(0) = [L_b(0), L_s(0), L_d(0), V(0), \dot{L}_b(0), \dot{L}_s(0), \dot{L}_d(0), \dot{V}(0)]^\top$$

4: **for** each time step t **do**
5: Predict next state: $X(t+1|t) = AX(t) + BU(t)$
6: Update using measurements: $Y(t) = CX(t) + W(t)$
7: Output estimated states: $\hat{L}_b(t)$, $\hat{L}_s(t)$, $\hat{L}_d(t)$, $\hat{V}(t)$
8: **end for**

MPC Optimization using MILP

9: **for** each control interval $t = 1$ to T **do**
10: Define decision variables:

- Pump setpoints: $P_1(t), P_2(t) \in [0, 100]$
- Flow rates: $Q_1(t), Q_2(t)$
- Tank volumes/levels: V_b, V_s, V_d, L_b, L_s, L_d
- Reactive power: $Q_{\text{reactive}}(t)$
- Optimized voltage $V(t)$
- Energy: $E(t)$, Cost: $C(t)$

11: Add constraints:

- $Q_i = \frac{P_i}{100} \cdot Q_{\max}$
- Tank mass balances from flow dynamics
- Level-volume relations: $L_x = \frac{V_x}{A_x / V_x}$ for each tank
- Estimated voltage: $\hat{V}(t)$ included directly
- Voltage limits: $0.95 \leq V(t) \leq 1.05$
- Runtime and ramp constraints on P_1, P_2

12: Minimize objective:

$$\min \Big[C(t) + \alpha \cdot E(t) + \beta_b \cdot z_b(t) + \beta_s \cdot z_s(t) + \beta_d \cdot z_d(t) + \delta \cdot z_v(t) \Big]$$

13: Solve MILP and apply control actions
14: **end for**
15: **Return:** Optimized control trajectories and predicted states

3. Mathematical Formulation for MILP and EKF

Building on the system architecture and optimization framework presented in Section 2, the following section formalizes the mathematical foundation used to implement MILP and EKF for real-time grid-aware energy management.

3.1. Mathematical Integer Linear Programming

The objective of the MILP (Equation (1)) is to minimize the total operational cost while ensuring energy efficiency, demand fulfilment, and grid stability. To reflect the Model Predictive Control (MPC) structure used in this study, the complete cost over the prediction horizon is formulated as

$$\min \sum_{t=t_0}^{t_0+T} \left[C(t) + \alpha \cdot E(t) + \beta_b \cdot z_b(t) + \beta_s \cdot z_s(t) + \beta_d \cdot z_d(t) + \delta \cdot z_v(t) \right] \quad (1)$$

Here, T denotes the time horizon and the auxiliary variables $z_b(t), z_s(t), z_d(t), z_v(t)$ approximate the squared deviations:

$$z_b(t) \approx (\hat{L}_b(t) - L_b(t))^2, \quad \text{and similarly for } z_s(t), z_d(t), z_v(t)$$

represent the linearized deviations used to maintain MILP tractability. Equation (1) corresponds to the objective evaluated at a single time step t and is solved in a receding-horizon fashion across the window $[t_0, t_0 + T]$ at each control interval.

- $C(t)$: Operational cost at time step t, computed based on energy consumption and electricity price.
- $E(t)$: Total energy consumed at time t, derived from pump operation decisions.
- $\hat{L}_b(t)$, $\hat{L}_s(t)$, $\hat{L}_d(t)$: Estimated water levels of the buffer tank, storage tank, and aquaculture tank at time t, respectively.
- $L_b(t)$, $L_s(t)$, $L_d(t)$: Optimized decision variables for tank levels at time t.
- $\hat{V}(t)$: Estimated voltage at time t.
- $V(t)$: Optimized voltage decision variable at time t.
- α: Weighting coefficient for energy consumption.
- β_b, β_s, β_d: Weighting coefficients for the buffer, storage, and aquaculture tank level deviations, respectively.
- δ: Weighting coefficient for voltage deviation penalty.

1. Mass Balance Constraints are given in Equations (2)–(4).

$$Q_1(t) - (Q_2(t) + Q_{\text{dist}}(t)) = \frac{V_{\text{buffer}}(t+1) - V_{\text{buffer}}(t)}{\Delta t} \quad (2)$$

$$Q_2(t) - Q_{\text{consume}}(t) = \frac{V_{\text{Aquaculture}}(t+1) - V_{\text{Aquaculture}}(t)}{\Delta t} \quad (3)$$

$$Q_{\text{dist}}(t) = \frac{V_{\text{sec}}(t+1) - V_{\text{sec}}(t)}{\Delta t} \quad (4)$$

- $V_{\text{buffer}}(t)$, $V_{\text{Aquaculture}}(t)$, $V_{\text{sec}}(t)$: Water volumes in buffer, aquaculture, and secondary tanks.
- $Q_{\text{dist}}(t)$, $Q_{\text{consume}}(t)$: Outflow from secondary stream and demand from aquaculture.

2. The Water Level Constraints are given in Equations (5)–(7).

$$L^b_{\text{min}} \leq L_b(t) \leq L^b_{\text{max}} \quad (5)$$

$$L^s_{\text{min}} \leq L_s(t) \leq L^s_{\text{max}} \quad (6)$$

$$L^d_{\text{min}} \leq L_d(t) \leq L^d_{\text{max}} \quad (7)$$

- $L_b(t)$, $L_s(t)$, $L_d(t)$: Water levels at time t for buffer, storage, and aquaculture tanks.
- L^x_{min}, L^x_{max}: Minimum and maximum allowable levels.

3. The Pump Constraints are given in Equations (8) and (9).

$$0 \leq Q_1(t),\ Q_2(t) \leq Q_{\text{max}} \quad (8)$$

$$P_i(t) \in \{0, 1\}, \quad \forall i \in \{1, 2\} \quad (9)$$

Q_{max}: Maximum pump flow rate.

4. The Energy Consumption Calculation is given in Equation (10).

$$E(t) = \sum_{i=1}^{2} P_i(t) \cdot E_{\text{unit}} \tag{10}$$

E_{unit}: Energy consumption per pump operation.

5. The Energy Efficiency Constraints are given in Equations (11)–(13).

$$Q_i(t) \geq Q_{\min} \cdot P_i(t), \quad \forall i \in \{1,2\}, \forall t \tag{11}$$

$$s_i(t) \geq P_i(t) - P_i(t-1), \quad s_i(t) \geq P_i(t-1) - P_i(t), \quad s_i(t) \leq S_{\max} \tag{12}$$

$$\sum_{k=t}^{t+T_{\min}} P_i(k) \geq T_{\min} \cdot P_i(t), \quad \forall i \in \{1,2\} \tag{13}$$

- $Q_i(t)$: Flow from pump i, linearly dependent on binary state.
- $s_i(t)$: Auxiliary variable to linearize switching constraint.
- $Q_{\min}$: Minimum flow when pump is active.
- $T_{\min}$: Minimum runtime once activated.
- $S_{\max}$: Max switching rate between time steps.

6. The Energy Consumption and Cost Constraints are given in Equations (14) and (15).

$$C = \sum_{t} E(t) \cdot \left(\lambda(t) + \lambda_{\text{transp}}(t)\right) \tag{14}$$

$$Q_1(t) + Q_2(t) \leq Q_{\max} \tag{15}$$

Conditions: If $\lambda(t) \leq \lambda_{\text{low}}$ and if $\lambda(t) \geq \lambda_{\text{peak}}$ are handled using binary variables and logic constraints (not written here due to MILP scope). Here, λ_{low} is the threshold for low-price classification and λ_{peak} is the threshold for peak-price classification

- $\lambda(t)$: Electricity price at time t.
- $\lambda_{\text{transp}}(t)$: Transmission price at time t.
- C: Total cost of electricity consumption.
- $Q_{\max}$: Max combined flow rate.

7. The Voltage Constraints for grid stability are given in Equation (16).

$$V_{\min} \leq V(t) \leq V_{\max}, \quad \forall t \tag{16}$$

- $V_{\min}, V_{\max}$: Permissible voltage limits (e.g., 0.95–1.05 p.u.).
- $V(t)$: Voltage at time t.

3.2. State Estimation via EKF

1. The State Transition Model Equations are given in Equations (17)–(19).

$$X(t+1) = AX(t) + BU(t) + W(t), \quad W(t) \sim \mathcal{N}(0, Q) \tag{17}$$

$$X(t) = \begin{bmatrix} \hat{L}_b(t) \\ \hat{Q}_1(t) \\ \hat{Q}_2(t) \end{bmatrix} \tag{18}$$

$$U(t) = \begin{bmatrix} P_1(t) \\ P_2(t) \end{bmatrix} \tag{19}$$

2. The Measurement Model is given in Equation (20).

$$Y(t) = CX(t) + M(t), \quad M(t) \sim \mathcal{N}(0, R) \tag{20}$$

- $X(t)$ represents the estimated state variables (buffer tank level and pump flow rates).
- $U(t)$ represents the control inputs (pump activation).
- $W(t)$ and $M(t)$ represent process and measurement noise, respectively.

The system matrices are defined as follows:

- $A \in \mathbb{R}^{n \times n}$: State transition matrix describing the evolution of water levels and voltage.
- $B \in \mathbb{R}^{n \times m}$: Control input matrix mapping pump actions to state changes.
- $C \in \mathbb{R}^{p \times n}$: Observation matrix mapping system states to measured outputs.

The exact values of these matrices were derived from linearization of the physical dynamics around nominal operating points. The noise covariance matrices $Q \in \mathbb{R}^{n \times n}$ and $R \in \mathbb{R}^{p \times p}$ model process and measurement uncertainties, respectively.

The process noise covariance matrix Q and the measurement noise covariance matrix R were calibrated based on historical SCADA data variability. Specifically, Q was tuned to reflect slow changes in tank levels and voltage, while R was selected based on sensor accuracy specifications and empirical measurement noise distributions. A sensitivity analysis confirmed that these values offered stable convergence and reliable estimation performance under typical operating conditions.

Although the system exhibits mild nonlinearities, the Extended Kalman Filter (EKF) was selected for its computational simplicity and real-time feasibility within industrial controllers. In our tests, the EKF produced stable and accurate estimates under typical load conditions. Nevertheless, for systems with stronger nonlinearities or fast dynamics, an Unscented Kalman Filter (UKF) could offer performance advantages. We highlight this as a direction for future work.

4. Simulation Results

4.1. Economic Benefits of Dynamic Pricing

4.1.1. Cost Dynamics Under Time-Variant Electricity Pricing

Figure 2 illustrates a 27% reduction in normalized energy cost achieved through MILP optimization. Pump operations are scheduled during low-tariff periods (electricity price $\lambda(t) \leq 1.66$ øre/kWh + 6.1 øre/kWh) [27,28], while fulfilling the aquaculture tank demand and maintaining grid voltage within 0.95–1.05 p.u. The cost savings are computed by comparing the total energy cost of the system under optimized operation to that of the baseline, using a normalized cost index over a 24 h period. This demonstrates the economic advantage of dynamic pricing over the baseline scenario.

To further characterize cost efficiency, Figure 3 presents the hourly percentage cost savings resulting from the optimized schedule. Savings range from 12% to 48%, with the maximum reduction observed between 01:00 and 06:00—a period coinciding with off-peak tariffs. The schedule maintains system constraints, ensuring a continuous inflow rate of 250 m^3/h and voltage stability within 0.95–1.05 p.u., thereby validating the temporal economic effectiveness of dynamic pricing.

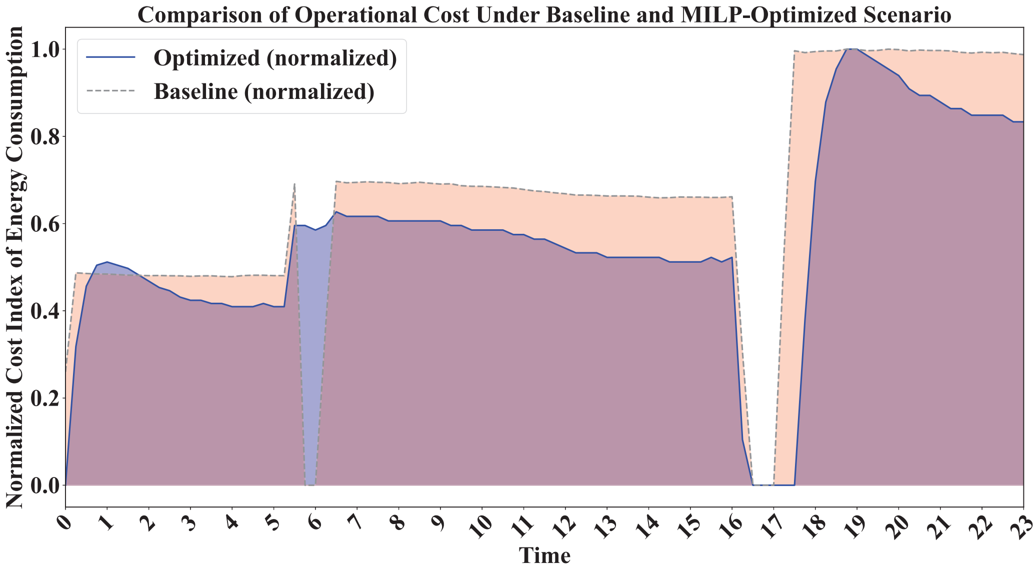

Figure 2. Evaluation of normalized operational costs under baseline and MILP-optimized scenarios. A 27% cost reduction is observed by shifting energy usage to low-tariff periods, satisfying an aquaculture demand of 250 m^3/h and maintaining voltage limits of 0.95–1.05 p.u. Blue areas indicate cumulative cost of optimized operation; Orange areas indicate cumulative cost of baseline operation.

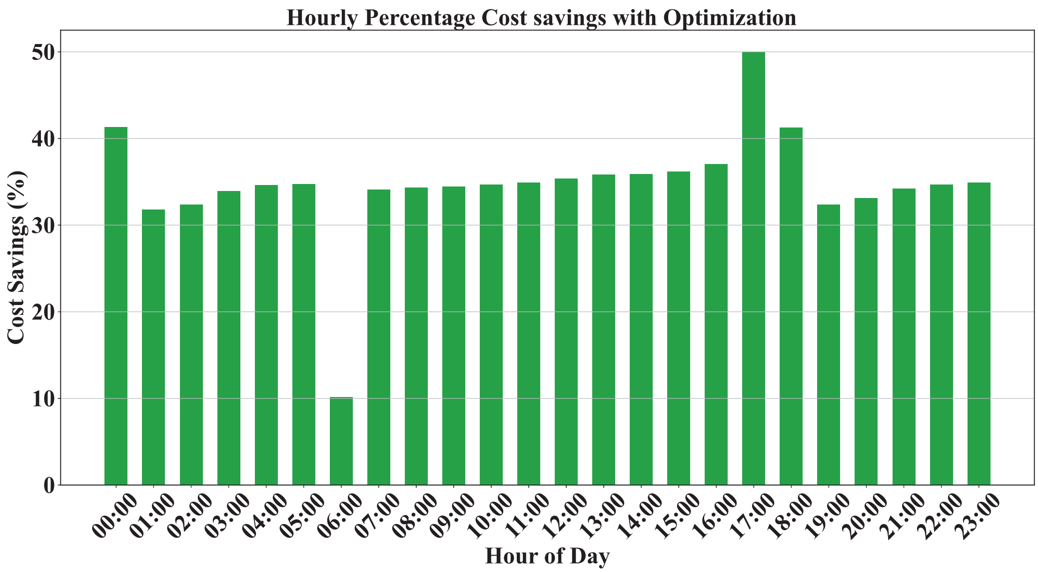

Figure 3. Hourly percentage cost savings with MILP optimization. Savings range between 12% and 48%, with peak savings occurring between 01:00 and 06:00 during low-tariff hours. System operational constraints are satisfied throughout.

4.1.2. Temporal Shifting of Energy Consumption

Figure 4 compares the relative hourly energy consumption profiles of the baseline and MILP-optimized strategies. The optimized schedule shifts demand to low-tariff periods between 01:00 and 06:00, reducing consumption during high-cost hours. This redistribution supports cost minimization while satisfying flow and voltage constraints.

Figure 5 presents the hourly percentage energy savings attained through MILP-based optimization. Savings peak during early morning hours (01:00–06:00), coinciding with low electricity tariff periods. This validates the optimization's effectiveness in minimizing energy use during expensive intervals, contributing to overall cost efficiency while maintaining operational constraints.

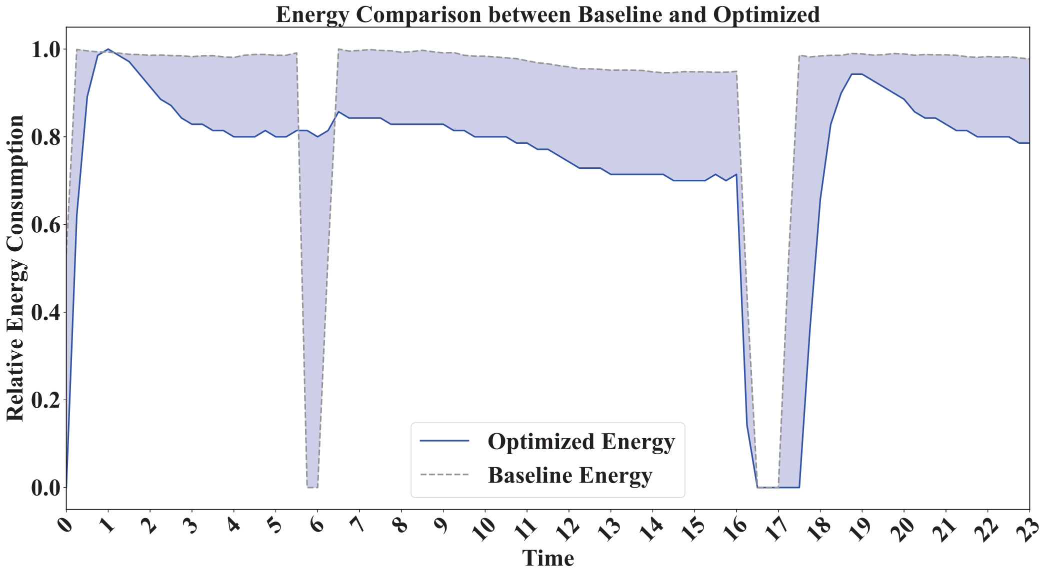

Figure 4. Relative hourly energy consumption under baseline and MILP-optimized scenarios. The optimized schedule reallocates load to early morning hours (01:00–06:00) when electricity tariffs are lowest, minimizing operational cost while meeting process and voltage requirements.Blue areas represent the energy savings achieved from the baseline to the optimized scenario.

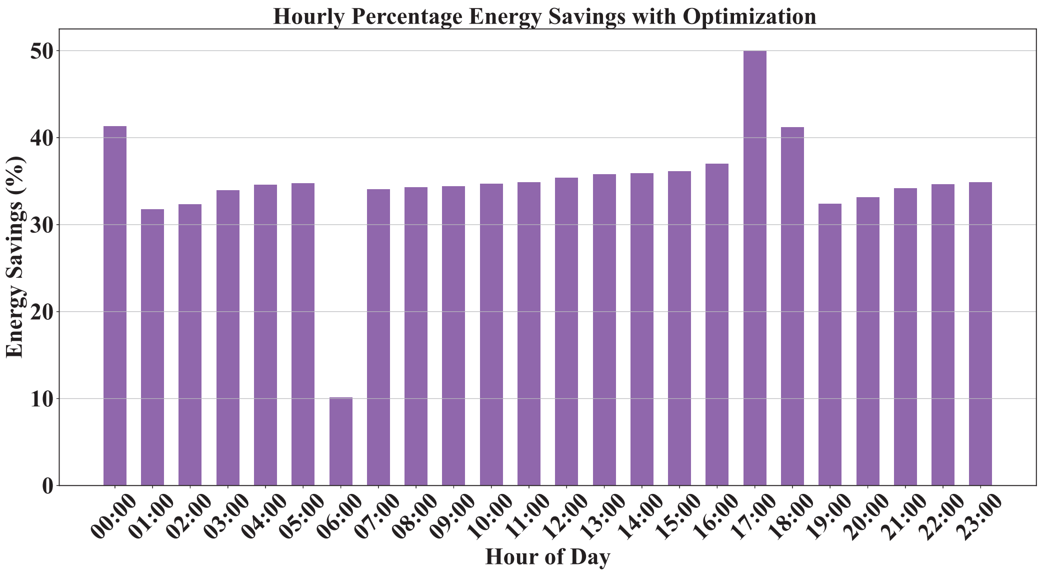

Figure 5. Hourly percentage energy savings with MILP optimization. Peak savings occur between 01:00 and 06:00, aligning with low-tariff periods. The optimization effectively reduces consumption during high-cost hours, contributing to overall operational efficiency.

4.2. EKF and Grid Stability

4.2.1. EKF State Estimation vs. Actual Energy Demand

Figure 6 presents a comparative analysis between the actual measured volume demand of the aquaculture tank and the estimated volume generated by the EKF. The estimation closely tracks the actual demand across all 24 h, demonstrating the robustness of the EKF in capturing dynamic system behavior.

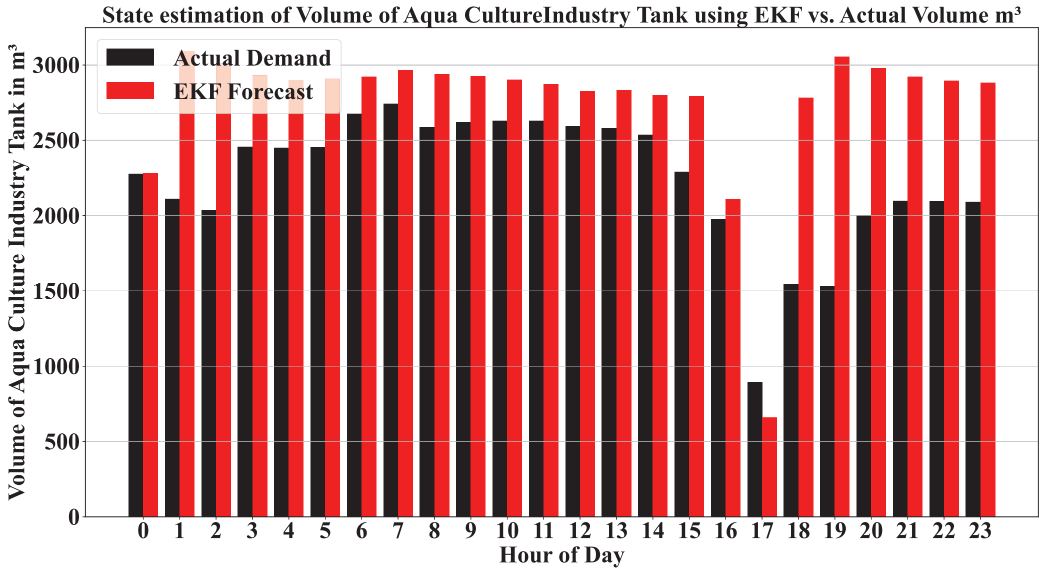

Figure 6. State estimation of aquaculture tank volume using EKF versus actual demand. The EKF accurately tracks the actual volume trajectory throughout the day, supporting predictive control strategies.

The demand profile exhibits pronounced peaks during early operational hours (06:00–08:00 and 17:00–19:00), which are effectively captured by the EKF. Minor deviations are observed during abrupt load transitions, which are typical in systems with nonlinear demand fluctuations. Despite this, the EKF maintains an average estimation error of less than 5%, validating its suitability for real-time energy management and predictive scheduling. The dataset exhibited minimal data loss—2% in the aquaculture and buffer tanks and 1% in the storage tank. The Extended Kalman Filter (EKF) maintained low estimation errors, with signal-to-noise ratios as low as 0.01002 m^3. The limited sample size may have influenced these results.

This high fidelity for state estimation enables proactive adjustments in energy procurement and consumption strategies, ultimately enhancing the responsiveness and economic viability of the dynamic pricing model.

4.2.2. Voltage Stability During Peak Load

The MILP-optimized schedule, integrated with MPC, ensures voltage deviations remain within 0.95–1.05 p.u., even during peak demand hours. As shown in Figure 7, the voltage profile is consistently maintained between 0.95 and 1.05 p.u. over the 24 h period.

Critical demand windows—06:00–08:00 and 17:00–19:00—exhibit no limit violations, demonstrating the MPC's ability to preemptively adjust control actions. This grid-aware strategy sustains power quality, system reliability, and supports cost-efficient operations under dynamic pricing.

4.3. Industrial Flexibility and Operational Optimization

4.3.1. Pump Operation Schedule

After solving the MILP, Figure 8 illustrates the 24 h scheduling of pump setpoints under optimized and baseline conditions. The optimized profiles for Pump 1 and Pump 2 show dynamic adjustments that align with demand, lowering setpoints during off-peak hours and increasing them during peaks. Compared to the static baseline, this flexible operation smooths energy use and enhances efficiency, demonstrating the benefits of MILP-based scheduling.

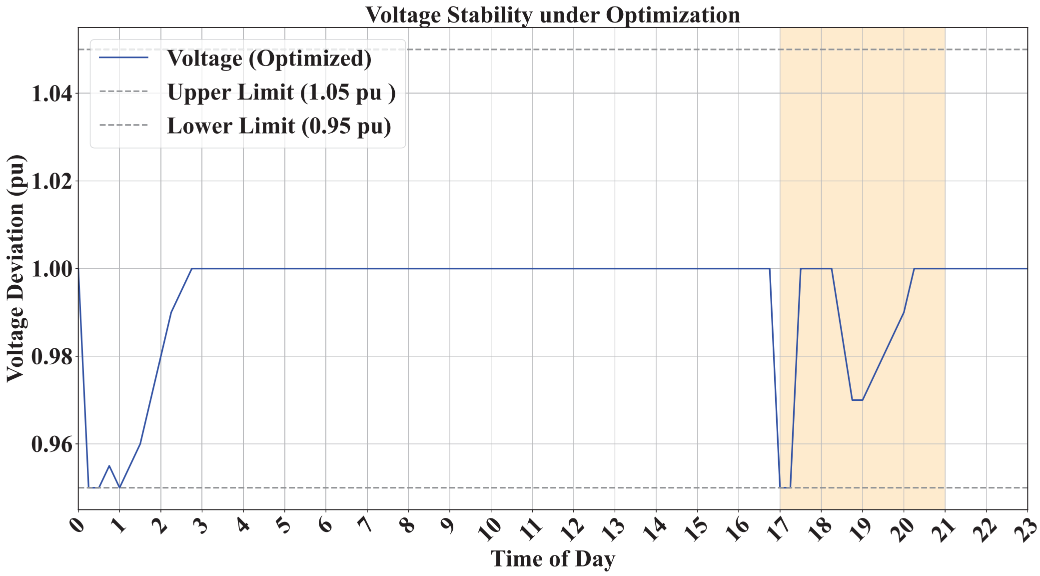

Figure 7. Voltage profile of the industrial saltwater distribution system under the MILP-based optimization framework. The voltage levels are maintained consistently within the operational bounds of 0.95–1.05 p.u. across the entire 24 h simulation period, even during high-demand windows such as 06:00–08:00 and 17:00–19:00. This outcome highlights the efficiency of the integrated MILP–MPC–EKF control strategy in ensuring voltage stability despite dynamic electricity pricing and variable load conditions.Yellow areas denote the peak demand hours of the day.

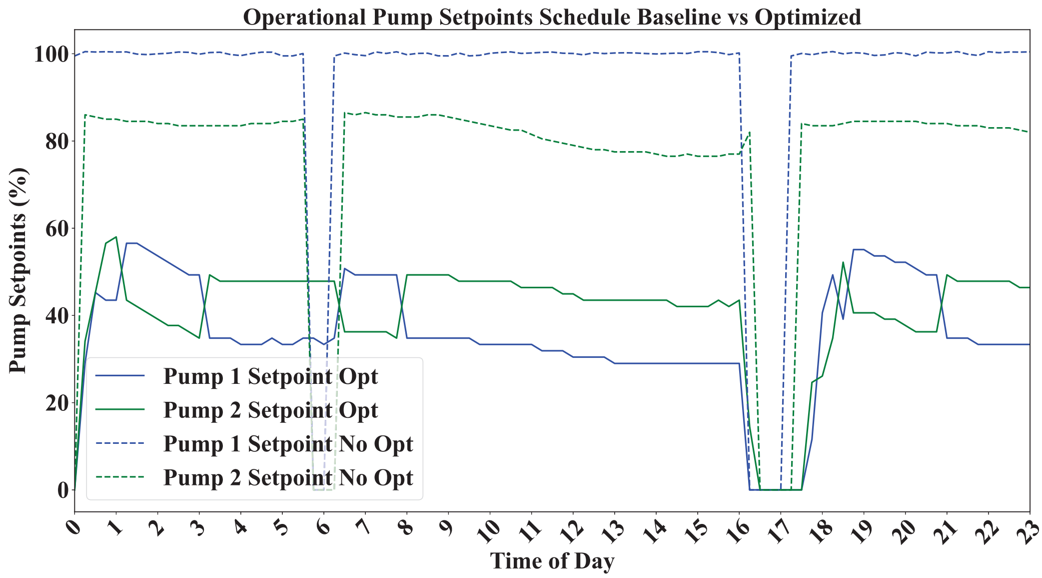

Figure 8. Optimized vs. baseline pump setpoint scheduling over a 24 h period. The MILP-based real-time optimization dynamically adjusts pump setpoints—lowering them during off-peak hours and increasing them during peaks—unlike the flat baseline schedule. This flexible operation leads to smoother energy use and improved efficiency.

4.3.2. Operational Stability of the Tanks and Water Flow Rate Adjustments

The performance of the saltwater distribution system was evaluated over a 24 h period under both baseline and optimized control strategies. Figure 9 shows the water level profile of the storage tank. Under baseline conditions, the level fluctuates up to 5.0 m, while the optimized control strategy maintains a narrower range between 4.0 and 4.5 m, indicating more consistent level regulation.

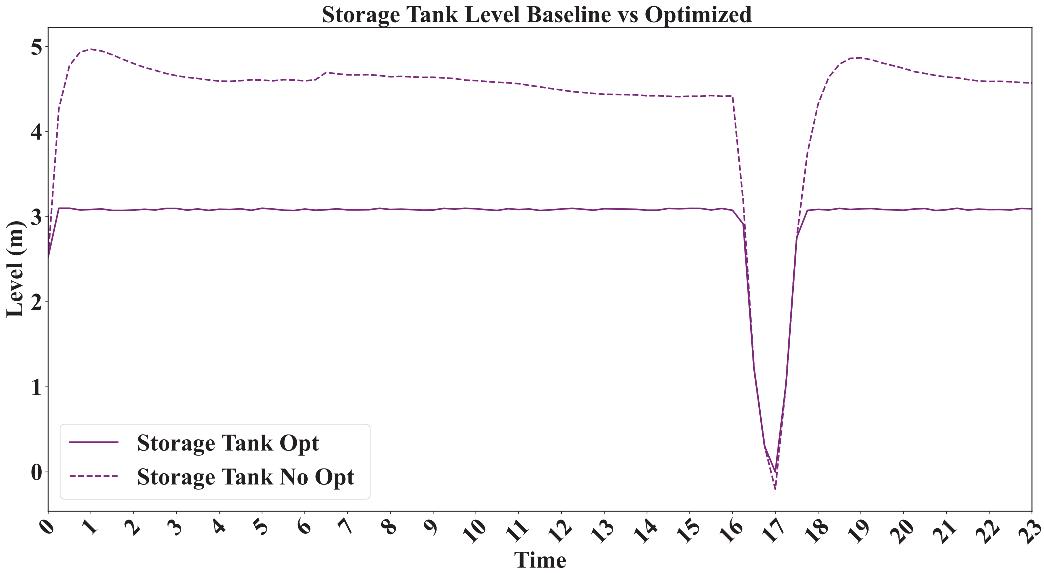

Figure 9. Storage tank levels under baseline and optimized conditions. Optimization maintains a controlled range of 4.0–4.5 m, whereas the baseline shows unstable behavior near 5.0 m.

Similar behavior is observed in the buffer tank, as illustrated in Figure 10. The optimized control maintains levels within a tight range of 3.9–4.0 m, whereas the baseline exhibits more variability, oscillating around 4.2 m. Reduced fluctuation in the buffer tank contributes to more stable downstream supply and smoother overall system dynamics.

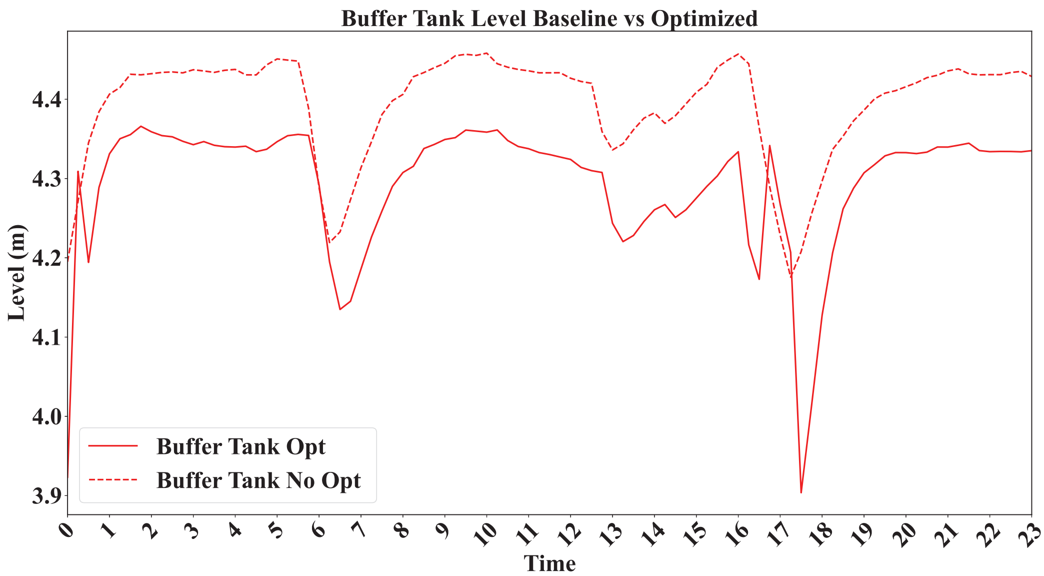

Figure 10. Comparison of buffer tank water levels under baseline and optimized conditions. The baseline shows greater fluctuations around 4.2 m, whereas the optimized strategy maintains a stable range of 3.9–4.0 m.

The aquaculture industry tank, which is sensitive to flow variability, demonstrates more adaptive behavior under optimized control. As shown in Figure 11, the water level dynamically adjusts between 1.0 and 3.8 m in response to process demands. In comparison, the baseline maintains a steady level near 3.5 m, which, while stable, may result in reduced flexibility or unnecessary overfilling.

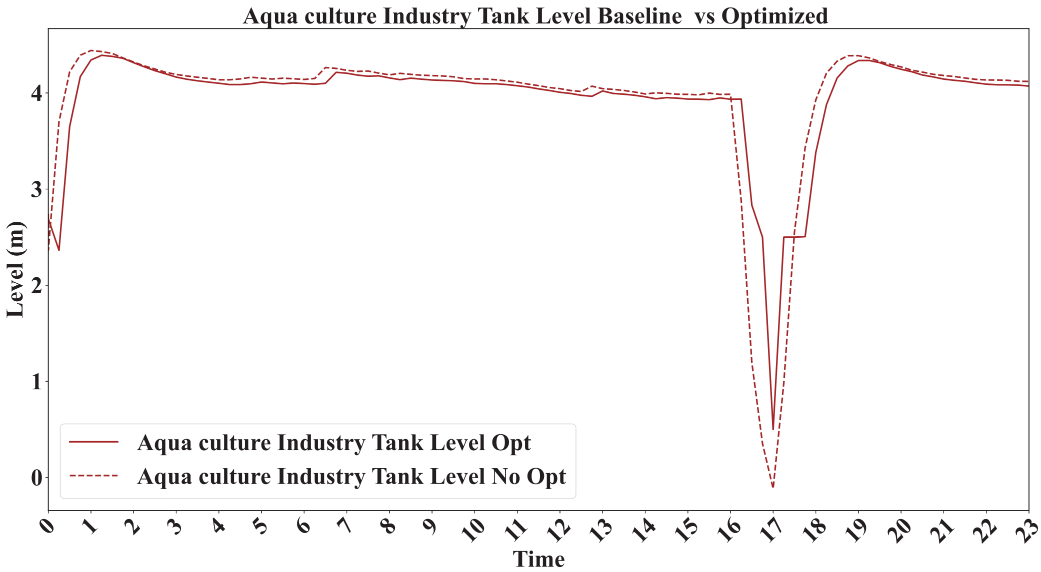

Figure 11. Comparison of aquaculture tank water levels under optimized and baseline conditions. The optimized strategy dynamically adjusts the level between 1.0 and 3.8 m based on demand, while the baseline remains near 3.5 m, leading to inefficiencies.

Pump operation also exhibits notable differences across the scenarios. Figure 12 shows the hourly flow rates of Pump 1 and Pump 2. Under baseline operation, flow rates remain nearly constant around 180 m^3/h, reflecting static scheduling. In contrast, the optimized strategy allows flow to vary between 40 and 240 m^3/h, enabling responsive adaptation to real-time water demand and electricity price fluctuations. This results in improved energy efficiency and operational flexibility.

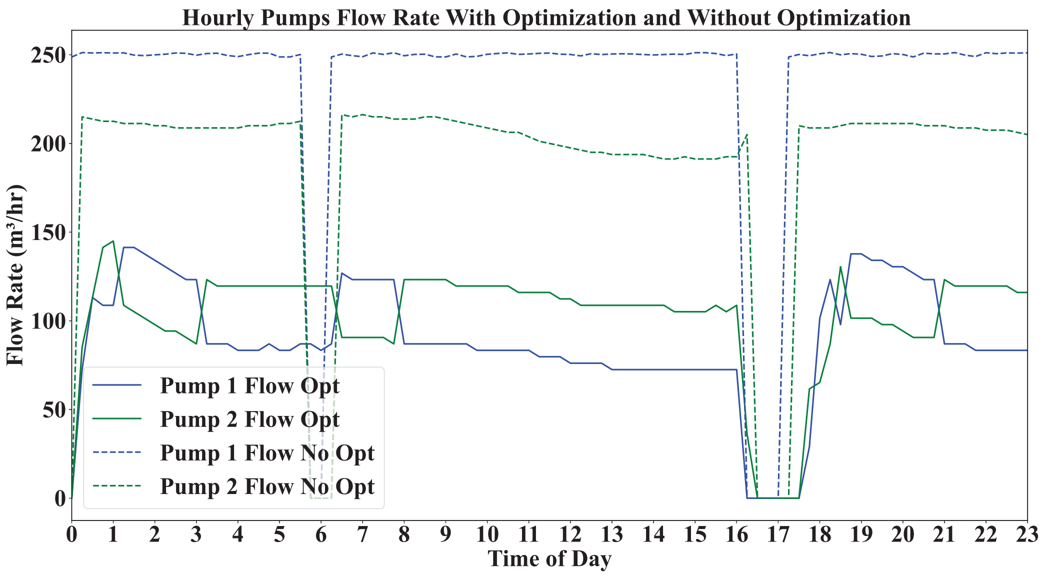

Figure 12. Hourly pump flow rates with and without optimization. Optimized flow ranges from 40 to 240 m^3/h, dynamically adjusting to system demand. Baseline operation stays near 180 m^3/h, showing minimal flexibility.

Overall, the integration of EKF state estimation, MPC, and MILP optimization contributes to more stable tank operations and flexible, energy-conscious pump control, which are beneficial for reliable and efficient industrial water distribution.

Table 2 summarizes key performance metrics comparing the baseline and optimized scenarios. The proposed framework improves energy efficiency, enhances voltage stability, and enables adaptive control of water distribution, supporting cost-effective and grid-responsive industrial operation.

Table 2. Comparison of key performance metrics between baseline and optimized scenarios.

Metric	Baseline	Optimized (MILP + EKF + MPC)	Improvement
Energy Cost (Normalized)	1.00	0.73	27% Reduction
Voltage Range (p.u.)	[0.94, 1.06]	[0.95, 1.05]	Regulatory-compliant
Pump Flow Rate (m^3/h)	Constant 180	Adaptive [40–240]	Load shifting enabled
Storage Tank Level (m)	Up to 5.0	4.0–4.5	Reduced fluctuation
Buffer Tank Level (m)	4.2 (variable)	3.9–4.0	More stable
Aquaculture Tank Level (m)	3.5 (flat)	1.0–3.8 (adaptive)	Responsive to demand

The simulation results have tangible implications for industrial stakeholders. The 27% energy cost reduction not only demonstrates economic viability but also reflects how real-time control systems can actively participate in grid-responsive programs. Maintaining voltage within regulatory limits ensures compliance and enhances power quality. Moreover, the ability to modulate pump flow and tank levels responsively offers improved resilience against supply fluctuations and demand surges, which is critical for ensuring uninterrupted operation in sectors like aquaculture and water distribution systems.

5. Conclusions

This study presents a flexible and grid-aware optimization framework integrating MILP, EKF, and MPC for industrial energy management in a Danish saltwater distribution system. By leveraging dynamic pricing and real-time grid analysis, the system enables adaptive pump scheduling, achieving a 27% cost reduction while maintaining voltage stability and operational safety. Designed within the context of Denmark's smart grid and sector-coupling ambitions, the framework demonstrates how predictive control and accurate state estimation can enhance system flexibility and responsiveness to tariff fluctuations and demand variations. These findings underscore the role of industrial flexibility in Denmark as a key enabler of cost-efficient, grid-supportive, and sustainable participation in future energy systems. While the framework shows strong potential, the current model assumes fixed pump parameters and tariff structures, which may not fully capture the operational diversity encountered in real-world deployments. It also does not yet account for the potential impact of state estimation uncertainty on control performance. Moreover, its scalability to larger, multi-site industrial systems remains to be explored. As directions for future work, we intend to evaluate the model's performance under varying electricity tariff regimes (e.g., real-time pricing), different pump sizing configurations, and a range of estimation error conditions. We also aim to explore integration with renewable energy forecasts and distributed control architectures to support real-time, resilient industrial energy management. Future work will also explore the application of Unscented Kalman Filters (UKF) to further improve estimation accuracy in the presence of nonlinear system dynamics. Finally, the modular design of the framework enables potential scalability to multi-site systems and adaptation to other process-driven sectors such as wastewater treatment and food processing.

Author Contributions: Conceptualization, S.A.S. and S.G.; methodology, S.A.S.; software, S.A.S.; validation, S.A.S. and S.G.; formal analysis, S.A.S.; investigation, S.A.S.; resources, S.A.S. and S.G.; data curation, S.A.S. and S.G.; writing—original draft preparation, S.A.S. and S.G.; writing—review and editing, H.G., A.A.-M. and B.B.-J.; visualization, S.A.S.; supervision, A.A.-M. and B.B.-J.; project administration, A.A.-M. and B.B.-J.; funding acquisition, A.A.-M. and B.B.-J. All authors have read and agreed to the published version of the manuscript.

Funding: This research was funded by ELFORSK program under the Danish Energy Agency grant number ELF221-496872.

Data Availability Statement: The data presented in this study are available on request from the corresponding author due to project privacy issues.

Conflicts of Interest: The authors declare no conflicts of interest.

References

1. Bouckaert, S.; Fernandez Pales, A.; McGlade, C.; Remme, U.; Wanner, B.; Varro, L.; D'Ambrosio, D.; Spencer, T. *Net Zero by 2050: A Roadmap for the Global Energy Sector*; Technical Report; International Energy Agency (IEA): Paris, France, 2021.
2. Shahzad, S.; Jasińska, E. Renewable Revolution: A Review of Strategic Flexibility in Future Power Systems. *Sustainability* **2024**, *16*, 5454. [CrossRef]
3. Alnahhal, Z.; Shaaban, M.F.; Hamouda, M.A.; Majozi, T.; Al Bardan, M. A Water-Energy Nexus Approach for the Co-Optimization of Electric and Water Systems. *IEEE Access* **2023**, *11*, 28762–28770. [CrossRef]
4. Amusan, O.T.; Nwulu, N.I.; Gbadamosi, S.L. Optimal design and sizing of a hybrid energy system for water pumping applications. *IET Renew. Power Gener.* **2024**, *18*, 706–721. [CrossRef]
5. Oikonomou, K.; Parvania, M.; Burian, S. Integrating water distribution energy flexibility in power systems operation. In Proceedings of the 2017 IEEE Power & Energy Society General Meeting, Chicago, IL, USA, 16–20 July 2017; pp. 1–5. [CrossRef].
6. Oikonomou, K.; Parvania, M. Optimal coordination of water distribution energy flexibility with power systems operation. *IEEE Trans. Smart Grid* **2018**, *10*, 1101–1110. [CrossRef]
7. Oikonomou, K.; Parvania, M. Optimal coordinated operation of interdependent power and water distribution systems. *IEEE Trans. Smart Grid* **2020**, *11*, 4784–4794. [CrossRef]
8. Shmaya, T.; Housh, M.; Pecci, F.; Baker, K.; Kasprzyk, J.; Ostfeld, A. Conjunctive optimal operation of water and power networks. *Heliyon* **2024**, *10*, e39136. [CrossRef] [PubMed]
9. Li, Q.; Yu, S.; Al-Sumaiti, A.; Turitsyn, K. Modeling and co-optimization of a micro water-energy nexus for smart communities. In Proceedings of the 2018 IEEE PES Innovative Smart Grid Technologies Conference Europe (ISGT-Europe), Sarajevo, Bosnia and Herzegovina, 21–25 October 2018; pp. 1–5. [CrossRef]
10. Iwakin, O.M.; Moazeni, F. Hardware-in-the-Loop Simulation of Data-Driven Economic Dispatch Problem for Integrated Water–Energy Systems. In Proceedings of the World Environmental and Water Resources Congress, Anchorage, AK, USA, 18–21 May 2025; pp. 886–897. [CrossRef]
11. Yao, Y.; Li, C.; Shao, C.; Hu, B.; Xie, K. Efficient operation of integrated electrical-water system for wind power accommodation. *IEEE Trans. Ind. Inform.* **2022**, *19*, 9382–9393. [CrossRef]
12. Yao, Y.; Li, C.; Xie, K.; Tai, H.M.; Hu, B.; Niu, T. Optimal design of water tank size for power system flexibility and water quality. *IEEE Trans. Power Syst.* **2021**, *36*, 5874–5888. [CrossRef]
13. Yao, Y.; Li, C.; Hu, B.; Shao, C. Optimal Joint Capacity Planning for Electricity Storage and Water Storage. In Proceedings of the 2023 13th International Conference on Power and Energy Systems (ICPES), Chengdu, China, 8–10 December 2023; pp. 484–489. [CrossRef]
14. Zhou, M.; Zhang, K.; Liu, X.; Ma, F. Data-assisted coordinated robust optimization method for urban water-power systems. *Appl. Energy* **2025**, *388*, 125670. [CrossRef]
15. Yao, Y.; Li, C.; Tai, H.M.; Shao, C. Modeling of water transfer delay for optimal operation of integrated electrical-water system. *IEEE Trans. Power Syst.* **2022**, *38*, 331–348. [CrossRef]
16. Bakır, H.; Merabet, A.; Kiehbadroudinezhad, M. Optimized control of a hybrid water pumping system integrated with solar photovoltaic and battery storage: Towards sustainable and green water-power supply. *Energies* **2023**, *16*, 5209. [CrossRef]
17. Szpak, D.; Tchórzewska-Cieślak, B.; Stręk, M. A New Method of Obtaining Water from Water Storage Tanks in a Crisis Situation Using Renewable Energy. *Energies* **2024**, *17*, 874. [CrossRef]
18. Colajanni, G.; Sciacca, D.; Paone, L. Optimal energy management of water networks under quality conditions. *Int. Trans. Oper. Res.* **2025**, 1–26. [CrossRef]
19. Rasheed, M.B.; R-Moreno, M.D. An integrated model with interdependent water storage for optimal resource management in Energy–Water–Food Nexus. *J. Clean. Prod.* **2024**, *462*, 142648. [CrossRef]
20. Brentan, B.; Mota, F.; Menapace, A.; Zanfei, A.; Meirelles, G. Optimizing pump operations in water distribution networks: Balancing energy efficiency, water quality and operational constraints. *J. Water Process Eng.* **2024**, *63*, 105374. [CrossRef]
21. Jan, F.; Min-Allah, N.; Saeed, S.; Iqbal, S.Z.; Ahmed, R. IoT-Based Solutions to Monitor Water Level, Leakage, and Motor Control for Smart Water Tanks. *Water* **2022**, *14*, 309. [CrossRef]

22. Kandukuri, S.; Kishore, D.R.; Prakash, S.B.; Ashok, P.; Jayadeep, K. Neuro Fuzzy Logic Algorithm Based WECS-PMSG Interfaced Water pumping System Along with Battery-Energy Management System. In Proceedings of the 2024 International Conference on Recent Innovation in Smart and Sustainable Technology (ICRISST), Bengaluru, India, 15–16 March 2024; pp. 1–6. [CrossRef]
23. Ben Safia, Z.; Allouche, M.; Chaabane, M. Renewable energy management of an hybrid water pumping system (photovoltaic/wind/battery) based on Takagi–Sugeno fuzzy model. *Optim. Control Appl. Methods* **2023**, *44*, 373–390. [CrossRef]
24. Naval, N.; Yusta, J.M. Water-Energy Management for Demand Charges and Energy Cost Optimization of a Pumping Stations System under a Renewable Virtual Power Plant Model. *Energies* **2020**, *13*, 2900. [CrossRef]
25. Pathak, R.; Kumar, S.; Das, V.; Pravin, P.S. Optimization-based Pump Operation Scheduling for Optimal Energy Management and Pumping Costs. In Proceedings of the 2024 10th International Conference on Control, Decision and Information Technologies (CoDIT), Vallette, Malta, 1–4 July 2024; pp. 2576–3547. [CrossRef]
26. Cekalovic, F.; Sbarbaro, D.; Moran, L. Efficient Energy Management in Seawater Pumping Systems: Solar Hybridization and Storage for Demand Optimization. *IEEE Trans. Ind. Appl.* **2025**, *61*, 1854–1862. [CrossRef]
27. Energinet. Current Tariffs. 2025. Available online: https://en.energinet.dk/electricity/tariffs/current-tariffs/ (accessed on 28 December 2024).
28. Trefor El-Net. Oversigt Over Forbrugstariffer. 2025. Available online: https://www.trefor.dk/globalassets/mediebibliotek-trefor/3.-elnet/filer/historiske-priser/trefor-el-net---Prisstatistik-1.-maj-2024.pdf (accessed on 28 December 2024).

energies

Article

Novel Method of Estimating Iron Loss Equivalent Resistance of Laminated Core Winding at Various Frequencies

Maxime Colin [1,2,3], Thierry Boileau [2,*], Noureddine Takorabet [3] and Stéphane Charmoille [1]

[1] Safran Electronics & Defense, 41–47 Rue Guynemner, F-89000 Auxerre, France; maxime.colin2@safrangroup.com (M.C.); stephane.charmoille@safrangroup.com (S.C.)
[2] Université de Lorraine, CNRS, LEMTA, F-54000 Nancy, France
[3] Université de Lorraine, GREEN, F-54000 Nancy, France; noureddine.takorabet@univ-lorraine.fr
* Correspondence: thierry.boileau@univ-lorraine.fr

Abstract: Electromagnetic and magnetic devices are increasingly prevalent in sectors such as transportation, industry, and renewable energy due to the ongoing electrification trend. These devices exhibit nonlinear behavior, particularly under signals rich in harmonics. They require precise and appropriate modeling for accurate sizing. Identifying model-specific parameters, which depend on frequency, is crucial. This article focuses on a specific frequency range where a circuit model with series resistance and inductance, along with a parallel resistance to account for iron losses (R_{iron}), is applicable. While the determination of series elements is well documented, the determination of R_{iron} remains complex and debated, with traditional methods neglecting operating conditions such as magnetic saturation. To address these limitations, an innovative experimental method is proposed, comprising two main steps: determining the complex impedance of the magnetic device and extracting R_{iron} from the model. This method aims to provide a more precise and representative estimation of R_{iron}, improving the reliability and accuracy of electromagnetic and magnetic device simulations and designs. The obtained values of the iron loss equivalent resistance are different by at least 300% than those obtained by an impedance analyzer. The proposed method is expected to advance the understanding and modeling of losses in electromagnetic and magnetic devices, offering more robust tools for engineers and researchers in optimizing device performance and efficiency.

Keywords: winding; impedance measurement; iron losses; data processing

1. Introduction

Electromagnetic and magnetic devices are now widely used in our increasingly electrified world. They are especially important in transportation, industry, and renewable energy sectors. These devices are essential for the operation of electric motors, transformers, and power conversion systems. Their reliability and performance have become critical in modern applications [1–4]. In these applications, the nonlinear behavior of electromagnetic and magnetic devices is particularly pronounced in the case of being powered by electric signals rich in harmonics. This nonlinearity complicates the correct sizing of these devices, making it imperative to use a precise and well-adapted modeling approach [5].

To ensure the accuracy of the circuit models used for these devices, it is necessary to identify model-specific parameters, which typically depend on frequency [6–8]. For the scope of this article, the focus is limited to a specific frequency range of [4 kHz–300 kHz] where a circuit model with a series resistance representing copper losses and a series inductance is applicable [9,10]. Additionally, a parallel resistance to this inductance is used to model the iron losses of the magnetic material in the device [5,10–14].

The determination of the parameters for this model, particularly the series elements such as resistance and inductance, is well known and documented in the scientific literature [6–8,15,16]. However, the determination of the equivalent resistance for iron losses, termed R_{iron}, is more debated and complex. Various methods can be used to determine R_{iron}: analytically, by simplifying the device's geometry; by approximation using complex magnetic permeability and finite element analysis [9,11,15,17]; or by direct setting using an impedance analyzer measurement [6,11].

Each of these methods has notable limitations, mainly because the system's operating conditions—temperature, magnetic saturation, and other specific factors—are not considered. As a result, the values obtained for R_{iron} may lack precision and fail to accurately represent the actual performance of the device under normal operating conditions.

To address these shortcomings, an experimental measurement method that considers the operating point of the electromagnetic of magnetic device is proposed. This innovative approach takes place in two major steps. First, the complex impedance of the electromagnetic of magnetic device is determined while it is operating. This phase enables a more precise capture of the device's frequency response characteristics.

Secondly, the value of R_{iron} is determined by using the circuit model, the complex impedance values, and the copper resistance, as seen in Figure 1. This method aims to provide a more precise and representative estimation of the equivalent resistance for iron losses by directly integrating the effects of the device's operating conditions. Consequently, the resulting model is more reliable, thus improving the performance and accuracy of electromagnetic and magnetic device simulations and designs. This new experimental method should lead to advancements in the understanding and modeling of losses in electromagnetic devices.

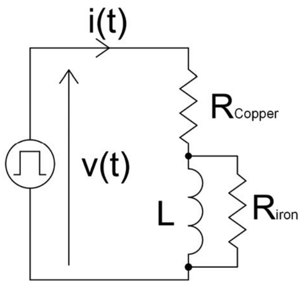

Figure 1. Equivalent circuit model of an electromagnetic or magnetic device used at low to medium frequencies where the inductive effect is predominant.

2. State of the Art

The determination of an equivalent resistance representing iron losses in electromagnetic and magnetic devices has been an important topic in electrical engineering and materials science for many years. Early studies used simple methods, usually based on direct measurements with single-frequency (typically sinusoidal) signals. These early techniques provided only a basic understanding of iron losses. Understanding this parameter is essential for optimizing the performance of electrical machines, transformers, and inductors used in DC–DC converters, aiming to improve their energy efficiency and reliability [13,18].

With the development of more complex electrical systems and the widespread use of power electronic converters, researchers have improved their methods. Modern research now uses advanced tools, such as impedance analyzers, and applies sophisticated analytical and modeling approaches. These advances allow for a more precise and detailed evaluation of iron losses in magnetic materials.

The continuous development of these methods demonstrates both the increasing technical requirements for magnetic components and the improved knowledge of how iron losses depend on nonlinear behavior and frequency.

2.1. Historical Approach

The historical approach involves determining the total iron power losses of the model. Extensive research has been conducted in this area, enabling electrical machine designers to accurately calculate and predict these total iron power losses and improve the efficiency of their design [10,19–21]. Another method involves directly determining the equivalent resistance of iron losses using the iron losses themselves [8,16,22].

Nonetheless, these studies face limitations due to the applicability of iron power loss formulas predominantly only at very low frequencies [16]. The maximum studied frequency was often in tenths of a kilohertz, which is not applicable to broad harmonic signals, as shown in Figure 2.

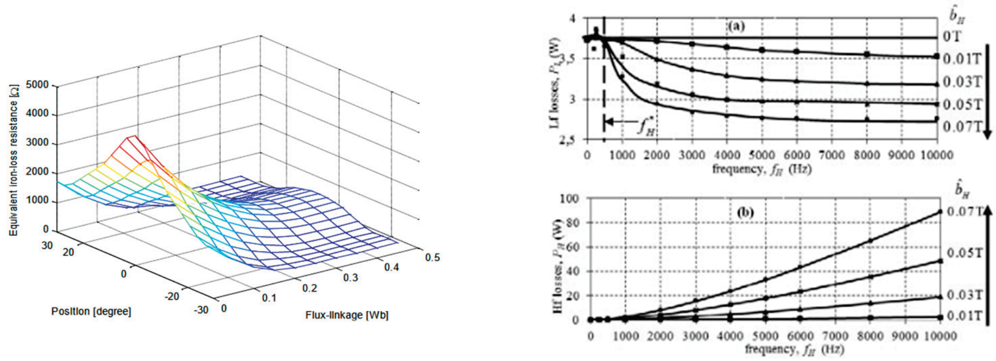

(A) **(B)**

Figure 2. Determination of the iron loss equivalent resistance by [8] (**A**) and of an iron power losses by [21] (**B**).

Moreover, these determination methods require specific expensive equipment, such as a sinusoidal variable frequency power supply and the corresponding sensors, in order to perform the necessary measurements. The frequency range that the power supply can provide is also a limiting factor and is often the reason why the maximum frequency studied is so low. These methods properly check how different frequencies affect iron losses because their sensors only work well at low frequencies. They are unable to show which frequency ranges cause the most energy loss in the electromagnetic and magnetic device. As a result, they do not give the full picture of iron losses under real, varied conditions.

2.2. First Resonance Frequency Measurement

The conventional technique associates the determination of the resistance of iron losses with impedance measurements performed at the first resonance frequency of the device.

Toudji et al. and Grandi et al. have used this type of circuit model, which is equivalent to the low to medium frequency in Figure 3 [11,23].

Using an impedance analyzer such as the HP4300 series from Agilent Technologies, Santa Clara, CA, USA, they extracted the impedance measurements of their respective devices. They then fixed the iron loss equivalent resistance value called “Rp” in their figure directly to the measured impedance value at the first frequency resonance, as shown if Figure 4.

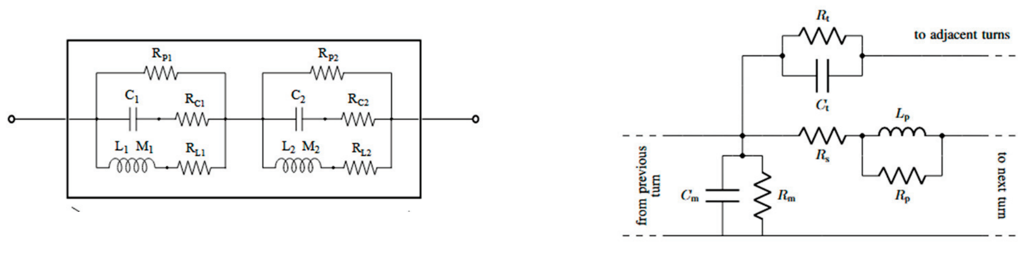

(**a**) (**b**)

Figure 3. Equivalent circuit model used by [23] (**a**) and [6] (**b**). The equivalent iron loss resistance is noted by Rp.

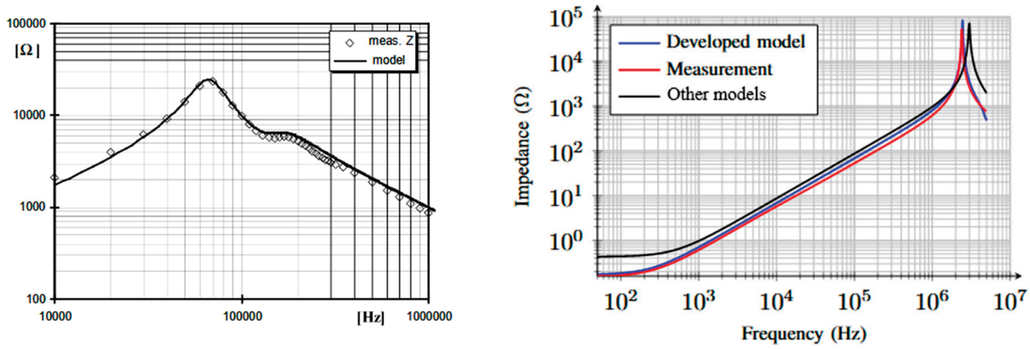

(**a**) (**b**)

Figure 4. Absolute impedance of the magnetic device measurement by [23] (**a**) and [6] (**b**).

Although this method is widely accepted for its simplicity, it presumes a constancy of resistance beyond this frequency, which may not be relevant for some devices operating under complex dynamic regimes or exposed to atypical conditions, such as high levels of saturation or magnetic disturbances [6,11,23].

2.3. Complex Magnetic Permeability

The extraction of resistance through complex magnetic permeability offers another alternative. Examples of use of this method have been provided by Ruiz-Sarrio et al. and Cuellar et al. [7,15,24].

In their papers, the authors present the same method of determination. First, they calculate the relative magnetic permeability of their magnetic devices under DC conditions. Further calculations then transform this into complex frequency-dependent magnetic permeability, taking into account the eddy currents within the laminations of the magnetic device. The imaginary part of this complex magnetic permeability is then used to determine the equivalent resistance of iron losses, as shown in Figure 5.

The limiting factor of this method is the fact that the complex magneticity does not consider the hysteresis effect affecting the magnetic device, which contributes to the nonlinearity [15]. Furthermore, an impedance measurement can also be used to extract the complex magnetic permeability in some cases, adding to the criticism in Section 2.2 [15]. Because of this, the results may not match real performance, making them less useful for designing and modeling actual devices.

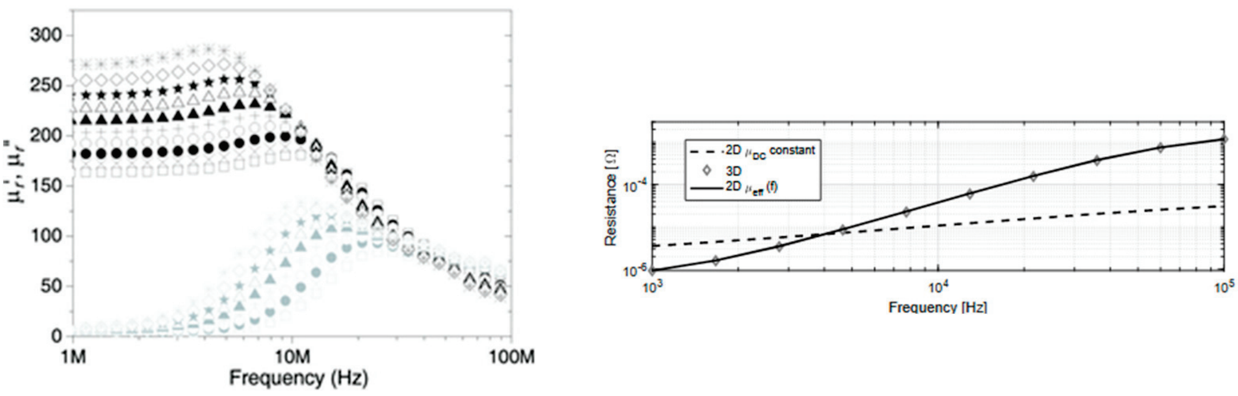

(**a**) (**b**)

Figure 5. Determination of the complex magnetic permeability by [24] (**a**) and [25] (**b**).

2.4. Limits of These Methods

The existing methods have certain limitations, as they do not fully represent the real operating conditions of electromagnetic and magnetic devices. For example, measuring the first resonance frequency at low signal levels does not account for important effects such as magnetic saturation and hysteresis. Additionally, calculations of complex magnetic permeability—which are used to estimate the iron loss equivalent resistance—are often based on simplifying assumptions. These assumptions usually ignore the effects of hysteresis.

For these reasons, we propose an experimental measurement approach that takes all of these physical effects into account. This method should allow a more precise measurement that the impedance analyzer in a respectable amount of time.

3. Measurement and Estimation Method

This method is based on the evaluation of the complex impedance of a magnetic device fed with a switching power supply corresponding to an operating point. Then, a rich, harmonics-broadband voltage signal will excite the magnetic device.

3.1. Method Description

To analyze the frequency response near the nominal operating point, the wound device is supplied using a voltage pulse characterized by a low duty cycle to ensure a broad harmonic spectrum.

The method's effectiveness is demonstrated through a MATLAB Simulink 2022b simulation featuring a circuit with constants such as copper resistance, inductance, and iron loss equivalent resistance, shown in Figure 1, given in the Section 1. A voltage pulse generator supplies the circuit, operating at 500 V amplitude, 10 kHz frequency, and a 2% duty cycle, as summarized in Table 1.

Table 1. Parameters of the pulse generator.

Parameters	Values
Voltage amplitude	500 V
Frequency	10 kHz
Duty cycle of the pulse	2%

In this simulation, the parameters are fixed with the copper resistance $R_{copper} = 2\ \Omega$, the inductance $L = 1$ mH, and the equivalent iron loss resistance $R_{iron} = 5000\ \Omega$.

Voltage and current steady-state periods are recorded at a fixed time step, determined by the desired maximum observable frequency, complying with the Shannon–Nyquist principle [26]. For this simulation, the time step is set at 1 ns, with data acquisition starting after reaching steady state.

In MATLAB, the signals are processed with the Fast Fourier Transform (FFT). From the Fourier series coefficients, impedance and phase values at corresponding frequencies are extracted.

The Fast Fourier Transform (FFT) is applied to the voltage and current signals as follows:

$$v(t)=\sum_{n=0}^{\infty} V_n e^{-jn\omega t} \tag{1}$$

$$i(t)=\sum_{n=0}^{\infty} I_n e^{-jn\omega t} \tag{2}$$

where V_n, I_n is the Fourier series complex coefficient of rank n, $\omega = 2\pi f_1$, and f_1 is the fundamental frequency of the supplied periodic pulse voltage.

The time signals and spectra are shown in Figure 6. In order to facilitate the display of the current spectrum, the DC component is removed from the spectrum graph. The value of the DC component of the current is 5.0 A.

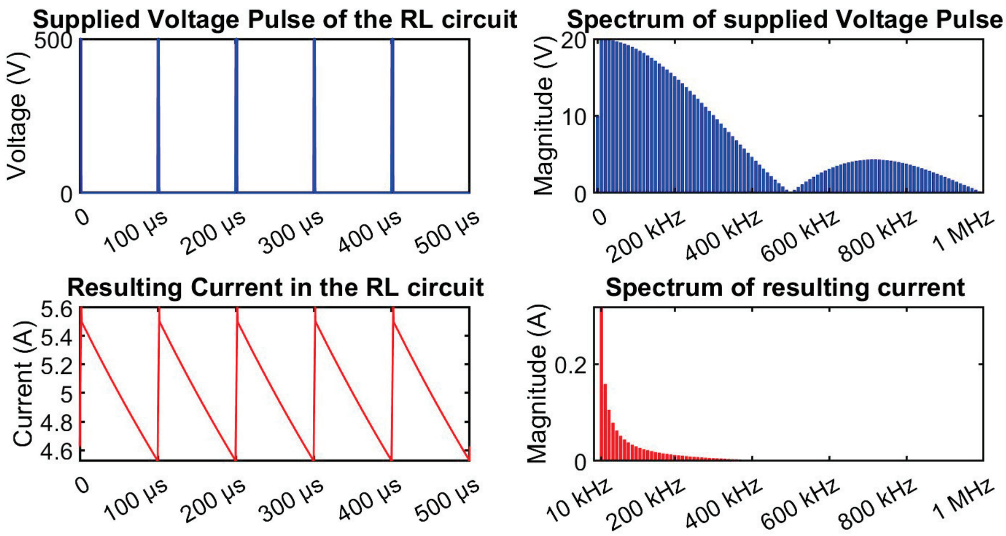

Figure 6. Voltage pulse and resulting current in the circuit and their respective spectra.

From the coefficients V_n and I_n, the values of the impedance Z and the phase φ of the circuit are determined at the corresponding frequencies:

$$Z(f_n) = Z(nf_1) = V_n/I_n \tag{3}$$

$$\varphi(f_n) = \arg(Z(f_n)) \tag{4}$$

Depending on the supply voltage signal, such as a pulse, the corresponding spectrum may contain harmonics with a magnitude close to zero, as shown in Figure 7. Digital processing may be required to prevent divergence in impedance calculations with these particular harmonics, such as a direct thresholding on the magnitude of the harmonics. Such methods are employed and explained by Creux et al. [27].

The resulting impedance modulus and phase are obtained in Figure 8. The fundamental frequency fixes the lowest observable value of the impedance.

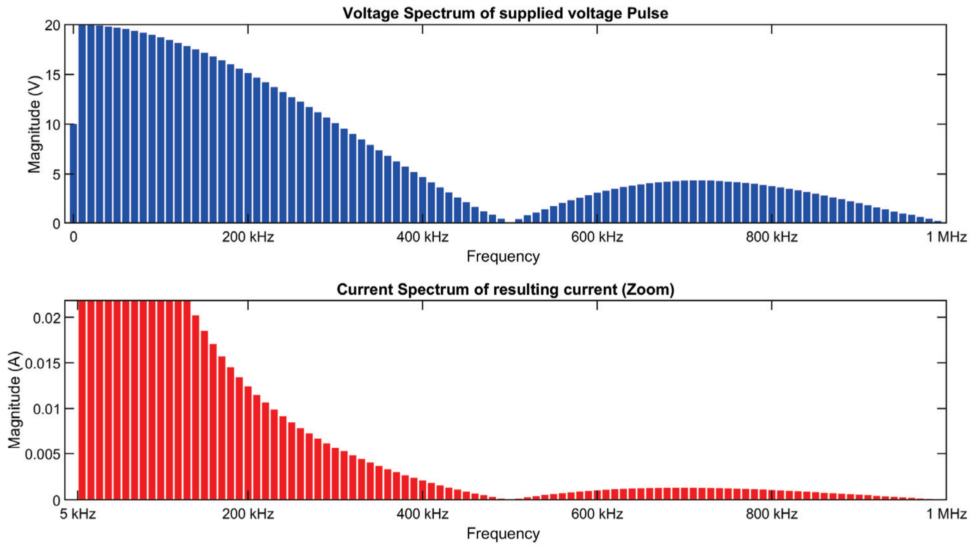

Figure 7. Highlighting close-to-zero voltage and currents harmonics at 500 kHz.

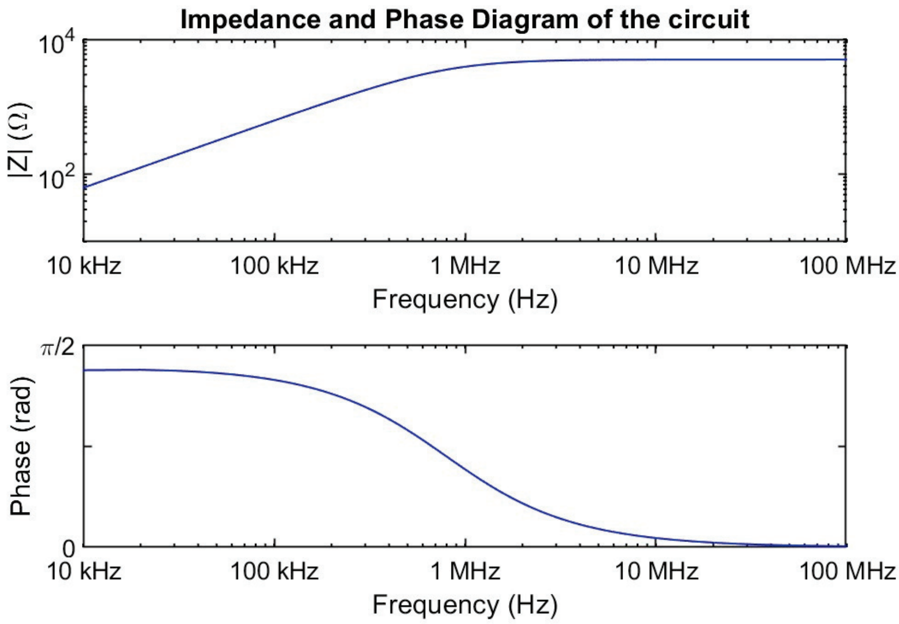

Figure 8. Resulting impedance and phase diagrams of the circuit.

3.2. Theoretical Determination of the Iron Loss Equivalent Resistance

Electrical equations of the circuit model in Figure 1 from the "Introduction" Section lead to the equivalent impedance Z:

$$Z = \frac{R_{copper}L^2\omega^2 + R_{copper}R_{iron}^2 + L^2\omega^2R_{iron}}{L^2\omega^2 + R_{iron}^2} + j\frac{R_{iron}^2L\omega}{L^2\omega^2 + R_{iron}^2} \quad (5)$$

The real and imaginary part of the impedance ((6) and (7)) can be used to determine R_{iron}.

$$Re(Z) = \frac{R_{copper}L^2\omega^2 + R_{copper}R_{iron}^2 + R_{iron}L^2\omega^2}{L^2\omega^2 + R_{iron}^2} \quad (6)$$

$$Im(Z) = \frac{R_{iron}^2L\omega}{L^2\omega^2 + R_{iron}^2} \quad (7)$$

From Im(Z), the expression of R^2_{iron} can be found in Equation (8):

$$R^2_{iron} = \frac{Im(Z)L^2\omega^2}{L\omega - Im(Z)} \quad (8)$$

From Re(Z), the expression of L^2 can be found in Equation (9):

$$L^2 = \frac{1}{\omega^2} \cdot \frac{R^2_{fer}(Re(Z) - R_s)}{R_s + R_{fer} - Re(Z)} \quad (9)$$

The following expression for R_{iron} is obtained:

$$R_{iron} = \frac{(Re(Z) - R_{copper})^2 + Im(Z)^2}{(Re(Z) - R_{copper})} \quad (10)$$

This result is independent of the inductance L but depends on the resistance R_{copper}.

In the case of our example and simulation, the following R_{iron} is obtained with a constant $R_{copper} = 2\ \Omega$ in Figure 9.

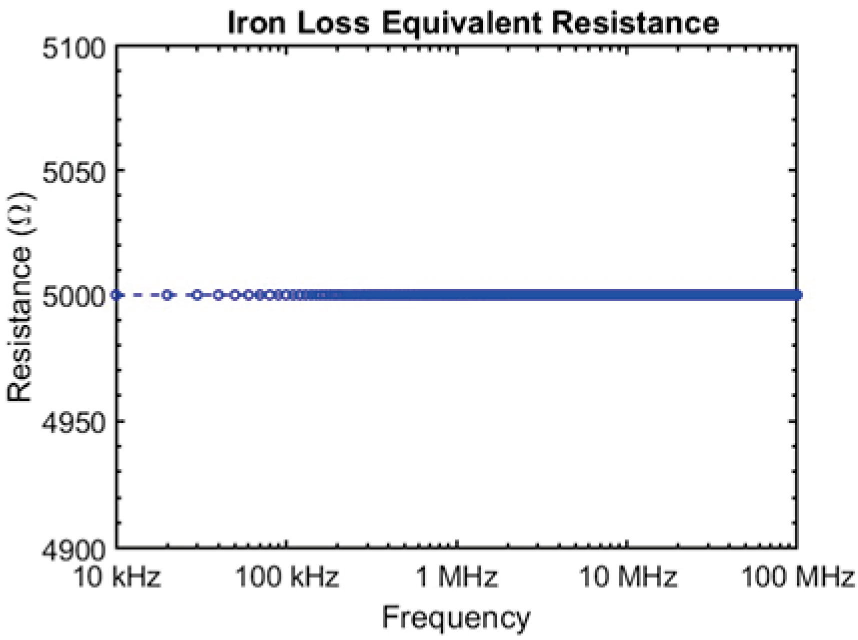

Figure 9. Iron Loss equivalent resistance of the simulated circuit.

By applying the method in simulation, it is possible to obtain the value of R_{iron} for different frequencies.

The iron loss equivalent resistance can only be determined at the frequencies present in the voltage pulse spectrum, provided that the copper resistance is known and the real and imaginary parts of the impedance are indirectly obtained from the measurements.

In most of the cases, the geometry of the wound devices is known, so R_{copper} values can be determined by using finite element method, considering skin and proximity effects.

4. Experimental Results

In order to apply the method, an experimental measuring test bench has been constructed with adapted sensors and the corresponding power supply.

To enable comparison, impedance measurements have been carried out using a T3LCR1100 impedance analyzer, from TeledyneLeCroy, Loomis, CA, USA.

4.1. Measurement Setup and Data Processing

The measurement setup consists of a DC power voltage supply with a maximum voltage of 600 V and a maximum current of 8.5 A. It is connected to a half inverter leg. The switch T1 is controlled by DSPACE, which allows it to be controlled at the desired frequency and duty cycle. The wound device is connected to the T2 switch directly, which is not driven. A schematic of the setup is shown in Figure 10.

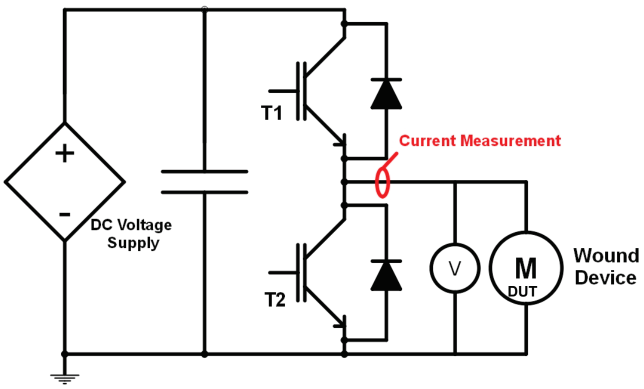

Figure 10. Measurement setup schematic.

The voltage is measured at the wound device terminals by a passive voltage probe with a 400 MHz bandwidth, from Lecroy, USA. The current is also measured at the wound device terminals by a RT-ZC20 Probe with an RT-ZA13 Amplifier, both from Rohdes & Schwarz, Munich, Germany, having a bandwidth of 100 MHz. Finally, the signals are visualized and recorded on a MS046 scope, from Tektronix, Beaverton, OR, USA, with a bandwidth of 600 MHz. Details are available in Table 2.

Table 2. Equipment used in the setup.

Equipment	Name	Relevant Parameters
Power Supply	GEN600-8.5, from TDK-Lambda, Achern, Germany	DC Voltage: 0–600 V DC Amps: 0–8.5 A
Scope	MSO46, from Tektronix, Beaverton, OR, USA	Bandwidth: 600 MHz Sample Rate: 10 GS/s
Voltage Sensor	Lecroy PPE 2 KV, from Lecroy, Chestnut Ridge, NY, USA	Bandwidth: 400 MHz Input Capacitance: <6 pF Attenuation: 1:100
Current Sensor	RT-ZC20 Probe + RT-ZA13 Amplifier, from Rohde & Schwarz, Munich, Germany	Bandwidth: 100 MHz Propagation Delay: 17 ns Sensitivity Range: 1 A/V–10 A/V
Thermal Camera	T200, from FLIR, Wilsonville, OR, USA	Temperature Range: −20 °C–1200 °C

In this experimental configuration, the wound device consists of a coil composed of 48 copper turns, located around a magnetic core made from NO20 Fe-Si laminated sheets, from Isolectra, Estrées-Deniécourt, France. The system is configured with a sampling frequency of 3.125 GHz. Pulse generation is achieved through the switching states of T1.

Synchronization of the oscilloscope with T1's control signal enables accurate acquisition of voltage and current signals flowing through the winding over a complete period. To mitigate acquisition noise inherent to the experimental setup, the averaging function of the oscilloscope is employed, allowing signal filtering without inducing phase shifts. Subsequently, the data is converted into MATLAB format.

During data processing, compensation for the 17 ns propagation delay, as detailed in Table 1, associated with the current probe and its amplifier, is necessary. The final data processing workflow aligns with the procedures outlined in Section 1. This methodology facilitates the estimation of various R_{iron} values corresponding to different operational points, utilizing the approach delineated in Section 1.

4.2. Measurement Results

These operating points are representative of the operating point of the coils in a DC–DC converter.

4.2.1. Results and Comparison

Two set of measurements are realized on the test bench in Figure 11. They are performed with the settings given in Table 3. Voltage and current acquisitions are displayed in Figure 12 for operating point 2.

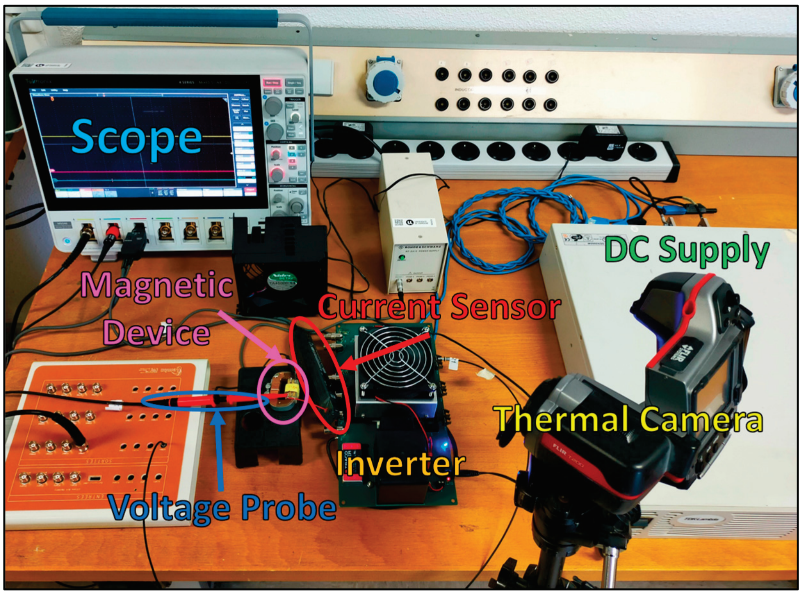

Figure 11. Picture zoomed in on the wound device and the used sensors and scope.

Table 3. Setting of the acquisition.

Parameters	Operating Point 1	Operating Point 2
Voltage amplitude	50 V	120 V
Frequency	5 kHz	5 kHz
Duty cycle of the pulse	1.6%	1.6%
Current DC component	300 mA	1.4 A

The ensuing spectra as well as impedance and phase diagrams are available, respectively, in Figures 13 and 14. DC component of the current spectrum is removed from the display and is equal to 1.4 A.

Impedance and phase obtained from the method developed in Section 1 and from the T3LCR1100 Impedance Analyzer, from TeledyneLecroy, Loomis, CA, USA are compared in Figure 14.

By analyzing the impedance and phase diagrams for each method, the difference is obvious. At this point, we can conclude that the operating point has an impact on the low- to medium-frequency behavior of the wound device.

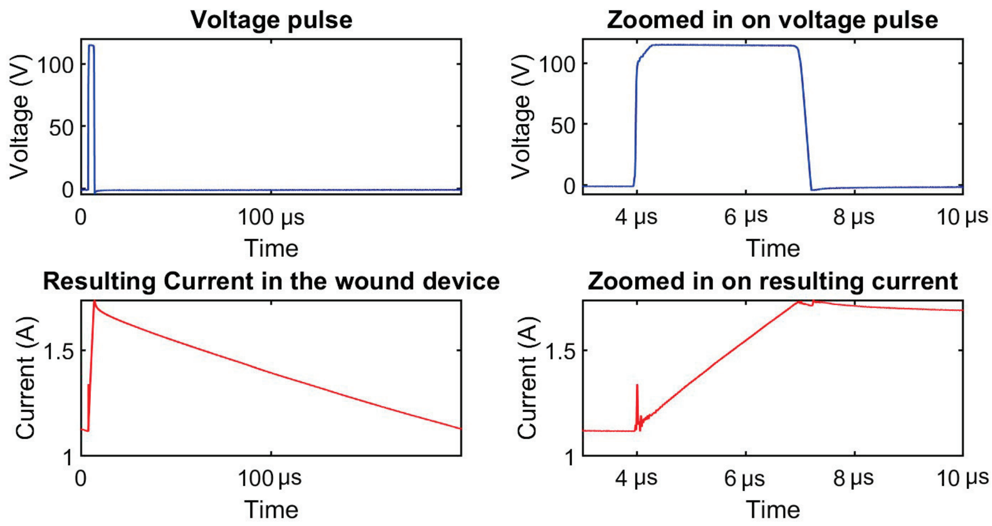

Figure 12. Voltage and resulting current in the wound device; magnified view on the right.

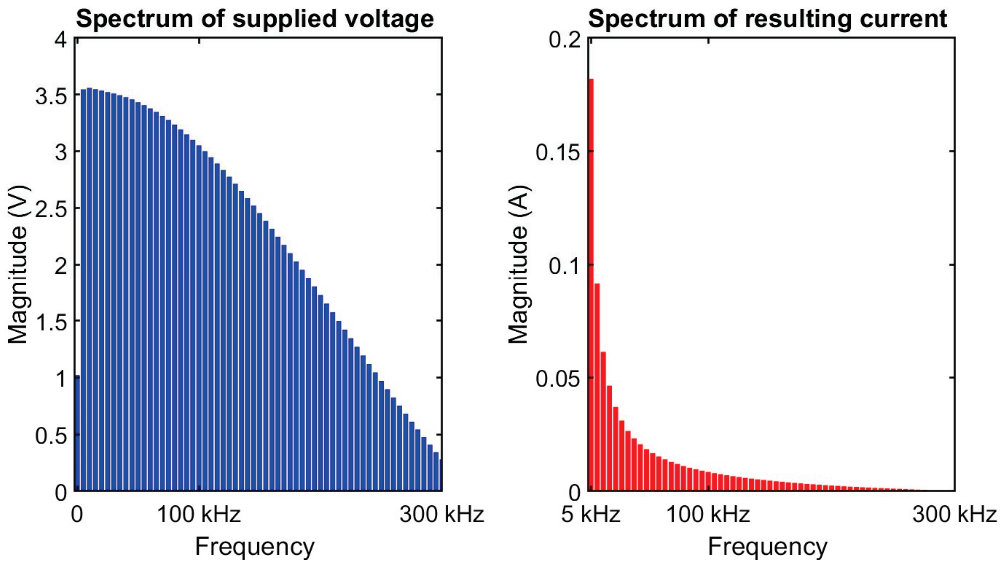

Figure 13. Spectra of the voltage pulse and the resulting current up to 300 kHz.

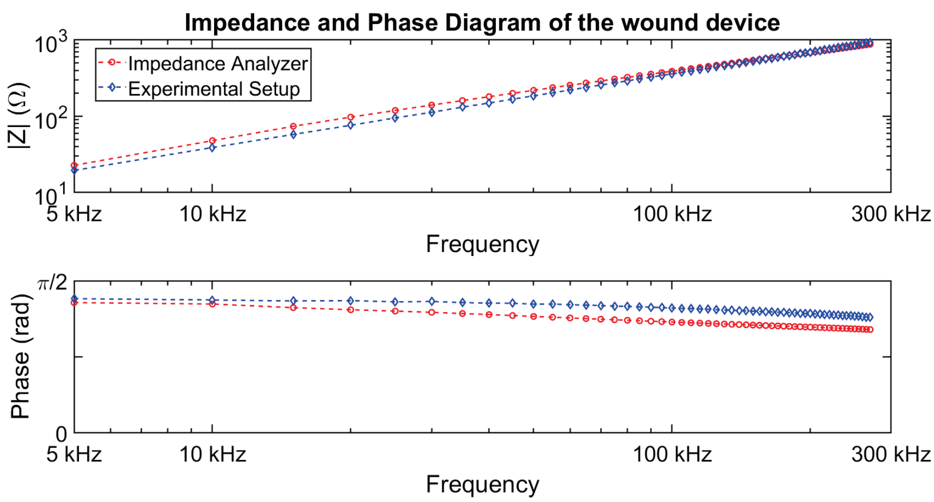

Figure 14. Impedance module and phase of the wound device up to 300 kHz.

The estimated parameters related to the equivalent circuit of wound devices (Figure 1) will be different depending on the measurement method.

In this paper, we focus our attention on the evaluation of the iron loss equivalent resistance (R_{iron}). As seen in Equation (8), it is possible to estimate R_{iron} with the knowledge of the complex impedance and the copper resistance (R_{copper}).

4.2.2. Determination of Copper Resistance

As stated previously, determining the value of the copper resistance is required to calculate the iron loss equivalent resistance.

In our case, a 2D finite element model with finite element software GetDp Version 3.30 of the wound device is used that takes into account frequency-dependent effects such as skin and proximity effects [28].

The conductivity of copper is set to the controlled temperature of 26 °C, which is the temperature at which previous measurements were conducted. The temperature measurement was carried out using a thermal camera directly pointed toward the magnetic device.

The finite element software, showcased in Figure 15, calculates the equivalent copper resistance R_{copper} of the wound device for the frequencies of the harmonic content of the voltage pulse.

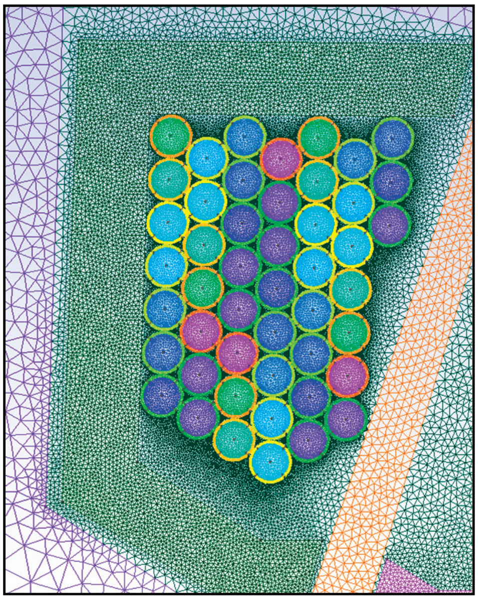

Figure 15. Display of the 2D meshed finite element model of the wound device.

As reported in other studies, the magnetic permeability μ_r function decreases as the frequency increases [29].

The apparent permeability of conductive magnetic materials, such as Fe-Si steel, decreases rapidly at higher frequencies due to increased eddy current losses [30,31]. Variations in R_{copper} depending of the relative magnetic permeability of the magnetic core μ_r in the wound device are shown in Figure 16.

In this frequency range, R_{copper} varies slightly and only affects the result of the iron loss equivalent resistance by less than 1% (Figure 17) with the lowest magnetic permeability. Our results are thus only slightly affected by the variation in the magnetic permeability.

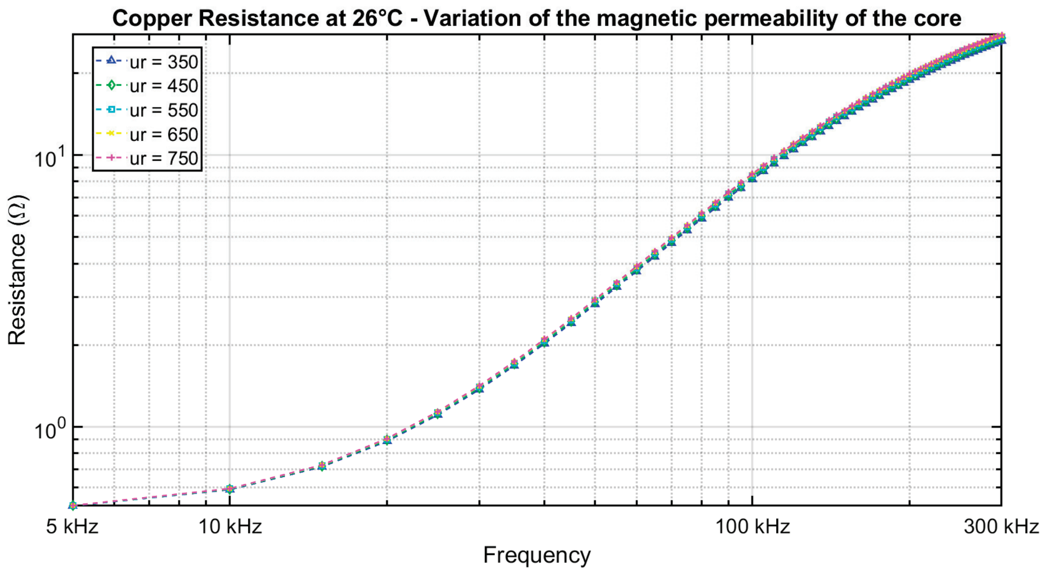

Figure 16. Variation in the copper resistance depending of the magnetic permeability of the core.

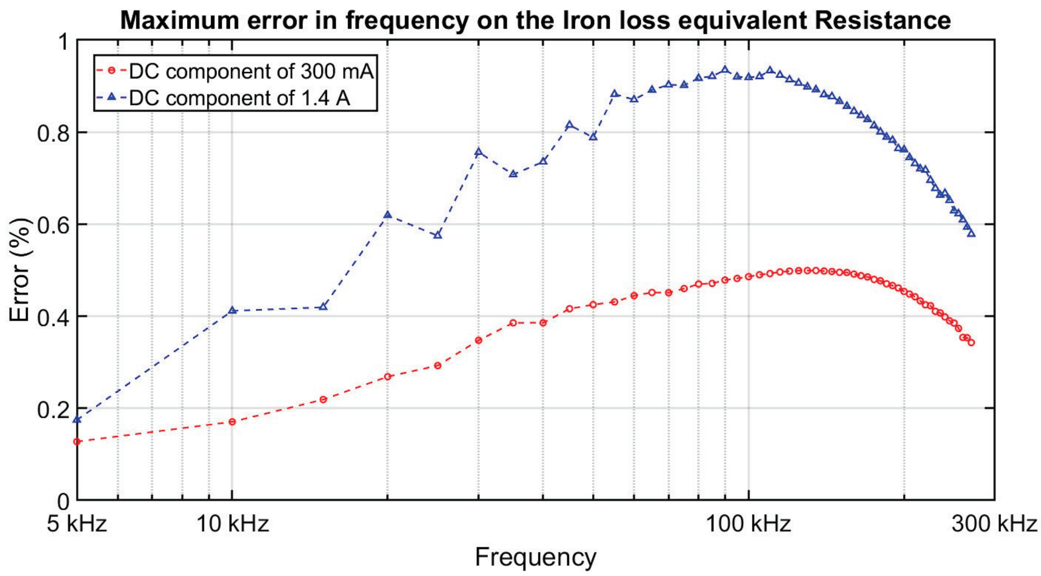

Figure 17. Error on the iron loss equivalent resistance between a magnetic permeability on the magnetic core of 750 and a lower permeability of 350.

4.3. Determination of the Iron Loss Equivalent Resistance

The iron loss equivalent resistance calculated according to the steps in Section 2.2 and the impedance analyzer are compared at Figure 18. Thermal steady state at 26 °C is ensured before signal acquisition, and determination of the copper resistance is also performed at 26 °C.

The sensitivity errors associated with the voltage and current sensors were taken into account, estimated at 2% and 3%, respectively. Numerical errors originating from the oscilloscope were also considered, but these were found to be negligible in comparison to the sensor errors.

A frequency dependence of the iron loss equivalent resistance is visualized, while also being dependent on the operating point at which the magnetic device is running. It validates the influence of the operating point on the evaluation of the iron loss equivalent resistance.

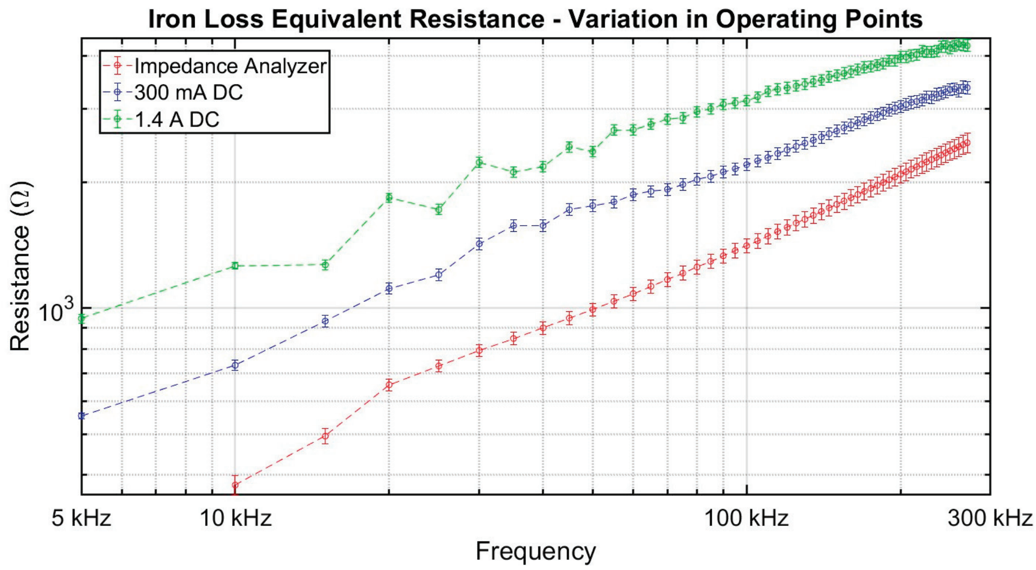

Figure 18. Iron loss equivalent resistance of the wound device from the impedance analyzer and the method at operating point at 300 mA DC and 1.4 A DC.

5. Discussion

The differences between our measurement approach and the one implemented with conventional impedance analyzers can largely be attributed to the nonlinear behavior exhibited by electromagnetic or magnetic devices. A key phenomenon explaining this difference is harmonic intermodulation. In a traditional impedance analyzer, only the fundamental component of the current, resulting from a perfectly sinusoidal voltage input, is taken into account in the measurement process, shown in Figure 19.

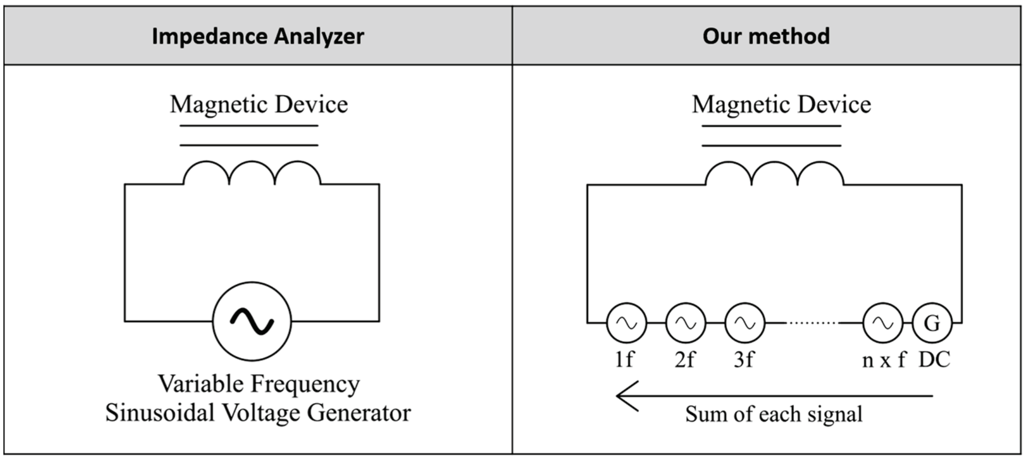

Figure 19. Circuit model equivalent of the method highlighting the differences between the measurements from the impedance analyzer and from our method.

By contrast, in our case, the nonlinear electromagnetic or magnetic device is subjected to voltage excitations containing numerous harmonics. This excitation generates an even higher number of current harmonics at the output, which significantly affects impedance determination. The generated current harmonics may add to or subtract from the existing ones, influencing the resulting signal and impedance determination.

In addition to this limitation, another physical phenomenon characteristic of magnetic materials, particularly of the ferromagnetic type, comes into play: the existence of minor hysteresis loops. Minor hysteresis loops are smaller cycles that develop around the major loop formed by the fundamental excitation component in an electromagnetic or magnetic device. According to Petrea et al., the presence of these minor loops around the major one leads to a reduction in both the material's dynamic coercivity and—most notably—its permeability, especially at high frequencies [21].

Further, Petrea et al.'s research demonstrates that high-frequency harmonic content directly impacts the low-frequency behavior of the device, establishing a clear link between the effects of minor loops and the methods used to measure the impedance of electromagnetic and magnetic devices. As a result, changes in magnetic properties in the presence of harmonic content influence not only the determination of the material's impedance but also our estimation of its equivalent iron loss resistance [21].

Finally, because the frequency sweep in an impedance analyzer is performed with a purely sinusoidal power supply, such an analyzer is fundamentally incapable of generating and exciting an electromagnetic or magnetic device in a manner that would give rise to minor hysteresis loops. This means that conventional impedance analyzers cannot capture these essential dynamic effects, resulting in measurement limitations when characterizing nonlinear magnetic materials under realistic, harmonic-rich excitation conditions.

In summary, by explicitly considering the effects of minor hysteresis loops and harmonic intermodulation, our method offers a more precise and realistic determination of iron loss equivalent resistance under real operating conditions, including phenomena such as electromagnetic and magnetic saturation. This approach is unique because it accounts for the actual dynamic behavior of magnetic devices under complex excitation, which traditional methods typically overlook. As a result, our methodology provides data that is not only more accurate but is also directly applicable to the modeling and design of advanced electromagnetic components. Such improved precision is particularly valuable for high-frequency transformers, power electronics, and other applications where understanding complex magnetic behavior is critical. This makes our results significantly more suitable and relevant for both detailed circuit modeling and the further development of next-generation electromagnetic and magnetic devices.

6. Conclusions

This work began by reviewing the development of measurement techniques for electromagnetic and magnetic devices, focusing on the challenges of characterizing iron loss equivalent resistance under realistic operating conditions. The state of the art highlights the growing importance of evaluating devices directly under their typical working points, especially as modern applications increasingly rely on complex, harmonic-rich excitations.

We have introduced a novel method for determining the iron loss equivalent resistance of magnetic devices directly at their actual operating point. This method involves exciting the magnetic device with a voltage signal rich in harmonics and measuring both this voltage and the resulting current. Using these measurements, the complex impedance of the winding can be directly determined through FFT (Fast Fourier Transform) analysis. This approach consists of three essential elements: accurate measurement during operation, careful calibration of the sensors to ensure reliable data, and dedicated digital processing to extract the relevant parameters from the measurements. Each of these steps contributes to the accuracy and repeatability of the method.

The method was successfully implemented on an electromagnetic device, confirming its practical viability. As an example of the results in Figure 18, at 10 kHz, the estimated iron loss equivalent resistance for a 1.4 A DC operating point is 1262 $\Omega \pm 23\ \Omega$, while for a 300 mA DC operating point, it is 731 $\Omega \pm 21\ \Omega$. For comparison, the value obtained with the impedance analyzer is $378 \pm 20\ \Omega$. This represents a difference of approximately 333% between the 1.4 A DC operating point and the impedance analyzer and about 193% for the 300 mA DC case. The study demonstrates that the DC component of the current has a clear impact on the impedance of electromagnetic devices and therefore on the iron loss equivalent resistance. This underlines the relevance and the importance of our method in applications where the operating currents may deviate from purely alternating forms.

A fundamental difference between our method and traditional impedance analyzer measurements can be attributed to the consideration of intermodulation effects and the complex magnetic phenomena known as minor loops. Unlike conventional techniques, our method takes into account these nonlinear effects, which results in a more accurate and comprehensive assessment.

To our knowledge, this practical measurement technique is not yet standard in the field, but it offers significant flexibility and adaptability. It can be applied to a wide range of electromagnetic and magnetic devices for the direct measurement of iron loss equivalent resistance, which is highly valuable for device design and optimization. Looking ahead, the method will be extended to analyze performance under various supply waveforms, including Pulse-Width Modulation (PWM). In particular, this includes validating the technique with multilevel PWM signals and in scenarios involving high switching frequencies—such as those found in advanced inverters equipped with Gallium Nitride (GaN) components driving electrical motors. These systems are increasingly common due to their high efficiency and ability to operate at very high switching speeds.

Overall, this method offers a reliable and innovative solution for characterizing iron loss equivalent resistance under realistic operating conditions. It paves the way for further research and development, making it particularly relevant for the measurement and design of next-generation magnetic components used in modern power electronic systems.

Author Contributions: Conceptualization, M.C. and T.B.; methodology, M.C., T.B. and N.T.; software, M.C., T.B. and N.T.; validation, M.C., T.B., N.T. and S.C.; formal analysis, M.C. and T.B.; investigation, M.C. and T.B.; resources, T.B., N.T. and S.C.; data curation, M.C.; writing—original draft preparation, M.C.; writing—review and editing, M.C. and T.B.; visualization, T.B., N.T. and S.C.; supervision, T.B., N.T. and S.C.; project administration T.B., N.T. and S.C.; funding acquisition, T.B., N.T. and S.C. All authors have read and agreed to the published version of the manuscript.

Funding: This research received no external funding.

Data Availability Statement: The data presented in this study is available on request from the corresponding author. The data is not publicly available due to privacy concerns for the participants involved in this study.

Conflicts of Interest: Authors Maxime Colin and Stéphane Charmoille were employed by the company Safran Electronics & Defense. The remaining authors declare that the research was conducted in the absence of any commercial or financial relationships that could be construed as a potential conflict of interest.

Abbreviations

The following abbreviations are used in this manuscript:

ILER	Iron Loss Equivalent Resistance
DC	Direct Current
PWM	Pulse-Width Modulation
FFT	Fast Fourier Transform

References

1. Ding, N.; Prasad, K.; Lie, T.T. The Electric Vehicle: A Review. *Int. J. Electr. Hybrid Veh.* **2017**, *9*, 49. [CrossRef]
2. Sarlioglu, B.; Morris, C.T. More Electric Aircraft: Review, Challenges, and Opportunities for Commercial Transport Aircraft. *IEEE Trans. Transp. Electrif.* **2015**, *1*, 54–64. [CrossRef]

3. Polinder, H.; Ferreira, J.A.; Jensen, B.B.; Abrahamsen, A.B.; Atallah, K.; McMahon, R.A. Trends in Wind Turbine Generator Systems. *IEEE J. Emerg. Sel. Top. Power Electron.* **2013**, *1*, 174–185. [CrossRef]
4. Wei, M.; McMillan, C.A.; de la Rue du Can, S. Electrification of Industry: Potential, Challenges and Outlook. *Curr. Sustain. Renew. Energy Rep.* **2019**, *6*, 140–148. [CrossRef]
5. Magdun, O.; Blatt, S.; Binder, A. Calculation of Stator Winding Parameters to Predict the Voltage Distributions in Inverter Fed AC Machines. In Proceedings of the 2013 9th IEEE International Symposium on Diagnostics for Electric Machines, Power Electronics and Drives (SDEMPED), Valencia, Spain, 27–30 August 2013; pp. 447–453.
6. Toudji, M.; Parent, G.; Duchesne, S.; Dular, P. Determination of Winding Lumped Parameter Equivalent Circuit by Means of Finite Element Method. *IEEE Trans. Magn.* **2017**, *53*, 9401904. [CrossRef]
7. Ruiz-Sarrio, J.E.; Chauvicourt, F.; Gyselinck, J.; Martis, C. Impedance Modeling Oriented Toward the Early Prediction of High-Frequency Response for Permanent Magnet Synchronous Machines. *IEEE Trans. Ind. Electron.* **2023**, *70*, 4548–4557. [CrossRef]
8. Memon, A.A.; Bukhari, S.S.H.; Ro, J.-S. Experimental Determination of Equivalent Iron Loss Resistance for Prediction of Iron Losses in a Switched Reluctance Machine. *IEEE Trans. Magn.* **2022**, *58*, 8102404. [CrossRef]
9. Hajji, T.E.; Hlioui, S.; Louf, F.; Gabsi, M.; Belahcen, A.; Mermaz-Rollet, G.; Belhadi, M. AC Losses in Windings: Review and Comparison of Models With Application in Electric Machines. *IEEE Access* **2024**, *12*, 1552–1569. [CrossRef]
10. Zhu, S.; Shi, B. Modeling of PWM-Induced Iron Losses With Frequency-Domain Methods and Low-Frequency Parameters. *IEEE Trans. Ind. Electron.* **2022**, *69*, 2402–2413. [CrossRef]
11. Grandi, G.; Kazimierczuk, M.K.; Massarini, A.; Reggiani, U.; Sancineto, G. Model of Laminated Iron-Core Inductors for High Frequencies. *IEEE Trans. Magn.* **2004**, *40*, 1839–1845. [CrossRef]
12. Mahdavi, S.; Hameyer, K. High Frequency Equivalent Circuit Model of the Stator Winding in Electrical Machines. In Proceedings of the 2012 XXth International Conference on Electrical Machines, Marseille, France, 2–5 September 2012; pp. 1706–1711.
13. Mombello, E.E. Impedances for the Calculation of Electromagnetic Transients within Transformers. *IEEE Trans. Power Deliv.* **2002**, *17*, 479–488. [CrossRef]
14. Suresh, G.; Toliyat, H.A.; Rendusara, D.A.; Enjeti, P.N. Predicting the Transient Effects of PWM Voltage Waveform on the Stator Windings of Random Wound Induction Motors. *IEEE Trans. Power Electron.* **1999**, *14*, 23–30. [CrossRef]
15. Cuellar, C.; Tan, W.; Margueron, X.; Benabou, A.; Idir, N. Measurement Method of the Complex Magnetic Permeability of Ferrites in High Frequency. In Proceedings of the 2012 IEEE International Instrumentation and Measurement Technology Conference Proceedings, Graz, Austria, 13–16 May 2012; pp. 63–68.
16. Corda, J.; Jamil, S.M. Experimental Determination of Equivalent-Circuit Parameters of a Tubular Switched Reluctance Machine With Solid-Steel Magnetic Core. *IEEE Trans. Ind. Electron.* **2010**, *57*, 304–310. [CrossRef]
17. Bjerkan, E. High Frequency Modeling of Power Transformers. Stresses and Diagnostics. 2005. Available online: https://www.osti.gov/etdeweb/biblio/20843756 (accessed on 1 July 2025).
18. Papamanolis, P.; Krismer, F.; Kolar, J.W. Minimum Loss Operation of High-Frequency Inductors. In Proceedings of the 2018 IEEE Applied Power Electronics Conference and Exposition (APEC), San Antonio, TX, USA, 4–8 March 2018; pp. 1756–1763.
19. Liu, R.; Mi, C.C.; Gao, D.W. Modeling of Eddy-Current Loss of Electrical Machines and Transformers Operated by Pulsewidth-Modulated Inverters. *IEEE Trans. Magn.* **2008**, *44*, 2021–2028. [CrossRef]
20. Chiniforoosh, S.; Davoudi, A.; Alaeinovin, P.; Jatskevich, J. Dynamic Modelling and Characterisation of Vehicular Power System Considering Alternator Iron Core and Rectifier Losses. *IET Electr. Syst. Transp.* **2012**, *2*, 58–67. [CrossRef]
21. Petrea, L.; Demian, C.; Brudny, J.F.; Belgrand, T. High-Frequency Harmonic Effects on Low-Frequency Iron Losses. *IEEE Trans. Magn.* **2014**, *50*, 6301204. [CrossRef]
22. Vukadinovic, D.; Grbin, Š.; Bašić, M. Novel Equivalent Circuit of Switched Reluctance Machine with Iron Losses. In Proceedings of the 4th European Conference for the Applied Mathematics and Informatics (AMATHI'13), Dubrovnik, Croatia, 25–27 June 2013.
23. Grandi, G.; Casadei, D.; Massarini, A. High Frequency Lumped Parameter Model for AC Motor Windings. *Eur. Conf. Power Electron. Appl.* **1997**, *2*, 2.578–2.583.
24. de Brito, V.L.O.; da Cunha Migliano, A.C.; Lemos, L.V.; Melo, F.C.L. Melo Ceramic Processing Route and Characterization of a Ni-Zn Ferrite for Application in a Pulsed-Current Monitor. *Prog. Electromagn. Res.* **2009**, *91*, 303–318. [CrossRef]
25. Ruiz-Sarrió, J.E.; Chauvicourt, F.; Gyselinck, J.; Martis, C. High-Frequency Modelling of Electrical Machine Windings Using Numerical Methods. In Proceedings of the 2021 IEEE International Electric Machines & Drives Conference (IEMDC), Hartford, CT, USA, 17–20 May 2021; pp. 1–7.
26. Shannon, C.E. Communication in the Presence of Noise. *Proc. IRE* **1949**, *37*, 10–21. [CrossRef]
27. Creux, J.; Haje Obeid, N.; Boileau, T.; Meibody-Tabar, F. Online High Frequency Impedance Identification Method of Inverter-Fed Electrical Machines for Stator Health Monitoring. *Appl. Sci.* **2024**, *14*, 911. [CrossRef]
28. GetDP: A General Environment for the Treatment of Discrete Problems. Available online: https://getdp.info/ (accessed on 20 June 2025).

29. Wrobel, R.; Salt, D.E.; Griffo, A.; Simpson, N.; Mellor, P.H. Derivation and Scaling of AC Copper Loss in Thermal Modeling of Electrical Machines. *IEEE Trans. Ind. Electron.* **2014**, *61*, 4412–4420. [CrossRef]
30. Goldman, A. *Modern Ferrite Technology*; Springer Science & Business Media: Berlin, Germany, 2006.
31. Bozorth, R.M. Ferromagnetism. 1993. Available online: https://archive.org/stream/in.ernet.dli.2015.140821/2015.140821.Ferromagnetism_djvu.txt (accessed on 1 July 2025).

energies

MDPI

Article

Problems in Modeling Three-Phase Three-Wire Circuits in the Case of Non-Sinusoidal Periodic Waveforms and Unbalanced Load

Konrad Zajkowski * and Stanislaw Duer

Department of Energy, Faculty of Mechanical Engineering and Energy, Koszalin University of Technology, 15-17 Raclawicka St., 75-620 Koszalin, Poland; stanislaw.duer@tu.koszalin.pl
* Correspondence: konrad.zajkowski@tu.koszalin.pl

Abstract: Asymmetry in the supply voltage in three-phase circuits disrupts the flow of currents. This worsens the efficiency of the distribution system and increases the problems in determining the mathematical model of the energy system. Among many power theories, the most accurate is the Currents' Physical Components (CPC) power theory, which tries to justify the physical essence of each component. Such knowledge can be used to improve efficiency and reduce transmission losses in the power system. This article discusses the method of mathematical decomposition of current components in the case of a three-wire line connecting an asymmetric power source with linear time-invariant (LTI) loads. Special cases where irregularities appear in the results of calculations according to the CPC theory are discussed. The problem of equivalent conductance in the case of a non-zero value of the constant voltage component is discussed. The method of determining symmetrical components for periodic non-sinusoidal waveforms is also discussed. These considerations are supported by numerical examples.

Keywords: Currents' Physical Components (CPC); power definitions; power theory

1. Introduction

Contemporary problems in the energy sector mainly focus on improving the efficiency of energy systems and improving energy quality [1–3]. These activities in the area of power engineering include, among others, monitoring the flow of current and actions to reduce transmission losses [4–6]. In this respect, developing methods to describe the mathematical model of the power system [7–11] and to determine the values of individual elements is crucial. Knowing the mathematical model of this system will make it possible to select the topology and parameters of the compensators [12–24].

In measurement practice, we most often only have data in the form of measured electrical quantities on the line connecting the load with the power source. This article focuses on the three-wire connection (Figure 1).

A linear time-invariant (LTI) load is supplied by a three-wire line with non-sinusoidal and asymmetrical voltage. The assumption of the LTI load is crucial here because in the case of a receiver generating harmonics [25–35], identifying all the parameters of the nonlinear load requires a more complicated measurement procedure [36–41]. The nonlinearity of the receiver causes a change in the direction of energy flow for some harmonics. This disrupts the operation of power systems operating on both micro and macro energy scales. The impact of a nonlinear receiver affects all receivers connected to a common power grid [37,38]. Disturbances in energy flow affect the measured active power and the control method in power electronic converters of electromechanical systems [39].

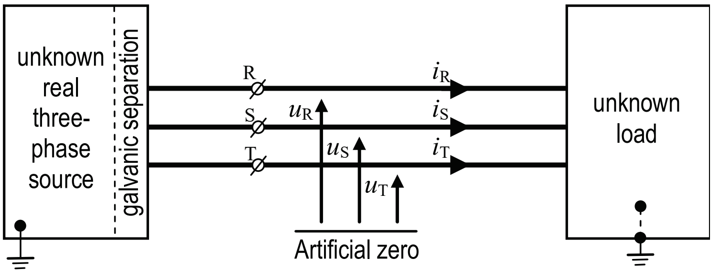

Figure 1. The tree-wire connection of the load with the source.

For easier presentation of the problems presented in this article, the case of harmonic generation by the load (Figure 1) is omitted. This means that the harmonics in the circuit were transferred from the outside to the tested measuring point of the power network using a real voltage source.

In the case of electromechanical systems, it should be borne in mind that under certain circumstances, an induction machine may cause the generation of energy in the opposite direction. Such generation may result from nonlinear magnetization characteristics (in motor operation) or the operation of a frequency converter, which results in the generation of energy with higher harmonics. A change in the direction of energy flow of the first harmonic will occur in generator operation. Such disturbances negatively affect the operation of the power grid and the service life of this machine [2]. The appearance of subharmonics and interharmonics in the current supplying an induction machine results in deformation of the rotating magnetic field. Improving the power factor in such a system is a big challenge.

There are several power theories that allow the description of an electric circuit in terms of energy [42–55]. The most important are two theories: the first is the IEEE Standard 1459 [56,57], which is treated as a standard for measurements in electric circuits, and the second is the CPC theory [58–70], which precisely recognizes the individual current components and allows for the parameters of compensators to be determined.

There is great conflict in the scientific community between several factions recognizing particular theories. When looking objectively at known power theories, it is necessary to emphasize the advantages of each.

The IEEE Standard 1459, due to its simplicity and simplification, is a good and sufficient way to describe the energy in an electric circuit for billing purposes. Due to the way in which components dependent on physical phenomena are determined, the CPC theory is an excellent tool for compensation purposes, design purposes, detailed mathematical analyses, and considerations for improving the efficiency of a power system.

The remarks on the CPC theory concerning the incorrectness of the considerations may be considered outdated over time as work on the detailed description is still in progress, and the results obtained bring us closer to honoring a universal power theory that does not arouse any controversy. Thanks to the way in which analyses are conducted in this theory, individual components of the current are added to the general mathematical description—analogously to puzzle pieces creating a unified graphic image. If at present day the CPC theory has not taken into account some electrical interaction in the circuit, one can be sure that in the future, an additional component will appear, which will be a new puzzle piece in the picture of power theory.

When performing circuit analysis using the CPC power theory, one may hit a dark area that has not yet been considered. This leads to misunderstandings and controversies regarding the entire CPC theory. So, it is important to find these unknown areas to learn the correct mathematical modeling of various electrical circuits.

The CPC theory is a method that allows for a broad view of all phenomena occurring in electrical circuits [71–74]. Thanks to continuous development, it provides the possibility of modeling various types of circuits. The first publications from the late 20th century provided insights into simple single-phase circuits. In subsequent stages, considerations took into account increasingly complex situations. Monitoring the progress of the CPC theory and pointing out ambiguities is beneficial because it allows for its development.

Is the current state of knowledge in CPC theory sufficient? Unfortunately not. During mathematical analyses of AC circuits, one can still come across problems that have not yet been solved. Therefore, it is important to continue research in this area. This article proposes a solution to several problems found. However, this does not mean that the topic is fully understood and that further research will no longer be needed.

The first few sections of this article point out several ambiguities that arise during mathematical analyses. Section 5 presents a revision of the CPC theory for a three-wire circuit connecting an asymmetric three-phase source to an unbalanced load.

2. Shift in Vectors by 90°

The voltage measurement [75–78] in a three-wire system is made with respect to an artificial zero (Figure 1). This circuit is designed in such a way that the three-phase voltage vector does not have a zero symmetrical component. This is possible when the three measuring channels of the voltmeters have the same internal impedances, Z_{V}. In practice, the Z_{V} value is many times greater than the source and receiver impedances in the tested system, i.e., the Z_{V} value does not affect the obtained measurements. The current is measured non-invasively using current transformers in the circuit powering a three-phase receiver. This means that the internal impedances Z_{A} of current meters are many times smaller than the source and receiver impedances. By measuring the instantaneous values of voltages and currents and using the FFT transform, amplitudes and phase shifts are separately obtained for each harmonic. The condition is that the current and voltage waveforms are periodic. When making measurements in a real measuring system, we only have access to the line connecting the source with the receiver (Figure 1). The source and receiver are unknown. As a result of measuring the instantaneous values of current and voltage and performing the FFT transformation, three-phase vectors are obtained in the form of

$$\begin{aligned}\mathbf{u}_n &= \begin{bmatrix} u_{\mathrm{R},n} \\ u_{\mathrm{S},n} \\ u_{\mathrm{T},n} \end{bmatrix} = \sqrt{2}\Re e \begin{bmatrix} \underline{U}_{\mathrm{R},n} \\ \underline{U}_{\mathrm{S},n} \\ \underline{U}_{\mathrm{T},n} \end{bmatrix} e^{jn\omega_1 t} = \sqrt{2}\Re e\{\underline{\mathbf{U}}_n\, e^{jn\omega_1 t}\},\ \mathbf{u} = \sum_n \mathbf{u}_n, \\ \mathbf{i}_n &= \begin{bmatrix} i_{\mathrm{R},n} \\ i_{\mathrm{S},n} \\ i_{\mathrm{T},n} \end{bmatrix} = \sqrt{2}\Re e \begin{bmatrix} \underline{I}_{\mathrm{R},n} \\ \underline{I}_{\mathrm{S},n} \\ \underline{I}_{\mathrm{T},n} \end{bmatrix} e^{jn\omega_1 t} = \sqrt{2}\Re e\{\underline{\mathbf{I}}_n\, e^{jn\omega_1 t}\},\ \mathbf{i} = \sum_n \mathbf{i}_n. \end{aligned} \tag{1}$$

Constant values of these elements can only be obtained in the case of continuous and periodic waveforms. So, this is the first and most important limitation that applies to most power theories.

When adopting the definitions of these vectors according to the CPC theory, it should be remembered that these vectors are shifted by 90° with respect to the other theories. In this case, the instantaneous values are based on the cosine function (2) and not the sine function. For example, for voltage, it would be

$$\mathbf{u} = U_0 + \sqrt{2}\sum_{n=1} |\underline{\mathbf{U}}_n| \cdot \cos(n\omega_1 t + \arg\{\underline{\mathbf{U}}_n\}). \tag{2}$$

It is known that the Fourier series coefficients a_n and b_n (3) determined in the period T are

$$a_n = \frac{2}{T}\int_0^T f(t)\cos(n\omega_1 t)dt,\ b_n = \frac{2}{T}\int_0^T f(t)\sin(n\omega_1 t)dt, \tag{3}$$

So, in CPC theory, these coefficients should be swapped as follows:

$$f(t) = \frac{a_0}{2} + \sum_{n=1}^{\infty}(b_n\cos(n\omega_1 t) + a_n\sin(n\omega_1 t)). \tag{4}$$

Phase shift is not a problem if it is taken into account in all results. In power systems, the cosine or sine function is used. Nevertheless, when comparing the results obtained between several theories, this should be kept in mind.

3. Problems with the Constant Voltage Component

The active component of current was proposed at the beginning of the 20th century by Prof. Fryze [79]. It makes physical sense for single- and three-phase circuits. As is known, the value of this component is related to the value of active power and the rms value of the voltage. For example, for single-phase circuits, the active component of the current is described by the following relations:

$$\|i_{\mathrm{a}}\| = \|u\|\cdot G_{\mathrm{e}} = \frac{P}{\|u\|},\ i_{\mathrm{a}} = G_{\mathrm{e}}u = G_{\mathrm{e}}U_0 + \sqrt{2}\Re e\left\{\sum_{n=1}^{N} G_{\mathrm{e}}\underline{U}_n e^{jn\omega_1 t}\right\}. \tag{5}$$

It can be seen in (5) that the value of the i_{a} component and the value of the power P depend on the equivalent conductance G_{e}. Therefore, G_{e} is a key parameter in determining the active component, and the value of this parameter is determined from the following relationship:

$$G_{\mathrm{e}} = P/\|u\|^2. \tag{6}$$

According to the accepted standards, in single-phase systems, the effective value of the voltage is equal:

$$\|u\| = \sqrt{U_0^2 + \sum_{n=1}|\underline{U}_n|^2}. \tag{7}$$

Let us note that the rms value of voltage (7) is influenced by all components of this voltage that create the instantaneous value $u(t)$ (e.g., for a three-phase system, it is expressed in Formula (2)). The effective value of the voltage depends on the subsequent harmonics and the constant voltage component. Therefore, all of these voltage components contribute to the power P and the equivalent conductance G_e (6).

Example 1. *Let us assume a single-phase receiver constructed from a series connection of a resistor* $R = 1\ \Omega$ *and a capacitor C, which, for a pulsation of* $\omega_1 = 1$ rad/s, *has a reactance of* $X_C = 1\ \Omega$. *This circuit is powered by voltage,* $u = 1 + \sqrt{2}[\cos(\omega_1 t) + \cos(3\omega_1 t)]$ V.

According to (7), the rms value of voltage is $\|u\| = \sqrt{U_0^2 + U_1^2 + U_3^2} = \sqrt{3}$ V. Active power is the power lost in the resistance R, where for the nth component, it is $P_n = |\underline{I}_n|^2 R$, while the current is $\underline{I}_n = \frac{U_n}{R - j\frac{X_C}{n\omega_1}}$.

The current values are obtained, $\underline{I} = [0;\ 0.5 + j0.5;\ 0.9 + j0.3]$ A, and the powers are $P = [0;\ 0.5;\ 0.9]$ W. The total active power is equal, $P = \sum_n P_n = 1.4$ W, i.e., the equivalent conductance (6) is $G_{\mathrm{e}} = 0.47$ S.

In a series RC connection, the voltage component U_0 has no energetic effect and does not affect the value of the current flowing through these elements. The direct current component is equal to I_0 = 0 and does not depend on the value of R.

The definition of the effective value (7) is standardized and should not be modified. It corresponds to the value presented by measuring instruments. However, knowing that the product of the effective value of voltage and current is used for power calculations, when the effective value of voltage (7) is taken into account in the RC circuit, the result will be incorrect. The value of power in an RC circuit is influenced only by those voltage components that produce an energy effect. The numerator in Equation (6) can be easily determined as the sum of active powers for individual harmonics. However, the value of the denominator of this equation must depend only on those harmonics that affect the value of the power P.

The correct voltage value in Formula (6) must be defined as a parameter that produces a certain effect in the circuit, so in this example, it should be determined based on components U_1 and U_3 (8).

$$U_{eff} \overset{def}{=} \sqrt{\sum_{n\in H} U_n^2}, \tag{8}$$

where H is the set of harmonics for which there is a plexus between the current I_H and the voltage U_H components, i.e., in this example, H = {1, 3}.

Equation (6) goes to the following notation:

$$G_\mathrm{e} = P/U_{eff}^2 \tag{9}$$

The voltage value determined from (8) is $U_{eff} = \sqrt{2}$ V, which means that the equivalent conductance (9) is G_e = 0.7 S. By determining the rms value of the active current component according to (5) and using (7), we obtain $\|i_\mathrm{a}\| = 1.4/\sqrt{3} = 0.81$ A, and after using (8), the value of this current is $\|i_\mathrm{a}\| = 1.4/\sqrt{2} = 0.99$ A.

For three-phase circuits, the CPC theory also determines the equivalent conductance [13–19]. The DC component of voltage in three-phase circuits is practically nonexistent. In three-phase circuits, the definition of the rms value of the three-phase voltage is

$$\|\mathbf{u}\| = \sqrt{\|u_\mathrm{R}\|^2 + \|u_\mathrm{S}\|^2 + \|u_\mathrm{T}\|^2}. \tag{10}$$

The rms values of the L-phase voltages, where L = {R, S, T}, are also determined from (7). If there are components of the voltage vector that do not participate in the current flow, the equivalent conductance G_e and the active component of the three-phase current $\|\mathbf{i}_\mathrm{a}\|$ will be determined incorrectly. Therefore, special attention should be paid to mathematical relationships.

4. Notes on Three-Phase Current Components Using Fortescue Transformation

In three-phase systems, when there is no symmetry in the power source, symmetrical voltage components with positive U^p, negative U^n, and zero U^z sequences are used to build mathematical relationships [80–83]. They are determined from (12), i.e., using three-phase symmetrical unit vectors of the positive $\mathbf{1}^\mathrm{p}$, negative $\mathbf{1}^\mathrm{n}$, and zero $\mathbf{1}^\mathrm{z}$ sequences, defined as

$$\mathbf{1}^\mathrm{p} = \begin{bmatrix} 1 \\ \alpha^2 \\ \alpha \end{bmatrix}, \ \mathbf{1}^\mathrm{n} = \begin{bmatrix} 1 \\ \alpha \\ \alpha^2 \end{bmatrix}, \ \mathbf{1}^\mathrm{z} = \begin{bmatrix} 1 \\ 1 \\ 1 \end{bmatrix}. \tag{11}$$

where α is the rotation operator which is $\alpha = e^{j120^{\mathrm{o}}} = e^{j\frac{2\pi}{3}}$.

$$\begin{bmatrix} \underline{U}^{\mathrm{z}} \\ \underline{U}^{\mathrm{p}} \\ \underline{U}^{\mathrm{n}} \end{bmatrix} = \frac{1}{3} \begin{bmatrix} 1 & 1 & 1 \\ 1 & \alpha & \alpha^2 \\ 1 & \alpha^2 & \alpha \end{bmatrix} \cdot \begin{bmatrix} \underline{U}_{\mathrm{R}} \\ \underline{U}_{\mathrm{S}} \\ \underline{U}_{\mathrm{T}} \end{bmatrix}. \tag{12}$$

From this point on, mathematical operations are performed individually on the crms values $\underline{U}^{\mathrm{p}}$, $\underline{U}^{\mathrm{n}}$, and $\underline{U}^{\mathrm{z}}$ as for a symmetric source. The transformation (12) is performed separately for each harmonic.

4.1. The Definition of Three-Phase Symmetrical Voltage in the Case of Multiple Harmonics

In three-phase unbalanced periodic and non-sinusoidal voltage waveforms for the nth harmonic (Figure 1), there is no symmetrical voltage component of zero sequence, and the following is true:

$$\underline{U}_{\mathrm{R},n} + \underline{U}_{\mathrm{S},n} + \underline{U}_{\mathrm{T},n} = 0, \tag{13}$$

In the case of symmetry, for each nth harmonic, the phase shift is equal to α or α^2. This can be written as an equation:

$$\begin{gathered} u_{\mathrm{L}} = \sqrt{2} \sum_{n=1} \left|\underline{U}_{\mathrm{L},n}\right| \cdot \cos[n(\omega_1 t + s_{\mathrm{L}} + \phi_n)] = \sqrt{2} \sum_{n=1} \left|\underline{U}_{\mathrm{L},n}\right| \cdot \cos\left(n\omega_1 t + \arg\left\{\underline{U}_{\mathrm{L},n}\right\}\right), \\ u_{\mathrm{L}} = \sqrt{2} \sum_{n=1} \Re e\left\{\underline{U}_{\mathrm{L},n} \cdot e^{jn\omega_1 t}\right\}, \end{gathered} \tag{14}$$

where L—the phase symbol, L = {R, S, T};

s_{L}—the phase shift equal to $s_{\mathrm{L}} = \left[0, \frac{-2\pi}{3}, \frac{2\pi}{3}\right]$, meaning $s_{\mathrm{R}} = 0$, $s_{\mathrm{S}} = \arg\left\{\alpha^2\right\}$, and $s_{\mathrm{T}} = \arg\{\alpha\}$;

φ_n—the phase shift between the current and voltage for the nth harmonic.

In (14) it can be seen that the argument of the complex number $\underline{U}_{\mathrm{L},n}$ contains the rotation vector α, the phase shift angle φ_n, and the nth harmonic order:

$$\arg\left\{\underline{U}_{\mathrm{L},n}\right\} \overset{\mathrm{def}}{=} n(s_{\mathrm{L}} + \phi_n). \tag{15}$$

Example 2. *For the instantaneous voltage value in R phase,* $u_{\mathrm{R}} = \sqrt{2} \cdot \Re e\left\{230e^{j\omega_1 t} + 20e^{j5(\omega_1 t + 2)} + 5e^{j7\omega_1 t}\right\}$ V, *it can be written in the time domain as follows:* $u_R = \sqrt{2} \cdot \{230\cos(\omega_1 t) + 20\cos(5(\omega_1 t + 2)) + 5\cos(7\omega_1 t)\}$ *V.*

In the case of symmetry, according to (14), the voltage curves in the remaining phases are

$$\begin{aligned} u_{\mathrm{S}} &= \sqrt{2} \cdot \left\{230\cos\left(\omega_1 t - \tfrac{2\pi}{3}\right) + 20\cos\left(5\left(\omega_1 t - \tfrac{2\pi}{3} + 2\right)\right) + 5\cos\left(7\left(\omega_1 t - \tfrac{2\pi}{3}\right)\right)\right\} \mathrm{V}, \\ u_{\mathrm{T}} &= \sqrt{2} \cdot \left\{230\cos\left(\omega_1 t + \tfrac{2\pi}{3}\right) + 20\cos\left(5\left(\omega_1 t + \tfrac{2\pi}{3} + 2\right)\right) + 5\cos\left(7\left(\omega_1 t + \tfrac{2\pi}{3}\right)\right)\right\} \mathrm{V}. \end{aligned}$$

The graphical waveforms of these voltages are presented in Figure 2.

In (14), the separation of the nth harmonic order and phase shifts, s_{L} and φ_n, simplifies the mathematical analysis of three-phase waveforms.

4.2. Using Fortescue Transformation in the Case of Multiple Harmonics

In the case of sinusoidal waveforms, the three-phase asymmetrical source is replaced by the sum of three symmetrical sources. Taking the phase R as the reference phase, from (12), we obtain

$$\underline{\mathbf{U}} = \underline{\mathbf{U}}^{\mathrm{z}} + \underline{\mathbf{U}}^{\mathrm{p}} + \underline{\mathbf{U}}^{\mathrm{n}} = \mathbf{1}^{\mathrm{z}}\underline{U}^{\mathrm{z}} + \mathbf{1}^{\mathrm{p}}\underline{U}^{\mathrm{p}} + \mathbf{1}^{\mathrm{n}}\underline{U}^{\mathrm{n}}. \tag{16}$$

where $\underline{\mathbf{U}} = \begin{bmatrix} \underline{U}_{\mathrm{R}} & \underline{U}_{\mathrm{S}} & \underline{U}_{\mathrm{T}} \end{bmatrix}^T$.

Similarly to (16), in reference [78], for non-sinusoidal periodic waveforms for the nth harmonic, the following relation is used:

$$\underline{\mathbf{U}}_n = \underline{\mathbf{U}}_n^{\mathrm{z}} + \underline{\mathbf{U}}_n^{\mathrm{p}} + \underline{\mathbf{U}}_n^{\mathrm{n}} = \mathbf{1}^{\mathrm{z}} \cdot \underline{U}_n^{\mathrm{z}} + \mathbf{1}^{\mathrm{p}} \cdot \underline{U}_n^{\mathrm{p}} + \mathbf{1}^{\mathrm{n}} \cdot \underline{U}_n^{\mathrm{n}}. \tag{17}$$

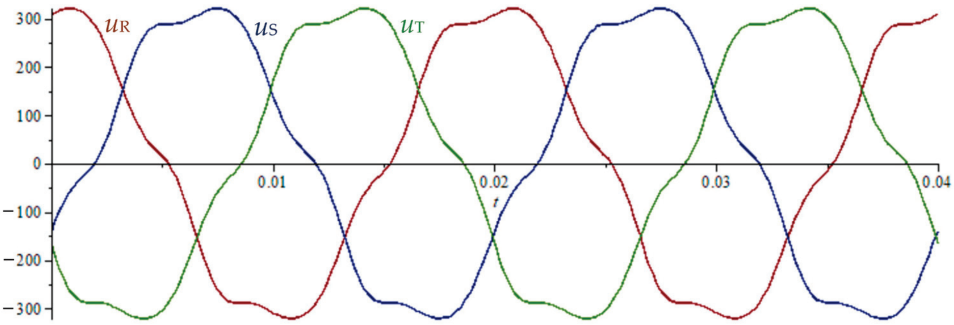

Figure 2. Symmetrical non-sinusoidal voltage waveforms from Example 2.

So far, in the case of periodic non-sinusoidal waveforms, the values of symmetrical components have been determined in the same way as for sinusoidal circuits—i.e., using transformation (12). For waveforms consisting of many harmonics, Formula (15) is valid. It follows that the turnover factor α is multiplied n times. Therefore, Equation (12) for the nth harmonic should look like the below:

$$\begin{bmatrix} \underline{U}_n^{\mathrm{z}} \\ \underline{U}_n^{\mathrm{p}} \\ \underline{U}_n^{\mathrm{n}} \end{bmatrix} \stackrel{\mathrm{def}}{=} \frac{1}{3} \begin{bmatrix} 1 & 1 & 1 \\ 1 & \alpha^n & \alpha^{2n} \\ 1 & \alpha^{2n} & \alpha^n \end{bmatrix} \cdot \begin{bmatrix} \underline{U}_{\mathrm{R},n} \\ \underline{U}_{\mathrm{S},n} \\ \underline{U}_{\mathrm{T},n} \end{bmatrix}, \tag{18}$$

while the inverse transformation is described by the following relationship:

$$\begin{bmatrix} \underline{U}_{\mathrm{R},n} \\ \underline{U}_{\mathrm{S},n} \\ \underline{U}_{\mathrm{T},n} \end{bmatrix} \stackrel{\mathrm{def}}{=} \begin{bmatrix} 1 & 1 & 1 \\ 1 & \alpha^{2n} & \alpha^n \\ 1 & \alpha^n & \alpha^{2n} \end{bmatrix} \cdot \begin{bmatrix} \underline{U}_n^{\mathrm{z}} \\ \underline{U}_n^{\mathrm{p}} \\ \underline{U}_n^{\mathrm{n}} \end{bmatrix}. \tag{19}$$

The new vectors $\mathbf{1}_n^{\mathrm{p}}$ and $\mathbf{1}_n^{\mathrm{n}}$ arise after raising the vectors shown in (11) to the nth power:

$$\mathbf{1}_n^{\mathrm{p}} \stackrel{\mathrm{def}}{=} (\mathbf{1}^{\mathrm{p}})^n = \begin{bmatrix} 1 \\ \alpha^{2\cdot n} \\ \alpha^n \end{bmatrix}, \ \mathbf{1}_n^{\mathrm{n}} \stackrel{\mathrm{def}}{=} (\mathbf{1}^{\mathrm{n}})^n = \begin{bmatrix} 1 \\ \alpha^n \\ \alpha^{2\cdot n} \end{bmatrix}. \tag{20}$$

The coefficients shown in (20) were called **multiplied three-phase unit vectors**.

When determining symmetric components using Fortescue transform in the presence of multiple harmonics, it is natural to raise the rotation factor α to the nth power. However, there is no formal note in the literature enabling such a transformation. Using the relationship between (18) and (19) is helpful in this case.

So far, the mathematical methods presented in [55] partially solved this problem by introducing additional vectors dependent on the nth harmonic. For example, the CPC theory [15,24] defines a coefficient β that depends on n and then multiplies it by the rotation vector α.

Example 3. *In the three-wire line from Figure 1, where the relationship* $\underline{U}_{\mathrm{R},n} + \underline{U}_{\mathrm{S},n} + \underline{U}_{\mathrm{T},n} = 0$ *is valid, the following voltage values were measured:*

$$\begin{aligned} u_{\mathrm{R}} &= \sqrt{2}\cdot\{300\sin(\omega_1 t) + 30\sin(5\omega_1 t) + 3\sin(9\omega_1 t)\}\ \mathrm{V}, \\ u_{\mathrm{S}} &= \sqrt{2}\cdot\{250\sin(\omega_1 t + s_{\mathrm{S}}) + 25\sin(5(\omega_1 t + s_{\mathrm{S}})) + 2\sin(9(\omega_1 t + s_{\mathrm{S}}))\}\ \mathrm{V}, \\ u_{\mathrm{T}} &= \sqrt{2}\cdot\left\{50\sqrt{31}\sin(\omega_1 t + 128.95^{\mathrm{o}}) + 5\sqrt{31}\sin(5\omega_1 t - 128.95^{\mathrm{o}}) + 5\sin(9\omega_1 t + 180^{\mathrm{o}})\right\}\ \mathrm{V}. \end{aligned} \tag{21}$$

The symmetric components (17) determined from (12) give the solution in the following form:

$$\begin{aligned} \underline{U}_n^{\mathrm{z}} &= \tfrac{1}{3}\left(\underline{U}_{\mathrm{R},n} + \underline{U}_{\mathrm{S},n} + \underline{U}_{\mathrm{T},n}\right), \\ \underline{U}_n^{\mathrm{p}} &= \tfrac{1}{3}\left(\underline{U}_{\mathrm{R},n} + \alpha\underline{U}_{\mathrm{S},n} + \alpha^2\underline{U}_{\mathrm{T},n}\right), \\ \underline{U}_n^{\mathrm{n}} &= \tfrac{1}{3}\left(\underline{U}_{\mathrm{R},n} + \alpha^2\underline{U}_{\mathrm{S},n} + \alpha\underline{U}_{\mathrm{T},n}\right). \end{aligned} \tag{22}$$

After substituting the numerical data, we get

$$\begin{bmatrix} \underline{U}_1^{\mathrm{p}} \\ \underline{U}_5^{\mathrm{p}} \\ \underline{U}_9^{\mathrm{p}} \end{bmatrix} = \begin{bmatrix} 275 + j\frac{25\sqrt{3}}{3} \\ \frac{5}{2} + j\frac{5\sqrt{3}}{6} \\ \frac{3}{2} + j\frac{7\sqrt{3}}{6} \end{bmatrix}, \begin{bmatrix} \underline{U}_1^{\mathrm{n}} \\ \underline{U}_5^{\mathrm{n}} \\ \underline{U}_9^{\mathrm{n}} \end{bmatrix} = \begin{bmatrix} 25 - j\frac{25\sqrt{3}}{3} \\ \frac{55}{2} - j\frac{5\sqrt{3}}{6} \\ \frac{3}{2} - j\frac{7\sqrt{3}}{6} \end{bmatrix}, \begin{bmatrix} \underline{U}_1^{\mathrm{z}} \\ \underline{U}_5^{\mathrm{z}} \\ \underline{U}_9^{\mathrm{z}} \end{bmatrix} = \begin{bmatrix} 0 \\ 0 \\ 0 \end{bmatrix}. \tag{23}$$

The same components determined from (19) give the following solution:

$$\begin{aligned} \underline{U}_n^{\mathrm{z}} &= \tfrac{1}{3}\left(\underline{U}_{\mathrm{R},n} + \underline{U}_{\mathrm{S},n} + \underline{U}_{\mathrm{T},n}\right), \\ \underline{U}_n^{\mathrm{p}} &= \tfrac{1}{3}\left(\underline{U}_{\mathrm{R},n} + \alpha^n\underline{U}_{\mathrm{S},n} + \alpha^{2n}\underline{U}_{\mathrm{T},n}\right), \\ \underline{U}_n^{\mathrm{n}} &= \tfrac{1}{3}\left(\underline{U}_{\mathrm{R},n} + \alpha^{2n}\underline{U}_{\mathrm{S},n} + \alpha^n\underline{U}_{\mathrm{T},n}\right), \end{aligned} \tag{24}$$

which, in this example, gives the following values:

$$\begin{bmatrix} \underline{U}_1^{\mathrm{p}} \\ \underline{U}_5^{\mathrm{p}} \\ \underline{U}_9^{\mathrm{p}} \end{bmatrix} = \begin{bmatrix} 275 + j\frac{25\sqrt{3}}{3} \\ \frac{55}{2} - j\frac{5\sqrt{3}}{6} \\ 0 \end{bmatrix}, \begin{bmatrix} \underline{U}_1^{\mathrm{n}} \\ \underline{U}_5^{\mathrm{n}} \\ \underline{U}_9^{\mathrm{n}} \end{bmatrix} = \begin{bmatrix} 25 - j\frac{25\sqrt{3}}{3} \\ \frac{5}{2} + j\frac{5\sqrt{3}}{6} \\ 0 \end{bmatrix}, \begin{bmatrix} \underline{U}_1^{\mathrm{z}} \\ \underline{U}_5^{\mathrm{z}} \\ \underline{U}_9^{\mathrm{z}} \end{bmatrix} = \begin{bmatrix} 0 \\ 0 \\ 0 \end{bmatrix}. \tag{25}$$

Comparing solutions (23) and (25), it should be noted that differences appear when $n > 1$. In practice, when n = 3k + 2 (where k is a natural number k ∈ {N$_+$}), the positive $\underline{U}_n^{\mathrm{p}}$ and negative $\underline{U}_n^{\mathrm{n}}$ symmetric components are swapped (Figure 3).

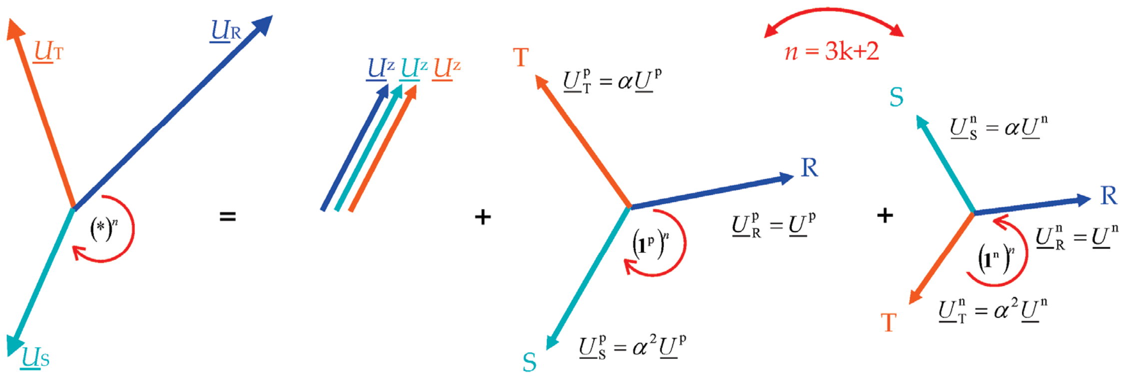

Figure 3. Graphical interpretation of multiplied three-phase unit vectors, where k is natural number k ∈ {N}, (*) is the real asymmetric vectors system.

The appearance of non-zero $\underline{U}_9^{\mathrm{p}}$ and $\underline{U}_9^{\mathrm{n}}$ components in Equation (23) also indicates an incorrect transformation. When the equation $\underline{U}_{\mathrm{R},n} + \underline{U}_{\mathrm{S},n} + \underline{U}_{\mathrm{T},n} = 0$ is satisfied, the appearance of zero-order harmonics (for n = 3k) is unnatural. In the functions shown in (21), in real systems, the amplitude of the ninth harmonic cannot be different from zero. This translates into zero values of a symmetrical component of the zero sequence $\underline{U}_n^{\mathrm{z}}$ for any nth harmonic.

5. Revised CPC Theory Definitions

The introduction of a correction to the decomposition into symmetrical components for periodic non-sinusoidal waveforms results in a different mathematical notation for electrical quantities for three-phase systems.

The vector of the supply voltage **u** as referenced to an artificial zero of the circuit (Figure 4) can be decomposed into symmetrical components of the positive and negative sequences:

$$\mathbf{u} = \sum_n \mathbf{u}_n = \sqrt{2}\Re e\left\{\sum_{n=1}\left(\mathbf{1}^{\mathrm{p}}\underline{U}_n^{\mathrm{p}} + \mathbf{1}^{\mathrm{n}}\underline{U}_n^{\mathrm{n}}\right)\cdot e^{jn\omega_1 t}\right\} = \mathbf{u}^{\mathrm{p}} + \mathbf{u}^{\mathrm{n}}. \tag{26}$$

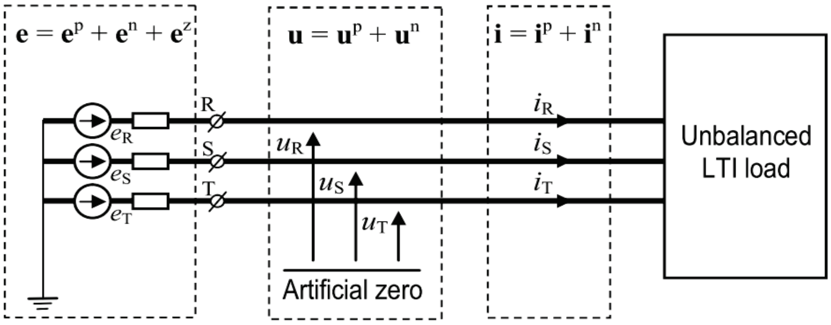

Figure 4. Decomposition into three-phase symmetrical components.

Symbols $\underline{U}_n^{\mathrm{p}}$ and $\underline{U}_n^{\mathrm{n}}$ in (26) denote the crms values of the symmetrical components of the nth order supply voltage harmonic with positive and negative sequences, respectively. They are

$$\begin{bmatrix}\underline{U}_n^{\mathrm{p}}\\ \underline{U}_n^{\mathrm{n}}\end{bmatrix} = \frac{1}{3}\begin{bmatrix}1 & \alpha^n & \alpha^{2n}\\ 1 & \alpha^{2n} & \alpha^n\end{bmatrix}\cdot\begin{bmatrix}\underline{U}_{\mathrm{R},n}\\ \underline{U}_{\mathrm{S},n}\\ \underline{U}_{\mathrm{T},n}\end{bmatrix}. \tag{27}$$

The three-phase rms value of the supply voltage, equal to the root of the sum of the squares of the effective values of the line voltages, is

$$\|\mathbf{u}\| = \sqrt{\sum_{\mathrm{L=R,S,T}}\|u_{\mathrm{L}}\|^2}, \text{ where } \|u_{\mathrm{L}}\| = \sqrt{\sum_{n=1}|\underline{U}_{\mathrm{L},n}|^2}. \tag{28}$$

The load in Figure 5 is equivalent with respect to the active power P to a balanced resistive load of conductance G_{b}:

$$G_{\mathrm{b}} = \frac{P}{\|\mathbf{u}\|^2}. \tag{29}$$

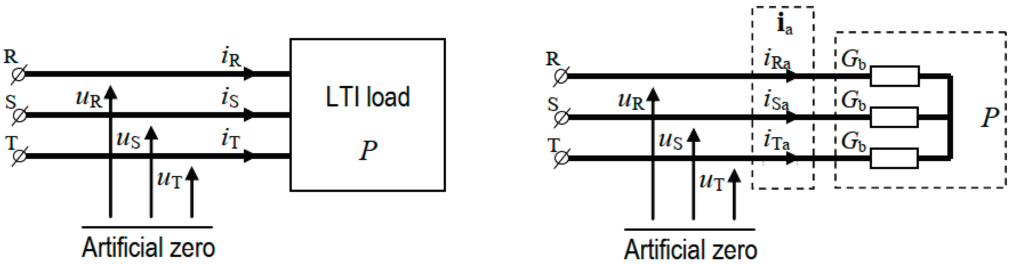

Figure 5. Three-phase load and balanced resistive load equivalent in terms of active power P.

The current flowing through such an equivalent load is called **the active current** and is as follows:

$$\mathbf{i}_{\mathrm{a}}=\begin{bmatrix} i_{\mathrm{Ra}} \\ i_{\mathrm{Sa}} \\ i_{\mathrm{Ta}} \end{bmatrix}=G_{\mathrm{b}}\mathbf{u}=\sqrt{2}\Re e\left\{\sum_{n=1} G_{\mathrm{b}}\left(\underbrace{\mathbf{1}^{\mathrm{p}}\underline{U}_{n}^{\mathrm{p}}}_{\mathbf{U}_{n}^{\mathrm{p}}}+\underbrace{\mathbf{1}^{\mathrm{n}}\underline{U}_{n}^{\mathrm{n}}}_{\mathbf{U}_{n}^{\mathrm{n}}}\right)\cdot e^{jn\omega_{1}t}\right\},\ \left\|\mathbf{i}_{\mathrm{a}}\right\|=G_{\mathrm{b}}\cdot\|\mathbf{u}\|. \tag{30}$$

As a result of calculating Equation (30), we obtain the same form as in the previous articles that did not take into account the multiplied vector in (27) because the $\underline{U}_n^{\mathrm{p}}$ and $\underline{U}_n^{\mathrm{n}}$ components are swapped—which does not affect the result in the case of their sum. However, to improve readability, the elementary division between these components should be maintained.

The load for each harmonic has active and reactive powers. For the nth order harmonic, they are as follows:

$$P_n=\Re e\left\{\mathbf{U}_n^T\cdot\mathbf{I}_n^*\right\}=\Re e\left\{\underline{U}_{\mathrm{R},n}\underline{I}_{\mathrm{R},n}^*+\underline{U}_{\mathrm{S},n}\underline{I}_{\mathrm{S},n}^*+\underline{U}_{\mathrm{T},n}\underline{I}_{\mathrm{T},n}^*\right\},\ Q_n=\Im m\left\{\mathbf{U}_n^T\cdot\mathbf{I}_n^*\right\}. \tag{31}$$

When for the nth order harmonic, the load is unbalanced, it is useful to define the balanced admittance $\underline{Y}_{\mathrm{b}}$. This admittance is already symmetrical and depends on the voltage $\mathbf{u}_n$, the active powers P_n, and the reactive powers Q_n, and it is as follows:

$$\underline{Y}_{\mathrm{b},n}=G_{\mathrm{b},n}+jB_{\mathrm{b},n}=\frac{P_n-jQ_n}{\|\mathbf{u}_n\|^2}=\frac{\underline{C}_n^*}{\sum\limits_{\mathrm{L=R,S,T}}\left|\underline{U}_{\mathrm{L},n}\right|^2}. \tag{32}$$

In definition (32), the symbol "C" was used instead of the symbol "S". This is an intentional action by the authors of [78] to avoid confusing the complex power $P_n + jQ_n$ with the apparent power S_n, which may also contain components other than only active and reactive power. These powers are shown in Figure 6.

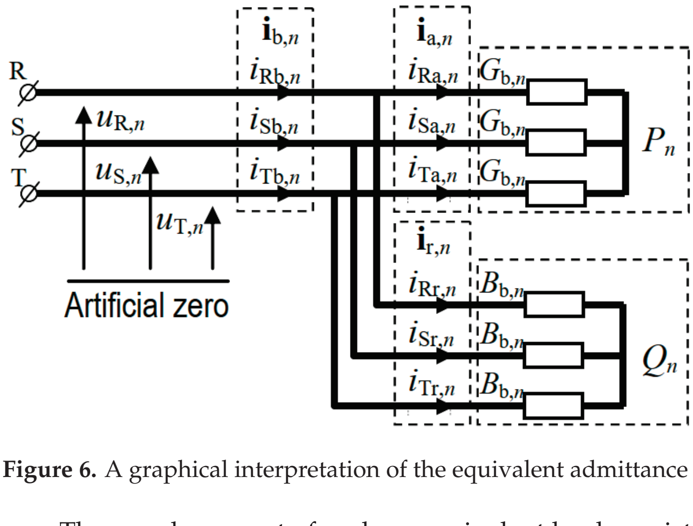

Figure 6. A graphical interpretation of the equivalent admittance for the nth order harmonic.

The supply current of such an equivalent load consists of the active current (33) and the reactive current (34):

$$\mathbf{i}_{\mathrm{a},n}=G_{\mathrm{b},n}\mathbf{u}_n=\sqrt{2}\Re e\left\{G_{\mathrm{b},n}\left(\mathbf{1}^{\mathrm{p}}\underline{U}_n^{\mathrm{p}}+\mathbf{1}^{\mathrm{n}}\underline{U}_n^{\mathrm{n}}\right)\cdot e^{jn\omega_1 t}\right\}, \tag{33}$$

$$\mathbf{i}_{\mathrm{r},n}=\sqrt{2}\Re e\left\{jB_{\mathrm{b},n}\left(\mathbf{1}^{\mathrm{p}}\underline{U}_n^{\mathrm{p}}+\mathbf{1}^{\mathrm{n}}\underline{U}_n^{\mathrm{n}}\right)\cdot e^{jn\omega_1 t}\right\}. \tag{34}$$

The $\mathbf{i}_\mathrm{r}$ current component appears in the load current because of the phase shift in the load current harmonics relative to the supply voltage harmonics. It can be considered as a **reactive current** component on the load, whose value is

$$\mathbf{i}_\mathrm{r} = \sum_n \mathbf{i}_{\mathrm{r},n} = \sqrt{2}\Re e\left\{\sum_{n=1} jB_{\mathrm{b},n}\left(\mathbf{1}^\mathrm{p}\underline{U}_n^\mathrm{p} + \mathbf{1}^\mathrm{n}\underline{U}_n^\mathrm{n}\right)\cdot e^{jn\omega_1 t}\right\}. \tag{35}$$

$\underline{Y}_{\mathrm{b},n}$ is the admittance of the equivalent balanced load for the nth order harmonic. In practice, the load may be unbalanced, so the nth order harmonic of the load current $\mathbf{i}_n$ may contain **the unbalanced current** component:

$$\begin{gathered}\mathbf{i}_{\mathrm{u},n} = \mathbf{i}_n - \mathbf{i}_{\mathrm{b},n} = \mathbf{i}_n - (\mathbf{i}_{\mathrm{a},n} + \mathbf{i}_{\mathrm{r},n}) = \sqrt{2}\Re e\left\{\underline{\mathbf{I}}_n - \underline{Y}_{\mathrm{b},n}\left(\mathbf{1}^\mathrm{p}\underline{U}_n^\mathrm{p} + \mathbf{1}^\mathrm{n}\underline{U}_n^\mathrm{n}\right)\cdot e^{jn\omega_1 t}\right\},\\ \mathbf{i}_\mathrm{u} = \sum_{n=1} \mathbf{i}_{\mathrm{u},n}.\end{gathered} \tag{36}$$

In the case of the (33) component, the relation holds:

$$\sum_{n=1} \mathbf{i}_{\mathrm{a},n} \neq \mathbf{i}_\mathrm{a} = G_\mathrm{b}\sum_{n=1} \mathbf{u}_n. \tag{37}$$

The inequality (37) occurs when the conductance $G_{\mathrm{b},n}$ for harmonic frequencies is different from the conductance G_b of the equivalent balanced load. The difference between these components is

$$\sum_{n=1} \mathbf{i}_{\mathrm{a},n} - \mathbf{i}_\mathrm{a} = \sqrt{2}\Re e\left\{(G_{\mathrm{b},n} - G_\mathrm{b})\cdot\left(\mathbf{1}^\mathrm{p}\underline{U}_n^\mathrm{p} + \mathbf{1}^\mathrm{n}\underline{U}_n^\mathrm{n}\right)\cdot e^{jn\omega_1 t}\right\} = \mathbf{i}_\mathrm{s}. \tag{38}$$

The current $\mathbf{i}_\mathrm{s}$ is called **a scattered current** component because conductances at harmonic frequencies $G_{\mathrm{b},n}$ are usually scattered around the balanced conductance G_b, and the current $\mathbf{i}_\mathrm{s}$ is the effect of this scattering.

The current of the load is presented as the sum of the specific components:

$$\mathbf{i} = \mathbf{i}_\mathrm{a} + \mathbf{i}_\mathrm{s} + \mathbf{i}_\mathrm{r} + \mathbf{i}_\mathrm{u}. \tag{39}$$

Because of the association of these load currents' components with physical phenomena in the load, these currents are referred to as the Currents' Physical Components (CPCs). However, this does not mean that these currents exist physically as they are mathematical entities, and not physical ones.

Each of these currents is associated with a different physical phenomenon in the load. The active current $\mathbf{i}_\mathrm{a}$ is related to the phenomenon of supplying active power P to the load. The scattered current $\mathbf{i}_\mathrm{s}$ is related to the phenomenon of changing the equivalent conductance $G_{\mathrm{b},n}$ with the harmonic order n. The reactive current $\mathbf{i}_\mathrm{r}$ is related to the phenomenon of phase shift in the current relative to the supply voltage for the nth harmonic. The unbalanced current $\mathbf{i}_\mathrm{u}$ is related to the load imbalance for the nth harmonic.

The correction introduced to the definitions presented so far in this article does not change the rms values of these components. Only the equations defined in the time domain change.

The situation becomes more complicated when the unbalanced current component is decomposed and the values of the compensator parameters are determined. In reference [61], the unbalanced current component was decomposed into two elements:

$$\mathbf{i}_\mathrm{u} = \mathbf{i}_\mathrm{u}^\mathrm{p} + \mathbf{i}_\mathrm{u}^\mathrm{n}. \tag{40}$$

The rms values of both components depend on the division into positive and negative sequence components. When Equation (17) is taken into account, these components can be represented in the following forms:

$$\mathbf{i}_{\mathrm{u}}^{\mathrm{p}} = \sqrt{2}\Re e\left\{\sum_{n=1}\left(\underline{Y}_{\mathrm{d},n}\underline{U}_{n}^{\mathrm{p}} + \underline{Y}_{\mathrm{u},n}^{\mathrm{n}}\underline{U}_{n}^{\mathrm{n}}\right)\mathbf{1}^{\mathrm{p}}e^{jn\omega_1 t}\right\}, \tag{41}$$

$$\mathbf{i}_{\mathrm{u}}^{\mathrm{n}} = \sqrt{2}\Re e\left\{\sum_{n=1}\left(\underline{Y}_{\mathrm{d},n}\underline{U}_{n}^{\mathrm{n}} + \underline{Y}_{\mathrm{u},n}^{\mathrm{p}}\underline{U}_{n}^{\mathrm{p}}\right)\mathbf{1}^{\mathrm{n}}e^{jn\omega_1 t}\right\}, \tag{42}$$

where, according to [61], the **voltage asymmetry dependent admittance is**

$$\underline{Y}_{\mathrm{d},n} = \underline{Y}_{\mathrm{e},n} - \underline{Y}_{\mathrm{b},n}, \tag{43}$$

the **equivalent admittance is**

$$\underline{Y}_{\mathrm{e},n} = \underline{Y}_{\mathrm{ST},n} + \underline{Y}_{\mathrm{TR},n} + \underline{Y}_{\mathrm{RS},n}, \tag{44}$$

and the **unbalanced admittances** are

$$\begin{aligned} \underline{Y}_{\mathrm{u},n}^{\mathrm{p}} &= -\left(\underline{Y}_{\mathrm{ST},n} + \alpha\underline{Y}_{\mathrm{TR},n} + \alpha^{2}\underline{Y}_{\mathrm{RS},n}\right), \\ \underline{Y}_{\mathrm{u},n}^{\mathrm{n}} &= -\left(\underline{Y}_{\mathrm{ST},n} + \alpha^{2}\underline{Y}_{\mathrm{TR},n} + \alpha\underline{Y}_{\mathrm{RS},n}\right). \end{aligned} \tag{45}$$

Admittances (43), (44), (45), and (32) depend on the admittance values of the three-phase load, while the rotation vector α acts in the same direction of rotation regardless of the harmonic order.

As a result of changing the values of the symmetrical voltage components $\underline{U}_{n}^{\mathrm{p}}$ and $\underline{U}_{n}^{\mathrm{n}}$, which should be determined from (27), the values of the current unbalanced components (41) and (42) will change. Defining these variables in a different way causes the instantaneous and rms values of both components to change, and the formulas determining the reactive compensator parameters must be re-developed.

6. Conclusions

The computational problems revealed in this article are important when performing mathematical analyses in electrical systems powered by sources with periodic non-sinusoidal waveforms.

1. The 90° shift in vectors discussed in point 2 is important in the case of time-domain notation and when comparing calculation results with oscilloscope measurements. To deal with this problem, one can use relationship (4), or each of the determined numerical values in the time domain can be shifted by a constant angle of −90°.
2. The problem shown in point 3 concerns a special case when components that do not participate in the transmission of the energy appear. An example is a situation when the load has a series capacitance, which, as is known, does not carry a DC component. In such a situation, Formula (8) should only be used for harmonics that are related to energetic interactions.
3. The method of notation of three-phase waveforms, discussed in point 4, revealed the need to change the definition of symmetrical components (18) when the instantaneous values are described by periodic non-sinusoidal functions. Determining the symmetric components using multiplied three-phase unit vectors (20) improves the mathematical notation. This observation revealed the need to improve the development of algorithms determining the unbalanced components and parameters of reactive compensators. These issues should be considered in further research.

The first problem may only occur when comparing the calculation results with the measurements and should instead be treated as a failure of the obligation to use a unified system for noting expressions in the time domain. This problem may arise when comparing power theories in the domain of instantaneous values.

The second problem concerns cases based on the CPC theory. Only in this theory is the equivalent conductance G_e determined. In other theories, the calculation for the DC component in a circuit connected in series with the capacitance is naturally omitted.

The third problem only applies to the case when Fortescue transformation is used. The degree of error committed cannot be determined in a general way. It depends on the degree of asymmetry of the three-phase voltage and current. Moreover, without knowledge of the equations determining the compensator parameters, based on (18) and (19), it is impossible to estimate the performance metric.

In summary, the remarks quoted cause imprecision in the description only in specific situations and do not affect the general relations between theories. A comparison of power theories with respect to the problems discussed is therefore pointless and would not contribute any cognitive information to this article.

It should be noted that this article discussed simple circuits and imperfections in power theory. However, the problems discussed here also affect the mathematical descriptions of power systems on a macro scale. Therefore, the significance of the presented results has great cognitive value.

In the case of cooperation between the power grid and power electronic converters, the problems occurring in the power description are still unclear. The CPC theory is based on the assumption that all harmonics are multiples of the fundamental harmonic. In practice, the switching frequency of the keys in a power electronic converter is not related to the frequency of the fundamental harmonic.

Future research should consider the correctness of analyses in the case of subharmonics and interharmonics [84].

Author Contributions: Conceptualization, K.Z.; methodology, K.Z.; validation, S.D.; formal analysis, K.Z.; investigation, K.Z.; resources, K.Z. and S.D.; data curation, K.Z.; writing—original draft preparation, K.Z.; writing—review and editing, K.Z.; visualization, K.Z.; supervision, K.Z.; project administration, K.Z. All authors have read and agreed to the published version of the manuscript.

Funding: This research received no external funding.

Institutional Review Board Statement: Not applicable.

Informed Consent Statement: Not applicable.

Data Availability Statement: The data is contained within the article.

Conflicts of Interest: The authors declare no conflicts of interest.

Abbreviations

Symbols

$\mathbf{1}$	three-phase symmetrical unit vector
a, b	Fourier series coefficients
α	rotation vector
B_b	balanced susceptance, S
C	capacitance, F
e	electromotive force, emf, V
φ	phase shift
G_b	balanced resistive load of conductance, S
G_e	equivalent conductance, S

$\mathbf{i}$	vector of instantaneous currents in three-phase system, A
$\underline{\mathbf{I}}$	vector of complex currents in three-phase system, A
i_R, i_S, i_T	instantaneous values of line currents, A
$\mathbf{i}_a$	active component of current—three-phase vector, A
$\mathbf{i}_r$	reactive component of current—three-phase vector, A
$\mathbf{i}_s$	scattered component of current—three-phase vector, A
$\mathbf{i}_u$	unbalanced component of current—three-phase vector, A
N	set of harmonics
P	active power, W
Q	reactive power, var
R	resistance, Ω
s_L	phase shift
t	time, s
T	repetition period of instantaneous value, rad/s
$\mathbf{u}$	vector of instantaneous voltages in three-phase system, V
$\underline{\mathbf{U}}$	vector of complex voltages in three-phase system, V
u_R, u_S, u_T	instantaneous voltage values relative to virtual star point, V
ω_1	basic pulsation, rad/s
X	reactance, Ω
$\underline{Y}_b$	balanced admittance, S
$\underline{Y}_d$	voltage asymmetry dependent admittance, S
$\underline{Y}_e$	equivalent admittance, S
$\underline{Y}_u$	unbalanced admittance, S
Subscripts, superscripts	
R, S, T, N	phase and neutral wires
n	harmonic number
L	phase number, L = {R, S, T}
p, n, z	positive, negative, zero sequence
Acronyms	
CPC	currents' physical components
crms	complex root mean square

References

1. Zajkowski, K. Reactive power compensation in a three-phase power supply system in an electric vehicle charging station. *J. Mech. Energy Eng.* **2018**, *2*, 75–84. [CrossRef]
2. Gubarevych, O.; Duer, S.; Melkonova, I.; Woźniak, M.; Paś, J.; Stawowy, M.; Rokosz, K.; Zajkowski, K.; Bernatowicz, D. Research and assessment of the reliability of railway transport systems with induction motors. *Energies* **2023**, *16*, 6888. [CrossRef]
3. Rosiński, A.; Paś, J.; Łukasiak, J.; Szulim, M. Safety Analysis for the Operation Process of Electronic Systems Used Within the Mobile Critical Infrastructure in the Case of Strong Electromagnetic Pulse Impact. In *Theory and Applications of Dependable Computer Systems*; DepCoS-RELCOMEX 2020; Advances in Intelligent Systems and Computing; Springer: Cham, Switzerland, 2020; Volume 1173. [CrossRef]
4. Zajkowski, K. An innovative hybrid insulation switch to enable/ disable electrical loads without overvoltages. *E3S Web Conf.* **2017**, *19*, 01033. [CrossRef]
5. Suproniuk, M.; Pas, J. Analysis of electrical energy consumption in a public utility buildings. *Przegląd Elektrotechniczny* **2019**, *95*, 97–100. [CrossRef]
6. Duer, S.; Woźniak, M.; Paś, J.; Zajkowski, K.; Bernatowicz, D.; Ostrowski, A.; Budniak, Z. Reliability Testing of Wind Farm Devices Based on the Mean-time Between Failures (MTBF). *Energies* **2023**, *16*, 1659. [CrossRef]
7. Siergiejczyk, M.; Pas, J.; Rosinski, A. Modeling of Process of Maintenance of Transport Systems Telematics with Regard to Electromagnetic Interferences. *Tools Transp. Telemat.* **2015**, *531*, 99–107.
8. Paś, J.; Rosiński, A.; Wiśnios, M.; Stawowy, M. Assessing the Operation System of Fire Alarm Systems for Detection Line and Circuit Devices with Various Damage Intensities. *Energies* **2022**, *15*, 3066. [CrossRef]
9. Wisnios, M.; Pas, J. The assessment of exploitation process of power for access control system. *E3S Web Conf.* **2017**, *19*, 01034. [CrossRef]

10. Hanzelka, Z. Blueprint for the combinatorial strategy in transactive energy-based control mechanism by using energy flexibility platform and interface. *CIRED Open Access Proc. J.* **2017**, *2017*, 1597–1600.
11. Taher, S.A.; Alaee, M.H.; Dehghani, A.Z. Model predictive control of PV-based shunt active power filter in single phase low voltage grid using conservative power theory. In Proceedings of the 2017 8th Power Electronics, Drive Systems & Technologies Conference (PEDSTC), Mashhad, Iran, 14–16 February 2017.
12. Czarnecki, L.S.; Bhattarai, P.D. A Method of Calculating LC Parameters of Balancing Compensators for AC Arc Furnaces. *IEEE Trans. Power Deliv.* **2017**, *32*, 688–695. [CrossRef]
13. Czarnecki, L.S.; Bhattarai, P.D. Reactive Compensation of LTI Loads in Three-Wire Systems at Asymmetrical Voltage. *Przegląd Elektrotechniczny* **2015**, *91*, 7–11. [CrossRef]
14. Czarnecki, L.S. Reactive and unbalanced currents compensation in three-phase circuits under nonsinusoidal conditions. *IEEE Trans.* **1989**, *IM-38*, 754–759.
15. Czarnecki, L.S.; Almousa, M. Adaptive balancing by reactive compensators of three-phase linear loads supplied by nonsinusoidal voltage from four-wire lines. *Am. J. Electr. Power Energy Syst.* **2021**, *10*, 32–42. [CrossRef]
16. Ginn, H.; Chen, G. Switching compensator control strategy based on CPC power theory. In Proceedings of the 2008 International School on Nonsinusoidal Currents and Compensation, Łagów, Poland, 10–13 June 2008.
17. Czarnecki, L.S.; Hsu, S.M. Thyristor controlled susceptances for balancing compensators operated under nonsinusoidal conditions. *IEE Proc.-Electr. Power Appl.* **1994**, *141*, 177–185. [CrossRef]
18. Zajkowski, K.; Rusica, I. The method of calculating LC parameters of balancing compensators in a three-phase four-wire circuit for an unbalanced linear receiver. *IOP Conf. Ser. Mater. Sci. Eng.* **2019**, *564*, 012134. [CrossRef]
19. Zajkowski, K. Two-stage reactive compensation in a three-phase four-wire systems at nonsinusoidal periodic waveforms. *Electr. Power Syst. Res.* **2020**, *184*, 106296. [CrossRef]
20. Busarello, T.D.C.; Simões, M.G. Power Quality Enhancement by Means of Shunt Compensators Based on the Conservative Power Theory. In Proceedings of the 2015 Clemson University Power Systems Conference (PSC), Clemson, SC, USA, 10–13 March 2015.
21. Haugan, T.S.; Tedeschi, E. Reactive and harmonic compensation using the conservative power theory. In Proceedings of the Tenth International Conference on Ecological Vehicles and Renewable Energies (EVER), Monte Carlo, Monaco, 31 March–2 April 2015.
22. Salim, C. Five-level series active power filter performances based on modified instantaneous reactive power theory for harmonic voltage disturbances compensation. In Proceedings of the 2017 5th International Conference on Electrical Engineering—Boumerdes (ICEE-B), Boumerdes, Algeria, 29–31 October 2017.
23. Savant, V.; Kadrolkar, A.; Gupte, S. Bidirectional tie-line inverter based on instantaneous reactive power theory for microgrid applications. In Proceedings of the 2017 Second International Conference on Electrical, Computer and Communication Technologies (ICECCT), Coimbatore, India, 22–24 February 2017.
24. Czarnecki, L.S. CPC–Based Reactive Balancing of Linear Loads in Four-Wire Supply Systems with Nonsinusoidal Voltage. *Przegląd Elektrotechniczny* **2019**, *95*, 19. [CrossRef]
25. Marcu, M.; Popescu, F.G.; Niculescu, T.; Pana, L.; Handra, A.D. Simulation of power active filter using instantaneous reactive power theory. In Proceedings of the 2014 16th International Conference on Harmonics and Quality of Power (ICHQP), Bucharest, Romania, 25–28 May 2014; pp. 581–585.
26. Haugan, T.S.; Tedeschi, E. Active power filtering under non-ideal voltage conditions using the conservative power theory. In Proceedings of the IEEE 13th Brazilian Power Electronics Conference and 1st Southern Power Electronics Conference (COBEP/SPEC), Fortaleza, Brazil, 29 November–2 December 2015.
27. Rosa, R.B.; Vahedi, H.; Godoy, R.B.; Pinto, J.O.P.; Al-Haddad, K. Conservative Power Theory Used in NPC-Based Shunt Active Power Filter to Eliminate Electric Metro System Harmonics. In Proceedings of the 2015 IEEE Vehicle Power and Propulsion Conference (VPPC), Montreal, QC, Canada, 19–22 October 2015.
28. Zhu, L.; Chang, L.; Yan, J.; Li, F.; Yang, Y.; Su, X.; Wu, Z.; Cui, D. Research on shunt active power filter based on the improved instantaneous reactive power theory. In Proceedings of the 2015 Sixth International Conference on Intelligent Control and Information Processing (ICICIP), Wuhan, China, 26–28 November 2015; pp. 459–464.
29. Abdullah, A.; Biswal, G.R.; Roy, A.K. Modeling and control of hybrid power filter using p-q theory. In Proceedings of the 2016 IEEE 1st International Conference on Power Electronics, Intelligent Control and Energy Systems (ICPEICES), Delhi, India, 4–6 July 2016.
30. Busarello, T.D.C.; Pomilio, J.A.; Simões, M.G. Passive Filter Aided by Shunt Compensators Based on the Conservative Power Theory. *IEEE Trans. Ind. Appl.* **2016**, *52*, 3340–3347. [CrossRef]
31. Hanzelka, Z.; Mondzik, A. Different LC power filter topologies—Effectiveness of reducing voltage distortion. *Renew. Energy Power Qual. J.* **2016**, *14*, 322–327.
32. Lada, M.Y.; Mohamad, S.S.; Gani, J.A.M.; Nawawi, M.R.M.; Kim, G.C. Reduction of harmonic using single phase shunt active power filter based on instantaneous power theory for cascaded multilevel inverter. In Proceedings of the 2016 IEEE International Conference on Power and Energy (PECon), Melaka, Malaysia, 28–30 November 2016.

33. Mboving, C.S.A.; Hanzelka, Z. Hybrid Power Active Filter—Effectiveness of Passive Filter on the Reduction of Voltage and Current Distortion. In Proceedings of the Electric Power Quality and Supply Reliability (PQ), Tallinn, Estonia, 29–31 August 2016.
34. Tobola, A.; Mikołajuk, K. Multiobjective Optimization Approach to the Active Power Filter Control. In Proceedings of the 17th International Conference Computational Problems of Electrical Engineering (CPEE), Sandomierz, Poland, 14–17 September 2016.
35. Tobała, A.; Mikołajuk, K. Reference Signal Detection for Voltage Harmonic Damping in Three-Phase Systems. In Proceedings of the 18th International Conference on Computational Problems of Electrical Engineering (CPEE), Kutna Hora, Czech Republic, 11–13 September 2017.
36. Moghaddam, F.K.; Farhangi, S. Improvement of the stand-alone DFIG performance feeding nonlinear and unbalanced loads using active and reactive power theory. In Proceedings of the 2015 IEEE Conference on Energy Conversion (CENCON), Johor Baru, Malaysia, 19–20 October 2015; pp. 128–133.
37. Zajkowski, K.; Rusica, I.; Palkova, Z. The use of CPC theory for energy description of two nonlinear receivers. *MATEC Web Conf.* **2018**, *178*, 09008. [CrossRef]
38. Zajkowski, K.; Duer, S.; Paś, J.; Pokorádi, L. Cooperation of a Non-Linear Receiver with a Three-Phase Power Grid. *Energies* **2023**, *16*, 1418. [CrossRef]
39. Bucolo, M.; Buscarino, A.; Famoso, C.; Fortuna, L.; Frasca, M. Control of imperfect dynamical systems. *Nonlinear Dyn.* **2019**, *98*, 2989–2999. [CrossRef]
40. Samet, H.; Ghanbari, T.; Ghaisari, J. Maximum performance of electric arc furnace by optimal setting of the series reactor and transformer taps using a nonlinear model. *IEEE Trans. Power Deliv.* **2015**, *30–32*, 764–772. [CrossRef]
41. Kumar, H.; Patra, J.; Yadav, A.; Pal, N. Power quality assessment and improvement of 3-phase 3-wire non-linear system using instantaneous power theory based DSTATCOM. In Proceedings of the 4th International Conference on Recent Advances in Information Technology (RAIT), Dhanbad, India, 15–17 March 2018.
42. Bielecki, S.; Skoczkowski, T. An enhanced concept of Q-power management. *Energy* **2018**, *162*, 335–353. [CrossRef]
43. Busarello, T.D.; Péres, A.; Mortezaei, A.; Simões, M.G. Application of the current decomposition of the Conservative Power Theory in Distributed Energy Resources. In Proceedings of the 12th IEEE International Conference on Industry Applications (INDUSCON), Curitiba, Brazil, 20–23 November 2016.
44. Busarello, T.D.C.; Mortezaei, A.; Peres, A.; Simoes, M.G. Application of the Conservative Power Theory Current Decomposition in a Load Power-Sharing Strategy Among Distributed Energy Resources. *IEEE Trans. Ind. Appl.* **2018**, *54*, 3771–3781. [CrossRef]
45. Janabi, A.; Wang, B. Hybrid matrix converter based on instantaneous reactive power theory. In Proceedings of the IECON 2015—41st Annual Conference of the IEEE Industrial Electronics Society, Yokohama, Japan, 9–12 November 2015.
46. Javadi, A.; Hamadi, A.; Al-Haddad, K. Three-phase power quality device tor weak Systems based on SRF and p-q theory controller. In Proceedings of the IECON 2015—41st Annual Conference of the IEEE Industrial Electronics Society, Yokohama, Japan, 9–12 November 2015.
47. Kong, X.; Yuan, Y.; Huang, H.; Wang, Y. Overview of the instantaneous reactive power theory in three-phase systems. In Proceedings of the 5th International Conference on Electric Utility Deregulation and Restructuring and Power Technologies (DRPT), Changsha, China, 26–29 November 2015; pp. 2331–2336.
48. Abbasi, M.; Tousi, B. Novel controllers based on instantaneous p-q power theory for transformerless SSSC and STATCOM. In Proceedings of the 2017 IEEE International Conference on Environment and Electrical Engineering and 2017 IEEE Industrial and Commercial Power Systems Europe (EEEIC/I&CPS Europe), Milan, Italy, 6–9 June 2017.
49. Mortezaei, A.; Simoes, M.G.; Savaghebi, M.; Guerrero, J.M.; Al-Durra, A. Cooperative control of multi-master-slave islanded microgrid with power quality enhancement based on conservative power theory. In Proceedings of the 2017 IEEE Power & Energy Society General Meeting, Chicago, IL, USA, 16–20 July 2017.
50. Oruganti, V.S.R.V.; Bubshait, A.S.; Dhanikonda, V.S.S.S.S.; Simões, M.G. Real-time control of hybrid active power filter using conservative power theory in industrial power system. *IET Power Electron.* **2017**, *10*, 196–207. [CrossRef]
51. Alaee, M.H.; Taher, S.A.; Dehghani, A.Z. Improved performance of single-phase shunt active power filter by using conservative power theory and model predictive control. In Proceedings of the 2018 9th Annual Power Electronics, Drives Systems and Technologies Conference (PEDSTC), Tehran, Iran, 13–15 February 2018.
52. Harirchi, F.; Simoes, M.G. Enhanced Instantaneous Power Theory Decomposition for Power Quality Smart Converter Applications. *IEEE Trans. Power Electron.* **2018**, *33*, 9344–9359. [CrossRef]
53. Souza, W.A.; Liberado, E.V.; Da Silva, L.C.; Paredes, H.K.; Marafão, F.P. Load Analyser Using Conservative Power Theory. In Proceedings of the International School on Nonsinusoidal Currents and Compensation 2013 (ISNCC 2013), Zielona Góra, Poland, 20–21 June 2013.
54. Busarello, T.D.C.; Pomilio, J.A. Synergistic operation of distributed compensators based on the conservative power theory. In Proceedings of the IEEE 13th Brazilian Power Electronics Conference and 1st Southern Power Electronics Conference (COBEP/SPEC), Fortaleza, Brazil, 29 November–2 December 2015.

55. Montoya, F.G.; Baños, R.; Alcayde, A.; Arrabal-Campos, F.M.; Pérez, J.R. Geometric Algebra Framework Applied to Symmetrical Balanced Three-Phase Systems for Sinusoidal and Non-Sinusoidal Voltage Supply. *Mathematics* **2021**, *9*, 1259. [CrossRef]
56. *IEEE 1459-2000*; IEEE Trial Use Standard for the Measurement of Electric Power Quantities Under Sinusoidal, Nonsinusoidal, Balanced and Unbalanced Conditions. IEEE: Piscataway, NJ, USA, 2000.
57. *IEEE 1459-2010*; IEEE Standard Definitions for the Measurement of Electric Power Quantities Under Sinusoidal, Nonsinusoidal, Balanced and Unbalanced Conditions. IEEE: Piscataway, NJ, USA, 2010.
58. Czarnecki, L.S. Orthogonal Decomposition of the Currents in a 3-Phase Nonilnear Asymmetrical Circuit with a Nonsinusoidal Voltage Source. *IEEE Trans. Instr. Measur.* **1988**, *37*, 30–34. [CrossRef]
59. Czarnecki, L.S. Currents' Physical Components (CPC) concept: A fundamental of Power Theory. *Przegląd Elektrotechniczny* **2008**, *84*, 28–37. [CrossRef]
60. Czarnecki, L.S.; Haley, P.M. Unbalanced Power in Four-Wire Systems and Its Reactive Compensation. *IEEE Trans. Power Deliv.* **2015**, *30*, 53–63. [CrossRef]
61. Czarnecki, L.S.; Bhattarai, P.D. CPC—Based Reactive Compensation of Linear Loads Supplied with Asymmetrical Non-sinusoidal Voltage. *Ann. Univ. Craiova* **2019**, *1*, 3–10.
62. Czarnecki, L.S. *Currents' Physical Components (CPC) in Systems with Semi-Periodic Voltages and Currents*; International School on Nonsinusoidal Currents and Compensation (ISNCC): Łagów, Poland, 2015.
63. Czarnecki, L.S.; Almousa, M. Conversion of fixed-parameters compensator in four-wire system with nonsinusoidal voltage into adaptive compensator. *Przegląd Elektrotechniczny* **2021**, *97*, 1.
64. Czarnecki, L.S.; Almousa, M. Adaptive Compensation of Reactive, Unbalanced and DC Currents of AC Arc Furnaces. *Przegląd Elektrotechniczny* **2023**, *99*, 14–20. [CrossRef]
65. Jeltsema, D.; Woude, J. Currents' Physical Components (CPC) in the time-domain: Single-phase systems. In Proceedings of the European Control Conference (ECC), Strasbourg, France, 24–27 June 2014.
66. Martell, F.; Izaguirre, A.; Macías, M. CPC Power Theory for Analysis of Arc Furnaces. In Proceedings of the 2015 International School on Nonsinusoidal Currents and Compensation (ISNCC), Łagów, Poland, 15–18 June 2015.
67. Li, W.; Rahmani, B.; Liu, G. Expansion of Current Physical Components (CPC) to Three-Phase Four-Wire Systems under Non-Ideal Waveforms by the AUPQS. In Proceedings of the 2016 Sixth International Conference on Instrumentation & Measurement, Computer, Communication and Control (IMCCC), Harbin, China, 21–23 July 2016.
68. Borges, A.M.; Alves, S. Currents' physical components (CPC): Case studies in single phase systems. In Proceedings of the 2018 Simposio Brasileiro de Sistemas Eletricos (SBSE), Niteroi, Brazil, 12–16 May 2018.
69. Calamero, N.; Beck, Y.; Shmilovitz, D. Defining the Unique Signatures of Loads Using the Currents' Physical Components Theory and Z-Transform. *IEEE Trans. Ind. Inform.* **2015**, *11*, 155–165. [CrossRef]
70. Popescu, M.; Bitoleanu, A.; Suru, V. Currents' Physical Components Theory Implementation in Shunt Active Power Filtering for Unbalanced Loads. In Proceedings of the International School on Nonsinusoidal Currents and Compensation 2013 (ISNCC 2013), Zielona Góra, Poland, 20–21 June 2013.
71. Mikulovic, J.; Sekava, T.; Skrbio, B. Currents' physical component (CPC) power theory for three-phase four-wire systems. In Proceedings of the Mediterranean Conference on Power Generation Transmission Distribution and Energy Conversion (MedPower), Athens, Greece, 3–6 November 2016; pp. 1–7. [CrossRef]
72. Grasso, F.; Luchetta, A.; Manetti, S.; Piccirilli, M.C.; Reatti, A.; Somma, M.; Cenghialta, F.; D'ANtuono, E. Improvement of Power Flow Analysis based on Currents' Physical Component (CPC) Theory. In Proceedings of the 2018 IEEE International Symposium on Circuits and Systems (ISCAS), Florence, Italy, 27–30 May 2018. [CrossRef]
73. Czarnecki, L.S.; Toups, T.N. Working and Reflected Active Powers of Three-Phase Loads. In Proceedings of the 12th International School on Nonsinusoidal Currents and Compensation (ISNCC), Łagów, Poland, 15–18 June 2015.
74. Izaguirre, A.R.; Macias, M.E.; Martell, F. Accurate CPC Power Analysis under Extreme EAF's Distortion Conditions. In Proceedings of the 12th International School on Nonsinusoidal Currents and Compensation (ISNCC), Łagów, Poland, 15–18 June 2015.
75. Zajkowski, K.; Rusica, I. Comparison of electric powers measured with digital devices relative to powers associated with distinctive physical phenomena. *IOP Conf. Ser. Mater. Sci. Eng.* **2019**, *564*, 012133. [CrossRef]
76. Zajkowski, K.; Smyczek, J. Simulation of overvoltages for switching off lagging load from mains. In Proceedings of the 2nd International Industrial Simulation Conference 2004, EUROSIS, Malaga, Spain, 7–6 June 2004; pp. 278–281.
77. Duer, S.; Zajkowski, K.; Scaticailov, S.; Wrzesień, P.; Slătineanu, L.; Merticaru, V.; Mihalache, A.; Dodun, O.; Ripanu, M.; Nagit, G.; et al. Analyses of the method development of decisions in an expert system with the use of information from an artificial neural network. *MATEC Web Conf.* **2018**, *178*, 07002. [CrossRef]
78. Bhattarai, P.D.; Czarnecki, L.S. Currents' Physical Components (CPC) of the Supply Current of Unbalanced LTI Loads at Asymmetrical and Nonsinusoidal Voltage. *Przegląd Elektrotechniczny* **2017**, *93*, 30–35. [CrossRef]
79. Fryze, S. Active, reactive and apparent power in circuits with nonsinusoidal voltages and currents. *Przegląd Elektrotechniczny* **1931**, *13*, 193–203.

80. Zajkowski, K.; Duer, S. Decomposition of the Voltages in a Three-Phase Asymmetrical Circuit with a Non-Sinusoidal Voltage Source. *Energies* **2023**, *16*, 7616. [CrossRef]
81. Czarnecki, L.S.; Haley, P.M. Power Properties of Four-Wire Systems at Nonsinusoidal Supply Voltage. *IEEE Trans. Power Deliv.* **2016**, *31–32*, 513–521. [CrossRef]
82. Czarnecki, L.S. Why the Power Theory has a Limited Contribution to Studies on the Supply and Loading Quality? In Proceedings of the 2018 18th International Conference on Harmonics and Quality of Power (ICHQP), Ljubljana, Slovenia, 13–16 May 2018. [CrossRef]
83. Czarnecki, L.S. Degradation of the Energy Transfer Effectiveness Described in Terms of Currents' Physical Components (CPC)-based Power Theory. In Proceedings of the 2017 International Symposium on Computer Science and Intelligent Controls (ISCSIC), Budapest, Hungary, 20–22 October 2017; pp. 39–48. [CrossRef]
84. Gnaciński, P.; Pepliński, M.; Szweda, M. Influence of Subharmonics and Interharmonics Voltage on Curents in Windings of an Induction Machine. *Maszyny Elektryczne* **2011**, *92*, 67–71.

MDPI AG
Grosspeteranlage 5
4052 Basel
Switzerland
Tel.: +41 61 683 77 34

Energies Editorial Office
E-mail: energies@mdpi.com
www.mdpi.com/journal/energies

MDPI

Academic Open
Access Publishing

mdpi.com

ISBN 978-3-7258-8950-1